Building up all-solid-state lithium batteries using sulfide solid electrolytes via liquid phase process

（液相法による硫化物固体電解質を用いた全固体リチウム電池の構築）

January, 2026

Doctor of Philosophy (Engineering)

Reiko Matsuda

松田　麗子

Toyohashi University of Technology

Abstract

Sulfide solid electrolytes (SSE) for all-solid-state lithium batteries (ASSLB) have been fabricated via liquid phase process, and their characteristics and the performance of batteries have also been evaluated in our research group of the department of electrical and electronic information engineering in Toyohashi University of Technology. SSEs in the $Li_2S-P_2S_5$ system were fabricated via liquid phase shaking (LS) process. In this study, the LS method was applied to synthesize Li_3PS_4 directly on the cathode active materials, $LiNi_{1/3}Mn_{1/3}Co_{1/3}O_2$ (NMC) to maintain good contact between the active material particles and SSE via liquid phased process, which was named SEED process. Spherical graphite (SG), anode active material, was coated with $Li_7P_2S_8I$ via SEED process because $Li_7P_2S_8I$ has high reduction resistance. To further improve ionic conductivity, a hetero-SE coating was fabricated with ultra-thin $Li_7P_2S_8I$ coating layer on the SG particles in combination with argyrodite-type SEs. A composite of 97 wt% SG, 3 wt% $Li_7P_2S_8I$, and argyrodite (SG: total SE = 70:30) exhibited excellent cycle performance in a half-cell, maintaining a capacity of 251 mAh g^{-1} after 100 cycles with a 95% capacity retention rate.

Phosphorous-containing SSE reacts with H_2O and generates toxic H_2S gas. To synthesize non-phosphorus SSE, Li_4SnS_4 and Li_3SbS_4, I offered ion-exchange process with aqueous solution in ambient air. In ion-exchange process, Na_2S was used for starting material, which is stable against H_2O. The obtained Na_4SnS_4 or Na_3SbS_4 were ion-exchanged to Li-ion using positive ion-exchange resins. The amounts of H_2S gas generation of these SSE were very low in 50 % relative humidity (RH) ambient air at room temperature.

To increase the energy density of ASSLB, the higher the weight ratio of active material in the cell, the better, which leads to a thinner separator. To decrease the weight ratio of SSE for the separators, self-standing SSE sheets were fabricated with SiO_2 fiber as a reinforcing filler using liquid phase process. Argyrodite-type $Li_{6-x}PS_{5-x}Cl_{1+x}$ and Li_4SnS_4 SSEs were dispersed in the mixed solvents with SiO_2 fiber. These slurries were poured into the polytetrafluoroethylene (PTFE) dishes and dried under low pressure. The LS method was applied to directly fabricate the $Li_7P_2S_8I$ SSE sheets with SiO_2 fiber. The thickness of these sheets was approximately 50 μm. Using obtained SSE-sheets and active materials sheets, thinner ASSLBs were built up and successfully operated.

Silicon (Si) is a promising anode active material for next generation ASSLB due to its large capacity. However, the volume change during charge-discharge cycles is more than 300 %, which decreases batteries capacity. Studying Si behavior as an anode active material is an especially

important issue. Using $Li_7P_2S_8I$ obtained by the LS method as SE, several Si anode composites were fabricated using different sizes of Si particles and evaluated the size effect for ASSLB performances. Further, the charge-discharge performances of the Si composites with different SSEs were evaluated using different SSE by scanning electron microscope (SEM) observation and Auger electron spectroscopy analysis. As a result, optimum microstructures to achieve good performance were clarified.

.

Table of Contents

Citation

The text of Chapter 3, in part, is a reprint of the material as it appears in

- R. Matsuda, E. Hirahara, N.H.H. Phuc, H. Tsukasaki, S. Mori, A. Matsuda, "Preparation of $LiNi_{1/3}Mn_{1/3}Co_{1/3}O_2/Li_3PS_4$ cathode composite particles using a new liquid-phase process and application to all-solid-state lithium batteries," Journal of the Ceramic Society of Japan, Vol. 126, No. 10, pp.826–831, 2018, published October 2018, © The Ceramics Society of Japan.
- Reiko Matsuda, Eito Hirabara, Nguyen Huu Huy Phuc, Hiroyuki Muto, Atsunori Matsuda, "Composite cathode of NCM Particles and Li_3PS_4-LiI electrolytes prepared using the SEED method for all-solid-state lithium batteries," IOP Conference Series Materials Science and Engineering, Vol. 429, No. 1, 012033 (5 pages) 2018, published under license by IOP Publishing Ltd.
- R. Matsuda, M. Takahashi, K. Hikima, H. Muto, A. Matsuda, "Hetero-coating of spherical graphite with sulfide solid electrolytes via the SEED process for all-solid-state lithium batteries," Journal of the Ceramic Society of Japan, Vol. 133, No. 9, pp. 1-8, 2025, published September 2025, © The Ceramics Society of Japan.

The text of Chapter 4, in part, is a reprint of the material as it appears in

- R. Matsuda, T. Kokubo, N.H.H. Phuc, H. Muto, A. Matsuda, "Preparation of ambient air-stable electrolyte Li_4SnS_4 by aqueous ion-exchange process," Solid State Ionics, Vol. 345, 115190 (4 pages), 2020, available online 19 December 2019, © 2019 published by Elsevier B.V.
- R. Matsuda, H. Muto, A. Matsuda, "Air-stable Li_3SbS_4–LiI electrolytes synthesized via an aqueous ion-exchange process and the unique temperature dependence of conductivity," ACS Applied Materials Interfaces, Vol. 14, No. 46, pp. 52440-52447, 2022, published November 2022, © 2022 American Chemical Society.

The text of Chapter 5, in part, is a reprint of the material as it appears in

- R. Matsuda, I. Y. Malya, T. Matsushita, K. Hikima, A. Matsuda, "Fabricating self-standing argyrodite electrolyte sheets containing SiO_2 fibers for all-solid-state batteries," Solid State Ionics, Vol. 417, 116684 (7 pages), 2024, available online September 2024, © 2024 published by Elsevier B.V.

The text of Chapter 6, in part, is a reprint of the material as it appears in

▪ R. Matsuda, A. Tanaka, K. Yanagihara, Y. Sasaki, K. Hikima, H. Muto, A. Matsuda, “Deterioration analysis of Si composite anodes for all-solid-state batteries during charge-discharge by Auger electron spectroscopy and scanning electron microscopy with energy dispersive spectroscopy,” Journal of Physical Chemistry C, Vol. 127, No. 33, pp. 6508–16514, 2023, published August 2023, © 2023 American Chemical Society.

The dissertation author was the first author. The co-authors in this publication directed, supervised, and co-worked on the research which forms the basis of this thesis.

Nomenclature

Abbreviations

abstract	SSE	sulfide solid electrolyte
	ASSLB	all-solid-state lithium battery
	LS	liquid phase shaking process
	NMC	$LiNi_{1/3}Mn_{1/3}Co_{1/3}O_2$
	SG	spherical graphite
	RH	relative humidity
	PTFE	polytetrafluoroethylene
	SEM	scanning electron microscope
Chapter 1	LIB	lithium-ion battery
	EV	electric vehicles
	SE	solid electrolyte
	ASSB	all-solid-state batterie
	ASSLIB	all-solid-state lithium ion battery
	LISICON	lithium super ionic conductor
	LGPS	Li_2S-GeS_2-P_2S_5 system
	LPS	Li_3PS_4
	LPSL	$Li_7P_2S_8I$
	HSAB	the fundamental principles of Hard and Soft Acids and Bases
	PVDF	polyvinylidene difluoride
	SEM	scanning electron microscope
	XRD	X-ray diffractometer
	RAMAN	Raman spectroscopy
	DTA-TG	differential thermal analysis- Thermogravimetry
	EDS	energy dispersive spectroscopy
	TEM	transmission electron microscope
	AES	Auger electron spectroscopy

	PEEK	polyetheretherketone
Chapter 2	SSE	sulfide solid electrolyte
	ASSLIB	all-solid-state lithium-ion battery
	LS	liquid phase shaking process
	LPS	Li_3PS_4
	DMC	dimethyl carbonate
	EA	ethyl acetate
	MM	mechanical milling
	EP	ethyl propionate
	LISICON	lithium super ionic conductor
	XRD	X-ray diffraction analysis
	MM	mechanical milling
	PEEK	polyetheretherketone
	LPSI	$Li_7P_2S_8I$
Chapter 3	LS	liquid phase shaking process
	LPS	Li_3PS_4
	NMC	$LiNi_{1/3}Mn_{1/3}Co_{1/3}O_2$
	EtOH	ethanol
	EP	ethyl propionate
	SEM	scanning electron microscope
	EDXS	energy dispersive X-ray spectroscopy
	TEM	transmission electron microscope
	XRD	X-ray diffractometer
	PEEK	polyetheretherketone
	$R_{SE,gb}$	grain boundary resistance of electrolyte
	$R_{SE/cathode}$	interfacial resistance between the electrolyte and active materials
	VGCF	vapor grown carbon fiber
	Li-In	lithium-indium

	SUS	stainless-steel
	SG	spherical graphite
Chapter 4	SE	solid electrolyte
	IE	ion-exchange
	IEW	ion exchanged water
	XRD	X-ray diffraction
	IC	ion chromatography
	ICP	inductively coupled plasma spectroscopy
	AA	atomic absorption analysis
	PEEK	polyetheretherketone
	TG-DTA	thermogravimetry-differential thermal analysis
	LSS	Li_4SnS_4
	NSS	Na_4SnS_4
	DC	direct-current
	PED	precession electron diffraction
	EDS	energy dispersive X-ray spectroscopy
	AB	acetylene black
	ICSD	inorganic crystal structure database
Chapter 5	ASSLIB	all-solid-state lithium ion battery
	SE	solid electrolyte
	PFAS	polyfluoroalkyl substances
	THF	tetrahydrofuran
	EP	ethyl propionate
	ACN	acetonitrile
	PTEF	polytetrafluoroethylene
	XRD	X-ray diffraction analysis
	SEM	scanning electron microscope
	NCM	$LiNiCoMnO_2$ (Ni:Co:Mn=5:2:3)

	LPSI	$Li_7P_2S_8I$
Chapter 6	ASSLIB	all-solid-state lithium ion battery
	SE	solid electrolyte
	argyro-SE	$Li_{5.5}PS_{4.5}Cl_{1.5}$ electrolyte
	LPSI-SE	$Li_7P_2S_8I$ electrolyte
	SEM	scanning electron microscope
	XRD	X-ray diffraction analysis
	EDS	energy dispersive spectroscopy
	AES	Auger electron spectroscopy
Chapter 7	ASSLIB	all-solid-state lithium ion battery
	LPS	Li_3PS_4
	LPSI	$Li_7P_2S_8I$
	LS	liquid phase shaking process
	SG	spherical graphite
	IE	ion exchange
	XRD	X-ray diffraction analysis
	TEM	transmission electron microscope
	SE	solid electrolyte

Chapter 1
General Introduction

Background ~understanding the history of lithium-ion batteries

Thanks to information technology, almost everything—from payments to applications—can now be handled online with digital equipment. This has created the need to carry a battery in our bag. We need lighter and safer batteries. For the establishment of a carbon-cycle society as a measure against global warming, environmentally conscious energy management is becoming increasingly important. Converting gasoline-powered vehicles to electric vehicles that use storage batteries as their main power source is essential for reducing carbon dioxide emissions. We require large quantities of high-capacity battery materials. Against this background, there is a great need for safe and reliable storage batteries with high energy density.

Research of lithium-ion batteries (LIB) as an advanced storage battery has rapidly evolved, enabling large-scale production for applications in electronic devices, electric vehicles (EVs) and households. The most widely used coin-type lithium batteries are primary batteries that use lithium metal as an anode active material. They use MnO_2 as a cathode active material. The typical product and its reaction equations for cathode and anode were shown in Fig. 1.1. Lithium metal has a large theoretical capacity, 3861 mAh g^{-1}, because it is one of the lightest materials. The capacities of major anode materials were shown in Table 1.1[1]. They have high energy density but are not suitable for repeated use.

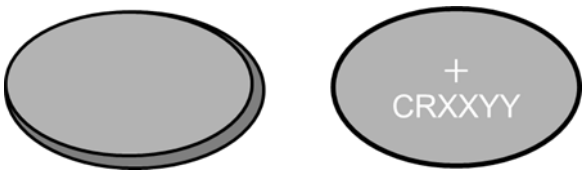

Coin type lithium batteries

Cathode: $\underset{(\mathrm{IV})}{MnO_2} + Li^+ + e^- \rightarrow \underset{(\mathrm{III})}{LiMnO_2}$

Anode: $Li \rightarrow Li^+ + e^-$

Fig. 1.1 Example of general-purpose coin-type lithium batteries and reaction equations at the cathode and anode.

Table 1.1 Capacity of several anode materials.

Anode material	Capacity / $mA\,hg^{-1}$
LiAl	790
Li_3Sb	564
Li_4Si	1919
$Li_{4.4}Sn$	790
LiC_6	340
Li	3861
SiO	1200
SnO_2	993
InO_2	747

T. Fujieda, *Materia Japan*, **38**, 488-492 (1999)[1)]

In the 1980s, lithium secondary batteries were actively researched. M.S. Wittingham et al. proposed an intercalation reaction of lithium-ion into TiS_2 and other transition metal dichalcogenide, which have a bilayer structure and take lithium-ion into and out reversibly[2)]. J. Goodenough et al. reported Li_xCoO_2 has a larger capacity than Li_xTiS_2, which was a suitable candidate as a cathode active material[3,4)]. The capacities and average voltage of several cathode materials were shown in Table 1.2.

A. Yoshino and Asahi Kasei corporation team established a basic concept of LIBs using lithium transition metal oxide like Li_xCoO_2 as a cathode, which has high capacity and lithium ions were contained in the structure, and carbon materials as an anode instead of lithium metal [4,5)]. Lithium batteries were worried about the danger of explosion because of a short circuit caused by lithium dendrite. Carbon-based materials, including graphite and carbon fiber composites, have been widely adopted as anode materials in place of lithium metal to enhance safety[5,6)]. To adopt carbon materials that have the capacity for lithium storage like graphite avoided from the explosion. The schematic image of a lithium-ion secondary battery was shown in Fig. 1.2. In the 1990s, LIBs became practical and were adopted as secondary batteries for a lot of electronic devices and home appliances. In recognition of these achievements, A. Yoshino, M.S. Wittingham and J. Goodenough were awarded the Nobel Prize in Chemistry in 2019.

Table 1.2 Capacities and average voltage of several cathode materials.

Cathode material	theoretical Capacity $mAhg^{-1}$	Nominal voltage V
$LiTiS_2$	239(180)	2.1
$LiCoO_2$	274(145)	3.7
$LiMn_2O_4$	140(110)	4.0
$LiNiO_2$	275(180)	3.5
$LiFePO_4$	170(150)	3.3
Li2FePO4F	100-148(115)	3.6
$LiCo_{1/3}Ni_{1/3}Mn_{1/3}O_2$	250(170)	3.6
$Li(Li_aNi_xMn_yCo_z)O_2$	(220)	4.2
$LiMn_xFe_{(1-x)}PO_4$	170(135)	3.7

Source: T. Fujieda, *Materia Japan*, **38**, 488-492 (1999)[1)]

Materials and Technology of LIB/ASSLIB (in Japanese), Edt. Y. Sakurai, (2021). Kagakujyoho Shuppan Co. Ltd, The Free Encyclopedia "WIKIPEDIA"

NEDO Secondary Battery Technology Development Roadmap 2013

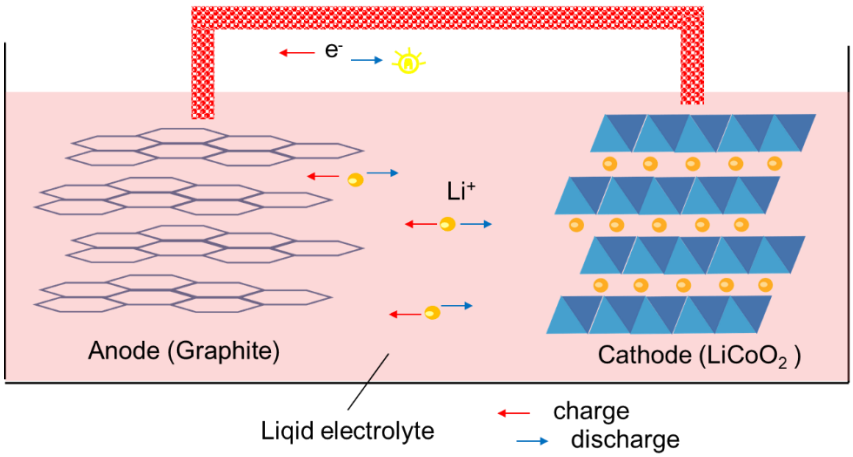

Fig. 1.2 Schematic image of a typical lithium-ion battery using $LiCoO_2$ as a cathode and graphite as an anode.

However, incidents of fire involving LIBs in computers, smartphones, and EVs highlight the need for improved safety[7]. Replacing flammable liquid electrolytes with nonflammable solid electrolytes (SEs) in all-solid-state batteries (ASSBs) addresses this concern. In Fig. 1.3, schematic images of a liquid type and an all-solid-state type of lithium-ion batteries were shown. High ionic conductivity is essential for electrolytes of ASSBs. A lot of ionic conductive materials of ceramics and polymers were researched for the solid electrolyte. Some works were picked up in Table 1.3.

Despite their safety advantages, SEs face challenges related to grain boundary resistance between active materials and SEs, necessitating mechanically and electrochemically stable interfaces for sustained performance during charge–discharge cycles.

As with many products, there are many challenges that need to be overcome in the development of all-solid-state lithium-ion batteries. Here, I picked up points that should have been considered when the batteries are built up. This thesis is structured according to the points.

1. Mass production
2. Contact between SE and active materials
3. Safety
4. Energy density
5. Next generation

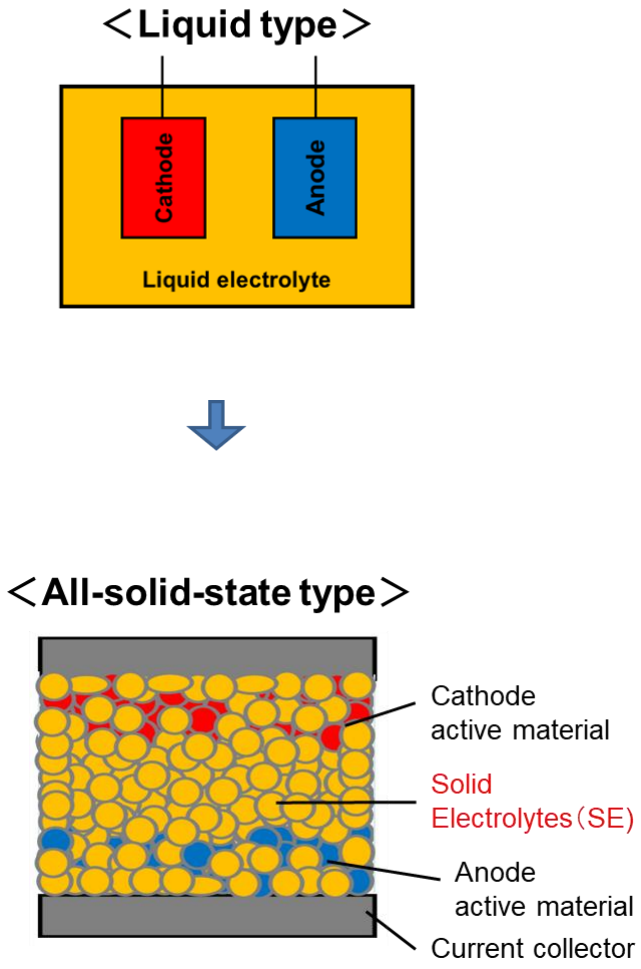

Fig. 1.3 Schematic images of lithium-ion battery, a liquid elecrtolyte type and an all-solid-state one.

Table 1.3 Ionic conductive materials of ceramics and polymers.

Electrolyte material	Structure	Conductivity at R.T. / S cm^{-1}
$Li_{0.34}La_{0.56}TiO_3$	Perovskite	1.2×10^{-3}
$Li_{3/8}Sr_{7/16}Ta_{3/4}M_{1/4}O_3$ (M = Zr, Hf)	Perovskite	3.8×10^{-4}
$Li_7La_3Zr_2O_{12}$	Garnet	$10^{-4} \sim 10^{-3}$
$Li_{1.3}Al_{0.7}Ge_{1.3}(PO_4)_3$	NASICON	3×10^{-3}
$Li_{2.88}PO_{3.73}N_{0.14}$ (LiPON)	Amorphous	3.3×10^{-6}
$Li_{2.9}Si_{0.45}PO_{1.6}N_{1.3}$ (LiSiPON)	Amorphous	2×10^{-5}
$70Li_2S{\cdot}30P_2S_5$	Glass	1.6×10^{-4}
$75Li_2S{\cdot}25P_2S_5$ (Li_3PS_4)	Glass	1.1×10^{-4}
$Li_7P_3S_{11}$	Glass-Ceramics	17×10^{-3}
Li_6PS_5Cl	Argyrodite	1.3×10^{-3}
$Li_{10}GeP_2S_{12}$	LGPS type	12×10^{-3}
$Li_{3.25}Ge_{0.25}P_{0.75}S_4$	Thio-LISCON	2.2×10^{-3}
Polyetylene glycol / $LiClO_4$	Polymer	2.2×10^{-3}
Siloxane / LiTFSI	Hybrid	2.2×10^{-3}

Materials and Technology of LIB/ASSLIB (in Japanese), Edt. Y. Sakurai, (2021). Kagakujyoho Shuppan Co. Ltd

T. Ikeda, *Ion-Conductive Polymer*, *J. Imaging Soc. Jpn.* **61,** 3, 225-235 (2022).

1.1 Sulfide solid electrolytes

Sulfide solid electrolytes (SSEs) are promising candidates for ASSBs owing to their high ionic conductivity and formability. For instance, argyrodite-type Li_6PS_5Cl exhibits ionic conductivity at room temperature on the order of 10^{-3} S cm^{-1}, while Cl-rich argyrodite, $Li_{5.5}PS_{4.5}Cl_{1.5}$, exhibits even higher conductivity[8-11]. R. Kanno et al. studied Li_2S-P_2S_5 systematically and proposed LISICON and Thio-LISICON family map in 2001[12]. The Li_2S-GeS_2-P_2S_5 system (LGPS), including thio-LISICON[13,14] phase, such as $Li_{10}GeP_2S_{12}$, exhibits exceptionally high ionic conductivity at room temperature of 1.2×10^{-2} S cm^{-1}, comparable to that of liquid organic electrolytes[15-17]. T. Minami et al. conducted vigorous research on ionic conductors of glass. Especially, his group members, M. Tatsumisago et al. have studied amorphous sulfide ionic conductors via mechanical milling using a planetary ball mill. Furthermore, amorphous Li_3PS_4 (LPS) fabricated via mechanical milling exhibits favorable ionic conductivity. These SSEs exhibit excellent formability and can be densified by pressing at room temperature[18-21]. LPS reacts gently with water and the generation of H_2S gas is more slowly than argyrodite and LGPS[22]. Also, the stability against lithium metal of $Li_7P_2S_8I$ (LPSI) is higher than other thio-LISICON family. The relationship between thio-LISICON family and LISOCON, and current major sulfide was shown in Fig. 1.4, which was cited from ref. 12. It indicates that sulfide SEs have higher ionic conductivity than oxide SEs.

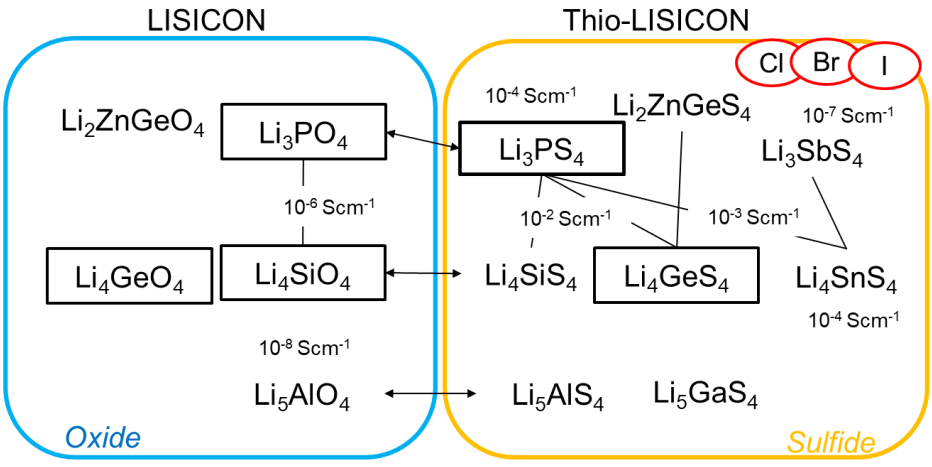

Fig. 1.4 The relationship of the thio-LISICON family and LISICON with their ionic conductivities. This figure was described by adapting a figure from *ref. 12)*.

1.2 Liquid phase shaking

These sulfide SEs such as argyrodite, LGPS, LPS and LPSI had been synthesized via sintering or melting in a quartz tube, which needed feverish temperature and was difficult to scale up. A. Hayashi et al. proposed mechanochemical synthesis of sulfide SEs, for example amorphous Li_2S-P_2S_5, using a planetary ball-mill [18]. The schematic image of mechanochemical method was shown in Fig. 1.5. This method does not simply mix the components; instead, it mechanically pulverizes them until they become amorphous. The advantage of this method is applicability to synthesize any kind of chemical composition via amorphous phase. However, this method is not suitable for mass production because it is difficult to scale up and time-consuming to retrieve samples.

Our research group of the department of electrical and electronic information engineering in Toyohashi University of Technology has been developing liquid-phase synthesis methods for sulfide SEs, especially LPS and LPSI, enhancing their applicability in ASSBs[23,24]. The advantage of the method can be enhancing reactions due to shaking with ZrO_2 balls and organic solvents. The schematic image of Liquid phase shaking method was shown in Fig. 1.6. The starting materials are shaken together with zirconia balls in the solvents. The key point of this process is the selection of suitable organic solvents for sulfide starting materials such as Li_2S and P_2S_5. This method can be manufactured with low energy and uses inexpensive tools. Furthermore, the equipment is safe due to its low energy consumption. Additionally, the reaction time is short, and sample recovery from the mixing medium is easy. Therefore, it is easily scalable. The details of the experiments were introduced in Chapter 2.

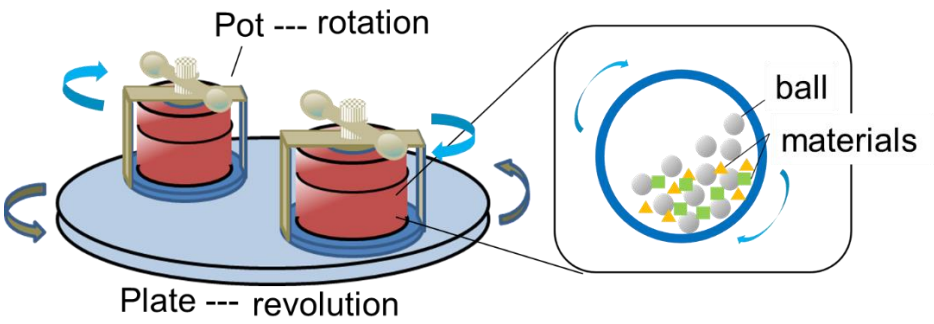

Fig. 1.5 Schematic image of mechanochemical method using a planetary ball mill.

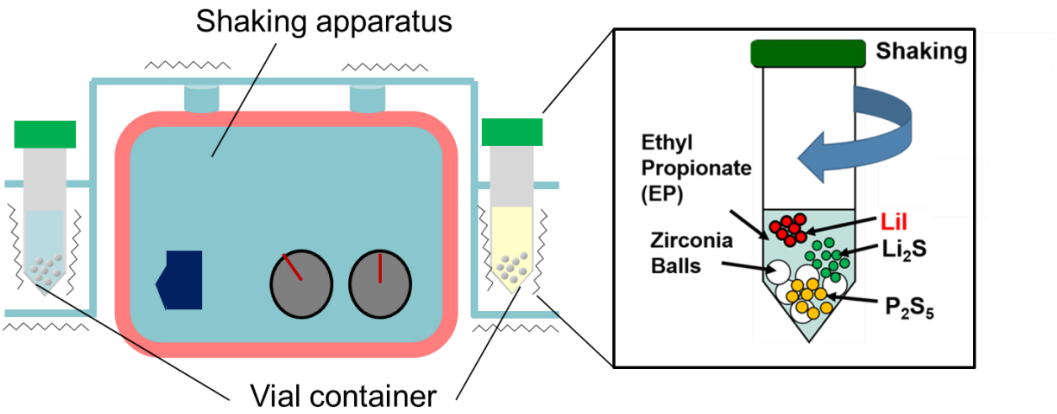

Fig. 1.6 Schematic image of shaking equipment for liquid phase shaking method.

1.3 Coating of active materials

To enhance interfacial contact between the active materials and SE, SSE coating has been applied via a liquid-phase method, wherein active material particles are mixed with SSEs dissolved in organic solvents followed by evaporation[25,26]. Several dry methods that eliminate the need for a liquid phase, such as pulsed laser deposition and dry coating via mechanical adsorption, have also been reported[27,28]. An alternative strategy, the SEED method, has been introduced, wherein LPS is directly synthesized on cathode-active material ($LiNi_{1/3}Mn_{1/3}Co_{1/3}O_2$ (NMC)) particles via a liquid-phase process[29]. In this approach, Li_2S is first deposited onto the active material particles as seed crystals, serving as nucleation sites for LPS growth. That is the reason for the name of "SEED method." The chemical reaction formula of Li_3PS_4-synthesis and schematic images of SEED method were shown in Fig. 1.7. Dividing the synthetic reaction step into two stages is an important advancement. The $Li_2P_2S_6$ solution is homogeneous, so the reaction proceeds uniformly on the active material. Therefore, the thin and meticulous coating is formed without gaps.

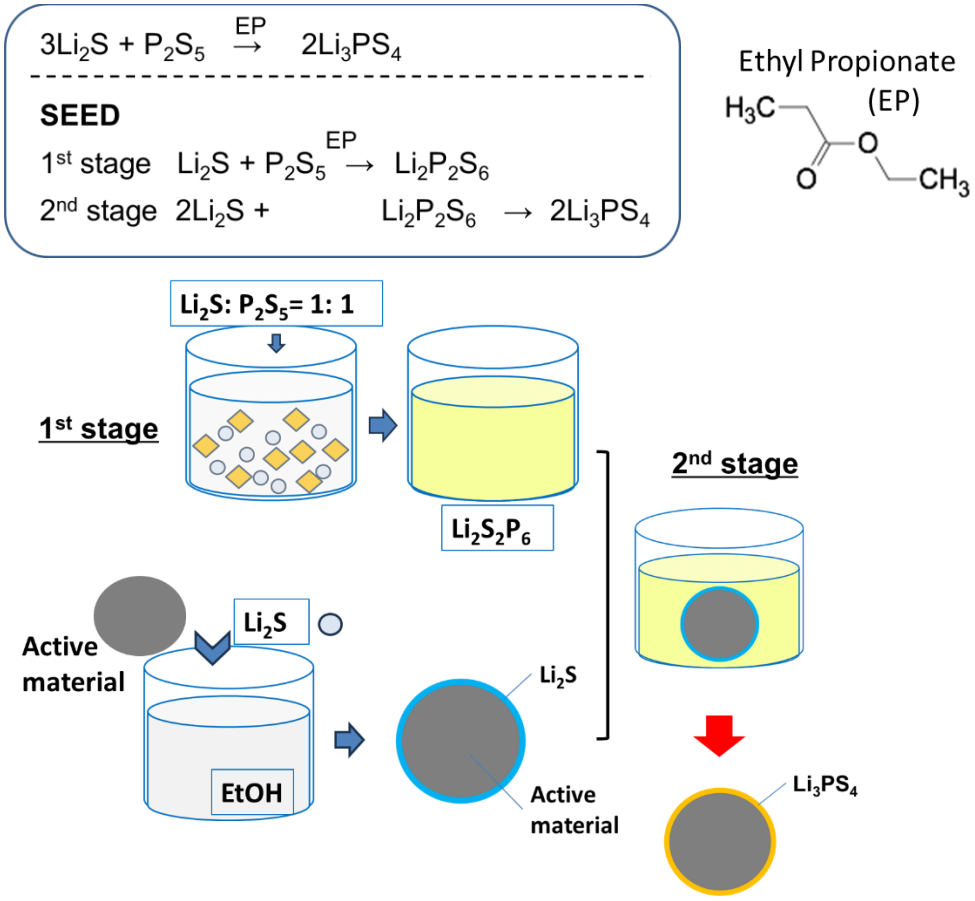

Fig. 1.7 Chemical reaction formula of L_3PS_4 synthesis and the schematic images of SEED method.

The schematic images of mixing with SEs were shown in Fig. 1.8. (a) is the active materials situation mixed with SE by hand in a mortal and partially aggregated. (b) is one mixed with SEs dispersed in a solvent and then evaporated the solvent. It is more homogeneous than (a), but some space remains between active materials and SEs. (c) is coating via SEED method, which has a wide contact area between active materials and SEs. It keeps the contact while expansion-contraction of active materials with charge-discharge cycles. ASSB cells incorporating NMC-LPS composites as cathode have shown excellent charge-discharge cycle performance. Furthermore, anode active materials like graphite were coated with LPSI, which is stable against lithium metal, via SEED method. The details of the experiments of SEED method were described in Chapter 3.

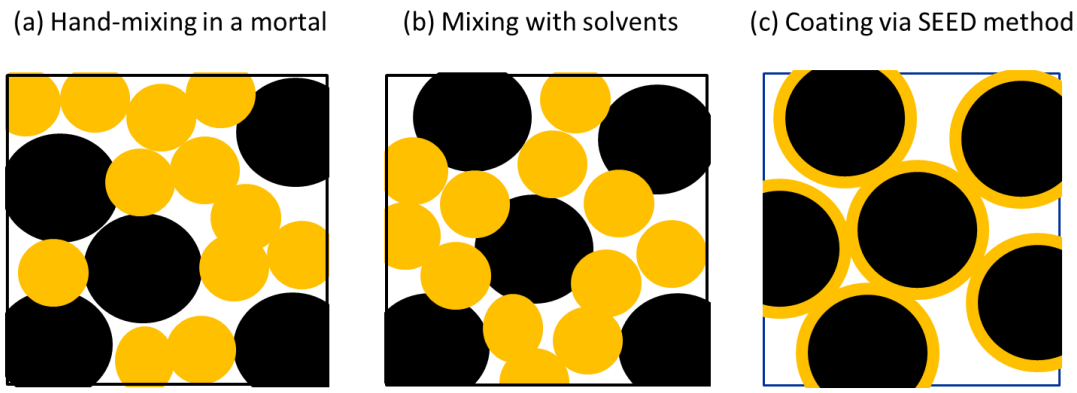

Fig. 1.8 Schematic images of active materials (black) mixed with SEs (yellow).

1.4 Air stable sulfide solid electrolytes

These sulfide-based SEs need to be treated in a glove box filled with argon, since they react with H_2O and generate H_2S gas when they are exposed to an ambient atmosphere. The synthesis under argon atmosphere is increased the fabrication cost and is an obstacle for mass production. Furthermore, the risk of H_2S gas generation is a cause for concern. Batteries are used in devices people wear, such as smart phones and small fans. Recently, the amount of their usage has increased dramatically. Working environments of the batteries production factory should be careful to be healthy. Therefore, the improvement of air stable SEs is a particularly important issue.

According to the fundamental principles of Hard and Soft Acids and Bases (HSAB) [30], the sulfides containing Sn, As and Sb are stable against H_2O, compared to sulfides containing P like LGPS. In the Fig. 1.9, schematic images of the principal of HSAB. Hard base containing phosphorus readily reacts with H_2O to form phosphates and then generate H_2S gas. Recently, the air-stable sulfide electrolyte Li_4SnS_4 was prepared from the corresponding starting materials by heat-treating in a quartz ampoule sealed under vacuum[26] and by milling in an argon gas atmosphere[31]. The ionic conductivities of these electrolytes reached 1.0×10^{-4} S cm^{-1} at room temperature.

In other words, Li_4SnS_4 is stable against water, suggesting it can be synthesized in air. So, I proposed that the fabrication method of Li_4SnS_4 using water as a solvent in the ambient air taking advantage of the fact that Sn sulfide does not react with water. Further, sodium sulfide is stable in the ambient air compared with lithium sulfide, sodium sulfide was used as a starting material. Fig.1.10 shows the schematic images of ion-exchange and that chemical formula. First, Na_4SnS_4 aqueous solution was prepared and ion-exchanged using positive ion exchange resin from Na-type to Li-type. The progression of ion exchange reactions is driven by the ion selectivity shown on Fig. 1.10. The resultant Li_4SnS_4 aqueous solution after ion-exchange was freeze dried and heat-treated to obtain Li_4SnS_4 powders. It was named ion-exchange method. Also, air-stable Li_3SbS_4-LiI SEs were synthesized by the ion-exchange and freeze drying. The temperature dependence of ionic conductivity of Li_3SbS_4-LiI was unique behavior, which drastically increased at 60 ℃. This suggests hydrated water engages in crystals and that it is likely to be a concentrated solution. The details of the aqueous ion exchange process and characteristics of Li_4SnS_4 and Li_3SbS_4-LiI thus obtained were described in Chapter 4.

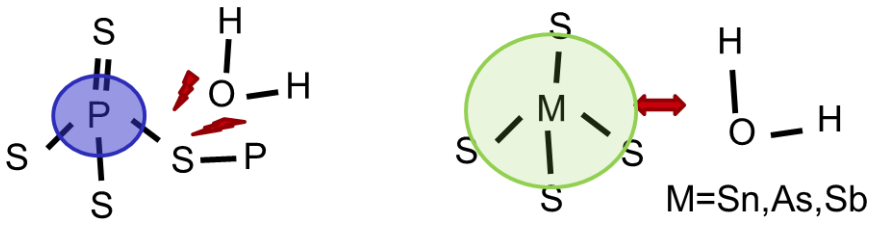

Fig. 1.9 Schematic images of the fundamental principles of Hard and Soft Acids and Bases.

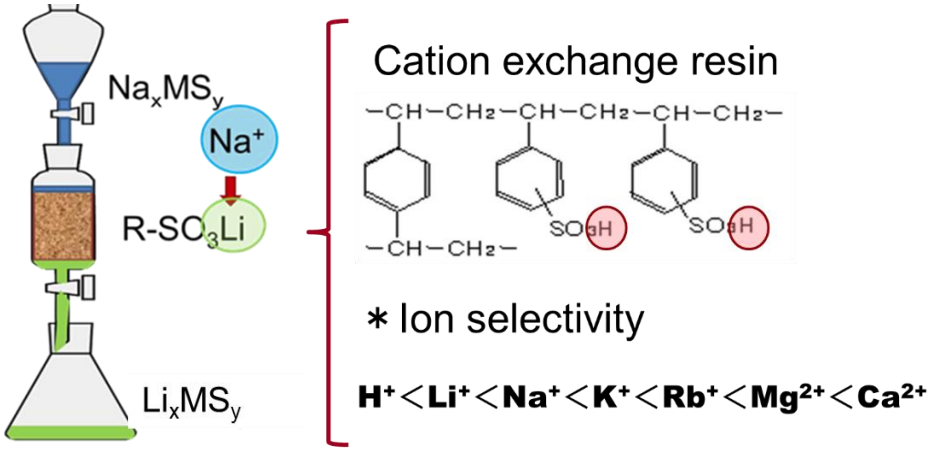

$$4R\text{-}(Ph\text{-}SO_3^-\,Li^+) + 4Na^+ + SnS_4^{4-} \rightarrow 4R\text{-}(Ph\text{-}SO_3^-\,Na^+) + 4Li^+ + SnS_4^{4-}$$

Fig. 1.10 Schematic images of ion-exchange and the chemical reaction formula.

1.5 Sulfide solid electrolyte thin sheets for separator

To improve the battery energy density, it is necessary to increase the ratio of active materials in ASSLIB. Therefore, the SE separator of an ASSLIB must be thin. The schematic image of ASSLIB using a thin SE sheet is shown in Fig. 1.11. Many challenges in fabricating thin SE sheets have been reported. Jingyi Wu et al. reviewed these thin SE-separator-related studies[32]. They reported that sulfide SEs such as Li_3PS_4 and Li_6PS_5Cl have been dissolved in organic solvents and subsequently composed with organic polymer sheets[33-35]. These organic polymer-supported SE sheets exhibited good flexibility. In particular, SE sheets using non-woven polyvinylidene difluoride (PVDF) had good flexibility and heat stability, and ASSLIB cells constructed using these sheets showed excellent cycle performance[36,37]. I have summarized these works in Table 1.4. However, these works used supported sheets, which is difficult to uniformly permeate SE-solution. Also, Li_3PS_4 and Li_6PS_5Cl dissolved in solvents such as ethanol exhibited low ionic conductivities when they were re-dried and heat-treated[38]. These sheets cannot be heat treated with appropriate high temperature because of containing organic polymers. Therefore, I considered adding SiO_2 fiber as a supporting filler that can withstand heat treatment. The SiO_2 fiber was shaken to the appropriate size in the centrifuge tube made of polypropylene with zirconia balls and organic solvents like ethyl propionate. The fiber-dispersed slurry was added to the Li_6PS_5Cl slurry and resultant mixture was poured in the plate, then dried at 300 ℃ under low pressure. The sheet can successfully take out from the plate. In the Fig.1.12, preparation flow of electrolyte sheets, previous and this work were shown. Using the obtained SE sheets, ASSLIB was built up and it showed good charge-discharge performance. Fabrication of self-standing electrolyte sheets using SiO_2 fiber for ASSBs described in detail in Chapter 5.

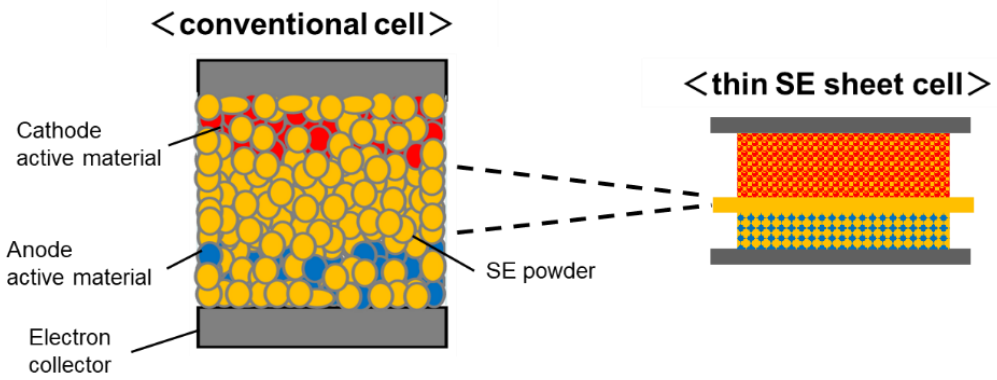

Fig. 1.11 Schematic images of ASSLIB using SE powders and a thin SE sheet.

Table 1.4 Previous works of electrolyte sheets [32]

SSEcomp	method	thickness[㎛]	σ_{25}[S/cm]
PEO	Melt infiltration to Polyimide fibers	10	6.7×10^{-6}
LLZO/PEO	in situ polymerization/tape	36	1.0×10^{-4}
LPS	Infiltration to Kevlar fibers	100	3.0×10^{-4}
LPS[Cl,Br]	Infiltration to Polyimide fibers	70	2.0×10^{-4}

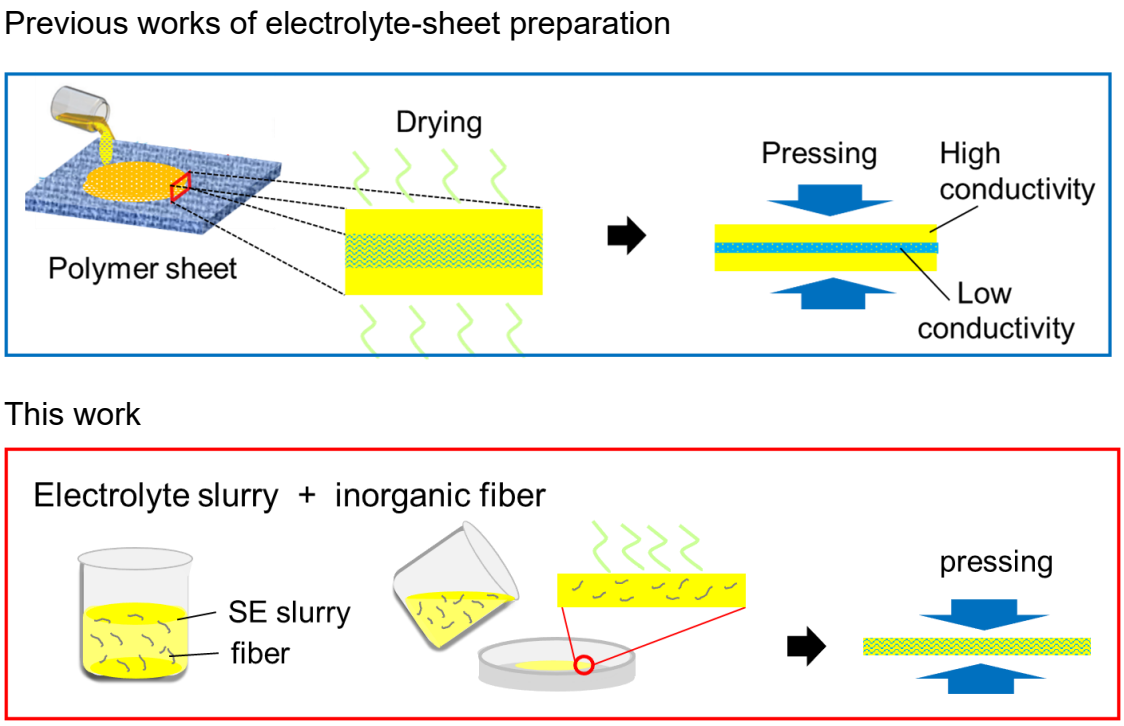

Fig. 1.12 Preparation flow of electrolyte sheets, previous and this work.

1.6 Next generation batteries

Recently, the electrification of vehicles and advancements in robotics have led to an increasing demand for batteries with high capacity and high energy density. Silicon (Si) is considered an important material as an anode for ASSLIB while designing a high-energy density battery due to its large theoretical capacity of 4200 mAh g^{-1}. To enhance the capacity of the ASSLIBs, the use of sulfur composite cells such as S or Li_2S composites as cathode materials are investigated[39,40]. These materials can achieve a capacity of more than 1000 mAh g^{-1}, which suggests that anodes with larger capacities are required. Table 1.5 shows comparison of theoretical capacities cathode vs. anode.

Table 1.5 Comparison of theoretical capacities of cathode and anode active materials.

Cathode	Theoretical cap. mAh g^{-1}	Anode	Theoretical cap. mAh g^{-1}
$LiNi_xCo_yMn_zO_2$	250～	Graphite	372
$LiFePO_4$	170	Silicon	4200
Li_2S	1170	Metallic Li	3860
S	1672	Li alloy	～1000

In literature, several attempts have been made to utilize Si as an anode in liquid-type lithium batteries; however, it was reported that the anodes were damaged and developed cracks and fractures due to large volume changes of Si by approximately 300 % during the charge–discharge cycles [41, 42] . Studies on ASSLIB using Si as an anode suggest that one of the problems was the rapid capacity reduction resulting from cracks at the boundary of Si particles [43, 44]. The surface roughness findings of Si particles after charge–discharge cycles using cross-section scanning electron microscopy (SEM) have been reported [45]. Meanwhile, the research on ASSLIB using Si anode is limited; hence, it is necessary to further evaluate the degradation of the Si anode. In this thesis, characterization of Si anode in ASSBs is reported in Chapter 6, and general conclusions with future works were summarized in Chapter 7.

1.7 Experimental equipment

1.7.1 Material characterization

Electrolytes and active materials prepared in this work were evaluated using an X-ray diffractometer (XRD; Ultima IV or Smart Lab, Rigaku) for structure analysis of crystals, Raman spectroscopy (RAMAN; NRS-3100 or -4500, Jasco) for detection of chemical species, differential thermal analysis- Thermogravimetry (DTA-TG; Rigaku) for assessing structure changes and solvent content.

These materials were observed using scanning electron microscopy (SEM; S4800, Hitachi or JEM-2100F, JEOL) and energy dispersive spectroscopy (EDS; HORIBA, OXFORD, or JEOL) for elemental analysis. A transmission electron microscope (TEM; JEOL) was used to observe the detailed structure of the material. These observations were carried out with the cooperation of Prof. Mori and Dr. Tsukasaki from Osaka Metropolitan University, and JEOL Co. Ltd.

The equipment used for this analysis is general-purpose equipment, and detailed explanations of their principles are omitted here.

Auger electron spectroscopy (AES) was used for cross section analysis in Chapter 6. Some explanations regarding the characteristics of this analytical method will be provided in comparison with SEM-EDS. AES involves observing Auger electrons emitted by electron irradiation. They have the specific energy of the material, enabling the identification of its composition. Figure 1.13 shows the schematic diagram of Auger effect, with an auger electron and its energy (E_{Auger}). Since the mean free path of Auger electrons is several nm, only Auger electrons emitted from the very surface of the sample are observed. Therefore, this method is widely used for surface analysis of samples. On the other hand, EDS analysis also performs elemental analysis of the sample using characteristic X-rays obtained from electron irradiation. To obtain characteristic X-rays, irradiation with a relatively high energy level is required. In this work, I used AES for cross section analysis of silicon anode with the cooperation of JEOL Co. Ltd. in Chapter 6. It is considered particularly suitable for analyzing surface condition and light elements.

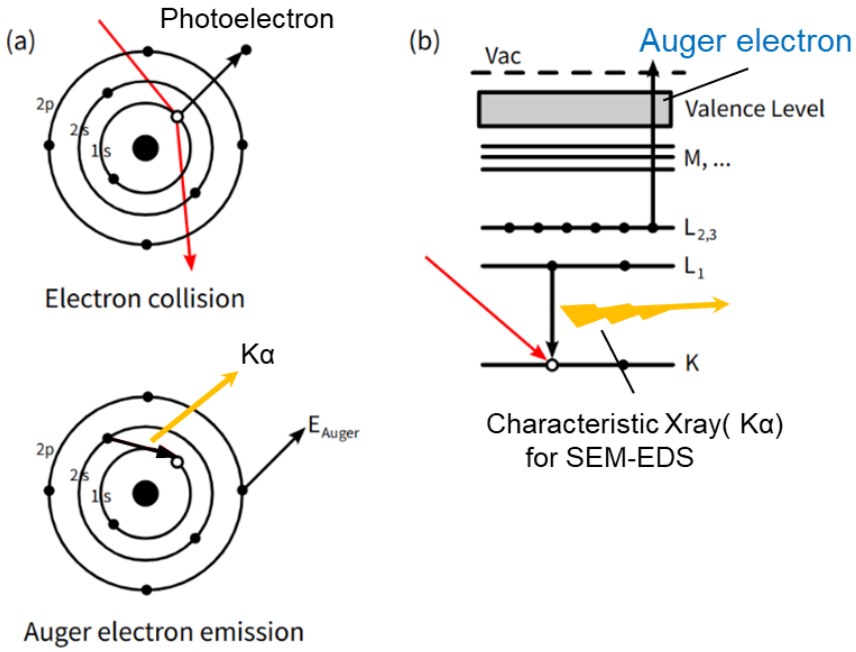

Fig. 1.13 This is a series of schematic drawings of the Auger effect. (a) provides a sequential view of Auger transitions in terms of atomic orbital energy (increasing radially) while (b) provides the same information in condensed format using spectroscopic notation. This figure is quoted from Wikipedia as follows and added some explanations.

https://ja.wikipedia.org/wiki/%E3%82%AA%E3%83%BC%E3%82%B8%E3%82%A7%E9%9B%BB%E5%AD%90#/media/%E3%83%95%E3%82%A1%E3%82%A4%E3%83%AB:Auger_Process.svg

1.7.2 Electrochemical characterization

Sulfide based SEs show high ionic conductivity, which causes to improve charge-discharge performance for all-solid-state lithium-ion batteries. The ability of ionic conduction is the most prominent issue. The temperature dependence of the total conductivity of the samples was measured using alternating-current impedance spectroscopy (EIS; SI 1260, Solatron) from 1 MHz to 10 Hz under dry Ar flow. In the Fig.1.14, schematic drawings of measurement cell. The 80 mg samples of the SE powder were placed in a holder made of polyetheretherketone (PEEK) and sandwiched between two stainless steel rods. The samples were pressed into a pellet of about 0.5 mm in thickness and 10.0 mm in diameter by uniaxial pressing at a pressure of approximately 240 MPa. The PEEK cell was fixed within a stainless-steel over-cell and placed inside a glass tube with argon gas flowing through it. The result example of measuring EIS was shown on Fig. 1.15. The semi-circle shows mixed resistance, bulk resistance ($R_{SE,bulk}$) and grain boundary one ($R_{SE,gb}$). The intersection points between the

semicircle and the line representing the Warburg impedance derived from the electrode resistance was taken as the total impedance. Temperature was controlled from room temperature to 130 ℃.

Using this blocking electrode and the system, cyclic voltammogram and electrical conductivity were measured (1282C, Solatron).

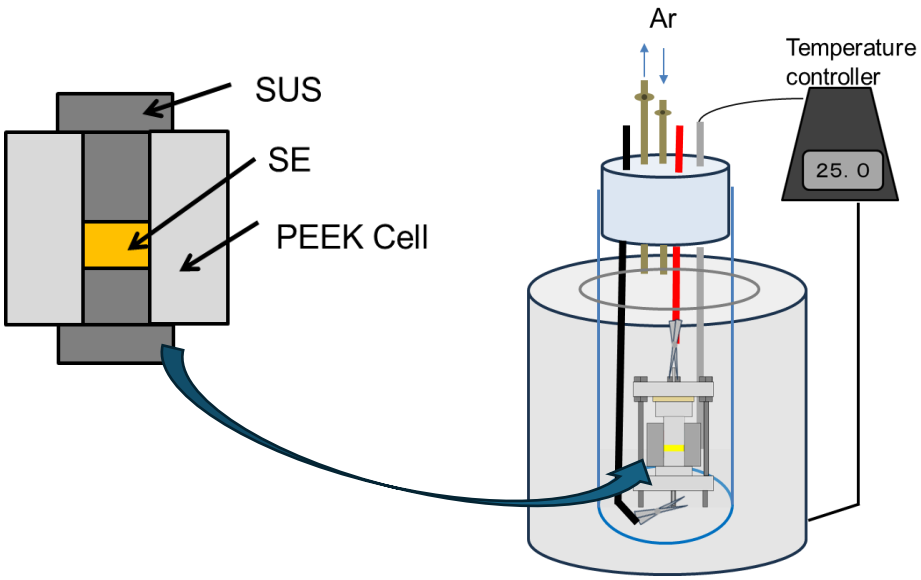

Fig. 1.14 Schematic drawings of the electrical impedance measurement system in our laboratory.

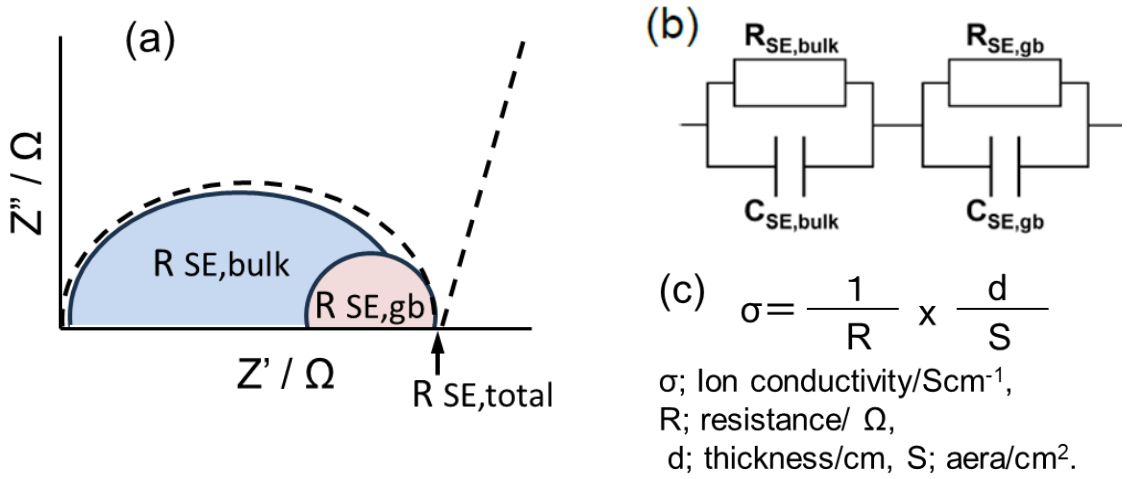

Fig. 1.15 Schematic diagram: (a) Nyquist plot, (b) equivalent circuit, and (c) equation for the calculation of ionic conductivity.

1.7.3 Battery performance

To evaluate battery performance of all-solid-state cells prepared SEs and active material composites, the PEEK cells shown in Fig. 1.16 were used. For example, when prepared SEs were evaluated as an electrolyte layer, $LiNi_{1/3}Mn_{1/3}Co_{1/3}O_2$ as a cathode and Indium (8mmφ, 0.1mm of thickness) and Lithium (5mmφ, 0.1mm thickness) foil (Li-In) as a counter electrode were used to build up half cells. When the full cell performance was tested, prepared anode composites such as Si and graphite were placed into counter electrode instead of Li-In. These cells were pressed by uniaxial pressing (about 80 mg of sample dried at 170°C) pellets of about 0.6 mm in thickness and 10.0 mm in diameter at a pressure of 200- 500 MPa (at room temperature). In Fig.1.17, schematic diagrams of charge-discharge curves of half cells and full cells were illustrated. The left side of diagram (a) is single charge-discharge curves of a half-cell placed cathode active materials on working electrode and the right side one is placed anode active materials on it. The red lines show charge curves and blue ones show discharge curves. In the left side of diagram (b), the charge curves in the case of cathode and anode were illustrated together. The voltage displayed when a full cell is assembled is the result of subtracting the two charge curve's values. The right one displayed when the discharge of full cell. The details of condition were shown in each chapter.

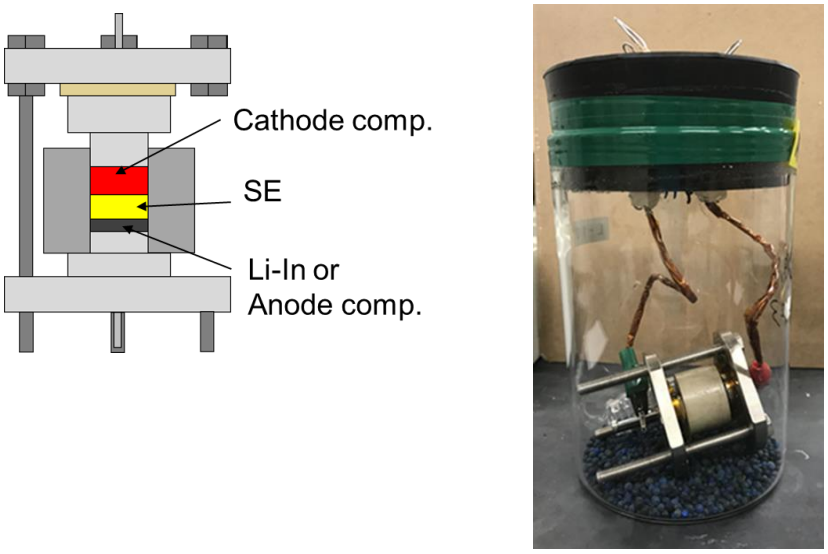

Fig. 1.16 Schematic image of a cell to evaluate battery performance and an appearance of test battery.

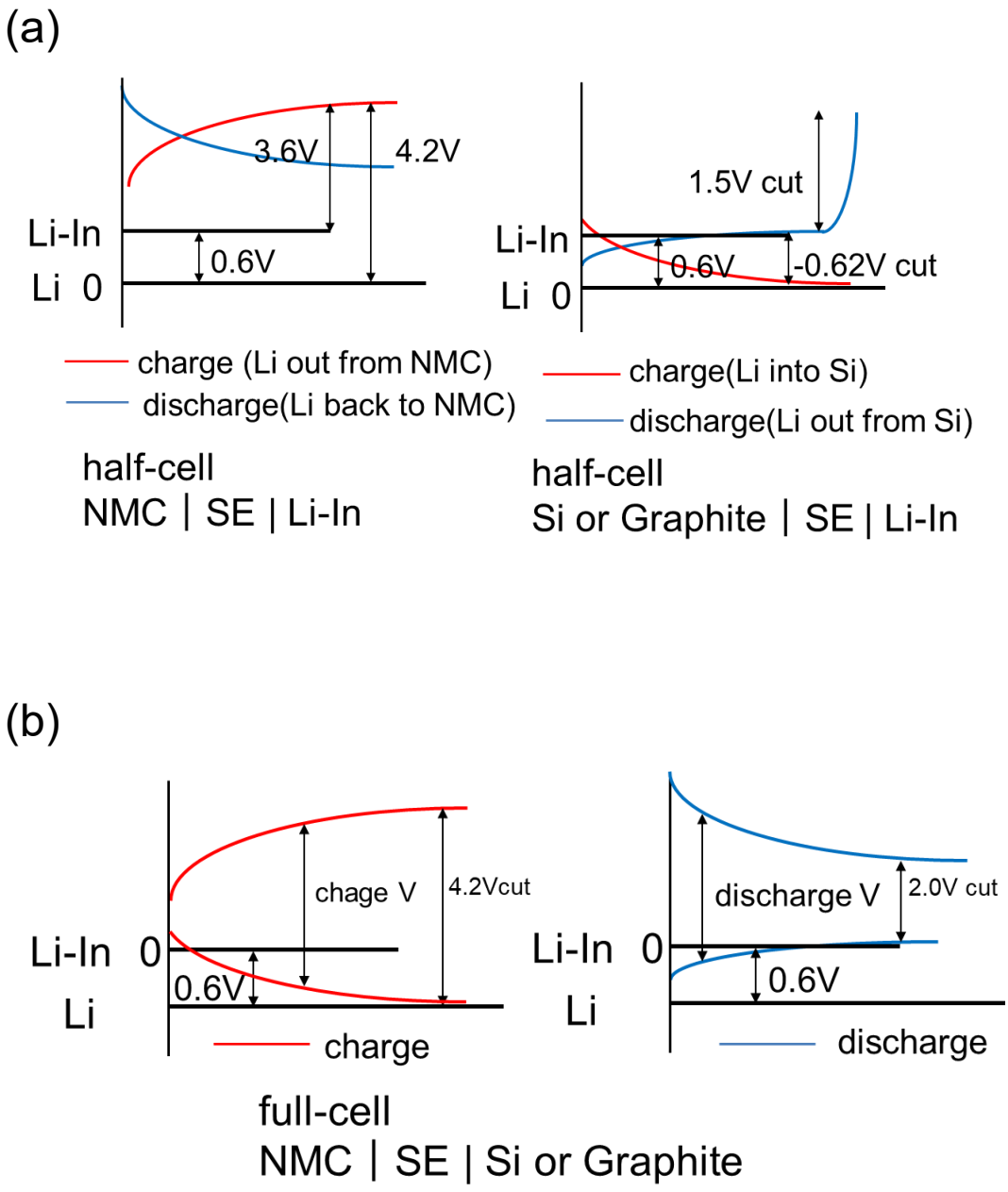

Fig. 1.17 Schematic diagrams of charge-discharge curves of (a) half cells and (b) full cells.

References

1) T. Fujieda, Negative electrode material for future lithium batteries (in Japanese), *Materia Japan* **38**, 488-492 (1999).

2) M.S. Wittingham, Intercalation chemistry and energy storage, *J. Solid State Chem.* **29**, 303-310 (1979).

3) K. Mizushima, P.C. Jones, P.J. Wiseman, J.B. Goodenough, Li_xCoO_2 (0<x<-1): A new cathode material for batteries of high energy density, *Mater. Res. Bull.* **15**, 783-789 (1980).

4) J.B. Goodenough, Y. Kim, Challenges for rechargeable Li batteries, *Chem. Mater*. **22**, 587-603 (2009).

5) A. Yoshino, "Lithium-Ion Batteries", Ed by Gianfranco Pistoia, Elsevier (2014) pp. 1-20.

6) S. Zhou, Z. Zheng, T. Mei, X. Wang, Structural design and material preparation of carbon-based electrodes for high-performance lithium storage systems, *Carbon* **144**, 127-146 (2019).

7) Q. Wang, B. Mao, S.I. Stoliarov, J. Sun, A review of lithium ion battery failure mechanisms and fire prevention strategies, *Prog. Energy Combust. Sci.* **73**, 95-131 (2019).

8) H.J. Deiseroth, S.T. Kong, H. Ecket, J. Vannahme, C. Reiner, T. Zaiß, M. Schlosser, Li_6PS_5X: a class of crystalline Li-rich solids with an unusually high Li^+ mobility, Angew. *Chem.* **120**, 767-770 (2008).

9) R.P. Rao, S. Adams, Studies of lithium argyrodite solid electrolytes for all-solid-state batteries, *Phys. Status Solidi A* **208**, 1804-1807 (2011).

10) X. Feng, P.H. Chien, Y. Wang, S. Patel, P. Wang, H. Liu, M. Immediato-Scuotto, Y.Y. Hu, Enhanced ion conduction by enforcing structural disorder in Li-deficient argyrodites $Li_{6-x}PS_{5-x}Cl_{1+x}$, *Energy Storage Mater.* **30**, 67-73 (2020).

11) L. Peng, S. Chen, C. Yu, C. Wei, C. Liao, Z. Wu, H.L. Wang, S. Cheng, J. Xie, Enhancing moisture and electrochemical stability of the $Li_{5.5}PS_{4.5}Cl_{1.5}$ electrolyte by oxygen doping, *ACS Appl. Mater Interfaces* **14**, 4197-4185 (2022).

12) R. Kanno, M. Murayama, Lithium ionic conductor thio-LISICON: The Li_2S-GeS_2-P_2S_5 system, *J. Electrochem. Soc.* **148**, A742 (2001).

13) R. Mercier, J-P. Malugani, B. Fahys, G. Robert, Superionic conduction in Li_2S-P_2S_5-LiI–glasses, *Solid State Ionics* **5**, 663-666 (1981).

14) Z. M. Zhang, J.H. Kennedy, Synthesis and characterization of the B_2S_3-Li_2S, the P_2S_5-Li_2S and the B_2S_3-P_2S_5-Li_2S glass systems, *Solid State Ionics* **38**, 217-224 (1990).

15) N. Kamaya, K. Homma, Y. Yamakawa, M. Hirayama. R. Kanno, M. Yonemura, T. Kato, S. Hama, K. Kawamota, A. Mitsui, A lithium superionic conductor, *Nat. Mater.* **10**, 682-686 (2011).

16) Y. Sun, K. Suzuki, S. Hori, M. Hirayama, R. Kanno, Superionic conductors: $Li_{10+\delta}[Sn_ySi_{1-y}]_{1+\delta}P_{2-\delta}S_{12}$ with a $Li_{10}GeP_2S_{12}$-type structure in the Li_3PS_4–Li_4SnS_4–Li_4SiS_4 quasi-ternary system, *Chem. Mater.* **29**, 5858-5864 (2017).

17) T. Yabuzaki, M Sato, H. Kim, K. Watanabe, N. Matsui, K. Suzuki, S. Hori, K. Hikima, S. Obokata, H. Moto, A. Matsuda, R. Kanno, M. Hirayama, Electrochemical and mechanical properties and chemical stability of $Li_{10}GeP_2S_{12}/Al_2O_3$ composite electrolytes, *J. Ceram. Soc. Japn.* **131**, 675-684 (2023).

18) A. Hayashi, S. Hama, H. Morimoto, M. Tatsumisago, T. Minami, Preparation of Li_2S–P_2S_5 amorphous solid electrolytes by mechanical milling, *J. Am. Ceram. Soc.* **84**, 477-479 (2001).

19) F. Mizuno, S. Hama, A. Hayashi, K. Tadanaga, T. Minami, M. Tatsumisago, All solid-state lithium secondary batteries using high lithium ion conducting Li_2S–P_2S_5 glass-ceramics, *Chem. Lett.* **31**, 1244-1245 (2002).

20) M. Tatsumisago, A. Hayashi, All-solid-state lithium secondary batteries using sulfide-based glass ceramic electrolytes, *Functional Materials Letters* **01**, 31-36 (2008).

21) A. Sakuda, A. Hayashi, M. Tatsumisago, Sulfide solid electrolyte with favorable mechanical property for all-solid-state Lithium Battery, *Sci. Rep.* **3**, 2261, 1-5 (2013).

22) H. Muramatsu, A. Hayashi, T. Ohtomo, S.Hama, M. Tatsumisago, Structural change of Li_2S–P_2S_5 sulfide solid electrolytes in the atmosphere, *Solid State Ionics,* **182**,116-119 (2011).

23) N.H.H. Phuc, K. Morikawa, M. Totani, H. Muto, A. Matsuda, Chemical synthesis of Li_3PS_4 precursor suspension by liquid-phase shaking, *Solid State Ionics* **285**, 2-5 (2016).

24) N.H.H. Phuc, E. Hirahara, K. Morikawa, H. Muto, A. Matsuda, One-pot liquid phase synthesis of $(100-x)Li_3PS_4$–$xLiI$ solid electrolytes, *J. Power Sources* **365**, 7-11 (2017).

25) S. Yubuchi, S. Teragawa, K. Aso, K. Tadanaga, A. Hayashi, M. Tatsumisago, Preparation of high lithium-ion conducting Li_6PS_5Cl solid electrolyte from ethanol solution for all-solid-state lithium batteries, *J. Power Sources* **293**, 941-945 (2015).

26) K. H. Park, D. Y. Oh, Y. E. Choi, Y. J. Nam, L. Han, J. Y. Kim, H. Xin, F. Lin, S. M. Oh, Y. S. Jung, Solution-processable glass LiI-Li_4SnS_4 superionic conductors for all-solid-state Li-ion batteries, *Adv. Mater.* **28**, 1874–1883 (2016).

27) A. Sakuda, A. Hayashi, T. Ohtomo, S. Hama, M. Tatsumisago, *J. Power Sources*, **196**, 6735-6741

(2011).

28) H. Nakamura, T. Kawaguchi, T. Masuyama, A. Sakuda, T. Saito, K. Kuratani, S. Ohsaki, S. Watano, Design of active-material/solid-electrolyte composite particles with conductive additives for all-solid-state lithium-ion batteries, *J. Power Sources* **448**, 227579 (2020).

29) R. Matsuda, E. Hirahara, N.H.H. Phuc, H. Muto, H. Tsukasaki, S. Mori, A. Matsuda, Preparation of $LiNi_{1/3}Mn_{1/3}Co_{1/3}O_2/Li_3PS_4$ cathode composite particles using a new liquid-phase process and application to all-solid-state lithium batteries, *J. Ceram. Soc. Japan* **126**, 826-831 (2018).

30) R.G. Pearson "Hard and soft acids and bases, HSAB, part 1: Fundamental principles" *J. Chem. Educ.* **45***,* 581–586 (1968).

31) K. Kanazawa, S. Yubuchi, C. Hotehama, M. Otoyama, S. Shimono, H. Ishibashi, Y. Kubota, A. Sakuda, A. Hayashi, M. Tatsumisago, Mechanochemical synthesis and characterization of metastable hexagonal Li_4SnS_4 solid electrolyte, *Inorg. Chem.* **57**, 9925–9930 (2018).

32) J. Wu, L. Yuan, W. Zhang, Z. Li, X. Xie and Y. Huang, Reducing the thickness of solid-state electrolyte membranes for high-energy lithium batteries, *Energy Environ. Sci.* **14,** 12–36 (2021).

33) R. Xu, J. Yue, S. Liu, J. Tu, F. Han, P. Liu, C. Wang, Cathode-supported all-solid-state lithium−sulfur batteries with high cell-level energy density, *ACS Energy Lett.*, **4,** 1073–1079 (2019).

34) Y. J. Nam, S. J. Cho, D. Y. Oh, J. M. Lim, S. Y. Kim, J. H. Song, Y. G. Lee, S. Y. Lee, Y. S. Jung, Bendable and Thin Sulfide Solid Electrolyte Film: A new electrolyte opportunity for free-standing and stackable high-energy all-solid-state lithium-ion batteries, *Nano Lett.* **15**, 3317–3323 (2015).

35) Y. Li, X. Wang, H. Zhou, X. Xing, A. Banerjee, J. Holoubek, H. Liu, Y. S. Meng, P. Liu, Thin solid electrolyte layers enabled by nanoscopic polymer binding, *ACS Energy Lett.* **5**, 955–961 (2020).

36) D.Y. Oh, K.T. Kim, S.H. Jung, D.H. Kim, S. Jun, S. Jeoung, H.R. Moon, Y.S. Jung, Tactical hybrids of Li^+-conductive dry polymer electrolytes with sulfide solid electrolytes: Toward practical all-solid-state batteries with wider temperature operability, *Materials Today* **53**, **7-15 (**2022).

37) D.H. Kim, Y.H. Lee, Y.B. Song, H. Kwak, S.Y. Lee and Y.S. Jung, Thin and flexible solid electrolyte membranes with ultrahigh thermal stability derived from solution-processable Li argyrodites for all-solid-state Li-ion batteries, *ACS Energy Lett.* **5**, 718–727 (2020).

38) S. Liu, L. Zhou, J. Han, K. Wen, S. Guan, C. Xue, Z. Zhang, B. Xu, Y. Lin, Y. Shen, L. Li, C.W.

Nan, Super long-cycling all-solid-state battery with thin Li_6PS_5Cl-based electrolyte, *Adv. Energy Mater.* **12**, 2200660 (2022).

39) M. Nagao, A. Hayashi, M. Tatsumisago, High-capacity Li_2S–nanocarbon composite electrode for all-solid-state rechargeable lithium batteries, *J. Mater. Chem.* **22**, 10015 (2012).

40) H. Gamo, N.H.H. Phuc, M. Ikari, K. Hikima, H. Muto, A. Matsuda, Electrochemical redox of Li_2S–CaS and –CaX_2 (X = Cl, Br, and I) cathode materials for all-solid-state lithium-sulfur batteries, *Electrochim. Acta* **431**, 141149 (2022).

41) D.H. Kim, H.A. Lee, Y.B. Song, J.W. Park, S.M. Lee, Y.S. Jung, Sheet-type Li_6PS_5Cl-infiltrated Si anodes fabricated by solution process for all-solid-state lithium-ion batteries, *J. Power Sources*, **426**, 143-150 (2019).

42) R. Miyazaki, N. Ohta, T. Ohnishi, I. Sakaguchi, K. Takada, Charge-discharge performances of Sn powder as a high capacity anode for all-solid-state lithium batteries, *J. Power Sources* **272**, 541-545 (2014).

43) J.R. Szczech, S. Jin, Nanostructured silicon for high capacity lithium battery anodes, *Energy Environ. Sci.* **4**, 56-72 (2011).

44) H. Wu, Y. Cui, Designing nanostructured Si anodes for high energy lithium ion batteries, *Nanotoday* **7**, 414-429 (2012).

45) M. Yamamoto, Y. Terauchi, A. Sakuda, A. Kato, M. Takahashi, Effects of volume variations under different compressive pressures on the performance and microstructure of all-solid-state batteries, *J. Power Sources* **473**, 228595 (2020).

Chapter 2
Fabrication and Characterization of Sulfide Solid Electrolyte via Liquid Phase Shaking

2.1 Background

Sulfide solid electrolytes (SSE) for all-solid-state lithium-ion batteries (ASSLIB) have been fabricated via liquid phase process, and their characterization and the performance of batteries are evaluated. $Li_2S-P_2S_5-LiI$ system SSEs were successfully fabricated via liquid phase shaking process (LS) by N.H.H. Phuc et al[1-4]. First, Li_3PS_4 (LPS) was synthesized via liquid phase shaking process with dimethyl carbonate (DMC) as a solvent and zirconia balls. The process was newly offered and named "LS method" in the work. The ionic conductivity of the obtained LPS was 6.4 x 10^{-6} S cm^{-1} at room temperature[1]. Using ethyl acetate (EA) as a solvent, the LPS was amorphous because the solvent remained and the ionic conductivity showed 3.3 x 10^{-4} S cm^{-1}, which was comparable to one of LPS prepared by the mechanical milling (MM) method[2]. When ethyl propionate (EP), which belongs to the same ester class as EA, was used as a solvent, the ionic conductivity was 2.0 x 10^{-4} S cm^{-1}. But the particle size of the LPS was very fine, with a thickness of 100− 200 nm, which was suitable to compose with active materials for ASSLB[3]. Further, (100-x) Li_3PS_4- xLiI SSEs were synthesized with EP via LS method. When x= 33.3, i.e. $Li_7P_2S_8I$, the ionic conductivity was 3.4 x 10^{-4} S cm^{-1} [4], which was lower than that of MM method, 6.3 x 10^{-4} S cm^{-1} [5], but the obtained LPS showed excellent performance at a lithium stability test using a cell sandwiched SE by two metal lithium foils.

K. Hikima, et al. suggested an improved process of fabrication of LPSI with shorter shaking time and modified drying conditions[6]. The ionic conductivity of the LPSI reached 1.0 x 10^{-3} S cm^{-1}. According to the XRD analysis, the LPSI had a new phase added to pristine LPSI suggested by Rangasamy et al [7].

In Chapter 2, these fabrication methods and evaluations were reviewed based on our laboratory's work [3] and my presentations [8] for some academic conferences in which I participated.

2.2 Fabrication and characterization of sulfide solid electrolyte, Li_3PS_4 via liquid phase shaking

2.2.1 Introduction

Stoichiometric compound, Li_3PS_4 (LPS) belongs to the thio-LISICON family and has been reported in the ternary Li-P-S system or in the binary Li_2S-P_2S_5 system[9-12], which has three types of structures, i.e. α, ß, and γ-phase according to temperature. The ionic conductivity of γ-phase structure is low. On the other hand, α, ß -phase are high. The γ-phase transform between 543 and 637 K to the ß-phase, and to the α-phase between 724 and 811 K in the heating process. However, in the cooling process, the α-phase directly transform to the γ-phase[13]. Kanno and Murayama have developed a series of thio-LISICON materials and reported that $Li_{4-x}Ge_{1-x}P_xS_4$ is divided into three composition regions: region I ($0<x\leqq0.6$), region II ($0.6<x<0.8$), and region III ($0.8\leqq x<1.0$). The thio-LISICON phase in region II has a special monoclinic superstructure and shows much higher conductivities over 10^{-3} S cm^{-1} than the other phases (regions I and III) and region III shows approximately 10^{-4} S cm^{-1} at room temperature[14]. The XRD pattern of ß-phase LPS is good agreement with thio-LISICON region III[15]. A. Hayashi et al. approached fabrication of LPS with mechanical milling (MM) and evaluated the thermodynamic stability of their structure phase and ß-phase LPS was meta-stable[16]. They successfully synthesized ß-phase LPS via MM and subsequently heat treatment by 300 ℃. Recently, there were reports on the synthesis of LPS using wet chemical methods via dissolving the starting materials, Li_2S and P_2S_5 in various organic solvents like tetrahydrofuran, N-methylformamide, and dimethoxyethane. Z. Liu et al. showed that the use of organic solvents makes synthesis of ß-phase of LPS easier[17].

In this part, I introduced a synthesis method of the suspension of LPS precursor using a liquid phase shaking process.

2.2.2 Experimental

Figure 2.2.1 shows schematic images of liquid phase shaking process for LPS. The raw materials with chemical composition(3:1), Li_2S (Mitsuwa, 99.9%), P_2S_5 (Aldrich, 99%) were shaken with 30 g of ZrO_2 balls (4 mm ϕ), and ethyl propionate (EP) as a solvent in polypropylene centrifugal tubes with constant shaking rate at 1500 rpm and 30 ℃ for 3 h. The obtained precursor slurry was centrifuged, and the supernatant was removed. Subsequently the precipitate was dried under low

pressure in approximately 5 h while the temperature was gradually increased from 25 to 130 ℃ and heat-treated in argon atmosphere at 170 ℃ for 2 h. This procedure resulted in the powder of LPS. The crystal structures of the samples using X-ray diffraction analysis (XRD) (Smart Lab, Rigaku) and the ionic conductivities at their variations with temperature were measured using alternating-current impedance spectroscopy (SI 1260, Solatron) from 1 MHz to 10 Hz at a temperature of 25 to 150 ℃.

An all-solid-state cell using the prepared 90 $LiNi_{1/3}Mn_{1/3}Co_{1/3}O_2$ (NMC)-10LPS composite as a positive electrode, LPS prepared by the liquid-phase shaking method invented by our laboratory[15] as an electrolyte layer and Indium foil (In, 99.99%, Nilaco) as a counter electrode was fabricated. The composed electrodes for electrochemical measurements were prepared by uniaxial pressing (about 80 mg of sample dried at 170 ℃) pellets of about 0.6 mm in thickness and 10.0 mm in diameter at a pressure of 330 MPa (at room temperature). The prepared pellet was placed in a holder made from polyetheretherketon (PEEK) with two stainless steel rods. The charge-discharge test of the cells was conducted at a constant current at 0.1 C.

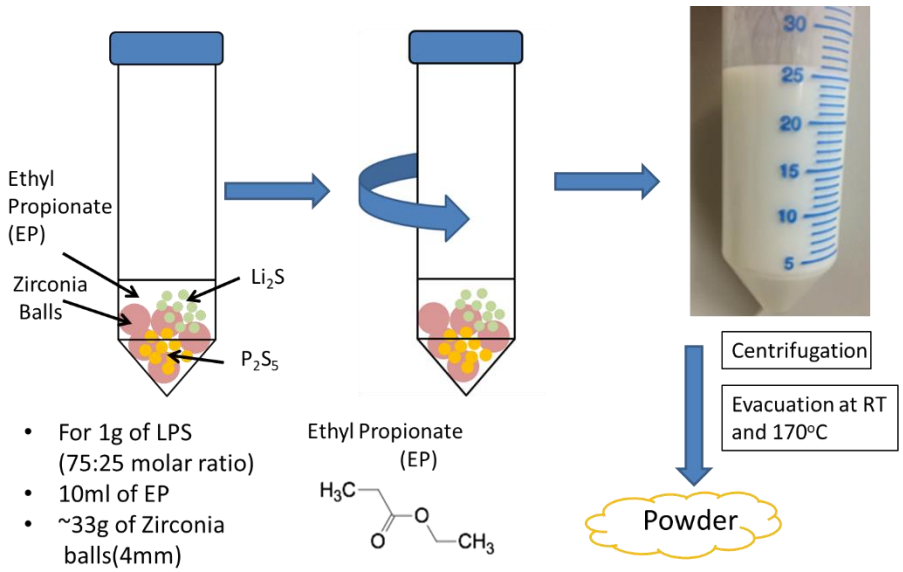

Fig. 2.2.1 Schematic images of the preparation of Li_3PS_4 (LPS) via liquid phase shaking process.

2.2.3 Results and Discussion

In Fig.2.2.2, SEM images of LPS via liquid phase shaking process (left) and mechanical milling (MM) (right). The particles synthesized via MM were 5 to 10 μm aggregated of primary particles of 1 to 2 μm. On the other hand, one via LS process were fine, ribbon-shaped particles with a width of 0.5 μm and a length of 1 to 2 μm. The observation using TEM showed that the structure obtained LPS was mixed with crystalline and amorphous in Fig. 2.2.3.

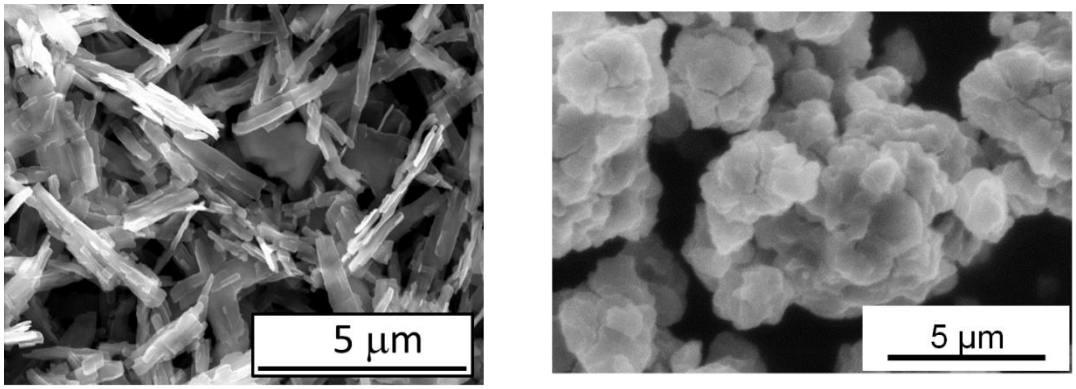

Fig. 2.2.2 SEM images of Li_3PS_4 via LS method (left) and Mechanical milling (right). This figure was cited from *ref. 3), Copyright@2017 Springer Nature.*

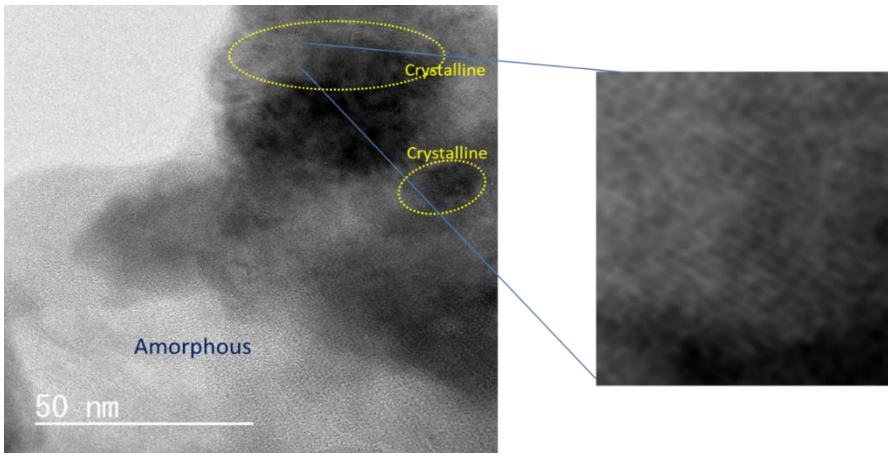

Fig. 2.2.3 TEM images of Li_3PS_4 (LPS) via LS method taken by Mori group in Osaka Prefecture University.

In Fig. 2.2.4, XRD patterns and Raman spectra of raw materials and the prepared samples. According to the XRD analysis, the structure of LPS via LS process and dried at 170 ℃ was corresponding to ß-phase-LPS. The precursor before drying already had a sharp Raman shift peak at 421 cm^{-1}. In the XRD pattern, the precursor did not show ß-phase. It suggests that the basic tetragonal were already generated while shaking and the crystal phase was composed in drying process. After the drying process, the peak of Raman spectrum at 2900 cm^{-1}, which shows EP left had almost disappeared.

In Fig. 2.2.5, the temperature dependence of ionic conductivity of obtained LPS was shown. It was measured using alternative current methods. The ionic conductivity at 25 ℃ was 1.5 x 10^{-4} S cm^{-1}. The particle size of the powder obtained by the LS process was small, which increased the surface resistance, resulting in a slightly lower value than that obtained by the MM process. Fig. 2.2.6 showed time dependence of conductivity of the prepared LPS at constant applied voltage of 1 V using blocking electrodes (SUS| LPS |SUS) and non-blocking electrodes (Li| LPS |Li). The measurement using direct current method with the blocking electrode shows electronic conductivity and that using non-blocking electrode shows ionic conductivity. The current value after 300 s was approximately 10^{-7} A at 1 v. It was calculated that electronic conductivity was 6.4 x10^{-9} S cm^{-1} and the transport number was more than 0.999.

Figure 2.2.7 shows the cyclic voltammogram of the prepared LPS using the cell constructed of Li | LPS | SUS at scan rate of 0.5 mV s^{-1}. None of peaks was observed in scanning range, -0.5− 5 V except for anodic and cathodic peaks. These results indicated that this LPS was a good candidate as an SE for ASSLIB. Fig. 2.2.8 shows the first charge-discharge curves of a half-cell of ASSLIB with 90NMC10LPS composite as a cathode and Li-In foil as a counter electrode and of the half cell.

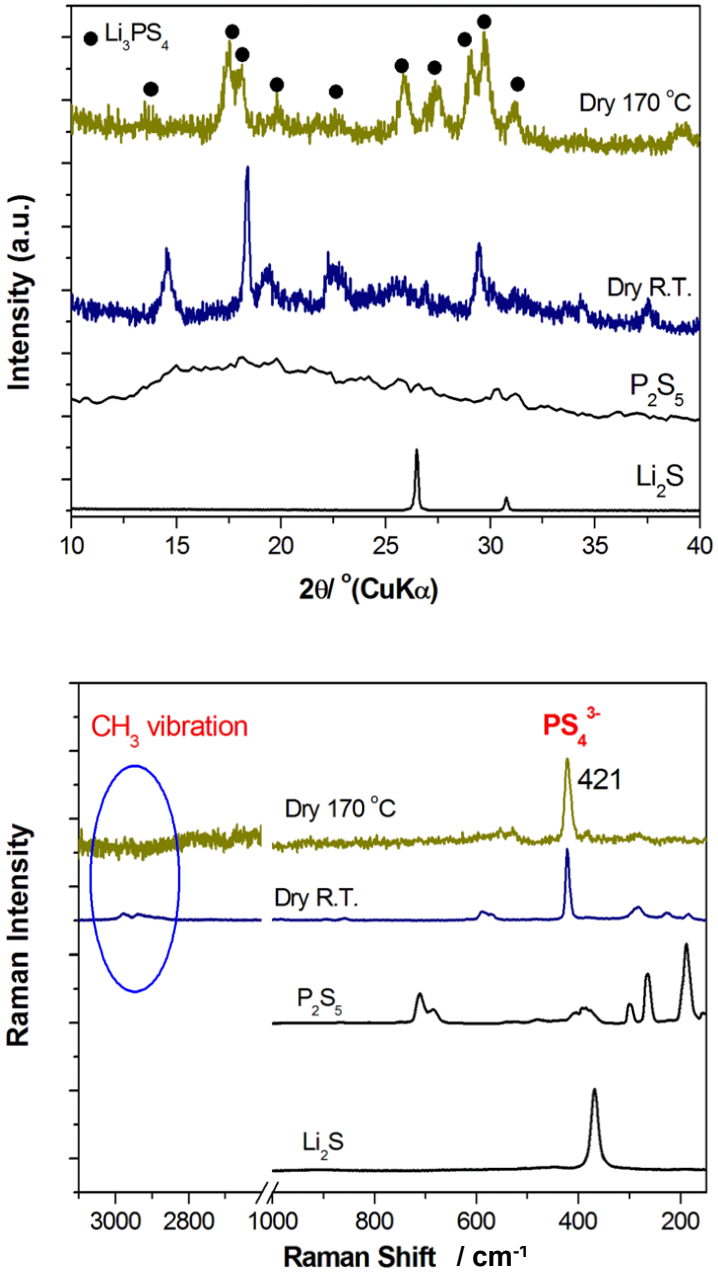

Fig. 2.2.4 XRD patterns and Raman spectra of raw materials and the prepared sample. These figures were cited from *ref. 3) , Copyright@2017 Springer Nature.*

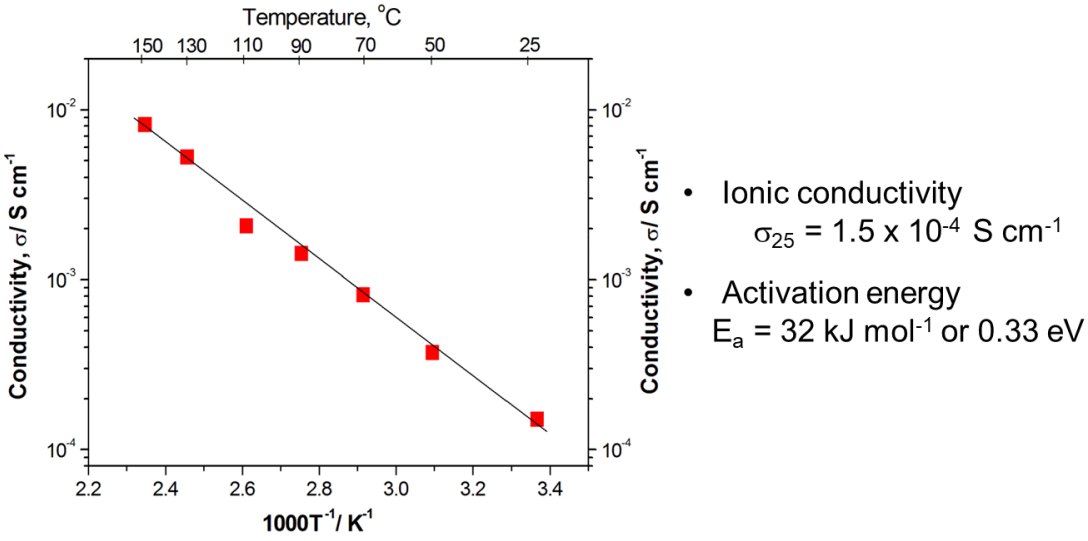

Fig. 2.2.5 Temperature dependence of the conductivity of the prepared LPS measured by impedance spectroscopy using blocking electrodes (SUS| LPS |SUS).

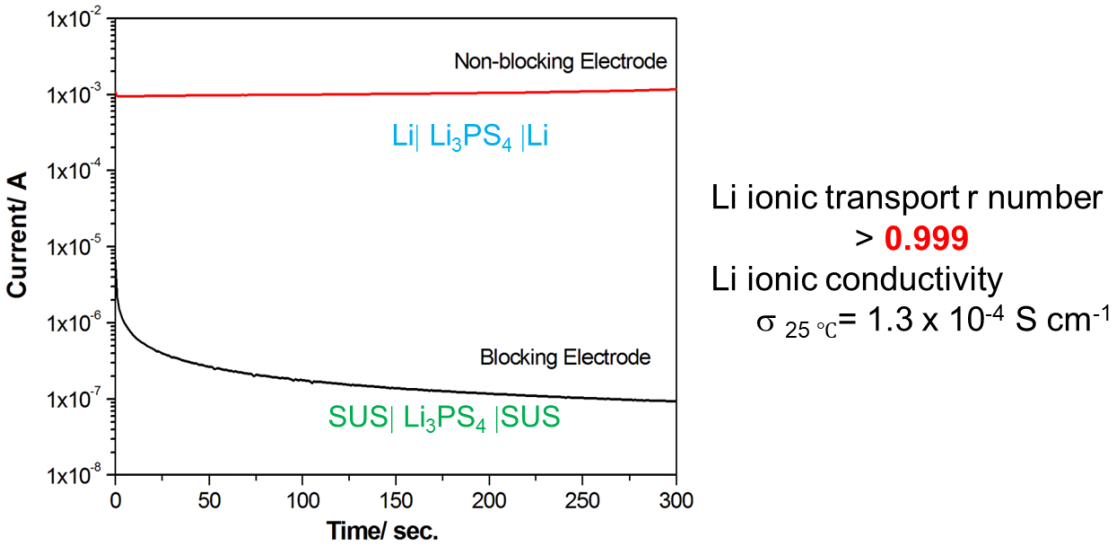

Fig. 2.2.6 Time dependence of conductivity of the prepared LPS at constant applied voltage of 1V using blocking electrodes (SUS| LPS |SUS) and non-blocking electrodes (Li| LPS |Li).

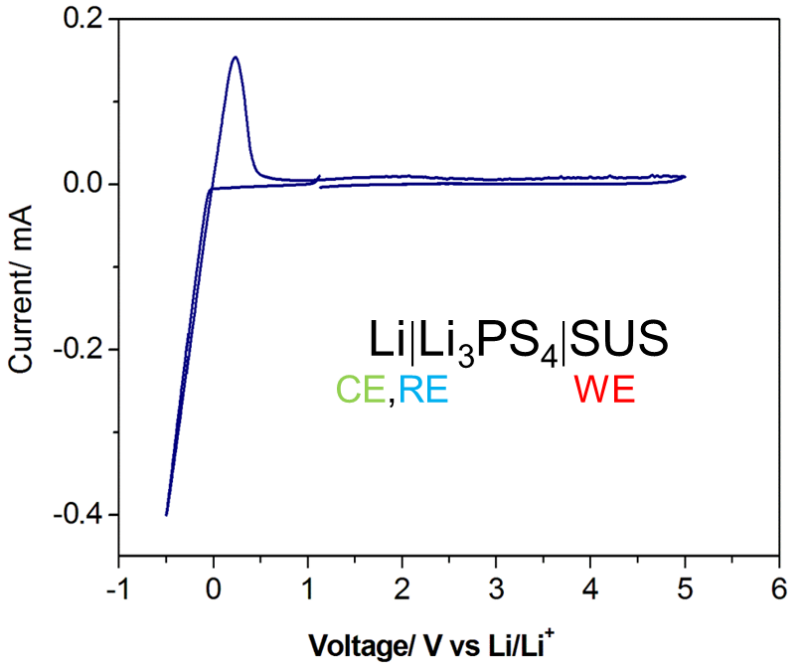

Fig. 2.2.7 Cyclic Voltammogram of the prepared LPS using the cell constructed of Li | LPS | SUS at scan rate of 0.5 mV s^{-1} This figure was cited from *ref. 3), Copyright@2017 Springer Nature.*

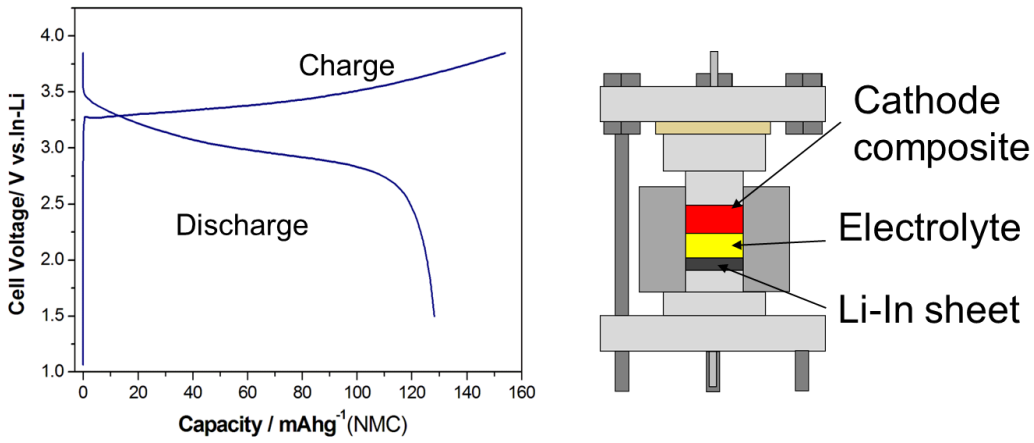

Fig.2.2.8 First charge-discharge curves of the all-solid-state cell prepared with 90NMC-10Li_3PS_4 composite.

Figure 2.2.9 shows a fabrication flow of LPSI preparation. LiI was added to the starting materials. The raw materials with chemical composition (3:1:1), Li_2S (Mitsuwa, 99.9%), P_2S_5 (Aldrich, 99%), LiI (Aldrich, 99%) were shaken with 30 g of ZrO_2 balls (4 mmφ), and EP as a solvent in polypropylene centrifugal tubes with constant shaking rate at 1500 rpm and 30 ℃ for basically 3 h. In this procedure, the solvent was removed by drying under low pressure and centrifugation was not performed to avoid the loss of LiI by discarding LiI remaining in the supernatant. The obtained LPSI powder was evaluated using XRD analysis. It was shown in Fig. 2.2.10. The red line is LPSI, blue one is LPS, and black are raw materials, LiI, P_2S_5, Li_2S. The obtained XRD pattern of LPSI corresponded to Rangasamy's results. Recently, S.J. Sedlmaier et al. reported Li_4PS_4I was synthesized by solvent-based soft chemistry approach[17]. It showed similar structure to LPSI via LS process. The ionic conductivity was 6.4 x 10^{-5} to 1.2 x 10^{-4} S cm^{-1} at 25 ℃.

The temperature dependance of ionic conductivity of LPSI and LPS via LS process was shown in Fig. 2.2.11. LPSI had higher ionic conductivity, 3.8 x 10^{-4} S cm^{-1} at 25 ℃ than LPS. Therefore, LPSI phase is located between stable Li_4PS_4I-phase and LPS-phase, and this is consistent with the chemical composition. This phase assumed unstable at high temperature heat treatment. LPSI via MM process and heat-treated, which structure is glass-ceramic, was one order of magnified more higher than LS process. Concerning ionic conductivity, LPSI has excellent potential.

In Fig. 2.2.12, XRD patterns of the obtained LPSI via LS process with different shaking time (1 h and 6 h) with raw materials, LiI, P_2S_5 and Li_2S are shown. There were small peaks corresponding to LPS in the XRD pattern of the sample with 6 h. It suggests that long reaction time generates LPS. In the XRD pattern of 1 h, some new peaks corresponding thio-LISICON region II were shown[14,15]. Fig.2.2.13 shows temperature dependence of the conductivity of obtained LPSI via LS process with shaking time of the sample with 1 h and 6 h. These conductivities at room temperature were almost the same.

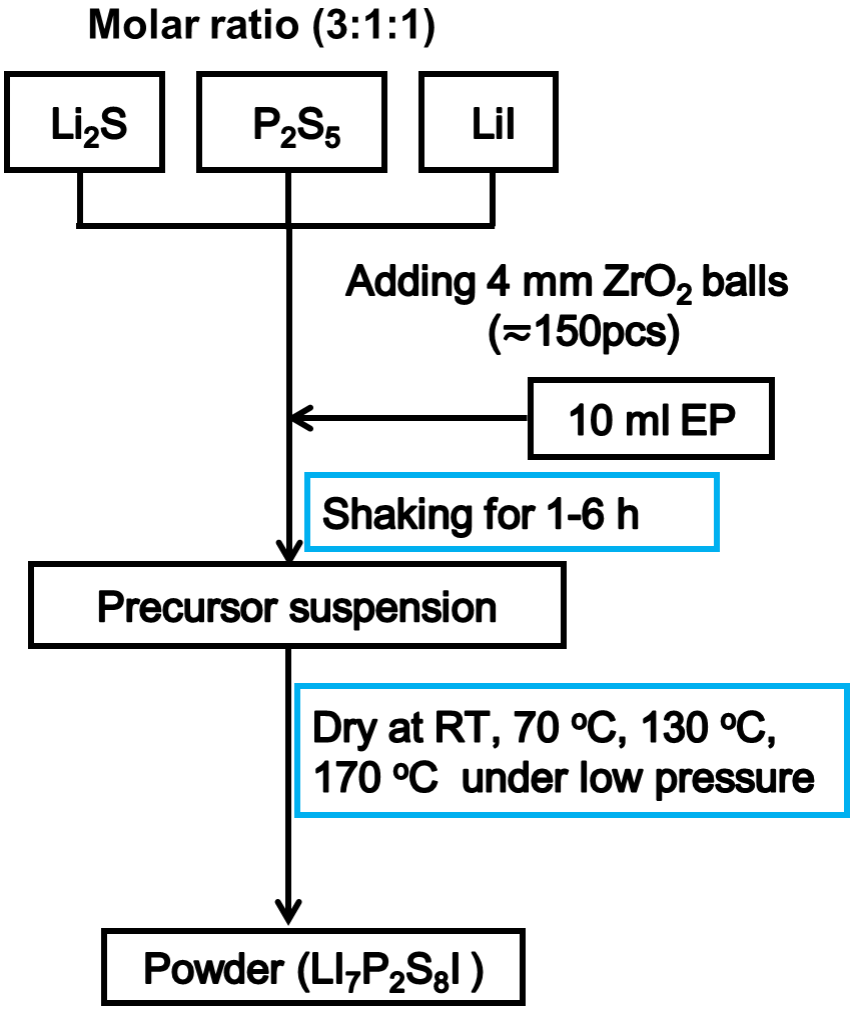

Fig. 2.2.9 Schematic images of the preparation of $Li_7P_2S_8I$ (LPSI) via liquid phase shaking method.

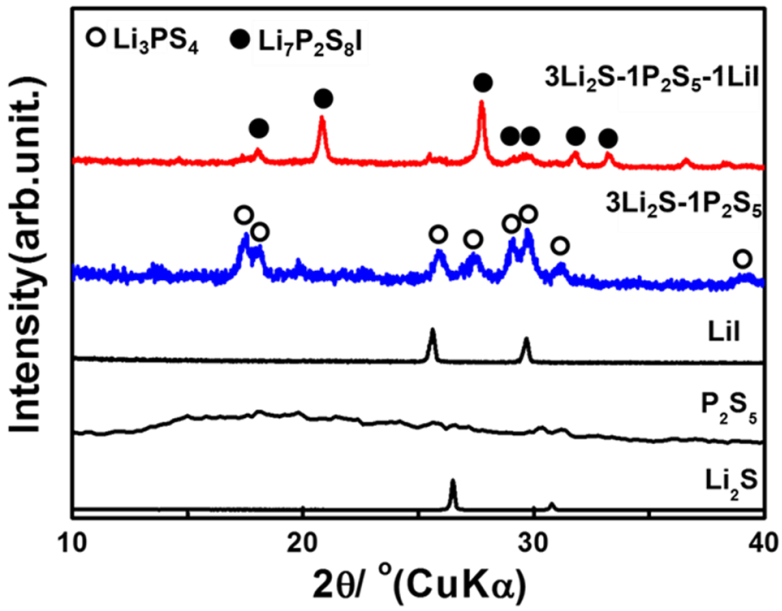

Fig. 2.2.10 XRD patterns of raw materials and the prepared samples via liquid phase shaking process, blue line for LPS and red one for LPSI. This figure was cited from *ref. 6) , Copyright@2020 Elsevier.*

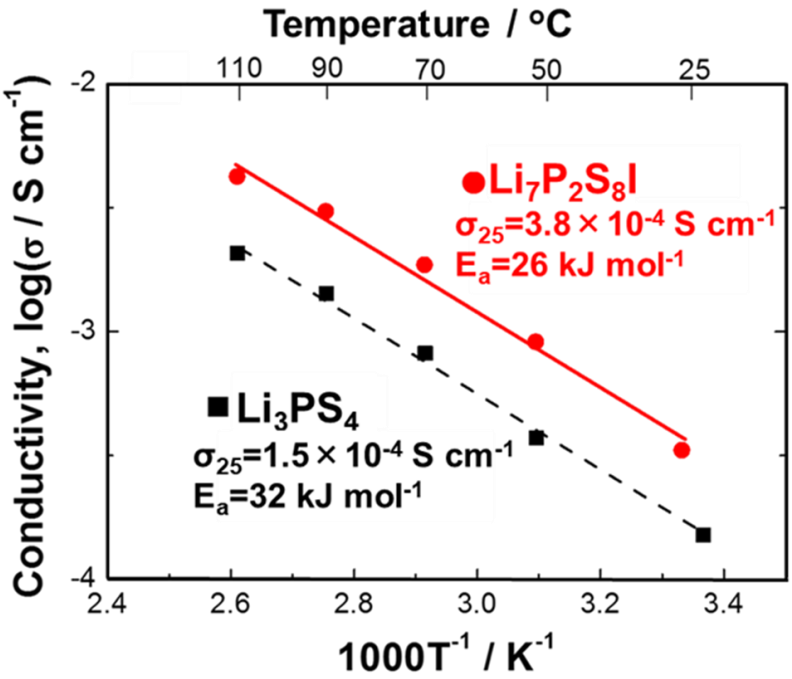

Fig. 2.2.11 Temperature dependence of the conductivity of the prepared LPS and LPSI measured by impedance spectroscopy using blocking electrodes (SUS| LPS |SUS).

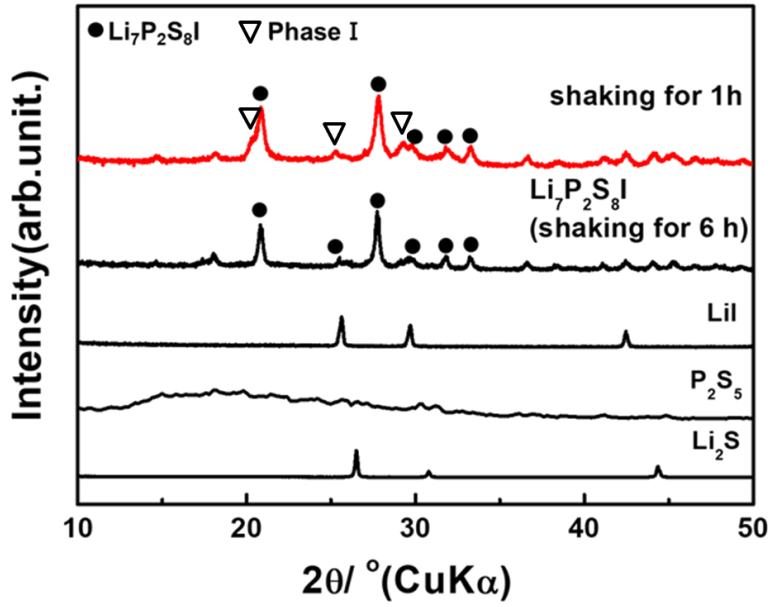

Fig. 2.2.12 XRD patterns of raw materials and the prepared samples with different shaking time via liquid phase shaking process.

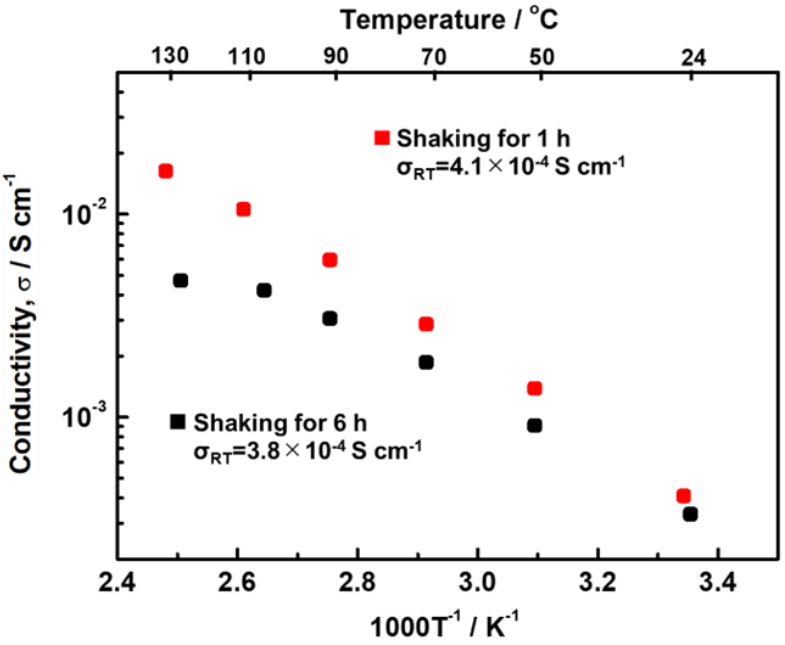

Fig. 2.2.13 Temperature dependence of the conductivity of obtained LPSI via LS process with different shaking time (1 h and 6 h) using blocking electrodes (SUS| LPS |SUS).

SEM observation was performed to understand the phase mixed state of the SE organization. Fig.2.2.14 shows a cross-section SEM backscattered electron image of an SE pellet obtained by shaking for 1 h and energy dispersive X-ray spectrometry (EDS) images of S, P, C, I, O. There were particles measuring 10 to 20 μm dispersed throughout the entire SE layer. Elemental analysis using EDS showed that the particles contain a large amount of sulfur, which is estimated to be Li_2S, a residue from the raw material. Despite the presence of a large amount of Li_2S residue, it was not detected in the LPSI layer by XRD analysis. From backscattered electron image, the color of edges of residue particle cross section appeared to change. It seemed that the particle surface was undergoing reaction. Except residues, the LPSI matrix contained dark and bright areas. It suggests that LPSI synthesized via LS process was composited more than two components. The dark area contained oxygen from EDS images. This suggests that the solvent remains in the dark area, and the bright area contains heavier elements, Iodide.

It assumed that when Li_2S is slightly less than the stoichiometric amount of LPSI, a highly conductive phase is likely to appear. Therefore, it is thought that the high conductivity phase can be maintained by shortening the agitation time to stop the reaction, and then after removing the solvent, heat treatment should be performed gently. Schematic images of relationships of heat treatment and SE composition were shown on Fig. 2.2.15.

In Fig. 2.2.16, XRD patterns of LPSI synthesized different heating conditions were shown. After removed the solvent at 130 ℃, when heat treatment in argon atmosphere, the high conductive phase was remaining. The temperature dependence of ionic conductivities of the samples obtained by several heat treatments were shown on Fig. 2.2.17. when heat treatment was carried out in argon atmosphere, the ionic conductivity was the highest, 1.0×10^{-3} S cm^{-1} at 25 ℃.

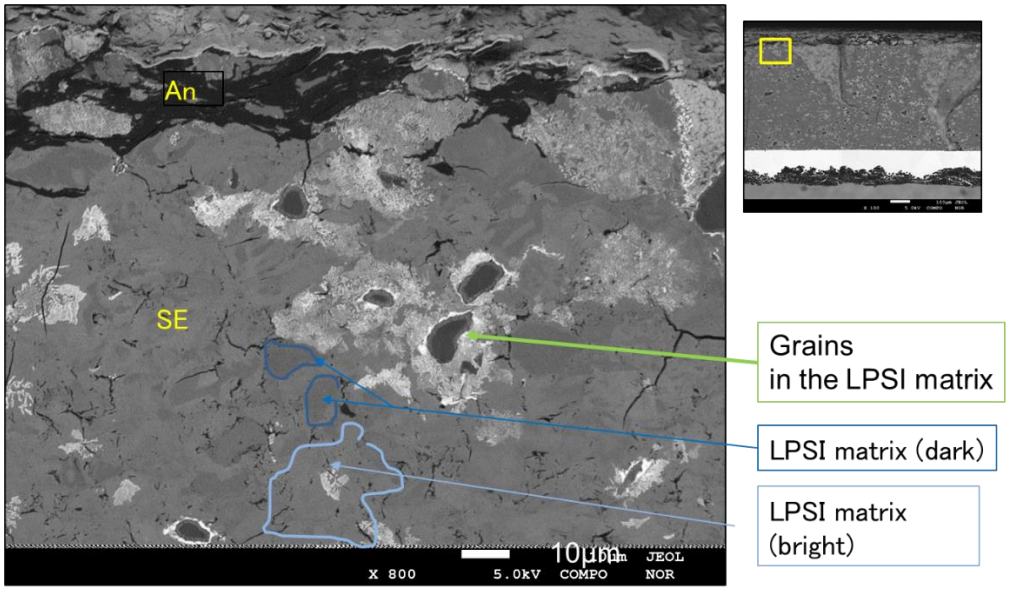

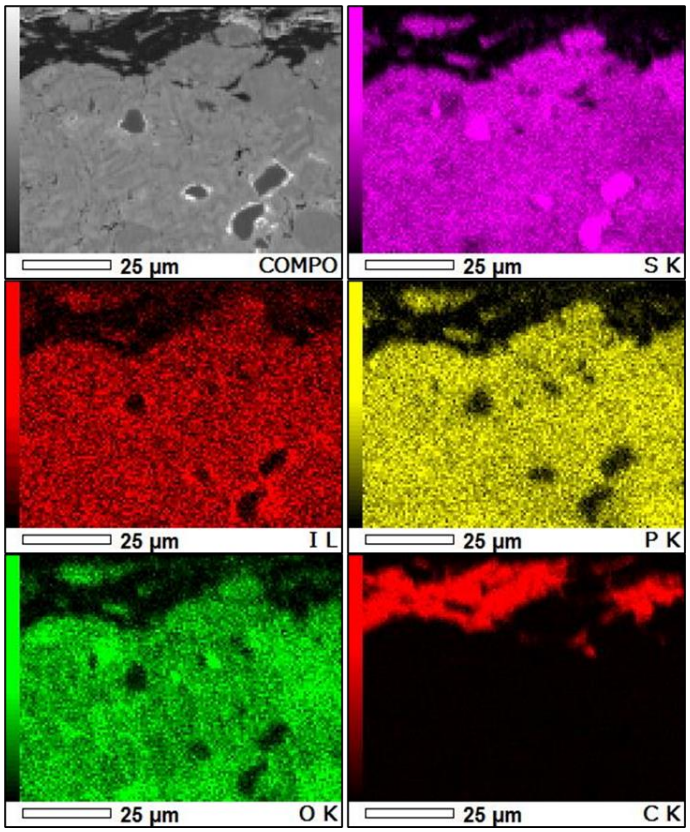

Fig. 2.2.14 SEM backscattered electron image and EDS analysis images (I, O, S, P, C) of LPSI via LS process.

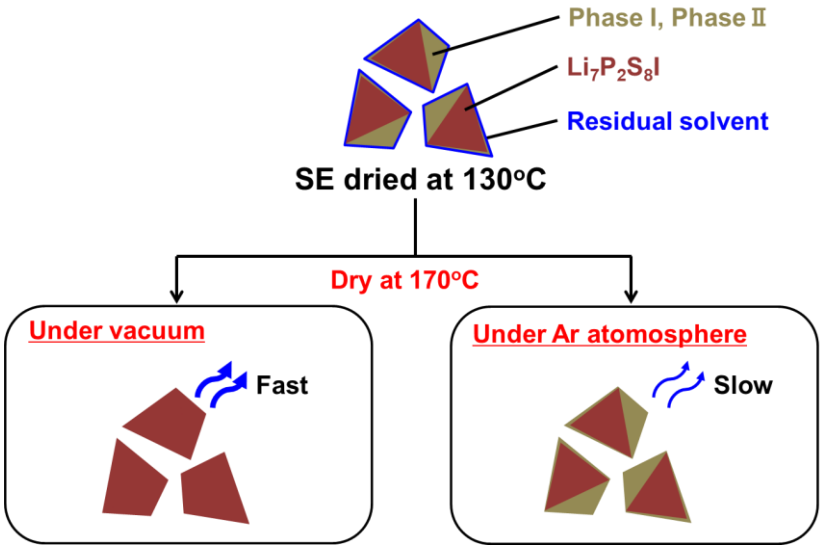

Fig. 2.2.15 Schematic images of relationships of heat treatment and SE composition.

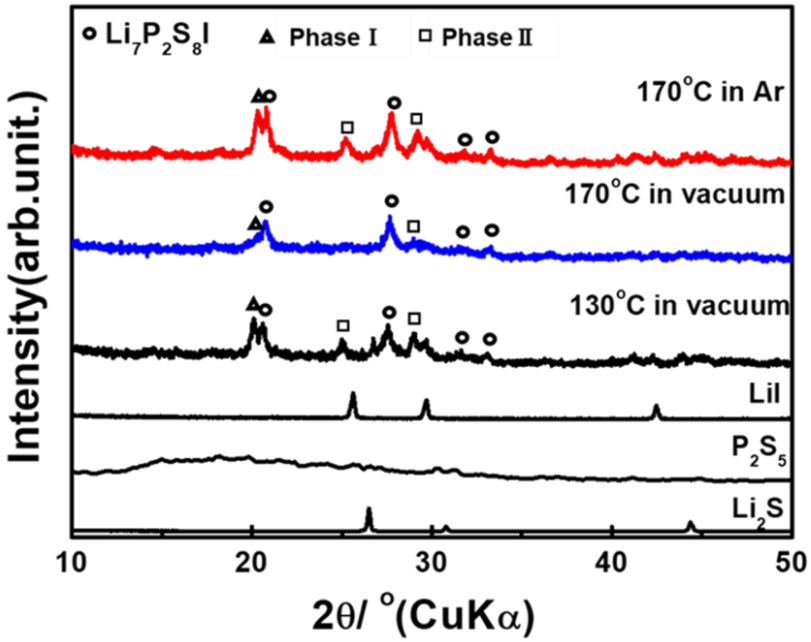

Fig. 2.2.16 XRD patterns of raw materials and the prepared LPSI with different drying condition via liquid phase shaking process. This figure was cited from *ref. 6), Copyright@2020 Elsevier.*

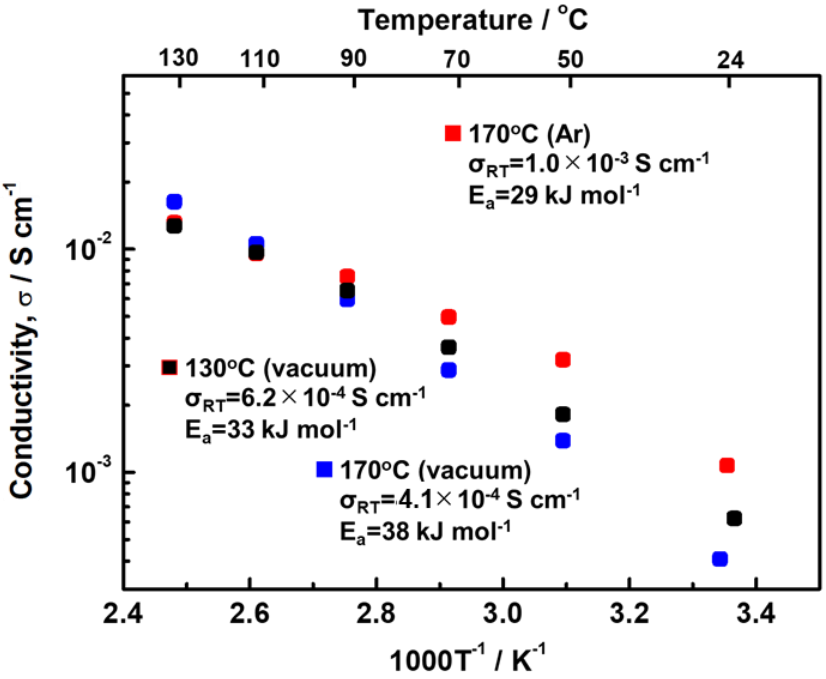

Fig. 2.2.17 Temperature dependence of the conductivity of obtained LPSI via LS process with different drying condition using blocking electrodes (SUS| LPS |SUS). This figure was cited from *ref. 6) , Copyright@2020 Elsevier.*.

2.2.4 Conclusions

The liquid phase shaking process was reviewed based on our laboratory's works. LPS was synthesized via LS process and the obtained LPS was evaluated as an electrolyte using XRD analysis, Raman, EIS, cyclic voltammogram. LPS via LS process was meta-stable ß-phase structure and the ionic conductivity was 1.5 x 10^{-4} S cm^{-1}. Further, the LPS was mixed with NMC and evaluated as a cathode for ASSLIB. LPSI was synthesized via LS process. It was indicated that the structure of LPSI was similar to the structure of Li_4PS_4I and the ionic conductivity was 3.8 x 10^{-4} S cm^{-1}. By adjusting the reaction conditions, a phase similar to the thio-LISICON region II observed in LGPS appeared in LPSI. The ionic conductivity reached 1.0 x 10^{-3} S cm^{-1} at 25 °C.

References

1) N.H.H. Phuc, K. Morikawa, M. Totani, H. Muto, A. Matsuda, Chemical synthesis of Li_3PS_4 precursor suspension by liquid-phase shaking, *Solid State Ionics* **285**, 2-5 (2016)
2) N.H.H. Phuc, M. Totani, K. Morikawa, H. Muto, A. Matsuda, Preparation of Li_3PS_4 solid electrolyte using ethyl acetate as synthetic medium, *Solid State Ionics* **288**, 240-243 (2016).
3) N.H.H. Phuc, K. Morikawa, M. Totani, H. Muto, A. Matsuda, Synthesis of plate-like Li_3PS_4 solid electrolyte via liquid-phase shaking for all-solid-state lithium batteries, *Ionics* **23**, 2061-2067 (2017).
4) N.H.H. Phuc, E. Hirahara, K. Morikawa, H. Muto, A. Matsuda, One-pot liquid phase synthesis of (100-*x*) Li_3PS_4− *x*LiI solid electrolytes, *J. Power Sources* **365**, 7-11 (2017).
5) A. Hayashi, S. Hama, H. Morimoto, M. Tatsumisago, T. Minami, Preparation of Li_2S− P_2S_5 amorphous solid electrolyte by mechanical milling, *J. Am. Ceram. Soc.* **84**, 2, 477-479 (2001).
6) K. Hikima, T. Yamamoto, N.H.H. Phuc, R. Matsuda, H. Muto, A. Matsuda, Improved ionic conductivity of Li_2S− P_2S_5− LiI solid electrolytes synthesized by liquid-phase synthesis, *Solid State Ionics* **354**, 115403 (2020).
7) E. Rangasamy, Z. Liu, M. Gobet, K. Pilar, G. Sahu, W. Zhou, H. Wu, S. Greenbarm, C. Liang, An iodide-based $Li_7P_2S_8I$ superionic conductor, *J. Am. Ceram. Soc*. **137**, 1384-1387 (2015).
8) R. Matsuda, N.H.H. Phuc, M. Totani, M. Morikawa, H. Muto, A. Matsuda, Preparation of nanosize Li_3PS_4 solid electrolyte by liquid-phase shaking method and its application in all-solid-state lithium ion battery, *56th Denchi touronnkai*, 1F23 (2015).
9) R. Kanno, T. Hata, Y. Kawamoto, M. Irie, Synthesis of a new lithium ionic conductor, thio-

LISICON-lithium germanium sulfide system, *Solid State Ionics* **130**, 97-104 (2000).

10) M. Murayama, R. Kanno, Y. Kawamoto, T. Kamiyama, Structure of the thio-LISICON, Li_4GeS_4, *Solid State Ionics* **154-155**, 789-794 (2002).

11) M. Murayama, N. Sonoyama, R. Kanno, Material design of new lithium ionic conductor, thio-LISICON, in the $Li_2S-P_2S_5$ system, *Solid State Ionics* **170**, 3-4, 173-180 (2004).

12) B. Tao, C. Ren, H. Li, B. Liu, X. Jiu, X. Dong, S. Zhang, H. Chang, Thio-LISICON and LGPS-type solid electrolytes for all-solid-state lithium-ion batteries, *Adv. Funct. Mater.* **32**, 2203551 (2022).

13) K. Homma, M. Yonemura, T. Kobayashi, M. Nagao, M. Hirayama, R. Kanno, Crystal structure and phase transitions of the lithium ionic conductor Li_3PS_4, *Solid State Ionics* **182**, 53-58 (2011).

14) R. Kanno, M. Murayama, Lithium ionic conductor thio-LISICON: The Li_2S-GeS_2-P_2S_5 system, *Electro. Chem. Soc.* **148**, 7, A742 (2001).

15) A. Hayashi, S. Hama, T. Minami, M. Tatsumisago, Formation of superionic crystals from mechanically milled $Li_2S-P_2S_5$ glasses, *Electrochem. Commun.* **5**, 111-114 (2003).

16) Z. Liu, W. Fu, E.A. Payzant, X. Yu, Z. Wu, N.J. Dudney, J. Kiggans, K. Hong, A.J. Rondinone, C. Liang, Anomalous high ionic conductivity of nanoporous β-Li_3PS_4, *J. Am. Chem. Soc.***135**, 975-978 (2013).

17) S.J. Sedlmaier, S. Indris, C. Dietrich, M. Yavuz, C. Dräger, F. Seggern, H. Sommer, J. Janek, Li_4PS_4I: A Li^+ superionic conductor synthesized by a solvent-based soft chemistry approach, *Chem. Mater.* **29**, 4, 1830-1835 (2017).

Chapter 3
Coatings of Active Materials for Improving Performance of All-Solid-State Batteries

3.1 Preparation of $LiNi_{1/3}Mn_{1/3}Co_{1/3}O_2/Li_3PS_4$ cathode composite particles using a new liquid-phase process and application to all-solid-state lithium batteries

3.1.1 Introduction

For all-solid-state lithium batteries, the electrochemical contact of the interface between active materials and solid electrolytes is one of the most important themes. It is difficult to coat the active material uniformly with the solid electrolyte. The sulfide-based solid electrolytes are currently well known as excellent candidates for all-solid-state battery and extensively studied because of their high lithium ionic conductivity comparable to organic electrolytes and suitable plasticity for good contact at the interface[1-3]. The various methods for composite fabrication of cathode active materials and solid electrolytes have been extensively studied[4-6]. The tightly packed composites were prepared using cold-pressing at room temperature or hot-pressing at relatively low temperature. However, volume change in the composite during charge-discharge cycles causes an increase in vacancy between active materials and electrolytes, which results in a decrease in the capacity of the all-solid-state battery. Thus, it is essential to develop a new concept to design the composite electrodes which can be following up such a volume change during the charge-discharge cycling.

Recently we have developed a new process, liquid-phase shaking (LS) method[7], to prepare electrolytes in the Li_2S-P_2S_5 system. The electrolyte prepared by LS method can be mixed homogeneously with active materials because the particles of the resultant electrolyte are very fine[8]. In this study, I propose a new preparation method of active materials and solid electrolytes composite based on the liquid phase process, which is named “SEED method”. In the SEED method, the solid electrolyte is prepared from the seed materials, which are nuclei precipitated on the surface of the active material and act as scaffold to prepare the electrode composite as shown in Fig. 3.1.1. Li_3PS_4 (LPS) solid electrolyte with excellent plasticity was prepared by the SEED method on the surface of $LiNi_{1/3}Mn_{1/3}$ $Co_{1/3}O_2$ (NMC) positive electrode active material with high-potential[3]. The structure of the NMC-LPS composite thus obtained and its battery characteristics were also evaluated in the present study.

3.1.2 Experimental

First, Li_2S (99.9%, Mitsuwa) was added to ethanol (EtOH, Super Dehydrated 99.5%, Wako) and dissolved by stirring treatment for 30 min. NMC (1 wt% $LiNbO_3$ coated, JST-ALCA-SPRING) was immersed in the obtained Li_2S EtOH solution and then evacuated at 170°C for 2 h to evaporate EtOH to prepare the NMC-Li_2S composite. Retention of Li_2S after EtOH evaporation was confirmed by using X-ray diffraction (XRD) measurement (Ultima IV, Rigaku). Second, Li_2S and P_2S_5 (99%, Merck) were mixed at a molar ratio of Li_2S:P_2S_5= 1:1 and dissolved in ethyl propionate (EP) by ultrasonic treatment (500 W, 23 Hz) for 1 h to obtain a transparent yellow solution. The NMC-Li_2S composite was added to the obtained transparent yellow 1Li_2S-1P_2S_5 EP solution, and agitation treatment (stirring 500 rpm at 50°C) was carried out for 6 h. Li_2S added to EtOH was fixed to be twice as much as the total amount of P_2S_5 in molar ratio in the EP solution (total Li_2S:P_2S_5 molar ratio in the EP solution was 3:1), and NMC: LPS weight ratio was expected as 90:10. The NMC coated with LPS precursor was heat treated at 170℃ for 2 h under reduced pressure after evaporating the solvent EP at room temperature under reduced pressure. The gray powders of NMC-LPS composites were obtained.

To confirm the formation reaction of LPS from Li_2S and $Li_2P_2S_6$ in EP during SEED process, in-situ observation of suspensions using Raman spectroscopy (NRS-3100, JΛSCO) was carried out. Twice amount of Li_2S in molar ratio was added to the solution of "Li_2S:P_2S_5 = 1:1 ($Li_2P_2S_6$) in EP" in the quartz sealed container with a cap. The Raman spectra were detected each time during stirring from 0 h to 6 h. The prepared composites were characterized using scanning electron microscopy (SEM; S4800, Hitachi). X-ray elemental maps were taken using an energy dispersive X-ray spectroscopy (EDXS, Horiba) detector attached to the SEM system. The TEM image and the electron diffraction patterns were obtained using JEM-2100F field-emission-type TEM (JEOL). The XRD pattern of LPS was also obtained.

An all-solid-state cell using the prepared 90NMC-10LPS composite as a positive electrode, LPS prepared by the liquid-phase shaking method invented by our laboratory[7,8] as an electrolyte layer and Indium foil (In, 99.99%, Nilaco) as a counter electrode was fabricated. The composed electrodes for electrochemical measurements were prepared by uniaxial pressing (about 80 mg of sample dried at 170°C) pellets of about 0.6 mm in thickness and 10.0 mm in diameter at a pressure of 330 MPa (at room temperature). The prepared pellet was placed in a holder made from polyetheretherketone (PEEK) with two stainless steel rods. The charge-discharge test of the cells was conducted at a constant

current at 0.1 C. In order to verify the effect of composite by the SEED method, the same test was also carried out on all-solid-state cells using a positive electrode composite prepared by hand mixing. All processes for preparing the composites and fabricating the all-solid-cells were performed in an Ar-filled dry box. The cell was placed in a glass tube filled with Ar when the electrochemical characterizations were performed.

3.1.3 Results and discussion

Figure 3.1.1 shows the concept of the preparation procedure of NMC-LPS composite by SEED method. Li_2S, as a seed material, coated on active materials NMC reacts with the '$Li_2P_2S_6$ in EP' solution and finally LPS (molar ratio Li_2S:P_2S_5 =3:1) is formed on the surface of NMC. The solution of '$Li_2P_2S_6$ in EP' prepared with Li_2S and P_2S_5 (molar ratio Li_2S:P_2S_5= 1:1) in EP is transparent and homogeneous. In the case of other ratios, some sediments were precipitated at Li_2S:P_2S_5= 6:4, and the solution was separated into two layers at Li_2S:P_2S_5= 3:7[9]. It is consequently suggested that Li_2S:P_2S_5 ratio in the EP solution is quite important to induce uniform reaction with Li_2S on NMC.

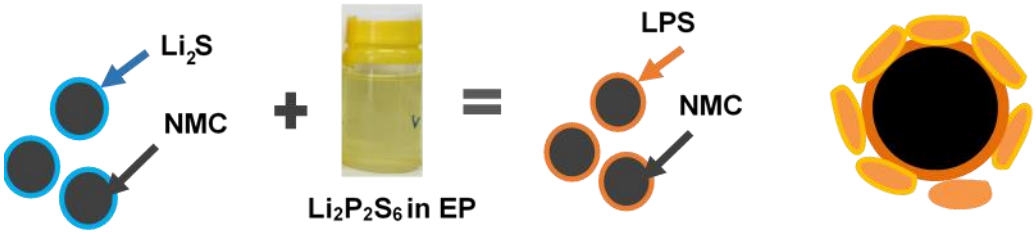

Fig. 3.1.1 The concept of the preparation procedure of NMC-LPS composite by the SEED method. NMC: $LiNi_{1/3}Mn_{1/3}Co_{1/3}O_2$, EP: ethyl propionate, LPS: Li_3PS_4.

To confirm the formation of LPS without NMC, Li_2S was added solely to the solution of '$Li_2P_2S_6$ in EP' and the changes in profile of the suspension were examined with in-situ Raman spectroscopy. Figure 3.1.2 shows the Raman spectra of the suspensions after Li_2S was added to '$Li_2P_2S_6$ in EP' and EP. The intensity of all suspension spectra was normalized with the highest peak intensity at around 2940 cm^{-1} assigned to the vibration of CH_3 group in EP[10]. All of the suspensions and EP solvent have bands at around 369 cm^{-1} assigned to EP in their spectra. The spectrum immediately obtained after adding Li_2S (0 h) shows a band at around 389 cm^{-1}, which is assigned to

$P_2S_6^{2-}$ ions[8, 11] and gradually dwindles. It is considered that the dimer of phosphorus sulfides such as $P_2S_6^{2-}$ ions and $P_2S_7^{4-}$ ions have been generated in the '$Li_2P_2S_6$ in EP' before adding Li_2S. Because the generated dimeric phosphorus sulfide ions have higher solubility in EP, the solution of '$Li_2P_2S_6$ in EP' is homogeneous, and the ions easily react with Li_2S added into the solution to form PS_4^{3-} ions. With the spectrum of 3 h after the addition of Li_2S, a band located around 419 cm^{-1} appeared and gradually increased. This band is assigned to PS_4^{3-} ions, indicating that the dimer ions cleaved with Li_2S to form the monomer ions and then LPS was finally generated in 6 h. That should be an important reason for the formation of LPS under mild conditions without high temperature or high mechanical impact.

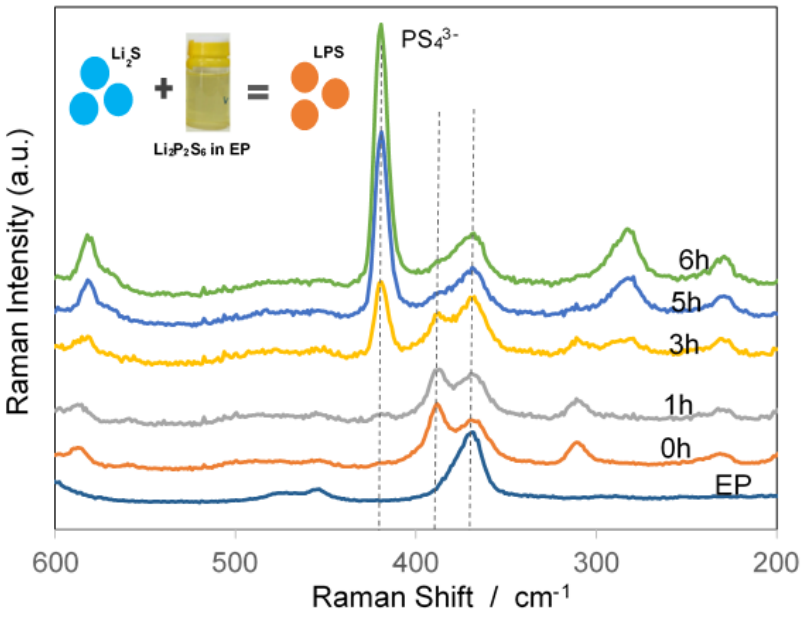

Fig. 3.1.2 Raman spectra of the suspensions after adding Li_2S into '$Li_2P_2S_6$ in EP' and EP solvent.

Figure 3.1.3 shows an SEM image and EDXS elemental mappings of P and S of the prepared active material NMC-electrolyte LPS composite produced by SEED method. There are some sheet-like solid particles on the center of the NMC particle surface, and some thin scale-like precipitates are seen on both sides of the NMC. According to the EDXS mappings, P and S are dispersed on the whole particle surface. This indicates that the thin film of LPS electrolyte was generated on the surface of the particles and then thin scale-like solid LPS grew on the NMC composite as illustrated in Fig. 3.1.1.

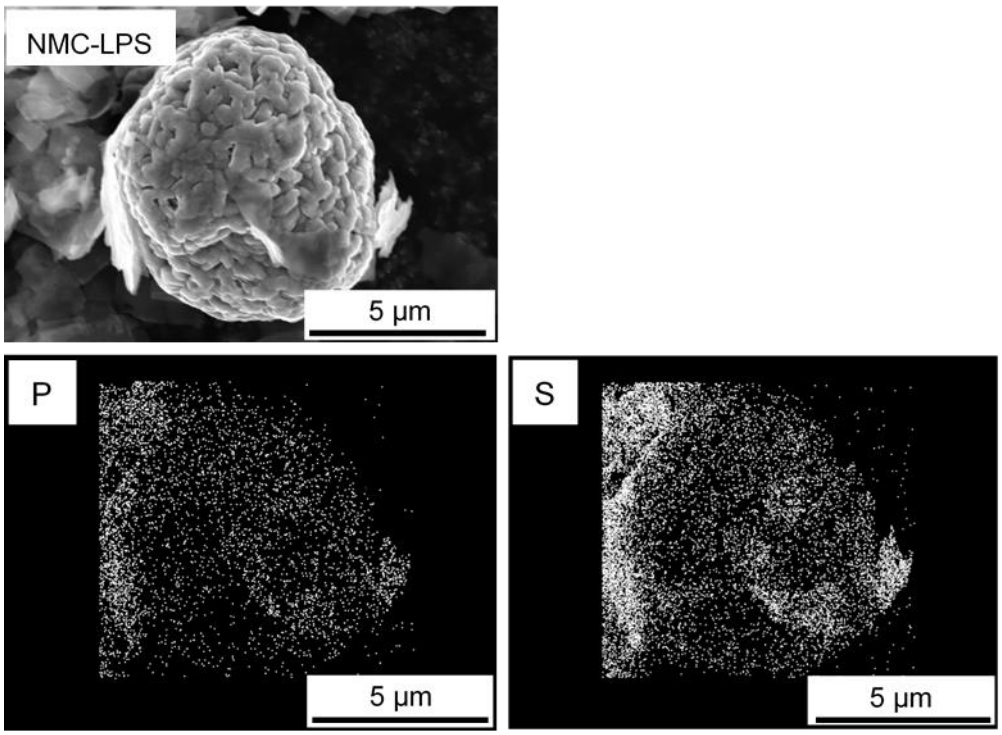

Fig. 3.1.3 SEM image of NMC-Li_3PS_4 composite particle and corresponding EDXS elemental mappings of P and S.

Figure 3.1.4 shows a TEM image and selected area electron diffraction patterns of the prepared activ material NMC-electrolyte LPS composite produced by SEED method. The center part of TEM image, which looks dark, is NMC. The translucent parts ① and ② are considered to be precipitated LPS electrolytes. The right side ring patterns ① and ② are corresponding to the parts of ① and ② on the TEM image. Part ① seems to be amorphous because of the halo pattern without spots.

Part ② shows clear spots in the pattern, indicating this part is crystalline. Therefore, the prepared electrolyte is a mixture of amorphous and crystalline parts.

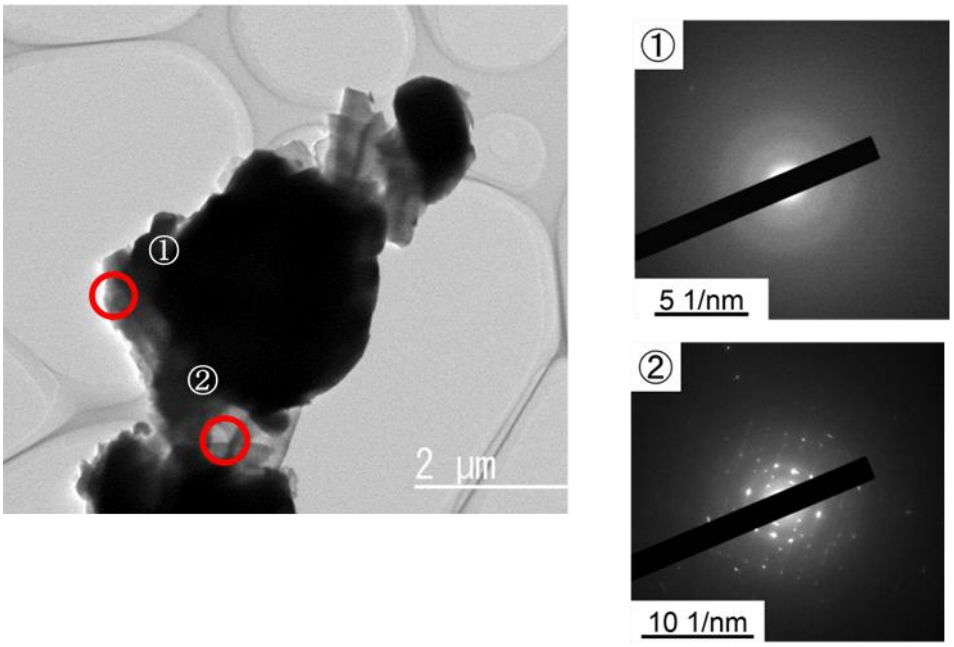

Fig. 3.1.4 TEM image of NMC-LPS composite produced by SEED method and electron diffraction patterns of circular area ① and ② in TEM image.

The intensity profile of the electron diffraction pattern for the composite is shown in Fig. 3.1.5, and the XRD intensities of β-Li_3PS_4 listed in the ICDD file (No. 01-076-0973) are also shown. These peaks of the profile are broad, but each one is identified from the strong lines of the β-Li_3PS_4. This result shows that β-Li_3PS_4 was generated on the NMC by SEED method.

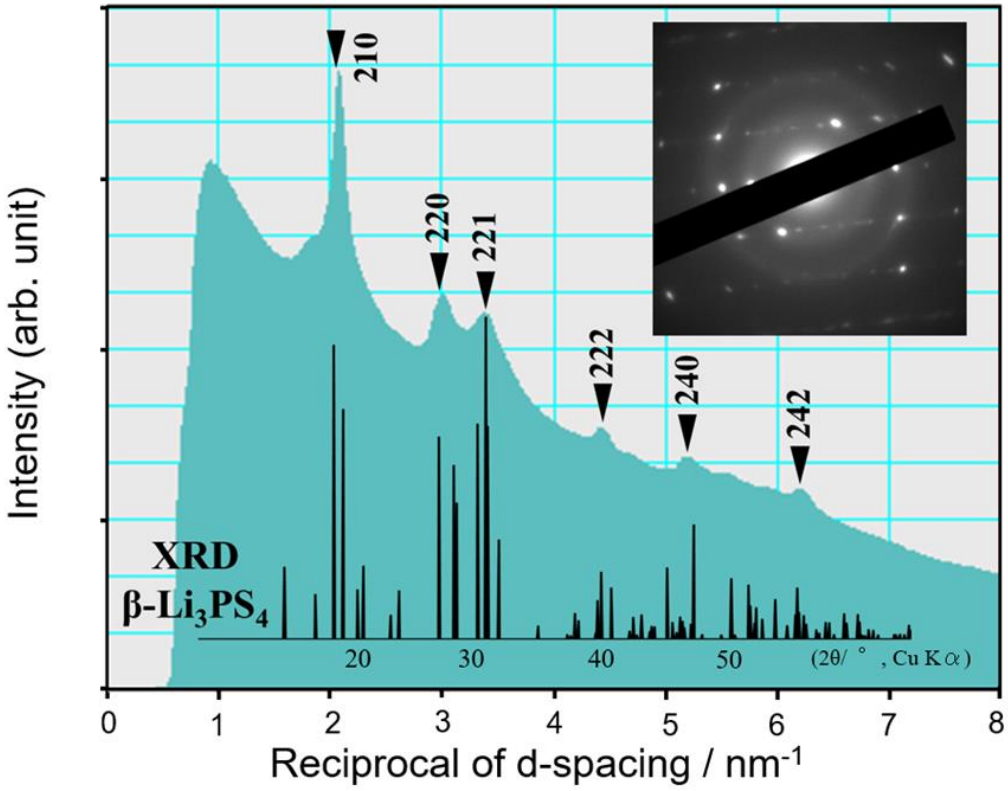

Fig. 3.1.5 Intensity profile and the corresponding electron diffraction pattern, which were obtained from the LPS area in the prepared NMC-LPS composite. Each intensity peak was almost identical to the XRD profile of β-Li_3PS_4 listed in ICDD file (No. 01-076-0973).

The all-solid-state cells were fabricated with the active material NMC-electrolyte LPS composite obtained by SEED method. The weight ratio of the composite is NMC: LPS= 90:10. The cell with hand-mixed active material, which was made of NMC and LPS, was also fabricated for comparison. The weight ratio is the same as that of the composite by SEED method. LPS used in hand-mixing was prepared by the liquid-phase shaking method. Figure 3.1.6 shows the charge-discharge curves of the cells at the current rate of 0.1 C. Both cells of cathode composite by hand-mixing and SEED method show high capacity more than 100 mAh g^{-1} though the amounts of electrolyte content are low. Because LPS particles by the liquid-phase method are very fine, LPS can be easily mixed with active materials.[8)] The cell with the composite by SEED method shows small IR-drop and keeps 3 V until 83 mAh g^{-1} (NMC) at first discharge, while the hand-mixing cell does not keep 3 V in the region higher than 56 g^{-1} as indicated with dotted lines.

Figure 3.1.7 shows the cycle performance of capacities and coulomb efficiencies of the corresponding cells in Fig. 3.1.6. The capacity of the cell using prepared composite by SEED method is 95 mAh g^{-1} at 9th cycle and higher than that of the cell using hand-mixed active material (80 mAh g^{-1}). The coulomb efficiency of the cell by SEED method was constantly higher than those of the cell by hand-mixing. Complex impedance plots for the fabricated all-solid-state cells after the first and 10th charges are shown in Figure 3.1.8. In the figure, (A) and (C) are the cell by hand-mixing, and (B) and (D) are those of the cell by the SEED method. All plots are composed of three semicircles divided by frequency into low areas (< 100 Hz) assigned to anode resistance, medium area (< 10 kHz) assigned to boundary resistance of the cell, and high area (> 10 kHz) assigned to bulk resistance of electrolyte shown in Fig. 3.1. 8(a). In the area of medium frequency, both plots of cells by the SEED method first (B) and 10th (D) charge show smaller semicircles than the cells by hand-mixing (A) and (C). This indicates that the boundary resistance of the cells by SEED method is lower, and it maintains better contact between NMC and electrolyte in comparison with that of the cells prepared by hand-mixing.

To further analysis of boundary resistance of the cells, the results of complex impedance plots were applied to fitting analysis using the equivalent circuit model shown in Fig. 3.1.8(b) [12-14)]. Figure 3.1.8(a) shows an example of fitting analysis corresponding the plots data in Fig. 3.1.8(A). The semicircle of plots in the medium frequency area is divided by fitting into grain boundary resistance of electrolyte ($R_{SE,gb}$) shown in an orange-colored semicircle and interfacial resistance between the electrolyte and active materials ($R_{SE/cathode}$) shown in a red colored semicircle. In the results of the fitting corresponding to all data in Figs. 3.1.8(A)-(D), the values of $R_{SE/cathode}$ are shown in Table 3.1.

Focusing on $R_{SE/cathode}$ after 10th charging, the $R_{SE/cathode}$ of the cell by using SEED method is smaller than that of the cell by hand-mixing. In comparison with the increasing rate, these values of the cell using SEED method is not so high against the cell by hand-mixing. This can be ascribed to good retention of electrochemical contact at the interface between NMC and LPS in the cell by SEED method during 10th charge-discharge cycles.

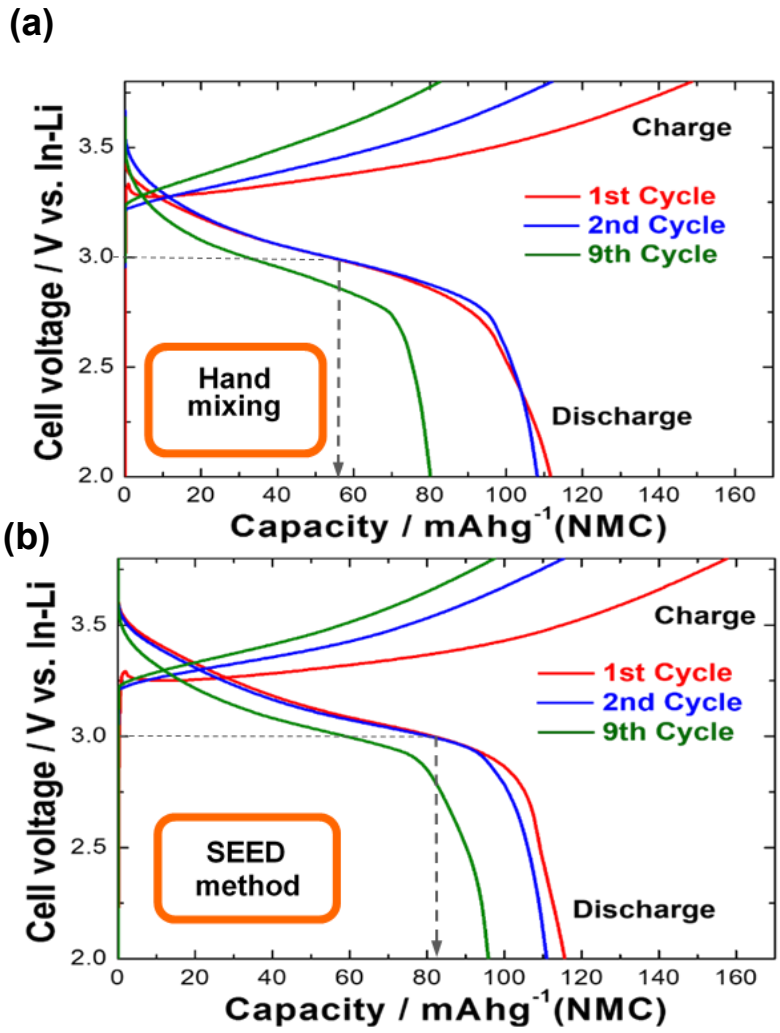

Fig. 3.1.6 Voltage profiles of charge-discharge cycles of the all-solid-state 90NMC-10LPS|LPS (LS method) Li-In cells at 30°C, 0.1C. Active material composites were prepared by (a) hand mixing and (b) SEED method.

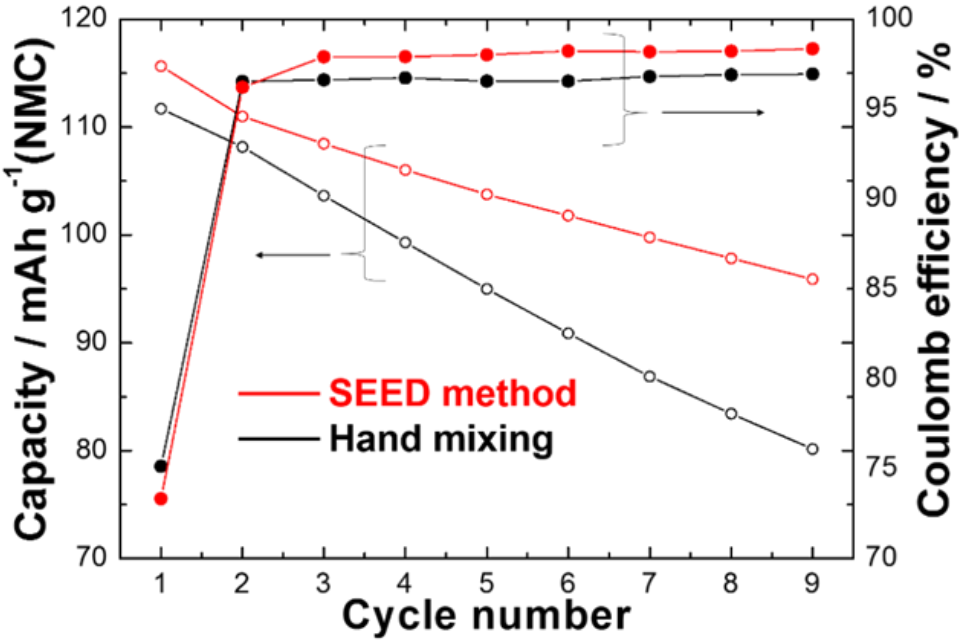

Fig. 3.1.7 Comparison of coulomb efficiency and discharge capacity of the all solid-state 90NMC-10LPS|LPS (LS method) In cells obtained by SEED method and hand mixing at 0.1 C.

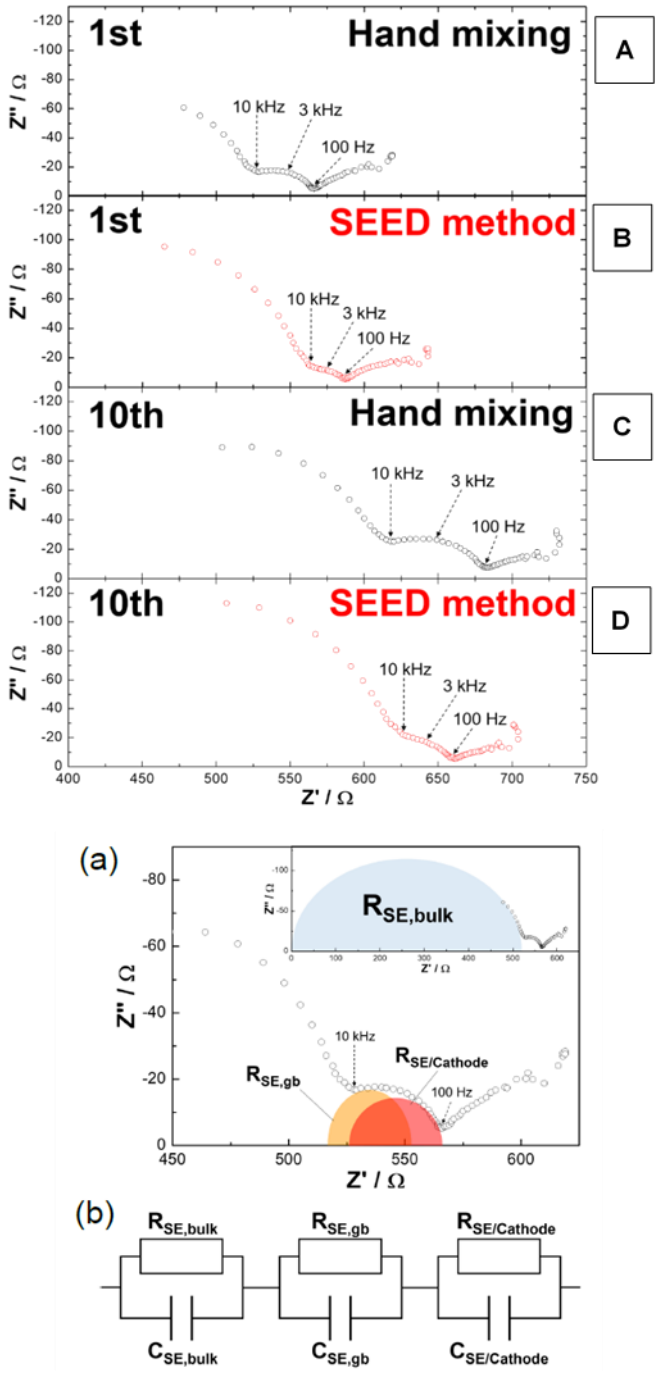

Fig. 3.1.8 Complex impedance plots for the all-solid-state 90NMC-10LPS|LPS (LS method) |Li-In cells obtained by (A, C) hand mixing and (B, D) SEED method. Measurements were conducted (A, B) after 1st and (C, D) after 10th charging to 3.8 V vs In-Li at 0.1 C. (a) The example of fitting analysis of complex impedance plots. (b) The model of the equivalent circuit for fitting.

Table 3.1 Comparison of $R_{SE/Cathode}$ after 1st and 10th charging to 3.8 V vs Li-In at the current density of 0.1 C and $R_{SE/Cathode}$ growth rate for the all-solid-state.

	$R_{SE/cathode}$ after 1st charging(Ω)	$R_{SE/cathode}$ after 10th charging(Ω)	$R_{SE/cathode}$ growth rate(%)
Hand mixing	23.8	38.3	161
SEED method	18.3	20.7	113

3.1.4 Conclusions

The cathode composite was successfully prepared using the SEED method. Li_3PS_4 was directly produced on the active material NMC on the basis of the liquid-phase shaking process. The impedance profiles showed that the composite interface between Li_3PS_4 and the active material by the SEED method maintained good contacts after the 10th charge-discharge cycles.

References

1) A. Hayashi, S. Hama, H. Morimoto, M. Tatsumisago, T. Minami, Mechanochemical synthesis of new amorphous materials of $60Li_2S{\cdot}40SiS_2$ with high lithium ion conductivity, *J. Am. Ceram. Soc.*, **84**, 477-479 (2001).
2) N. Kamaya, K. Homma, Y. Yamakawa, M. Hirayama, R. Kanno, M. Yomemura, T. Kamiyama, Y. Kato, S. Hama, K. Kawamoto, A. Mitsui, A lithium superionic conductor, *Nat. Mater*, **10**, 682-686 (2011).
3) A. Sakuda, A. Hayashi, M. Tatsumisago, Sulfide solid electrolyte with favorable mechanical property for all-solid-state lithium battery, *Sci. Rep.* **3**, 2261 (2013)
4) A. Sakuda, A. Hayashi, T. Ohtomo, S. Hama, M. Tatsumisago, $LiCoO_2$ electrode particles coated with Li_2S-P_2S_5 solid electrolyte for all-solid-state batteries, *Electrochem. Solid-State Lett*. **13**, A73-A75 (2010).
5) S. Teragawa, K. Aso, K. Tadanaga, A. Hayashi, M. Tatsumisago, Liquid-phase synthesis of a Li_3PS_4 solid electrolyte using N-methylformamide for all-solid-state lithium batteries, *J. Mater. Chem. A* **2**, 5095-5099 (2014).
6) S. Yubuchi, S. Teragawa, K. Aso, K. Tadanaga, A. Hayashi, M. Tatsumisago, Preparation of high lithium-ion conducting Li_6PS_5Cl solid electrolyte from ethanol solution for all-solid-state

lithium batteries, *J. Power Sources* **293**, 941-945 (2015).

7) N.H.H. Phuc, M. Totani, K. Morikawa, H. Muto, A. Matsuda, Chemical synthesis of Li_3PS_4 precursor suspension by liquid-phase shaking, *Solid State Ionics* **285**, 2-5 (2016).
8) N.H.H. Phuc, K. Morikawa, M. Totani, H. Muto, A. Matsuda, Synthesis of plate-like Li_3PS_4 solid electrolyte via liquid-phase shaking for all-solid-state lithium batteries, *Ionics* **23**, 2061-2067 (2017).
9) N.H.H. Phuc, A. Matsuda, Liquid phase synthesis of a Li_3PS_4 solid electrolyte precursor, *Advances in Chemistry Research* **42**, Chapter 8, pp.261-272 (2018).
10) B. Dutta, T. Tanaka, A. Banerjee, J. Chowdhury, Conformational preferences of ethyl propionate molecule: Raman, temperature dependent FTIR spectroscopic study aided by ab initio quantum chemical and Car–Parrinello molecular dynamics simulation studies, *J. Phys. Chem. A* **117**,4838-4850 (2013).
11) C. Dietrich, D.A. Weber, S. Culver, A. Senyshyn, S.J. Sedlmaier, S. Indris, J. Janek, W.G. Zeier, Synthesis, structural characterization, and lithium ion conductivity of the lithium thiophosphate $Li_2P_2S_6$, *Inorg. Chem.* **56**, 6681-6687 (2017).
12) J. Auvergniot, A. Cassel, J. Ledeuil, V. Viallet, V. Seznec, R. Dedryvere, Interface stability of argyrodite Li_6PS_5Cl toward $LiCoO_2$, $LiNi_{1/3}Co_{1/3}Mn_{1/3}O_2$, and $LiMn_2O_4$ in bulk all-solid-state batteries, *Chem. Mater.* **29,** 3883–3890 (2017).
13) A. Sakuda, A. Hayashi, M. Tatsumisago, Interfacial observation between $LiCoO_2$ electrode and $Li_2S{-}P_2S_5$ solid electrolytes of all-solid-state lithium secondary batteries using transmission electron microscopy, *Chem. Mater.* **22**, 949-956 (2010).
14) W. Zhang, D.A. Weber, H. Weigand, T. Arlt, I. Menke, D. Schröder, R. Koerver, T. Leichtweiß, P. Hartmann, W.G. Zeier, J. Janek, Interfacial processes and influence of composite cathode microstructure controlling the performance of all-solid-state lithium batteries, *ACS Appl. Mater. Interf.* **9**, 17835-17845 (2017).

3.2 Preparation of the composite $LiNi_{1/3}Mn_{1/3}Co_{1/3}O_2$ particles and Li_3PS_4-LiI electrolytes using the new liquid-phase shaking process and application to all-solid-state lithium batteries

3.2.1 Introduction

Design of high ion conducting paths and good electrochemical contact between active materials and solid electrolytes is crucial for fabrication of all-solid-state lithium batteries. The sulfide-based solid electrolytes are currently well known as a promising candidate for all-solid-state batteries and extensively studied due to their high lithium ionic conductivities and suitable plasticity for good contacts at the interface[1,2]. Various methods for composite fabrication of cathode active materials and solid electrolytes have been extensively studied[3-5]. However, the volume change in the composites during charge-discharge cycles causes in the gap increment between active materials and electrolytes, which results in a decrease in the capacity of the all-solid-state battery. Thus, it is essential to design composite electrodes which can adjust and/or follow the gap according to the volume change during the charge-discharge cycling.

Recently our research group developed a new process, liquid-phase shaking (LS) method [6] for preparation of electrolytes used in the Li_2S-P_2S_5 system. The electrolytes prepared by LS method can be mixed with active materials homogeneously due to the fine particle sizes of the resultant electrolytes[6]. I described in the section 3.1 a new preparation method named as 'SEED method' to fabricate composites of active materials and solid electrolytes based on the liquid-phase process. In this method, the solid electrolytes were prepared from Li_2S using as seed materials, which are nuclei precipitated on the surface of the active materials that act as scaffold for the composite's preparation. The composite of electrolyte Li_3PS_4 (LPS) and $LiNi_{1/3}Co_{1/3}Mn_{1/3}O_2$ positive electrode active material (NMC) which is a high-potential oxide active material was obtained using the SEED method[7]. In section 3.2, I prepared, $Li_7P_2S_8I$ (LPSI) solid electrolyte in the Li_3PS_4-LiI system, which shows higher ionic conductivity than LPS [8, 9], was prepared by the SEED method on the surface of NMC. The NMC-LPSI composites were obtained, and their battery characteristics were evaluated.

3.2.2 Experimental

Figure 3.2.1 shows the preparation procedure of NMC-LPSI composite by the SEED method. Li_2S coating on active material NMC reacts with $Li_3P_2S_6I$ ethyl propionate (EP) solution and then the

composites of NMC and electrolyte LPSI with molar ratio of Li_2S:P_2S_5: LiI =3:1:1 was obtained. The illustration shown in Fig.3.2.1 is the concept of the SEED method. Two-thirds of Li_2S that were required for preparation of LPSI were coated on active materials NMC while the remaining required one-third of Li_2S was dissolved in the solution to containing '$Li_3P_2S_6I$ with a molar ratio of Li_2S:P_2S_5: LiI =1:1:1. The resultant solution was transparent and homogeneous[10].

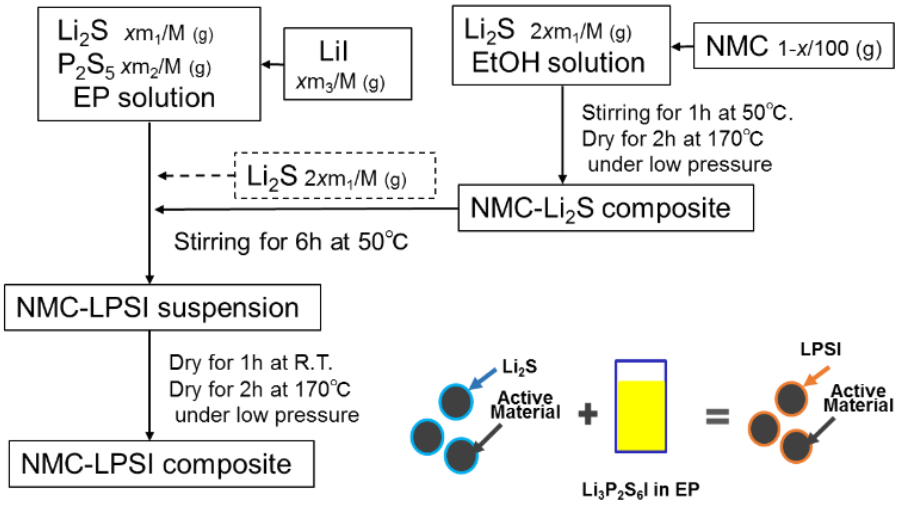

Fig. 3.2.1 The preparation procedure of NMC-LPSI composites. The weight ratio of NMC: LPSI is (100-x): x. In the figure, m_1, m_2, m_3 and M (=$3m_1+m_2+m_3$) are the molar weight of Li_2S, P_2S_5, LiI and LPSI, respectively.

The detailed preparation procedure of NMC-LPSI composite is as follows. Firstly, the NMC was coated with Li_2S. Li_2S (99.9%, Mitsuwa) was added to ethanol (EtOH, Super Dehydrated (99.5%, Wako) and dissolved by stirring treatment for 1 h. NMC (1 wt% $LiNbO_3$ coated) was immersed in the as-obtained Li_2S EtOH solution and then EtOH was evacuated at 170 ºC for 2 h under reduced pressure to form the NMC-Li_2S composite. Secondly, Li_2S, P_2S_5 (99%, Merck) and LiI (99%, Aldrich) were mixed and dissolved in EP by stirring treatment for 30 min. The obtained EP solution ($Li_3P_2S_6I$ in EP) was transparent and pale yellow. The NMC-Li_2S composite was then added to the '$Li_3P_2S_6I$ in EP' and agitation treatment with stirring was carried out for 6 h at 50 ˚C. The precursor of NMC-LPSI was

heat treated at 170 ℃ for 2 h under reduced pressure after evaporated the solvent EP at room temperature. The gray powders of NMC-LPSI composites were obtained.

The prepared composites were characterized using scanning electron microscopy (SEM; S4800, Hitachi). Elemental mapping was taken using an energy dispersive X-ray spectroscopy (EDXS, Horiba) detector attached to the SEM system. The X-ray diffraction patterns of LPSI were obtained using Ultima IV (Rigaku).

All-solid-state cells were fabricated using the prepared composite as a cathode material, LPS prepared by the liquid-phase shaking method [6] as an electrolyte layer and indium foil (diameter about 8 mm) as a counter electrode. To form electronic conducting paths to the composites, vapor grown carbon fiber (VGCF) was hand mixed with the composites. The cathode composites consist of 90NMC-10LPSI-3VGCF (wt. %). The composite electrodes for electrochemical measurements were prepared by uniaxial pressing (about 80 mg of sample dried at 170 °C) pellets of approximately 0.6 mm in thickness and 10.0 mm in diameter at a pressure of 330 MPa at room temperature. The prepared pellet was then placed in a holder made from polyetheretherketone (PEEK) and switched between two stainless steel rods. The charge-discharge tests of the cells were conducted at a constant current at 0.1 C. In order to compare the effect of composite by the SEED method, similar tests were also carried out on all-solid-state cells fabricated using positive electrodes composite prepared by hand mixing of NMC and LPSI. All processes for preparing the composites and fabrication of the all-solid-cells were performed in an Ar-filled dry box. The cells were placed in a glass tube filled with Ar during the electrochemical characterization measurements.

3.2.3 Results and discussion

Figure 3.2.2 shows an SEM image and EDXS elemental mappings of P, S and I of the composites composed of NMC and LPSI produced by the SEED method. There are some sheet-like solids on the surface of NMC particles. From the EDXS mappings, it can be observed that P, S and I are dispersed on the whole particle surface. This indicates that the thin film of LPSI electrolyte was generated on the surface of the particle and followed by growth of sheet-like solid LPSI grew on the NMC.

According to the procedure shown in Fig. 3.2.1, the LPSI electrolyte was prepared using the SEED method without NMC particles to confirm the properties of the composite electrolytes obtained by this method. The Li_2S was added to the $Li_3P_2S_6I$ EP solution instead of the NMC-Li_2S composite that is shown with dotted line in Fig. 3.2.1. Figure 3.2.3 shows XRD patterns and SEM images of

electrolytes prepared by SEED method and the LS method. Both electrolytes are exhibited with almost similar XRD patterns assigned to the crystalline $Li_7P_2S_8I$. It is noteworthy that $Li_7P_2S_8I$ crystals were precipitated from the $Li_3P_2S_6I$ in EP by adding Li_2S where a molar ratio of Li_2S:P_2S_5: LiI was 3:1:1. The SEM image of the electrolyte obtained by SEED method shows sheet-like structure and irregular-shaped particles compared with the electrolyte formed by the LS method. This electrolyte formed by SEED method exhibited almost the same profile of the temperature dependence of ionic conductivities as shown in Fig. 3.2.4. The ionic conductivity of the electrolyte formed by SEED method at room temperature was 2.5 $x10^{-4}$ S cm^{-1} which is higher than the ionic conductivity of LPS but still slightly lower than that of LPSI formed by conventional LS method. Thus, described that the LPSI on the active material composite produced by SEED method is considered to possess almost similar properties as the LPSI prepared by the previous method.

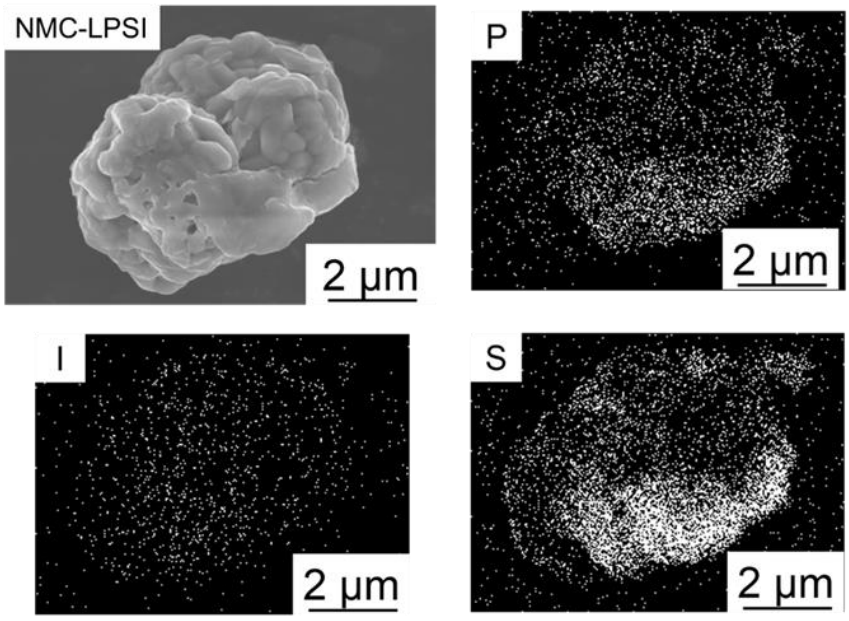

Fig. 3.2.2 An SEM image of the NMC-LPSI composite particle and corresponding EDXS elemental mappings of P, S and I.

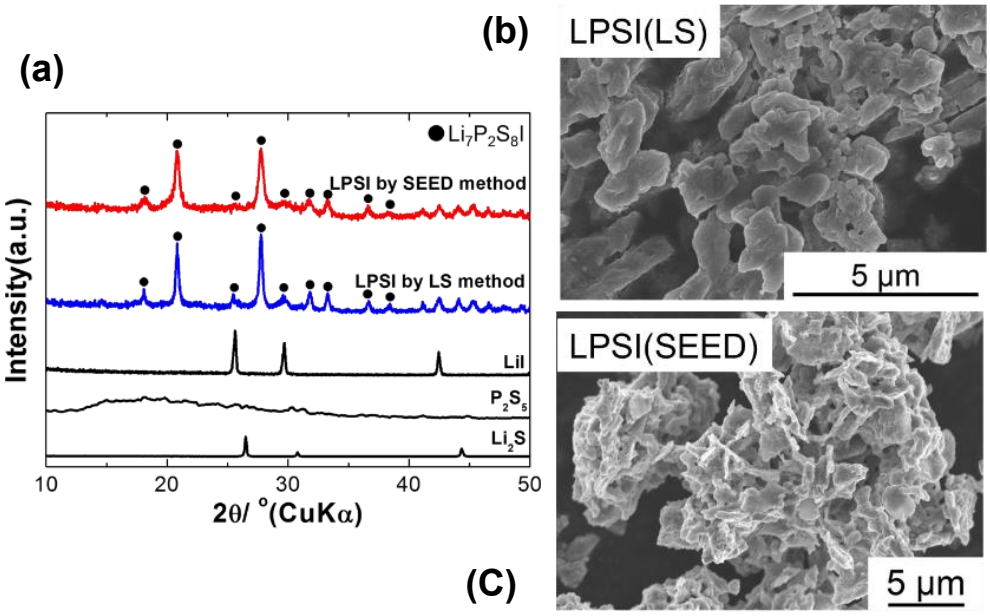

Fig. 3.2.3 (a) XRD patterns and SEM images of $Li_7P_2S_8I$ prepared by (b) the LS method and (c) the SEED method.

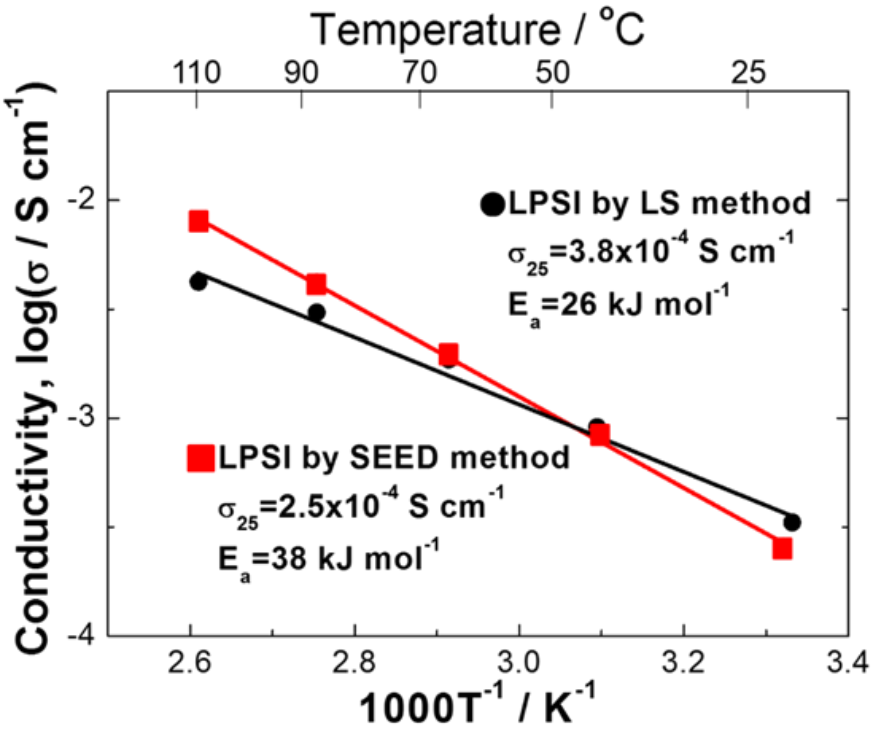

Fig. 3.2.4 The temperature dependence of ionic conductivities of LPSI electrolytes prepared by SEED method (■) and LS method (●).

The all-solid-state cell using as-obtained active material NMC-electrolyte LPSI composite by SEED method was fabricated. The weight ratio of the composite used was NMC: LPSI =90:10. The cell with hand-mixed active material consisting of NMC and LPSI was also fabricated for comparison. The weight ratio was the same as that of the composite formed by SEED method. LPSI used in the hand-mixed active material was prepared by the LS method.

Figure 3.2.5 shows the initial charge-discharge curves of the cells at 0.1C. The discharge capacity of the cell using the hand mixed active material as cathode was only 27 mA Lih g^{-1}(dash line in Fig. 3.2.5) because of the amount of electrolyte content was too low to be mixed homogenously with NMC. On the other hand, the discharge capacity of the cell using NMC-LPSI composite formed by SEED method in the present study exhibited more than 90 mAh g^{-1} (solid line in Fig. 3.2.5) and good performance compared to the cell formed by the hand-mixing although the amount of electrolyte content was same. This result indicates that the NMC particles were coated homogenously with the LPSI electrolyte and formed good contacts by using SEED method.

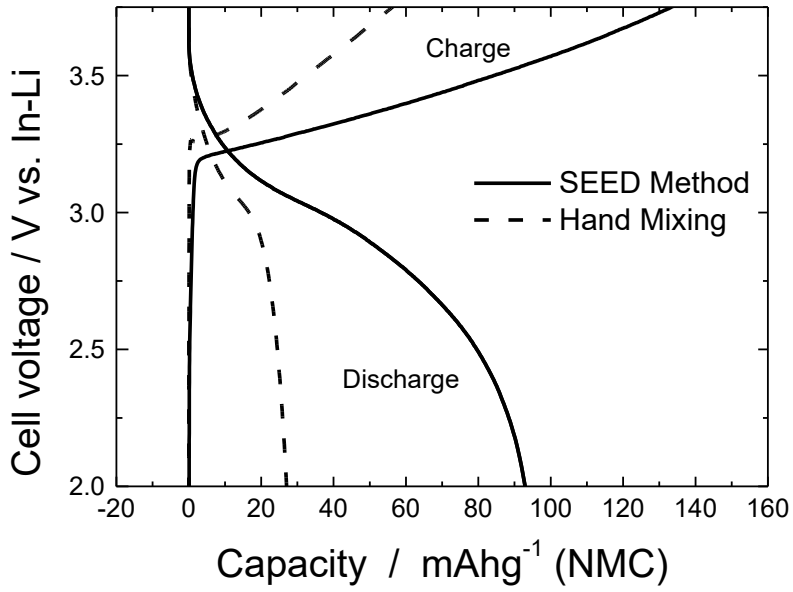

Fig. 3.2.5 Charge-discharge voltage profiles in the first cycle of the all-solid-state cells fabricated using 90NMC-10LPSI-3VGCF |LPS (LS method)|Li-In at 30 ºC, 0.1C. Cathode electrode composites were prepared by hand mixing (dash line) and SEED method (solid line).

3.2.4 Conclusions

The cathode composite was successfully prepared using the SEED method. Crystalline $Li_7P_2S_8I$ electrolyte was directly produced on the active material NMC in the similar way of Li_3PS_4 by the SEED method. The charge-discharge profiles of the all-solid-state cells show that the composite interface between LPSI and the active material formed by SEED method has good contacts. The SEED method developed in this study can be applied not only to cathode composites but also to anode composites using Li metal or carbon.

References

1) A. Hayashi, S. Hama, H. Morimoto, M. Tatsumisago, T. Minami, Preparation of Li_2S–P_2S_5 amorphous solid electrolytes by mechanical milling, *J. Am. Ceram. Soc.* **84,** 477-479 (2001).

2) N. Kamaya, K. Homma, Y. Yamakawa, M. Hirayama, R. Kanno, M. Yomemura, T. Kamiyama, Y. Kato, S. Hama, K. Kawamoto, A. Mitsui, A lithium superionic conductor, *Nat. Mater.* **10,** 682-686 (2011).

3) A. Sakuda, A. Hayashi, M. Tatsumisago, *Sci. Rep.* **3,** 2261 (2013).

4) S. Yubuchi, S. Teragawa, K. Aso, K. Tadanaga, A. Hayashi, M. Tatsumisago, Preparation of high lithium-ion conducting Li_6PS_5Cl solid electrolyte from ethanol solution for all-solid-state lithium batteries, *J. Power Sources* **293**, 941-945 (2015).

5) D.H. Kim, D.Y. Oh, K.H. Park, Y.E. Choi, Y.J. Nam, H.A. Lee, S-M. Lee, Y. S. Jung, Infiltration of solution-processable solid electrolytes into conventional Li-ion-battery electrodes for all-solid-state Li-ion batteries, *Nano Lett*. **17**, 3013–3020 (2017).

6) N.H.H. Phuc, K. Morikawa, M. Totani, H. Muto, A. Matsuda, Synthesis of plate-like Li_3PS_4 solid electrolyte via liquid-phase shaking for all-solid-state lithium batteries, *Ionics* **23**, 2061-2067 (2017).

7) E. Hirahara, N.H.H. Phuc, R. Matsuda, H. Muto, A. Matsuda, *56th The Ceramic Society of Japan Basic Meeting* 1E10 (2018).

8) S. Ujiie, A. Hayashi, M. Tatsumisago, Structure, ionic conductivity and electrochemical stability of Li_2S–P_2S_5–LiI glass and glass–ceramic electrolytes, *Solid State Ionics* **211,** 42-45 (2012).

9) N.H.H. Phuc, E. Hirahara, K. Morikawa, H. Muto, A. Matsuda, *J. Power Sources* **365**, 7-11 (2017).

10) N.H.H. Phuc and A. Matsuda, Liquid phase synthesis of a Li_3PS_4 solid electrolyte precursor, *Advances in Chemistry Research* **42**, Chapter 8, pp.261-272 (2018).

3.3 Hetero-coating of spherical graphite with sulfide solid electrolytes via the SEED process for all-solid-state lithium batteries

3.3.1 Introduction

To enhance interfacial contact between the active materials and SE, SSE coating has been applied via a liquid-phase method, wherein active materials are mixed with SSEs dissolved in organic solvents followed by evaporation[1]. Several dry methods that eliminate the need for a liquid phase, such as pulsed laser deposition and dry coating via mechanical adsorption, have also been reported[2-4]. An alternative strategy, the SEED method, has been introduced, wherein LPS is directly synthesized on cathode-active material ($LiNi_{1/3}Mn_{1/3}Co_{1/3}O_2$ (NMC)) particles via a liquid-phase process[5]. In this approach, Li_2S is first deposited onto the particles as seed crystals, serving as nucleation sites for LPS growth. That is the reason for the name of "SEED method". ASSB cells incorporating NMC-LPS composites as cathode have shown excellent charge-discharge cycle performance.

Recently, the SEED method has been extended to the anode, where $Li_7P_3S_{11}$ was coated onto graphite particles via a liquid phase process using the SEED method with acetonitrile. The resulting composite exhibited high capacity during the initial stage of the charge–discharge cycling test in an ASSB assembly[6]. However, in this study, the SE content in the composite was high, which made it difficult to demonstrate the advantages of the SEED method over simple mortar mixing. In addition, the cycling performance was not examined. Glass-ceramic $Li_7P_3S_{11}$ possesses high ionic conductivity[7-9] but is unstable toward metallic lithium[10,11]. By contrast, LPSI obtained via a liquid-phase process showed high reduction resistance and enhanced stability against lithium metal[12-14]. These findings suggest that LPSI-coated anode active materials offer a more suitable and promising approach in ASSBs.

This research explores the liquid-phase coating of spherical graphite (SG) particles with LPSI to improve anode performance in ASSBs. In this section 3.3, I evaluated the appropriate SE content in the composite via the SEED process, and these cells showed good cycling performance. Furthermore, a hetero-coating approach incorporating an argyrodite-type electrolyte was employed to enhance ionic conductivity. The electrochemical properties and cycling stability of the optimized anodes were systematically evaluated.

3.3.2 Experimental

LPSI was synthesized on SG particles in the essentially the same way as in section 3.2 via the SEED method. The LPSI coating was prepared using commercial reagents Li_2S (99.9%, Mitsuwa), P_2S_5 (99%, Merck), and LiI (99%, Sigma-Aldrich) in a molar ratio of Li_2S: P_2S_5: LiI = 3:1:1. Two-thirds of the Li_2S was dissolved in ethanol, and graphite particles were added to the Li_2S-ethanol solution, followed by drying at 150 °C under low pressure. A solution of $Li_3P_2S_6I$-ethyl propionate (EP) was prepared by dissolving one-third of the residual Li_2S, P_2S_5, and LiI, in EP. The Li_2S-coated graphite particles were then added to this solution, stirred for 4.5 h at room temperature, and the resulting dark gray slurry was dried and heat-treated at 170 °C under low pressure. The weight ratio of LPSI coating on the graphite particles varied from 1 to 30 wt%. For ultrathin LPSI coatings (1–5 wt%), the coated graphite particles were further mixed with an argyrodite-type SE, which was synthesized via mechanical milling and exhibited an ionic conductivity of approximately 2 mS cm^{-1} at room temperature. The total SE content in the composite was adjusted to 30 wt%.

The LPSI and Li_2S-coated graphite particles were characterized using X-ray diffraction (XRD; Ultima IV, Rigaku) and scanning electron microscopy (SEM; S4800, Hitachi). Elemental mapping was performed using an energy-dispersive X-ray spectroscopy (EDS; ULTIM MAX, Oxford) detector attached to the SEM system. To confirm the formation of the ultrathin LPSI coating on the graphite particles, cross-section imaging was conducted using a field-emission-type transmission electron microscope (TEM; JEM-2100F, JEOL). The electronic conductivity of the graphite composite powder was measured using a direct current method at room temperature. The samples were uniaxially pressed at 250 MPa into pellets (0.6 mm in thickness and 10.0 mm in diameter) using a poly(ether-ether-ketone) cell and stainless-steel rods (SUS304). To evaluate the electrochemical performance of the graphite particle composites as anodes, all-solid-state battery half-cells were assembled using the same cell configuration as for the electrical measurements with 80 mg of LPSI or argyrodite-type SE as the separator and lithium-indium (Li-In) metal as the counter electrode, respectively. All processes related to the composite preparation and cell fabrication were performed in an Ar-filled glove box. The battery performance was evaluated using a battery charge-discharge measurement device (BTS-2004H, Nagano). Li-ions insertion into SG occurred during “discharge” because of the SG composite material was used as working electrode. Conversely, during “charge,” Li-ions move from SG to Li-In. Therefore, in this work, “discharge” means Li-ion insertion into SG and “charge” means Li-ion going back to Li-In. This graphite composite layer, which was evaluated as the negative-electrode active material for ASSB, is described as the “anode” in some parts of the report.

3.3.3 Results and discussion

Figure 3.3.1a and 1b present SEM images of the SG surface. Figure 3.3.1a shows SG particles coated with Li_2S, while Figure 3.3.1b shows the surface morphology after the SEED process, revealing a smooth and homogeneous coating. Figure 3.3.1c shows the XRD pattern of Li_2S dissolved in ethanol and subsequently dried 150 °C under low pressure, along with a reference pattern from the Inorganic Crystal Structure Database (ICSD; ICSD#54396). The pattern of Li_2S after ethanol treatment corresponds to crystalline Li_2S, and the broadening of the peaks indicates that the crystallinity decreased because of the dissolution of Li_2S in ethanol. Figure 3.3.1d illustrates the XRD patterns of SG (70 wt%) coated with LPSI (30 wt%) by the SEED process, along with those of bare SG, LPSI synthesized through a liquid-phase shaking process, and commercial reagent LiI, and Li_2S. The peak near 20°, marked by a blue dot in the XRD pattern of SG treated via the SEED process, corresponds to LPSI, confirming its successful deposition.

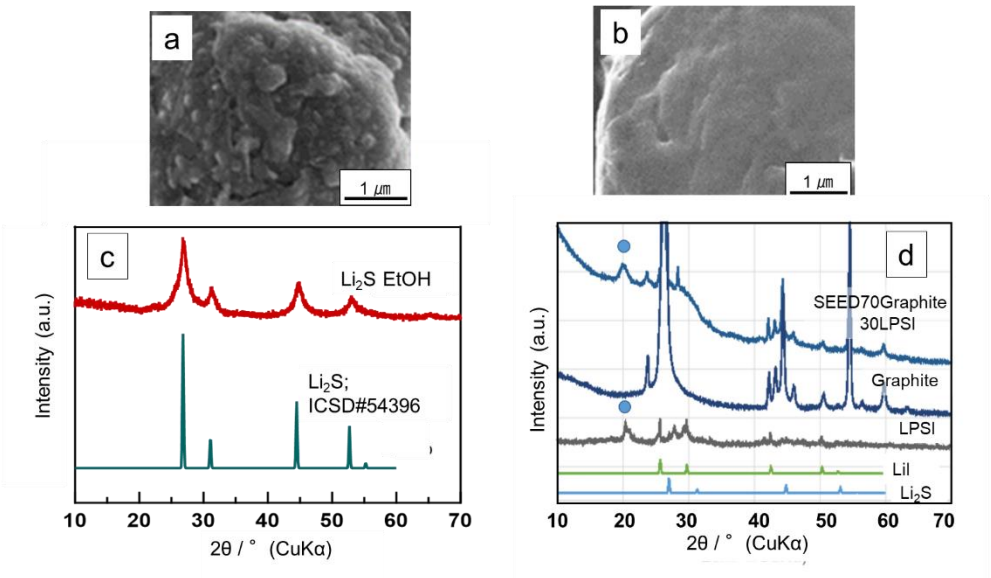

Fig. 3.3.1 SEM images of SG surface: (a) coated with Li_2S and (b) after treated by SEED process. (c) XRD patterns of Li_2S from the ICSD and treated with ethanol. (d) XRD patterns comparing SG after the SEED process, untreated graphite, LPSI, commercial Li_2S, and LiI.

Using the composites of SG and LPSI obtained by the SEED process as the anode, half-cells of ASSBs were fabricated, and their electrical properties were measured. Figure 3.3.2 shows the charge–discharge performance of the half-cells. The charge (return of Li ions to Li-In)−discharge (insertion of Li ions into SG) curves in Figure 3.3.2a–2c, 2e, and 2f correspond to composite weight ratios of SG:LPSI as follows: 80:20 for 2a, 90:10 for 2b, 95:5 for 2c, and 87:13 for 2e and 2f. The density of graphite is typically 2.25 g cm^{-2} [15], while the density of LPSI prepared by liquid-phase process was measured to be 2.07 g cm^{-2} when pressed at 250 MPa in a uniaxial press. Therefore, the volume ratio of SG to LPSI was considered approximately equal to the weight ratio. Figure 3.3.2a–2c present the charge−discharge curves of 100 cycles, shown at intervals of every 10 cycles. The capacity retention was excellent; however, when the SG weight ratio exceeded 90 wt%, the capacity significantly reduced owing to the insufficient SE content. At an SG ratio of 80 wt%, the capacity was approximately 150 mAh g^{-1} after 100 cycles. At 70 wt%, the cell performance was inferior to that of cells with a higher SG weight ratio, with a charge capacity of approximately 80 mAh g^{-1}(SG), despite the SE weight ratio being 30 wt%. The SG composites synthesized via SEED process contained no electron-conductive additives, such as acetylene black (AB). This suggests that the electronic conductivity of the SG composite decreased, likely due to the nearly complete coating of SG particles—intrinsically conductive materials—with LPSI during the SEED process. Figure3.4. 2d presents the rate performance for SG: LPSI = 87:13 (wt%). In the pink area, the charge and discharge currents for each rate are constant (CC), under the same conditions as those in Figures 3.3.2a to 2c at 0.1C. Figure 3.4.2e shows the charge−discharge curves corresponding to the pink area in Figure 3.4.2d. The initial charge capacity for the SG cell: LPSI = 87:13 reached 260 mAh g^{-1} (SG). The efficiency of the cell showed more than 99% after the 4^{th} cycle. Following the high current rate test, the efficiency of the cycles remained more than 99.5% at 0.1 C. However, the capacity was severely reduced in the high current test and exhibited a significant decline at higher current rates of 0.5 C, 1 C, and 2 C. In the blue-colored area, the cells with SG: LPSI = 87:13 were discharged at constant current down to -0.6 V. followed by constant discharge voltage at -0.6 V. This indicates that when the battery undergoes sufficient discharge, its output characteristics are significantly improved. The results suggest that the SEED process effectively expanded the contact area between SG and SE, despite the low SE weight ratio.

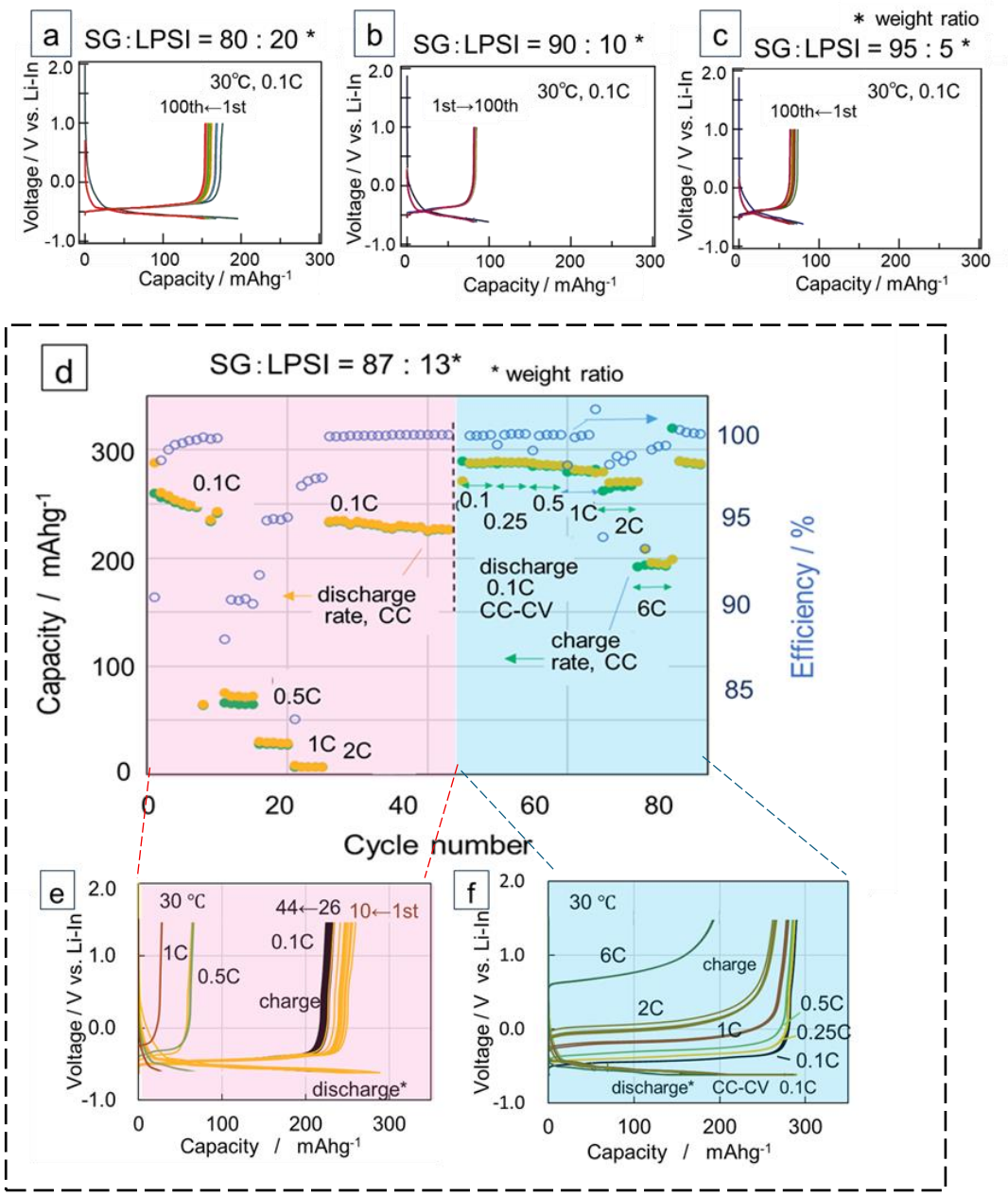

Fig. 3.3.2 Charge–discharge performance of the half cells at 30℃. The charge 2c (return of Li-ions to Li-In)–discharge (insertion of Li-ions into SG) curves in Figure 2a-, 2e, and 2f show that in the case of the composite weight ratio of SG:LPSI = 80:20 for 2a, 90:10 for 2b, 95:5 for 2c, and 87:13 for 2e and 2f, respectively. 2d is the rate performance for SG: LPSI = 87: 13 (wt%), the pink part shows constant current (CC) test, and the blue part is constant voltage (CV) test after CC. The cells were constructed as follows, SG composites | LPSI 80 mg | Li-In foil.

The electronic conductivities of the SG composites are shown in Figure 3.3.3-a1. The blue dots are the result of the SG composites mixed with LPSI by hand mixing in a mortar. The red dots represent those obtained via SEED process. The SG composites mixed with a mortar and pestle appeared to percolate when the SG content was 20 wt%. By contrast, the electronic conductivity of the SG composites prepared via SEED process decreased significantly when the SG content decreased from 80 to 70 wt%. This is because each SG particle was coated completely with LPSI, which has low electronic conductivity. Figure 3.3.3-a2 shows schematic images of the electronic conduction in the anode layer. The left schematic represents a composite hand-mixed in a mortar, while the right shows a composite fabricated using the SEED process. When the SEED process uses more than 20 wt% SE (i.e. SG is less than 80 wt%), conductive agents such as acetylene black (AB) should be added. Therefore, it is necessary to consider the appropriate timing of AB addition to avoid coating AB with SE. AB was not used in this experiment of coating ASSB by the SEED process because it deals primarily with SG contents above 80 wt%. Figure 3.3.3b shows the first (dashed line) and 10^{th} (solid line) charge capacities of the half-cells using SG composites with varying SG: LPSI weight ratios obtained via the SEED process. When the SG content of the SG composites was 87 wt%, the capacity of the half-cell was the highest among the five cell types. Figure 3.3.3c shows a schematic of the variation in the ionic and electronic conductivities with SG content. The higher the SG content, that is, the lower the SE, the lower the ionic conductivity. In particular, when the SG content exceeds 90 wt%, the ionic conductivity decreases drastically. Conversely, the higher the SG content, the higher the electronic conductivity, especially when the SG content was above 80 wt%, and the electronic conductive paths were considered to be percolating. Therefore, it is assumed that cells with SG contents between 80 and 90 wt% showed good performance.

Figure 3.3.4 shows the SEM cross-sectional images of half-cells using SG composites as the anode; the SG content was 87 wt% in 4a and 70 wt% in 4b. In both images, the LPSI layers synthesized by the SEED process were not only shown on the surface of the SG particles but also on their inner layers. In image 4b, a large amount of LPSI is located around the SG particles, so Li ions are abundant around the SG particles. However, the SG particles did not come into contact with each other, and the electronic connections were broken. In Figure 3.3.4a, the entire layer appeared as homogeneous horizontal strips, and the SG particle boundaries could not be identified. This indicates that the layer has a large contact area between the SG particle surface and the LPSI. Therefore, the output performance is excellent (Figure 3.4.2d, blue part). In other words, the Li-ion insertion reaction did

not improve, which significantly reduced the capacity for Li-ion insertion at a high rate above 0.5 C (Figure 3.3.2d, pink part).

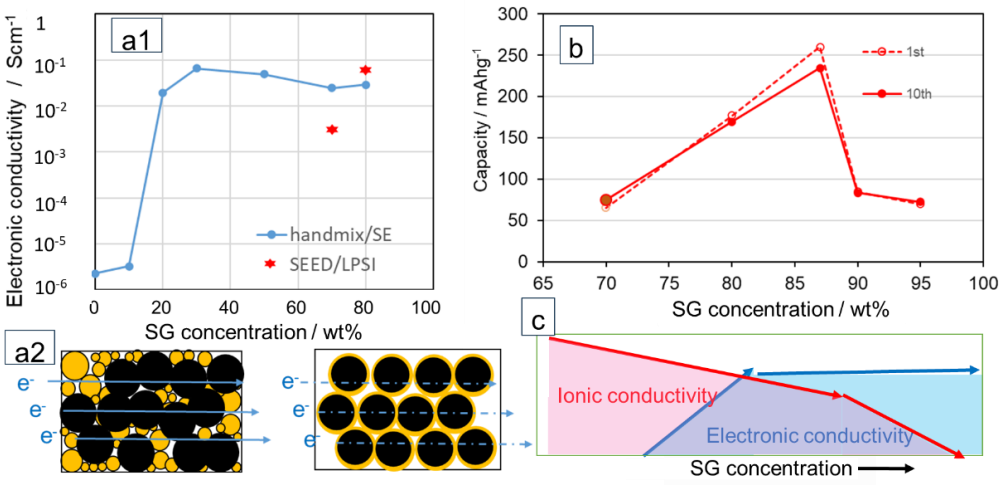

Fig. 3.3.3 SG content dependence of a1: electronic conductivity of SG composites by hand-mix (blue) and SEED process (red dot), b: charge capacity of first (dashed line) and 10th cycle (solid line) for the cells using SG composites. a2: schematic images of the electronic conduction in the anode layer. c: schematic of the relationship of ionic conductivity and electronic conductivity.

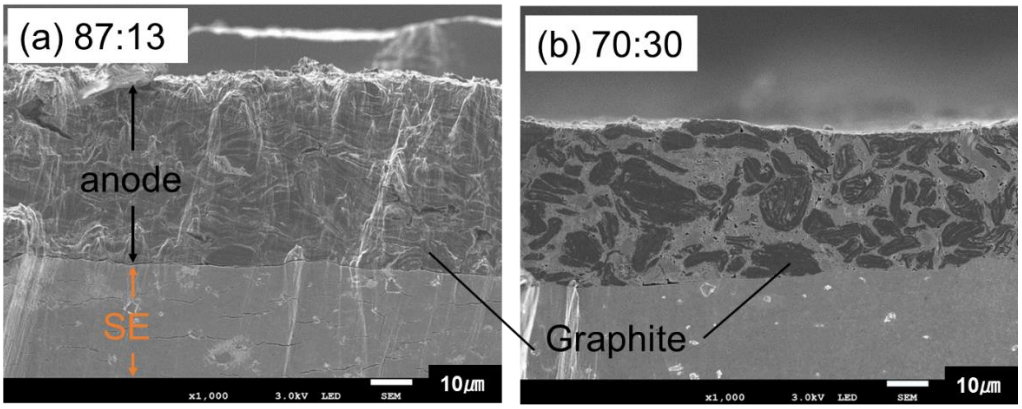

Fig. 3.3.4 SEM cross sectional images of the SG composite layer side of the half-cell; the SG content in the layer is 87 wt% in 4a, 70 wt% in 4b.

To further improve the Li-ion insertion reaction and the capacity retention rate, an SG coating was designed using a hetero-SE. The LPSI coating on the SG particles via the SEED process was as thin and homogeneous as possible to maintain the electronic contact. The obtained SG particles coated with the super-thin LPSI layer were hand-mixed using a mortar and pestle with an argyrodite-type SE to improve ionic conductivity. SG: total SE (LPSI and argyrodite) ratio was fixed at a 70:30 weight ratio, and the different amounts of LPSI (1− 5 wt%) of thin layers were synthesized by the SEED process. Figure 3.3.5a shows an SEM image of an SG particle coated with 3 wt% LPSI by the SEED process, where the LPSI layer could not be identified. Figure 3.3.5b and 5c show EDS images of phosphorus and sulfur, respectively. These images suggested that the LPSI layer was homogeneously formed on the SG particles. The SG composites with hetero-SEs (i.e., LPSI thin layers and argyrodite added later) were observed using TEM and SEM. Figure 3.3.5d shows a cross-sectional TEM image of the boundary area between the SG particles and the 3 wt% LPSI layer, and Figure 3.3.5e shows one of the SEM-EDS images for chlorine and iodine. As shown in Fig. 3.3.5d, the thickness of the LPSI layer was approximately 20 nm. In Fig. 3.3.5e, iodine-colored green indicates the LPSI, and chlorine-colored red indicates the argyrodite SE. Figure 3.3.5e shows an LPSI layer between the SG particles and the argyrodite SE, which is attached to the SG particles.

Using the hetero-SE-coated SG composites as anodes, half-cells of ASSB were built, and the charge–discharge performance was evaluated. Figure 3.3.6a shows the charge–discharge curves every 10 cycles until 100^{th} for SG composites with only the argyrodite-type SE, which shows that the capacity gradually decreases. Figure 3.3.6b shows the SG composite hetero-SE coated with a 3 wt% LPSI thin layer and argyrodite-SE. The capacity exceeded 260 mAh g^{-1} (SG) in the first cycle and was maintained up to the 100th cycle. Figure 3.3.6c shows the cycle performance of half-cells using SG particles hetero-SE coated with LPSI (1–5 wt%) and an argyrodite-type SE. The insertion of Li ions into the SG anode is marked with triangles, and the return of Li ions to the Li-In is marked with diamonds. When the LPSI layer ratio was 5 wt%, the capacity was lower than that at 3 wt%. It was assumed that the electronic conductivity of the SG particles coated with more than 3 wt% LPSI was lower because of their homogeneous insulating LPSI layers. Conversely, when the ratio of LPSI layers was less than 3 wt%, the contact area between the SG particles and SE was smaller at lower LPSI ratios, resulting in lower capacity retention. Therefore, when the ratio of LPSI layers was 3 wt%, the cycling performance was the best, maintaining a high capacity and retention rate. For further evaluation, the electrical impedance of batteries using the obtained composite as the anode was

measured every 10 cycles until 100th during measurement of cycle performance.

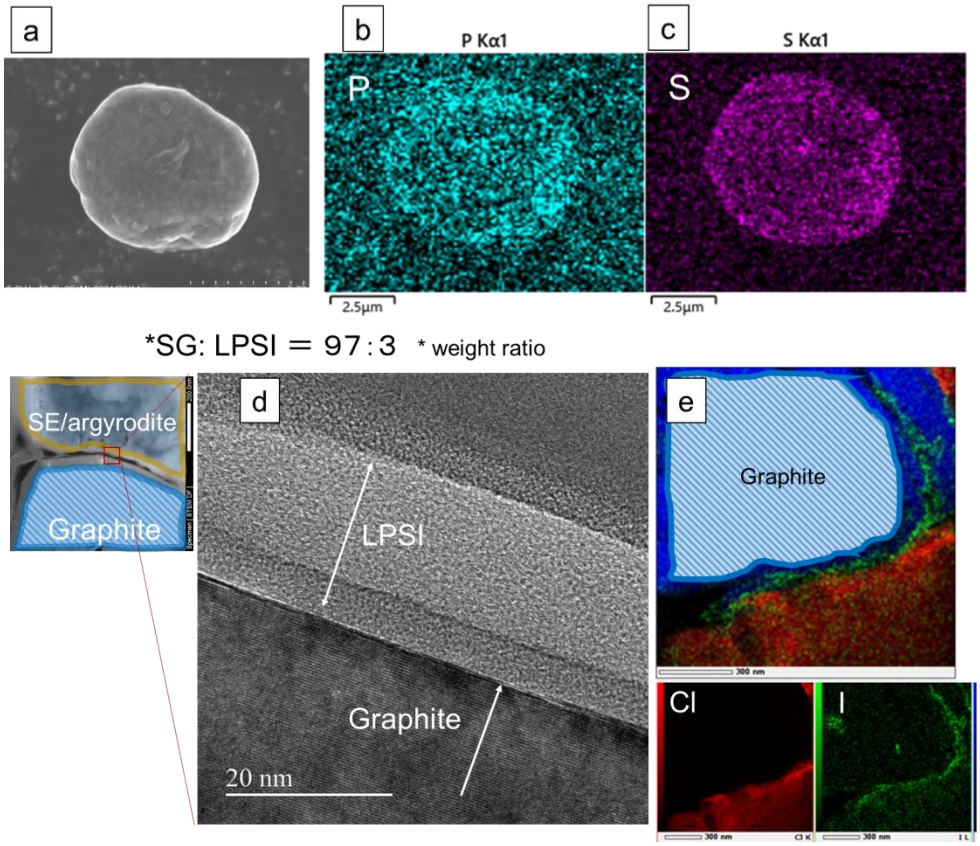

Fig. 3.3.5 5a: SEM image of an SG particle coated 3 wt% LPSI by SEED process and SEM-EDS images of that for 5b: phosphorus and 5c: sulfur. 5d: cross-section TEM image of a boundary area between the SG particle and 3 wt% LPSI layer and 5e is one of SEM-EDS images for chlorine (red) and iodine (green).

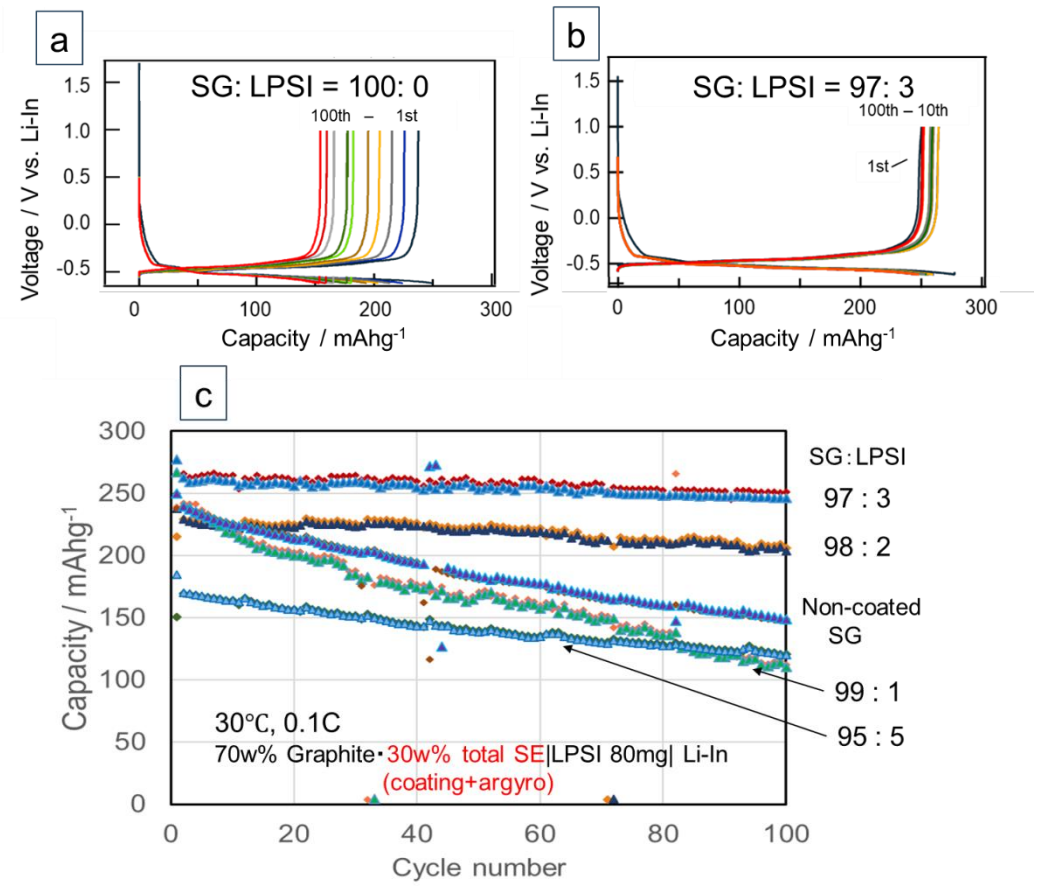

Fig. 3.3.6 Charge–discharge curves every 10 cycles till 100th for SG composites with 6a: only argyrodite-type SE and 6b: for SG composite hetero-coated with 3 wt% LPSI thin layer and argyrodite-SE. 6c is cycle performances of half-cells using SG particles hetero-coated with LPSI (1− 5 wt%) and argyrodite-type SE. The cells were constructed as follows, SG composites powder | LPSI 80mg | Li-In foil

Figure 3.3.7 shows the Nyquist plots of 7a for the cell of the non-SEED process shown in Fig. 3.3.6a, and 3.3.7b for the cell with the 3 wt% LPSI SEED process shown in Fig. 3.3.6b. In both figures, the small semicircles on the high-frequency side are considered to be the boundary resistance of the separator-SE, and the main semicircles are those of the anode composites, that is, between the SG particles and SEs. The semicircles gradually become larger in Fig. 3.3.7a for the cell using non-LPSI-coated SG particle composites. This suggests that the slight volume changes of the SG particles during charge–discharge cycles increase the gaps between the SG particles and SEs. As shown in Fig. 3.4.7b, for the cell using 3 wt% LPSI-coated SG particle composites, the semicircles show only a few changes until the 100^{th} cycle. This indicates that the interfacial contact between the SG particles and SEs was stable and maintained during cycling. We were sure that the resistance between both SEs, the thin LPSI and argyrodite-type SE, was included in the semicircle. Although these resistances could not be separated in this work, the semicircle remained almost unchanged from the first to the 100^{th} cycle, as shown in Fig. 3.3.7b. This further indicates that the interfacial resistance between the two SEs also remained stable over repeated cycles.

Figure 3.3.8 shows the rate performance (0.1 C− 6 C) of the ASSB using SG composite hetero-coated with 3 wt% LPSI thin layer and argyrodite-SE at 30 ^{o}C (Li-ion insertion: green circle, Li-ion return: yellow circle) and 60 ^{o}C (Li-ion insertion: blue triangle, Li-ion return: red triangle). The tests were applied at a constant-current measurement. Figure 3.3.2 shows the rate performance of the ASSB using a composite material consisting of 87 wt% SG and 13 wt% LPSI as anodes. This ASSB showed a significant decrease in capacity at 0.5 C and exhibited an incredibly low capacity at 2 C when tested at 30 °C. In contrast, Figure 3.3.8 shows that the hetero-coated SG exhibited to keep approximately 200 mAh g^{-1} at 0.5 C and approximately 60 mAh g^{-1} at 2 C at 30 °C and reached 150 mAh g^{-1} at 60 °C.

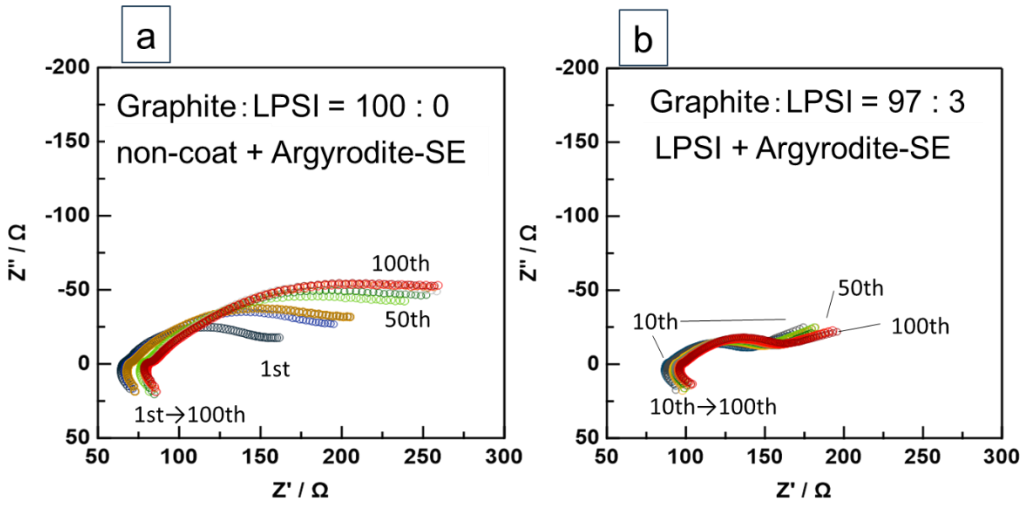

Fig. 3.3.7 Nyquist plots of impedance spectra for the cell after charge–discharge every 10 cycles till 100th for SG composites with 7a: only argyrodite-type SE and 7b: for SG composite hetero-coated with 3 wt% LPSI thin layer and argyrodite-type SE. The cells were constructed as follows, SG composite powder | LPSI 80mg | Li-In foil. Measurement condition was frequency: 1 MHz– 0.01 Hz at room temperature.

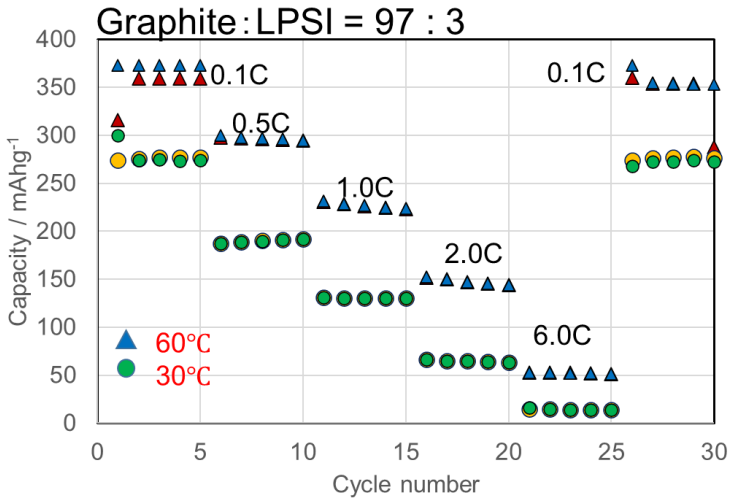

Fig. 3.3.8 Rate performance (0.1 C− 6 C) of the ASSB using SG composite 97 wt% hetero-coated with 3 wt% LPSI at 30 ℃ (Li-ion insertion: ●, Li-ion return: ●) and 60 ℃ (Li-ion insertion: ▲, Li-ion return: ▲). This test was applied at a constant-current measurement. The cells were constructed as follows, SG composites powder | argyrodite-type SE 80mg | Li-In foil.

3.3.4 Conclusions

SG particles used as anodes for ASSB were coated with the sulfide solid electrolyte LPSI using the SEED process, and ASSBs were assembled using the obtained SG composites, sulfide solid electrolytes such as argyrodite, and LPSI. Cross-sectional observation using SEM confirmed that the LPSI coating was not only on the surface of the SG particles but also inside them. When the weight ratio SG to LPSI was 87:13, the interfacial contact area increased, resulting in good output performance for the ASSB. To further enhance the charge–discharge performance, a hetero-SE coating was applied. In this approach, SG particles were first coated with an ultra-thin LPSI layer and then hand-mixed in a mortar with an argyrodite SE. When the thin-coated SG (SG: LPSI = 97:3) was mixed with the argyrodite SE (SG:total SE =70:30), the ASSB exhibited an excellent capacity retention rate owing to the improved interface contact between the SG particles and SEs. Boundary control between active materials and SEs is one of the most critical issues for fabricating ASSBs. This LPSI coating via SEED process is a promising method to solve the problem.

References

1) S. Yubuchi, S. Teragawa, K. Aso, K. Tadanaga, A. Hayashi, M. Tatsumisago, Preparation of high lithium-ion conducting Li_6PS_5Cl solid electrolyte from ethanol solution for all-solid-state lithium batteries, *J. Power Sources* **293**, 941-945 (2015).
2) K.H. Park, D.Y. Oh, Y.E. Choi, Y.J. Nam, L. Han, J.Y. Kim, H. Xin, F. Lin, S.M. Oh, Y.S. Jung, Solution-processable glass LiI-Li_4SnS_4 superionic conductors for all-solid-state Li-ion batteries, *Adv. Mater.* **28**, 1874–1883 (2016).
3) A. Sakuda, A. Hayashi, T. Ohtomo, S. Hama, M. Tatsumisago, All-solid-state lithium secondary batteries using $LiCoO_2$ particles with pulsed laser deposition coatings of Li_2S–P_2S_5 solid electrolytes, *J. Power Sources* **196**, 6735-6741 (2011).
4) H. Nakamura, T. Kawaguchi, T. Masuyama, A. Sakuda, T. Saito, K. Kuratani, S. Ohsaki, S. Watano, Dry coating of active material particles with sulfide solid electrolytes for an all-solid-state lithium battery, *J. Power Sources* **448**, 227579 (2020).
5) R. Matsuda, E. Hirahara, N.H.H. Phuc, H. Muto, H. Tsukasaki, S. Mori, A. Matsuda, Preparation of $LiNi_{1/3}Mn_{1/3}Co_{1/3}O_2$/$Li_3PS_4$ cathode composite particles using a new liquid-phase process and application to all-solid-state lithium batteries, *J. Ceram. Soc. Japan* **126**, 826-831 (2018).
6) M. Calpa, A.C. Rosero-Navarro, A. Miura, K. Tadanaga, A. Matsuda, Graphite/$Li_7P_3S_{11}$

composite prepared by “seed” process for all-solid-state batteries, *Solid State Ionics* **372**, 115789 (2021).

7) F. Mizuno, A. Hayashi, K. Tadanaga, M. Tatsumisago, High lithium ion conducting glass-ceramics in the system Li_2S–P_2S_5, *Solid State Ionics* **177**, 2721-2725 (2006).

8) S. Ito, M. Nakakita, Y. Aihara, T. Uehara, N. Machida, A synthesis of crystalline $Li_7P_3S_{11}$ solid electrolyte from 1,2-dimethoxyethane solvent, *J. Power Sources* **271**, 342-345 (2014).

9) M. Calpa, A.C. Rosero-Navarro, A. Miura, K. Tadanaga, Instantaneous preparation of high lithium-ion conducting sulfide solid electrolyte $Li_7P_3S_{11}$ by a liquid phase process, *RSC Adv.* **7**, 46499 (2017).

10) S. Chen, D. Xie, G. Liu, J.P. Mwizerwa, Q. Zhang, Y. Zhao, X. Xu, X. Yao, Sulfide solid electrolytes for all-solid-state lithium batteries: Structure, conductivity, stability and application, *Energy Storage Mater.* **14**, 58-74 (2018).

11) S. Wenzel, D.A. Weber, T. Leichtweiss, M.R. Busche, J. Sann, J. Janek, Interphase formation and degradation of charge transfer kinetics between a lithium metal anode and highly crystalline $Li_7P_3S_{11}$ solid electrolyte, *Solid State Ionics* **286**, 24-33 (2016).

12) H. Sano, Y. Morino, Y. Matsumura, K. Kawamoto, H. Higuchi, N. Yamamoto, A. Matsuda, H. Tsukasaki, S. Mori, A. Sakuda, A. Hayashi, Surface degeneration of Li_3PS_4–LiI glass-ceramic electrolyte by exposure to humidity-controlled air and its recovery by thermal treatment, *Electrochemistry* **91,** 057004 (2023).

13) K. Hikima, T. Yamamoto, N.H.H. Phuc, R. Matsuda, H. Muto, A. Matsuda, Improved ionic conductivity of Li_2S-P_2S_5-LiI solid electrolytes synthesized by liquid-phase synthesis, *Solid State Ionics* **354**, 115403 (2020).

14) R. Rajagopal, J.U. Cho, Y. Subramanian, Y.J. Jung, S. Kang, Y.C. Ha, K.S. Ryu, Preparation of metal-oxide-doped $Li_7P_2S_8Br_{0.25}I_{0.75}$ solid electrolytes for all-solid-state lithium batteries, *Chem. Engineering J.* **428**, 132155 (2022).

15) M. Wissler, Graphite and carbon powders for electrochemical applications, *J. Power Sources* **156**, 142-150 (2006).

Chapter 4
Fabrication and Characterization of Air Stable Sulfide Solid Electrolytes via Ion-Exchange Method

4.1 Preparation of ambient air-stable electrolyte Li_4SnS_4 by aqueous ion exchange process

4.1.1 Introduction

Sulfide-based solid electrolytes (SEs) for use in all-solid-state lithium-ion batteries have been extensively studied because of their high ionic conductivity and unique mechanical properties, which are needed form good contact with active materials[1]. The conductivity of $Li_{10}GeP_2S_{12}$ at room temperature has been shown to reach 1.2×10^{-2} S cm^{-1} [2] and Li_6PS_5Cl which has a structure of argyrodite, reached 1.9×10^{-3} S cm^{-1} [3]. These conductivities are comparable to those of the electrolytes using organic solvents for conventional lithium-ion batteries. $Li_7P_2S_8I$ also shows high ionic conductivity and good stability against lithium metals[4,5]. The density of Li_3PS_4–based electrolytes can be increased by pressing at room temperature due to their mechanical properties, in particular their plasticity, which can achieve good contact between active materials and electrolytes[6]. However, these sulfide-based SEs need to be treated in a glove box filled with argon, since they react with H_2O and generate H_2S gas when they are exposed to an ambient atmosphere. It is important to eliminate or reduce the generation of H_2S gas from a safety point of view, for instance if batteries using the electrolyte for electric-vehicles and mobile-PC's break open and are exposed to ambient air.

According to the fundamental principles of Hard and Soft Acids and Bases [7], the sulfides containing Sn, As and Sb are stable against H_2O, compared to sulfides containing P. Recently, the air-stable sulfide electrolyte Li_4SnS_4 was prepared from corresponding starting materials by heat-treating in a quartz ampoule sealed under vacuum[8] and by milling in an Ar gas atmosphere[9]. The ionic conductivities of these electrolytes reached 1.0×10^{-4} S cm^{-1} at room temperature.

This study took advantage of the stability of Li_4SnS_4 is stable against H_2O and developed a new, unique preparation of Li_4SnS_4 in an aqueous solution is newly developed, namely, an ion-exchange (IE) process from the Na_4SnS_4 aqueous solution to Li_4SnS_4. Because almost all of the starting materials of electrolytes containing Li ions are unstable against H_2O as Li_2S and P_2S_5, non-aqueous organic solvents or dehydrated alcohols are usually used as the solvents in the liquid phase process and all

preparation needs to be carried out in a glove box filled with Ar gas. On the other hand, using my newly developed IE process, first, sodium sulfide electrolyte Na_4SnS_4 is prepared from Na_2S and $SnCl_4$[10], both of which are comparably stable against H_2O in aqueous solution. Second, Na ions of the Na_4SnS_4 aqueous solution are exchanged to Li ions by IE resins utilizing the ion selectivity of the cation exchange resin for Na ions, which is higher than for Li ions[11,12]. From a practical application perspective, all these procedures can be carried out in ambient air, meaning that this newly developed process allows for cost effective, large-scale production.

4.1.2 Experimental

First, Na_4SnS_4 was prepared as follows. Sodium sulfide (Na_2S, 98%, Wako) and tin chloride ($SnCl_4 \cdot 5H_2O$, 98%, Wako) were mixed with a molar ratio of 2:1 and the resulting solution was stirred for 30 min in ion exchange water (IEW) at room temperature. A yellowish SnS_2, like slurry was gradually precipitated. It was rinsed about five times to remove the NaCl using a centrifuge (5922, Kubota) at 3000-10000 rpm for 5 min with IEW. The prepared SnS_2 and Na_2S were stirred in IEW at room temperature and filtered. The obtained Na_4SnS_4 aqueous solution was pale yellow and transparent. Second, the Na_4SnS_4 aqueous solution was dropped into a glass column filled with the ion exchange resin and IEW, which had been already changed from H^+ to Li^+ form. Figure 4.1.1 shows an example of the ion exchange process. The pale green solution was dripping out of the column and the resin was rinsed with IEW. The solution and the IEW used for rinsing were evaporated to condense it. This ion exchange process was carried out twice. The obtained solution was condensed again and freeze dried (FDU-1200, EYELA) for 2 days. A pale-yellow powder was obtained which was the precursor of Li_4SnS_4.

The Raman shifts of the powder samples were detected using Raman spectroscopy (NRS-3100, JASCO). The powders were placed on a special glass sample holder, covered with a thin glass sheet and sealed with paraffin jelly. Its thermal profile was measured using thermo-gravimetry and differential thermal analysis (TG-DTA) (Thermo plus EVO2, Rigaku) from 25 ℃ to 450 ℃ at 5 ℃ min^{-1} under flowing Ar gas at 100 mL min^{-1} in order to determine suitable heat-treatment temperatures for removing the hydrated water. The precursors were heat-treated at 150 ℃ and 240 ℃ under low pressure. The structure of the prepared samples was characterized using X-ray diffraction (XRD) (Ultima IV, Rigaku). During the measurements, the samples were placed in a cell with a beryllium window, which was sealed against air to avoid humidity.

To confirm the ion exchange from Na ions to Li ions by cation exchange resin, the amounts of Na ions and Li ions in the obtained powder were measured using Ion Chromatography (IC) (IC7000, Yokokawa). The aqueous solutions of Li_4SnS_4 powder samples were diluted to about 50mg/L for IC measurement. The chemical composition analyses were carried out by atomic absorption analysis (AA) using SHIMADZU AA-7000 and by inductively coupled plasma spectroscopy (ICP) using Agilent 5110 ICP-OES.

The temperature dependence of the total conductivities of the samples was measured using alternating-current impedance spectroscopy (SI 1260, Solatron) from 1 MHz to 10 Hz under dry Ar flow. The 80 mg samples of the obtained powder were placed in a holder made of polyetheretherketon (PEEK) and sandwiched between two stainless steel rods. The samples were pressed into a pellet of about 0.5 mm in thickness and 10.0 mm in diameter by uniaxial pressing at a pressure of 240 MPa.

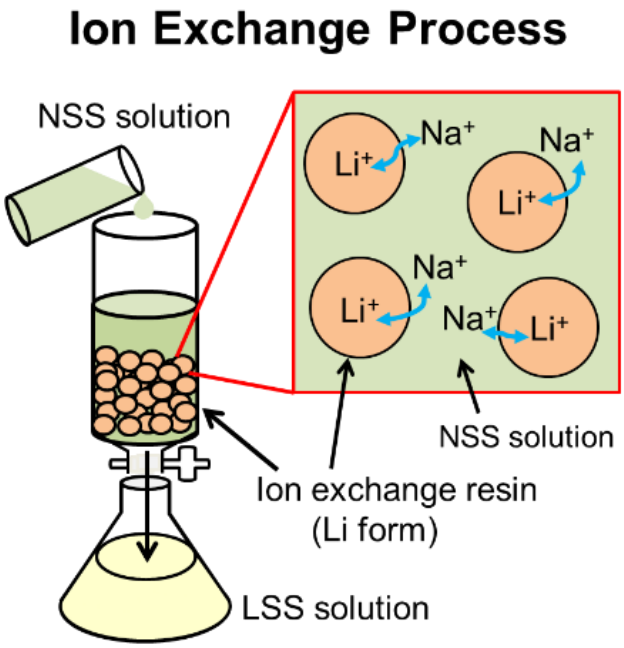

Fig. 4.1.1 Example of ion exchange process. NSS stands for Na_4SnS_4 and LSS stands for Li_4SnS_4.

4.1.3 Results and discussion

Figure 4.1.2 shows TG-DTA profiles of the freeze-dried sample after ion-exchange. The endothermic peaks are seen from 50 ℃ to 150 ℃. These peaks suggest removal of H_2O from the freeze-dried samples. According to weight loss till about 100 ºC of the TG profile, adsorbed water molecules were estimated to be two against a single unit of Li_4SnS_4. From the weight loss measured when the large endothermic peak reached around 150 ºC, there were three hydrated water molecules to a single unit of Li_4SnS_4. After 150 ºC, the TG profile shows a gradual and slight decrease and a small exothermic peak was seen at about 225 ℃, which suggests the occurrence of a phase change. Therefore, the obtained powder was separately heat-treated at 150 ºC and 240 ℃.

Figure 4.1.3 shows XRD patterns of the obtained powder samples. The lowest pattern (a) of the figure is the sample before ion exchange and heat-treatment at 150 ºC. This pattern agrees well with the Na_4SnS_4 (NSS) listed JCPD files No: 00-025-0874. The upper patterns (b) and (c) are of samples where the ion exchange process was twice applied and heat-treated at 150 ºC and 240 ºC, respectively. They show a completely different pattern from that of NSS and correspond to the pattern of Li_4SnS_4 (LSS) which is the data reported by Kanazawa et al[9]. This indicates that Na ions in the aqueous solution of NSS were exchanged to Li ions. The X-ray patterns of the samples heat-treated at 150 ºC and 240 ºC shown in Fig. 4.1.3 (b) and (c), show that the amorphous phase partially remained. This suggests that the freeze-drying method, due to remove water kept a freezing situation to a certain degree similar to the quenching method. On the other hand, the X-ray pattern of the obtained sample heat-treated at 240 ºC in Fig. 4.1.3 (c) already showed not only a hallo-like pattern but also had an orthorhombic phase at about 2θ = 17-19 º [8].

The component analysis carried out for the ion exchanged sample using IC. Na^+ / Li^+ atomic ratio in the sample aqueous solution was 0.019, which indicates the remaining amount of Na ions in the sample solution was under 2% as opposed to the Li ions. In the cases where the ion exchange process was repeated, Na ions were not reduced, suggesting that Na ions were almost fully exchanged to Li ions in a single processing. In addition, the chemical composition of the samples was Li / Sn = 4.21 from AA measurement, whereas Li / Sn = 4.4 and S / Sn = 6.7 from ICP measurement. There was divergence between the results of AA and ICP measurements. It was considered that Sn was detected in smaller amounts in ICP because the Sn compound didn't dissolve completely due to the use of IEW as a solvent in the case of ICP measurement. In the synthesis of Na_4SnS_4, an intermediate product, SnS_2, was rinsed with IEW using a centrifuge to remove NaCl several times and the supernatant was

separated. It was presumed that some moieties of the Sn compounds were lost at that time. As a result, there was an excess of sulfur compared to Sn.

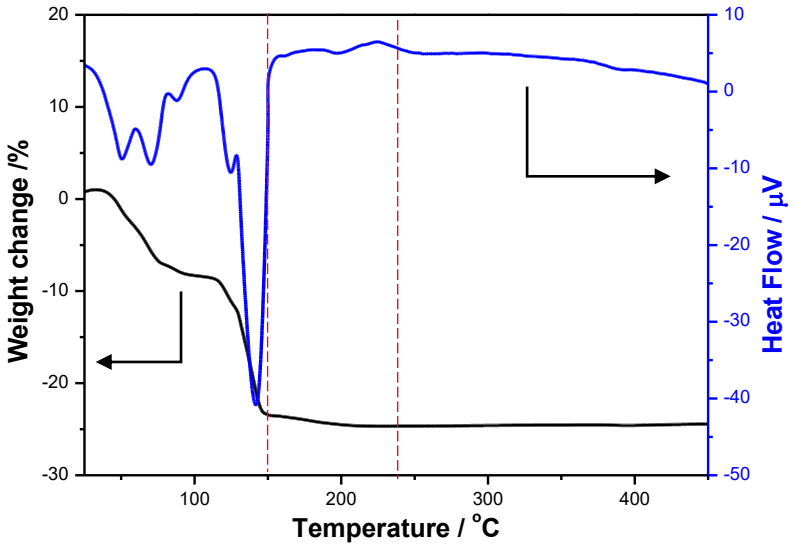

Fig. 4.1.2 TG-DTA profile of exchanged powder after freeze-drying.

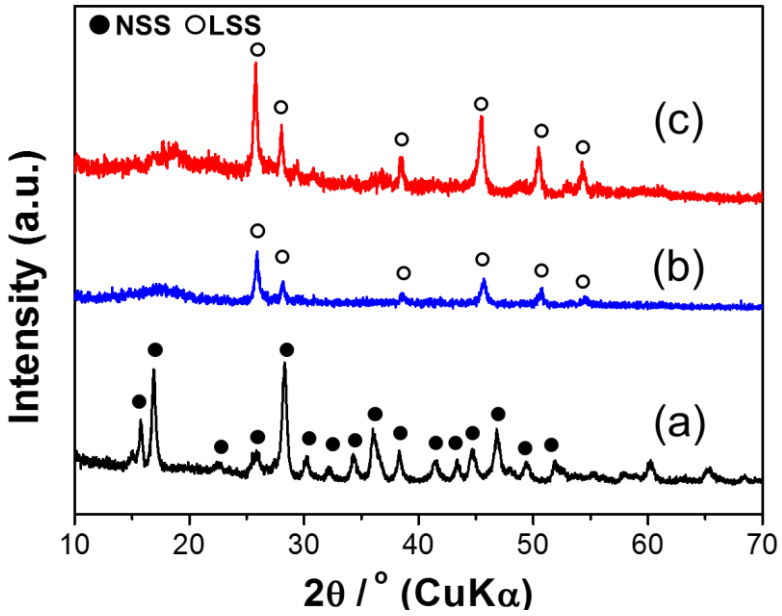

Fig. 4.1.3 XRD patterns of the obtained powder (a) NSS before ion exchange heat-treated at 150 °C, and LSS after ion exchange, heat-treated at (b) 150 °C and (c) 240 °C.

Figure 4.1.4 shows Raman shifts of obtained samples before and after applying the process. Both samples have a band at around 350 cm^{-1} assigned to the SnS_4^{4-} ion, showing that SnS_4^{4-} ions in NSS were kept after the IE process.

Figure 4.1.5 shows the temperature dependence of ionic conductivity for the samples before and after the IE process. In Fig. 4.1.5, (a) is for NSS before the IE process and heat-treated at 150 ℃. (b) and (c) are for LSS after the IE process and heat-treatment at 150 ℃ and at 240 ℃, respectively. Conductivities of ion exchanged samples are about two orders of magnitude higher than those of NSS. The ionic conductivities at 25 ℃ of sample (c), which was heat-treated at 240 ℃ reached 1.0×10^{-4} S cm^{-1}, higher than that at 25 ℃ (2.5×10^{-5} S cm^{-1}) of the sample heat-treated at 150 ℃. This suggests that sublimation of the excessive sulfur was due to the small loss of Sn and Li during the synthesis of the intermediate product. Promotion of the crystallization of LSS till heat-treating at 240 ℃ caused the remarkable increase in Li ion conductivity.

The temperature dependence of the conductivity of NSS shows a straight line, indicating an Arrhenius-type conduction mechanism. The apparent activation energy for the conduction of NSS was estimated to be 53 kJ mol^{-1} from the linear relationship. However, both LLSs, when heat-treated at 150 °C and 240 °C, show a curvilineal temperature dependence. There are two possible reasons for this. One is the difficulty in precisely measuring the very low resistivity of an LLS sample at higher temperatures due to its very high conductivity, which is known to result in the apparent saturation of the conductivity. The other can be ascribed to changes in the ion conduction mechanism, with variable apparent activation energy due to, for example, structural changes such as phase transition. Further detailed analysis and measurement will be necessary to clarify the possibility of the changes in the conduction mechanism with an increase in temperature.

To confirm the atmospheric stability of the LSS obtained by IE process and heat-treatment at 240 ℃, atmosphere-exposure tests were undertaken. The obtained LSS was exposed to ambient air (about at 25 ℃ and relative humidity 50%) for 1 day and then heat-treated again at 240 ℃. There was no generation of H_2S gas, as confirmed by the lack of oder. Figure 4.1.6 shows XDR patterns of the LSS by ion exchange before and after exprosure to the atmosphere and re-heat-treatment at 240 ℃. The pattern of the LSS after exposure and re-heat-treatment was almost the same as before exposing. These results suggest that the LSS obtained in the present IE process is stable in ambient air and the recycling of the components in all solid lithium batteries using LSS as a solid electrolyte can be expected to be achieved.

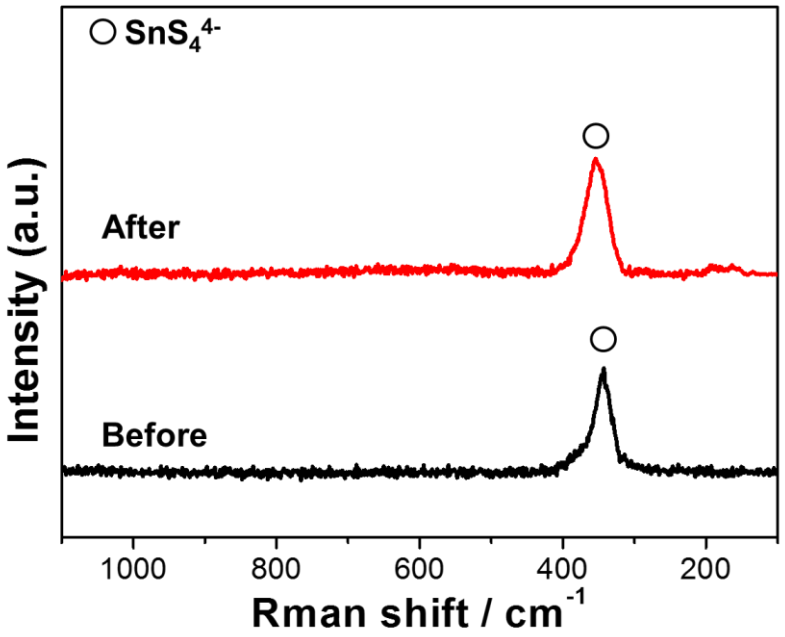

Fig. 4.1.4 Raman shifts of obtained powders before and after ion exchange and heat-treatment at 150 ^{o}C.

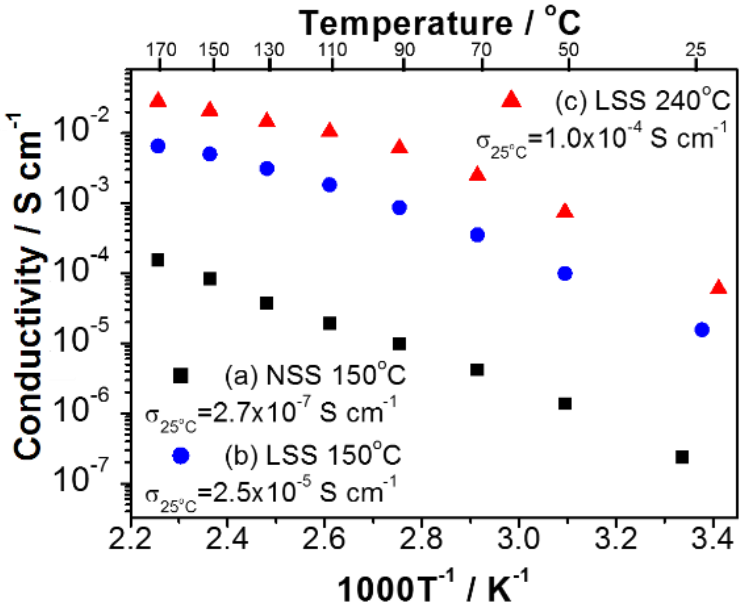

Fig. 4.1.5 Temperature dependence of ionic conductivities of (a) NSS heat-treated at 150 ºC and LSS by ion-exchange and heat-treatment (b) at 150 ºC and (c) at 240 ºC.

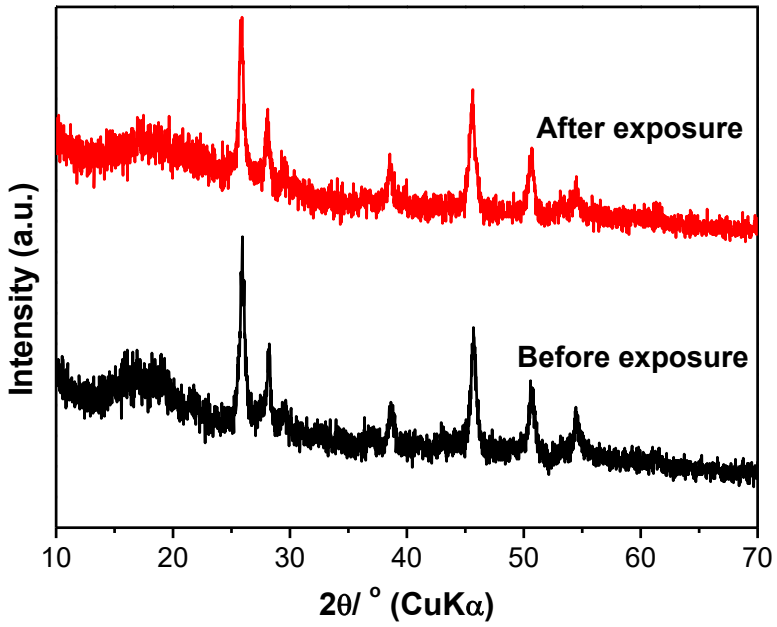

Fig. 4.1.6 XRD patterns of the obtained powder before exposing and after atmosphere-exposing and re-heating-treatment at 240 ℃.

4.1.4 Conclusions

The Li_4SnS_4 electrolyte was prepared from Na_4SnS_4 aqueous solution by ion exchange, freeze drying and subsequent heat-treatment. Na ions in the Na_4SnS_4 were almost exchanged to Li ions using cation exchange resins. The ionic conductivity of Li_4SnS_4 obtained by a twice-repeated ion exchange and heat-treated at 240 ℃ showed 1.0×10^{-4} S cm^{-1} at 25 ℃. The XRD pattern of the Li_4SnS_4 after exposure to ambient air and re-heat-treatment at 240 ℃ was essentially the same as before. Because of its stability in both the atmosphere and water, it was suggested that the Li_4SnS_4 obtained via this process could be recycled as electrolyte for all solid lithium batteries.

References

1) A. Hayashi, S. Hama, H. Morimoto, M. Tatsumisago, T. Minami, Preparation of Li_2S–P_2S_5 amorphous solid electrolytes by mechanical milling, *J. Am. Ceram. Soc*. **84**, 477-479 (2001).
2) N. Kamaya, K. Homma, Y. Yamakawa, M. Hirayama, R. Kanno, M. Yonemura, T. Kamiyama, Y. Kato, S. Hama, K. Kawamoto, A. Mitsui, A lithium superionic conductor, *Nat. Mater*. **10**, 682-686 (2011).
3) R.P. Rao, S. Adams, Studies of lithium argyrodite solid electrolytes for all-solid-state batteries, *Phys. Status Solid A* **208**, 1804-1807 (2011).
4) E. Rangasamy, Z. Liu, M. Gobet, K. Pilar, G. Sahu, W. Zhou, H. Wu, S. Greenbaum, C. Liang, An iodide-based $Li_7P_2S_8I$ supereionic conductor, *J. Am. Chem. Soc.* **137**, 1384-1387 (2015).
5) N.H.H. Phuc, K. Morikawa, M. Totani, H. Muto, A. Matsuda, Synthesis of plate-like Li_3PS_4 solid electrolyte via liquid-phase shaking for all-solid-state lithium batteries, *Ionics* **23**, 2061-2067 (2017).
6) A. Sakuda, A. Hayashi, M. Tatsumisago, Sulfide Solid Electrolyte with Favorable Mechanical Property for All-Solid-State Lithium Battery, *Sci. Rep.* **3**, 2261-2266 (2013).
7) Ralph G. Pearson “Hard and soft acids and bases, HSAB, part 1: Fundamental principles” *J. Chem. Educ.* **45,** 581–586 (1968).
8) K.H. Park, D.Y. Oh, Y.E. Choi, Y.J. Nam, L.H. Han, J.Y. Kim, H. Xin, F. Lin, S.M. Oh, Y.S. Jung, Solution-processable glass LiI-Li_4SnS_4 superionic conductors for all-solid-state Li-ion batteries, *Adv. Mater.* **28**, 874-1883 (2016).
9) K. Kanazawa, S. Yubuchi, C. Hotehama, M. Otoyama, S. Shimono, H. Ishibashi, Y. Kubota, A. Sakuda, A. Hayashi, M. Tatsumisago, Mechanochemical synthesis and characterization of

metastable hexagonal Li_4SnS_4 solid electrolyte, *Inorg. Chem.* **57**, 9925–9930 (2018).

10) W. Schiwy, S. Pohl, B. Krebs, Darstellung und Struktur von Na_4SnS_4 - 14 H_2O, *ZAAC - Journal of Inorganic and General Chemistry* **402**, 77-86 (1973).

11) F. Helfferich, “Ion Exchange”, *Dover Publications, Inc. New York* (1995) 1-25.

12) Y. Kanzaki, N. Suzuki, On the selectivity of ion exchange reaction, *J. Ion exchange* **12**, 57-66 (2001).

4.2 Air-stable Li_3SbS_4–LiI electrolytes synthesized via an aqueous ion-exchange process and the unique temperature dependence of conductivity

4.2.1 Introduction

The use of electricity as a power source for automobiles and airplanes is critical from an environmental standpoint. A significant factor that determines the practical application of a power source is the safety of those using the equipment. Therefore, all-solid-state lithium-ion batteries have recently attracted significant attention as rechargeable power sources for vehicles, airplanes, and electronic devices due to their nonflammability.

Sulfide-based compound solid electrolytes (SEs) containing phosphorus show high lithium-ion conductivity and plasticity, which is also known as room temperature pressure sintering[1]. These SEs are promising candidates for all-solid-state batteries and actively studied by many researchers due to their unique mechanical property of forming good contact with the active materials of lithium-ion batteries[2,3]. For example, β-Li_3PS_4 and other thio-LISICON families were synthesized via mechanical milling[4,5] and liquid phase synthesis using organic solvents, such as acetonitrile, tetrahydrofuran and ethylpropionate[6-8], and showed high ionic conductivities. Particularly, the conductivity of $Li_{10}GeP_2S_{12}$ reached 1.2×10^{-2} S cm^{-1} (25 °C)[9,10]. However, these sulfide-based SEs should be treated in a glove box filled with argon; otherwise, they will react with H_2O in the ambient atmosphere and generate H_2S gas. It is important to reduce the generation of H_2S gas for safety reasons.

An air-stable sulfide electrolyte, Li_4SnS_4, has been recently synthesized by heat treatment in a quartz ampoule sealed under vacuum[11,12] and by mechanical milling in Ar gas atmosphere[13]. The ionic conductivity of these electrolytes was 1.0×10^{-4} S cm^{-1} at room temperature. Alternatively, we recently developed a new process for synthesizing Li_4SnS_4 in an aqueous solution, i.e., an ion-exchange (IE) process, from the Na_4SnS_4 aqueous solution to Li_4SnS_4 through subsequent freeze-drying and heat treatment[14].

Sulfides containing Sn, As, and Sb are more stable against H_2O than sulfides containing P, according to the fundamental principles of hard and soft acids and bases[15]. Sintering was used to create Li_3SbS_4, a sulfide containing Sb, with a structure similar to that of γ-Li_3PS_4[16]. The ionic conductivity of crystalline Li_3SbS_4 is lower than 10^{-8} S cm^{-1} at room temperature. Li_3SbS_4 glass was synthesized via mechanical milling and the ionic conductivity was increased to 1.5×10^{-6} S cm^{-1} at room temperature[17].

In this study, Li_3SbS_4 and Li_3SbS_4–LiI electrolytes, which were expected to have similar structures as Li_3PS_4–LiI system, were synthesized via the IE process without high-temperature heat treatment. Here I report a unique temperature dependence of ionic conductivities of Li_3Sb_4–LiI SEs obtained via the IE process and the chemical state of the boundary area of the obtained SE particles. The good charge–discharge properties for all-solid-state lithium batteries using a cathode composite containing TiS_2 active material and Li_3SbS_4–LiI SE are also demonstrated.

4.2.2 Experimental

Li_3SbS_4 was synthesized via an IE process reported in our previous reference.[14] First, Na_3SbS_4 was prepared. Particularly, 3.00 g of sodium sulfide (Na_2S, 98%, Wako), 3.20 g of antimony sulfide (Sb_2S_3, 98%, Wako), and 0.90 g of sulfur (S, 98%, Wako) were added and stirred for 2 h in 90 mL of ion exchange water (IEW) (Elix and SimplicityUV, Merck) at 70 °C. A green–yellowish transparent solution was obtained. The solution was filtered to remove impurities. 30 ml acetone was added to the filtrate solution and stored in a refrigerator for 2 d. The crystalline particles of Na_3SbS_4 hydrate were gradually precipitated in the solution. The particles were separated from the solution by filtration and kept for 1 d to dry at room temperature in ambient air. Then, the Na_3SbS_4 particles were dissolved in 100 mL of IEW, and the solution was added dropwise into a glass column filled with ion-exchange-resin beads, which was preliminarily changed from H^+ to Li^+ form. The pale yellowish solution that had dripped out from the column was condensed and freeze-dried for 2 d using a freezing dryer (FDU-1200, EYELA). A yellow-orange powder of Li_3SbS_4 hydrate was obtained. The thermal profile was measured using thermogravimetry and differential thermal analysis (TG-DTA) (Thermo plus EVO2, Rigaku) from 25 °C to 450 °C at a rate of 5 °C min^{-1} under flowing Ar gas at 100 mL min^{-1} to determine a suitable heat-treatment temperature for removing hydrated water. The precursors were heated to 140 °C under low pressure.

For the $(100 - x)$ Li_3SbS_4–xLiI system, a 0.1 g/mL LiI IEW solution was added to the Li_3SbS_4-solution after the IE process. These $(100 - x)$ Li_3SbS_4–xLiI solutions were dried by freeze-drying and heated, which is essentially the same as the process for preparing Li_3SbS_4.

The structure of the prepared samples was characterized by X-ray diffraction (XRD) (Ultima IV, Rigaku). During the measurements, the samples were placed in a cell with a beryllium window and the cell was sealed to avoid humidity. The XRD patterns at various temperatures were measured; the samples were placed in the differential scanning calorimetry (DSC) attachment of Ultima IV and

heated. To confirm the ion exchange from Na ions to Li ions by cation exchange resin, the amounts of Na and Li ions in the obtained powder were measured using ion chromatography (IC) (IC7000, Yokokawa). The temperature dependence of the total conductivities of the samples was measured using alternating-current impedance spectroscopy (SI 1260, Solatron) from 1 MHz to 10 Hz, under dry Ar flow. 80 mg samples of the obtained powder were placed in a holder made of polyetheretherketone (PEEK), sandwiched between two stainless steel rods, and pressed into pellets (with an approximately 0.3–0.5 mm thickness and 10.0-mm diameter) by uniaxial pressing at a pressure of 240 MPa. The transport number was estimated. Blocking electrodes had cell compositions similar to those used for impedance measurement to measure direct-current (DC) electronic conductivity. The DC ionic conductivity was measured using nonblocking electrodes. For nonblocking electrodes, Li foil and 20 mg of $Li_7P_2S_8I$ electrolyte powder, which is stable against Li metal[18], were placed in front of both sides of a steel rod, and the obtained Li_3SbS_4–LiI electrolyte powder was sandwiched with the two rods. Li_7PS_8I SE was obtained by a liquid phase shaking process and heat-treated at 170 °C under low pressure[18].

In the milling process, obtained powders were put into a zirconia pot (45 ml) with 50 g zirconia balls (diameter = 4 mm) and the pot was rotated at 360 rpm for 5–20 h using a planetary type of ball mill (Pulverisette 7, Fritsch). The milled powders were pressed with the PEEK cell at 240 MPa and annealed at 140 °C under dry Ar flow.

Transmission electron microscope (TEM) images of the electrolytes were obtained using JEM-2100F field-emission-type TEM (JEOL). The element mapping images were obtained using the energy dispersive X-ray spectroscopy (EDS) feature of TEM (JED-2300T). The phase mapping was obtained using a precession electron diffraction (PED) method (ASTAR/TOPSPIN, NanoMEGAS). Scanning electron microscope (SEM) images of the electrolytes and cathode composites were obtained using SEM-S4800 (Hitachi).

The amounts of H_2S gas generated from Li_3SbS_4, $60Li_3SbS_4$·40LiI obtained via the IE process, and Li_3PS_4 obtained from liquid phase shaking process[8] were measured. The samples were placed in a 10-L vessel filled with ambient air of about 50% relative humidity at 23 °C.

The cathode composite was prepared by freeze-drying the aqueous solution of $60Li_3SbS_4$·40LiI (mol%) with the active material, TiS_2, and acetylene black (AB). The charge–discharge performance tests of the cathode composite were conducted at 60 °C using the same holder and electrode rods as those used for the conductivity measurement. The cell composition was as follows;

$50TiS_2 \cdot 50(60Li_3SbS_4 \cdot 40LiI) \cdot 5AB$ in weight ratio of 5 mg | Li_7PS_8I 80 mg | Li-In.

4.2.3 Results and discussion

Figure 4.2.1(A) shows the TG-DTA profiles of Li_3SbS_4 hydrate, which is the freeze-dried sample after ion-exchange. Endothermic double peaks are observed at 80 °C–120 °C. These peaks indicate the removal of H_2O from the freeze-dried sample. The weight loss with a large endothermic peak at about 120 °C in the TG profile was approximately 10%. This result suggests that hydrated water was removed from $Li_3SbS_4 \cdot nH_2O$. The number of hydrated water molecules, n, was estimated to be 1.5 for the Li_3SbS_4 single unit. The TG profile becomes almost constant above 140 °C. Therefore, the obtained powder was heat-treated at 140 °C for 2 h under low pressure.

Figure 4.2.1(B) shows the XRD patterns of the obtained powder samples. From the Figure, (a) shows a pattern of the sample before ion exchange, and (b) is a pattern of the ion-exchanged sample. Both samples were heat-treated at 140 °C. The pattern (a) corresponds to that of Na_3SbS_4 in a previous study[19]. Pattern (b) is completely different from that of Na_3SbS_4 and corresponds to the pattern of Li_3SbS_4, which is the data reported by Huber[16]. Therefore, lithium conductive sulfide electrolyte, Li_3SbS_4, can be obtained via the IE process under ambient air due to the exchange of Na ions with Li ions in Na_3SbS_4 aqueous solution.

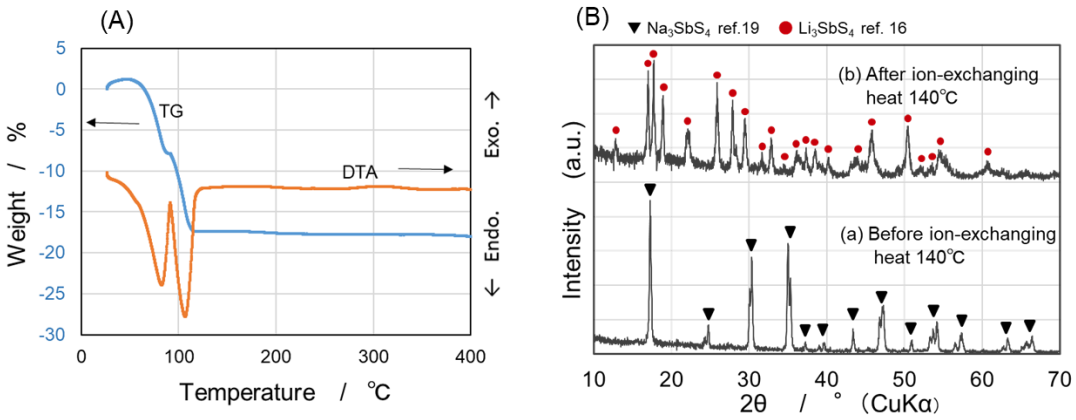

Fig. 4.2.1 TG-DTA profiles of Li_3SbS_4 obtained by ion-exchange and heat-treatment at 140°C in (A). (B) shows XRD patterns of (a) before and (b) after ion-exchanging Na_3SbS_4 prepared and heat-treated at 140°C for 2 h with Na_3SbS_4 (ref.19) and Li_3SbS_4 (ref.16) of standard peaks.

The component analysis was conducted for the ion-exchanged sample using IC. The Na^+/Li^+ atomic ratio in the aqueous solution sample was 0.024. This result suggests that Na ions were almost fully exchanged with Li ions in the IE process. The ionic conductivity of Li_3SbS_4 obtained via the IE process was 8.5×10^{-8} S cm^{-1} at 50 °C. The apparent activation energy of Li-ion conduction was 56 kJ mol^{-1}, which was estimated from the temperature dependence of ionic conductivity. The Nyquist plots are depicted in Fig. 4.2.2. The results are consistent with those reported in the previous studies[16,17].

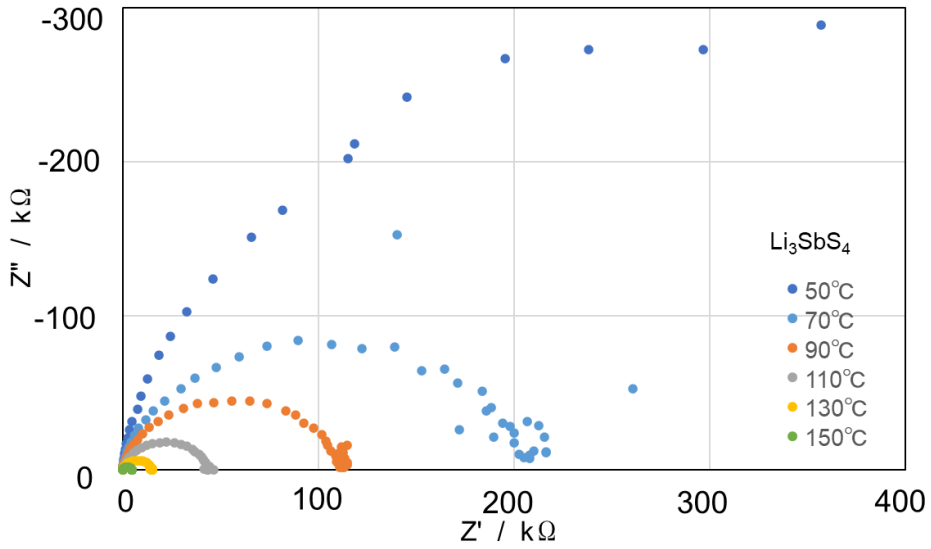

Fig. 4.2.2 Complex impedance plots for Li_3SbS_4 synthesized via ion-exchange process.

$(100 - x)$ Li_3SbS_4·x LiI (in mol%) system electrolytes were synthesized using the IE process. Figure 4.2.3(A) shows XRD patterns of $(100 - x)$ Li_3SbS_4·xLiI obtained via the IE process. The XRD patterns of the samples were similar until x = 40 mol%, except for the small unknown peaks shown with (◆) in the pattern of x = 40. A portion of LiI between $60Li_3SbS_4$·40LiI particles is assumed to form LiI hydrates. Figure 4.2.3(B) shows the patterns focused on the peak near 2θ = 25.9°. The peak near 2θ = 25.9° shifts to a higher angle as the LiI content increases. The interplanar spacing of (110) calculated using the shifts of angles narrowed from 3.436 to 3.428 Å.

I believe that these peaks correspond to LiI hydrates, and that they are a mixture of various

hydrates, as shown in Fig. 4.2.4.

The pattern of LiI was revealed in the $50Li_3SbS_4 \cdot 50LiI$. SEM images of Li_3SbS_4 and $60Li_3SbS_4 \cdot 40LiI$ were shown in Fig. 4.2.5(A) and (B). Brick-like-shaped crystalline particles were observed in the image of $60Li_3SbS_4 \cdot 40LiI$, which were different from those of Li_3SbS_4. TEM-EDS mapping images of $60Li_3SbS_4 \cdot 40LiI$ obtained via the IE process were also shown in Fig. 4.2.5(C)–(F). The EDS mapping images indicate that sulfur (D), antimony (E), and iodide (F) were homogeneously dispersed on the particles. These results suggest that Li_3SbS_4 and LiI formed a solid solution until approximately $x = 40$ mol %.

Figure 4.2.6 shows the temperature dependence of ionic conductivities on heating for $(100 - x)$ $Li_3SbS_4 \cdot xLiI$ obtained via the IE process. The results showed unique behavior, i.e. extremely high conductivities at temperatures higher than 50 °C except for Li_3SbS_4 ($x = 0$). Particularly, the conductivity of $60Li_3SbS_4 \cdot 40LiI$ reached 8.4×10^{-3} S cm^{-1} at 65 °C. This unique behavior was reversibly repeated when the measurement was continued with heating and cooling. The DC ionic conductivity of $60Li_3SbS_4 \cdot 40LiI$ (when it is used as a nonblocking electrode) and its electronic conductivity (when it is used as a blocking electrode) were 1.2×10^{-4} S cm^{-1} and 1.3×10^{-6} S cm^{-1} at 50 °C, respectively. Therefore, the Li-ion transport was estimated to be 0.99. The evaluation method is shown in section 4.2.S1 in the supporting information. The electrolyte has relatively high electronic conductivity. It suggests that Sb oxidation number would be changed due to the addition of LiI. Table 4.2.1 shows electronic conductivities of other electrolytes. At room temperature, the conductivities of the obtained $(100 - x)$ $Li_3SbS_4 \cdot xLiI$ ($x = 10$, 20, and 33) were approximately 10^{-6} S cm^{-1}, which are two orders of magnitude higher than Li_3SbS_4. However, the conductivities decreased to approximately 10^{-7} S cm^{-1} in the case of x = 40 and 50. When the LiI content exceeds 40 mol%, the LiI layers thicken and crystalline LiI forms during drying process. Therefore, the conductivity of $50Li_3SbS_4 \cdot 50LiI$ reduced because crystalline LiI has very low. The activation energies based on Arrhenius plots in Fig. 4.2.6 are shown in Fig. 4.2.7(A), 4.2.7(B).

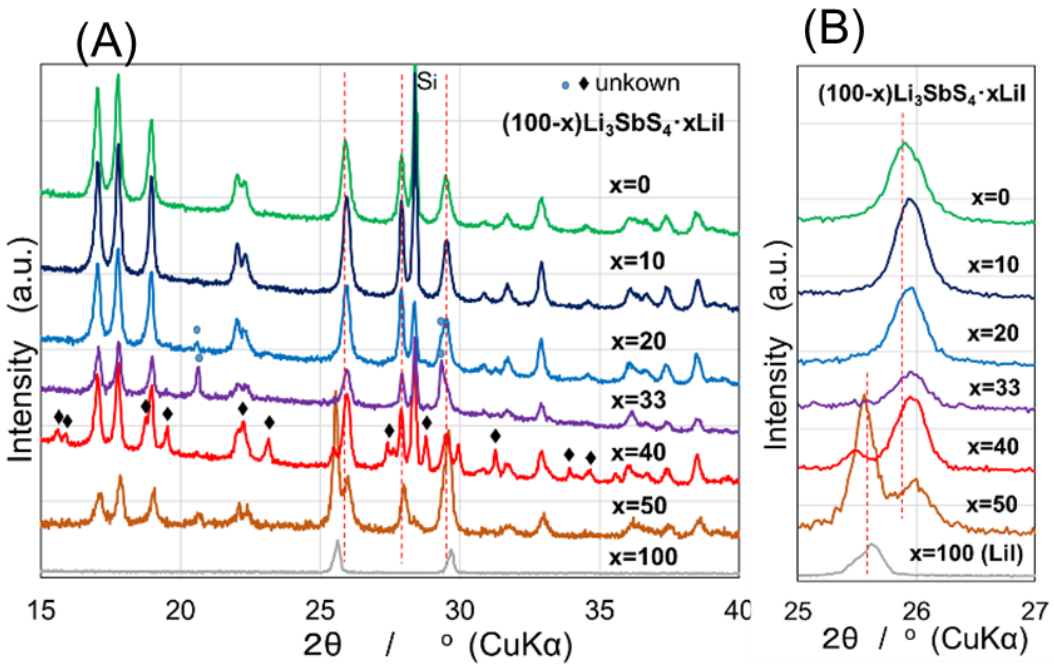

Fig. 4.2.3 (A)XRD patterns of $(100-x)\ Li_3SbS_4\ \cdot xLiI$ (in mol%) obtained via the IE process. All samples were heat-treated at 140℃ for 2 h. (B) is zoomed in at around 2θ = 26° of (A).

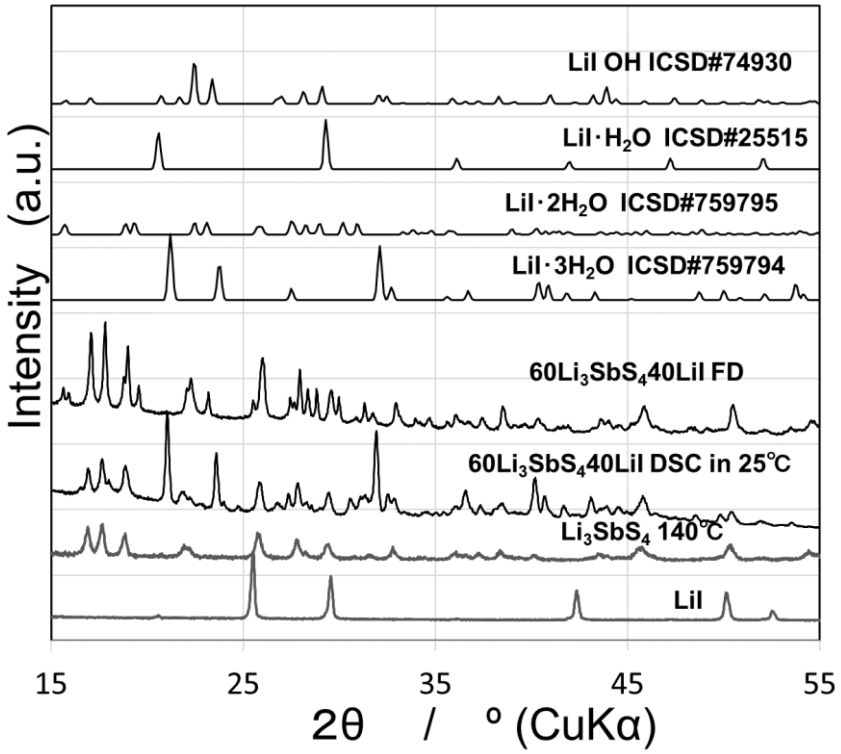

Fig. 4.2.4 XRD patterns of starting materials of crystalline-LiI, and as-prepared $60Li_3SbS_4$ at 140ºC, and obtained samples of $60Li_3SbS_4 \cdot 40LiI$ after freeze drying (FD) and after DSC measurement. Those of LiI hydrates based on ICSD numbers #25515, #759794, #75955, and LiI hydroxide based on ICSD number #74930 are also shown for comparison.

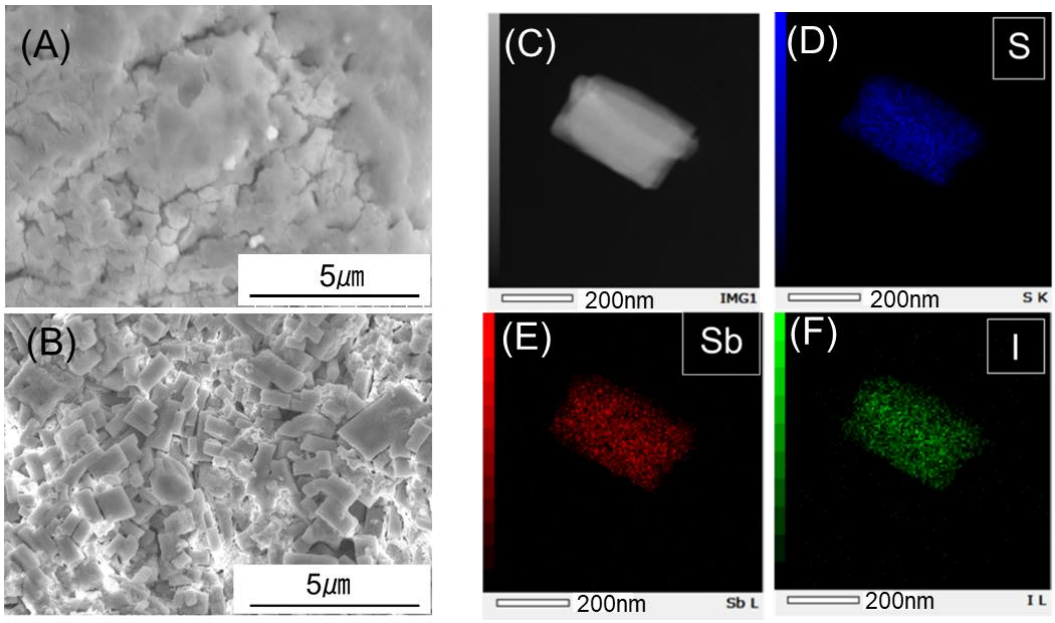

Fig. 4.2.5 SEM images of (A) Li_3SbS_4 and (B) 60 Li_3SbS_4·40LiI obtained via the IE process. (C) is a TEM image, (D), (E) and (F) are EDS mapping images for sulfur, antimony, and iodide, respectively, of the 60 Li_3SbS_4·40LiI.

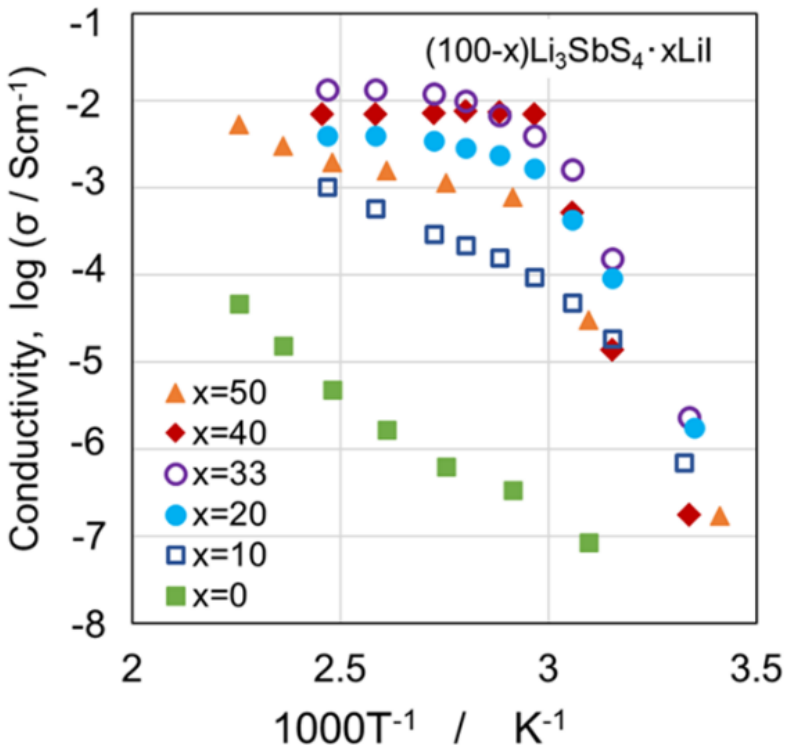

Fig. 4.2.6 Temperature dependences on heating of the ionic conductivity for (100 − *x*) Li_3SbS_4 ·*x*LiI (in mol%) obtained via the IE process. All samples were heat-treated at 140°C for 2 h.

Table 4.2.1 Electronic conductivities of the sulfide electrolytes obtained at 50°C (S cm^{-1}).

Electrolyte	**Conductivity at 50 °C** **S cm^{-1}**
$67Li_3PS_4 \cdot 33LiI$	5.2×10^{-8}
$60Li_3PS_4 \cdot 40LiI$	1.3×10^{-6}
Li_3SbS_4	7.1×10^{-8}

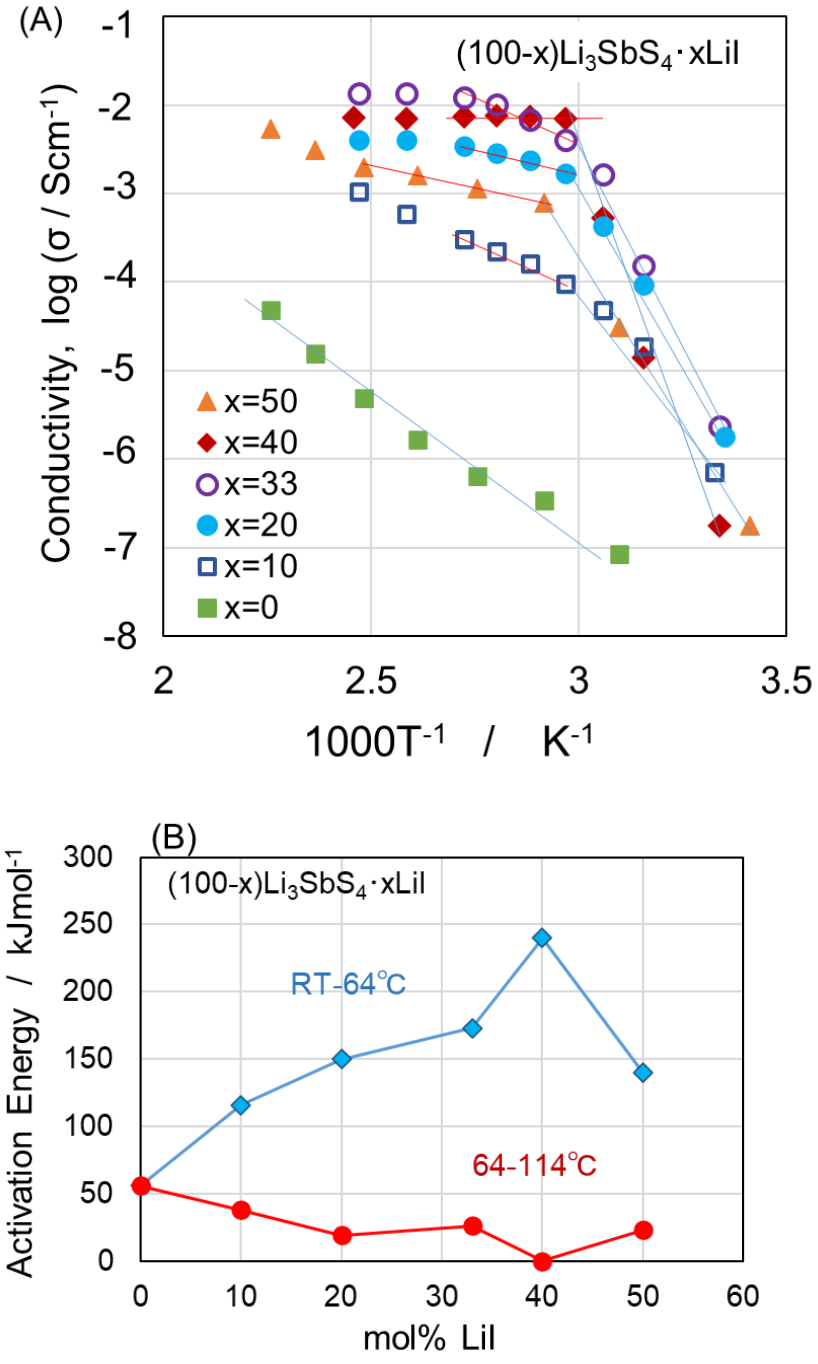

Fig. 4.2.7 (A) Temperature dependences on heating of the ionic conductivity for (100 − *x*) Li_3SbS_4 ·*x*LiI (in mol%) obtained via the IE process. All samples were heat-treated at 140℃ for 2 h. (B) Activation energies for ionic conductivities calculated from slops in fig. 4(A). Blue dots are calculated from slops of low temperature region (room temperature − 64 °C). Red dots are high temperature region (64 − 114 °C).

To investigate the mechanism that causes such considerable changes in conductivities due to temperature change, TEM observations at high temperatures and the XRD patterns of $60Li_3SbS_4 \cdot 40LiI$ at the various temperatures were measured during DCS measurement was conducted under N_2 flow. Figure 4.2.8(A) and (B) show the darkfield TEM images of $60Li_3SbS_4 \cdot 40LiI$ at 25 °C and 80 °C, respectively. Bright contrasts in the images indicate crystalline regions, as denoted by the yellow arrows. The crystallites were approximately 35 nm. No significant difference in the nano crystallite size between the images at 25 °C and 80 °C was observed, and the electron diffraction patterns were almost the same. The melting of the sample powder was not observed in these results and the shapes of both images. Therefore, the basic structure of $60Li_3SbS_4 \cdot 40LiI$ is maintained at this temperature range. Both diffraction patterns have spots and bleary halo rings, indicating that the obtained electrolyte contains crystalline and amorphous regions. During DSC measurement, the powder sample was heated from 25 °C to 90 °C, then cooled to room temperature. Figure 4.2.8(C) shows the DSC profile and XRD measurement points. Small LiI peaks and unknown peaks, which are possibly LiI hydrates of $LiI \cdot 2H_2O$, were observed in the patterns of $60Li_3SbS_4 \cdot 40LiI$ from 25 °C to 60 °C in Fig. 4.2.8(D). These peaks disappeared at temperatures higher than 60 °C and only a typical Li_3SbS_4 pattern was observed. Typically, hydrates have low melting point. It is assumed that the thin layers of the LiI hydrate in $60Li_3SbS_4 \cdot 40LiI$ melt at temperatures over 60 °C or become amorphous. Different peaks emerged when the temperature reached 90 °C and then dropped to room temperature, which was identified as $LiI \cdot 3H_2O$. Therefore, an exothermic peak on the DSC profile near 60 °C implies the crystallization of $LiI \cdot 3H_2O$. The H_2O was expected to be supplied from N_2 gas running in the DSC container during the measurement. This indicates that some amount of LiI was present on the surface of $60Li_3SbS_4 \cdot 40LiI$ particles, which reacted with the H_2O to form $LiI \cdot 3H_2O$.

For further analysis of the $60Li_3SbS_4 \cdot 40LiI$ surface, TEM observation using the PED method was conducted. Figure 4.2.9(A) shows a composition mapping image of $60Li_3SbS_4 \cdot 40LiI$. A diffraction pattern at a part of an aera divided into large number of pixels was recorded using the PED method. I focused on the LiI hydrates ($LiI \cdot nH_2O$) on the surface of $60Li_3SbS_4 \cdot 40LiI$ and the composition of each pixel was determined by comparing the recorded diffraction pattern to a database of known patterns, where ICDS numbers were shown on the right side of Fig. 4.2.9(C), and colored to the corresponding composition. Figure 4.2.9(B) shows the TEM image of the field and Fig. 4.2.9(C) shows that the composite mapping image of Figs. 4.2.9(A) and (B). Figure 4.2.9(C) shows that the red parts of Fig. 4.2.9(A) overlap with the particle images in Fig. 4.2.9(B). The particles are considered

$60Li_3SbS_4 \cdot 40LiI$ because the diffraction pattern of $60Li_3SbS_4 \cdot 40LiI$ is similar to that of Li_3SbS_4. Thus, $LiI \cdot 2H_2O$ colored in purple was observed on the surface of $60Li_3SbS_4 \cdot 40LiI$. There were a few aeras of crystal-LiI and an unspecified amorphous aera in the region. These results show that the LiI hydrates, $LiI \cdot 2H_2O$, and amorphous LiI coexist around particles of $60Li_3SbS_4 \cdot 40LiI$ and they were heterogeneously dispersed. It is considered that existence of the LiI layers and the state change of these substances cause the unique conducive behavior of $60Li_3SbS_4 \cdot 40LiI$ with temperature changes in the range of 50 °C−70 °C (Fig. 4.2.6).

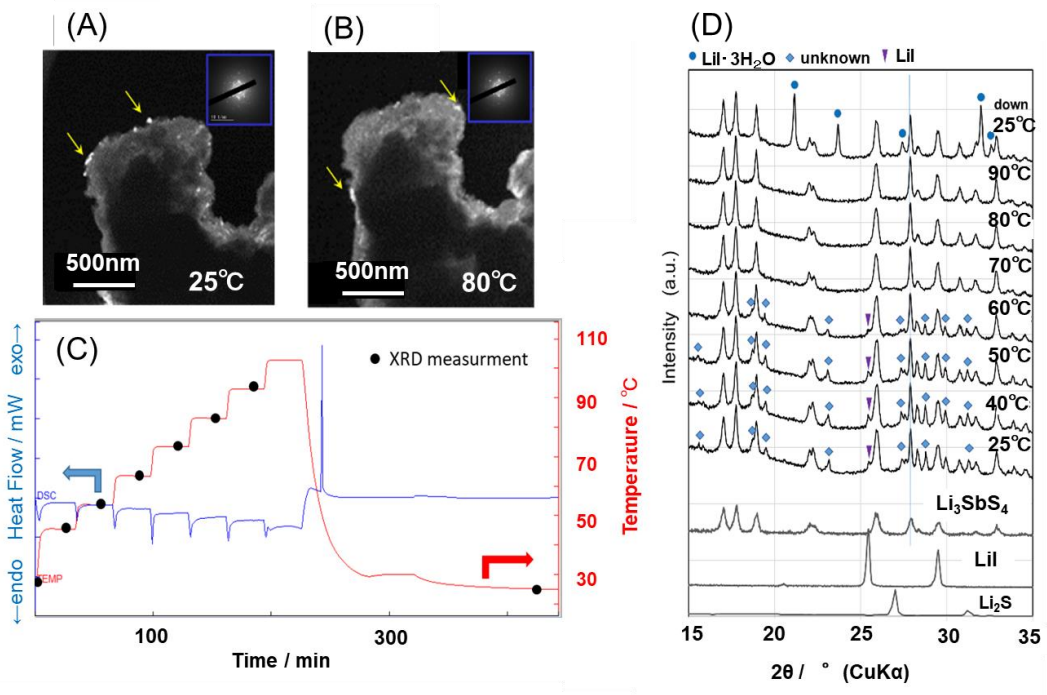

Fig. 4.2.8 Darkfield TEM images at (A) room temperature and (B) 80°C, with the corresponding electron diffraction patterns in the insets of $60Li_3SbS_4 \cdot 40LiI$ obtained via the IE process. (C) shows the heating process and DSC profiles. (D) shows the XRD patterns at several temperatures with the measurement points.

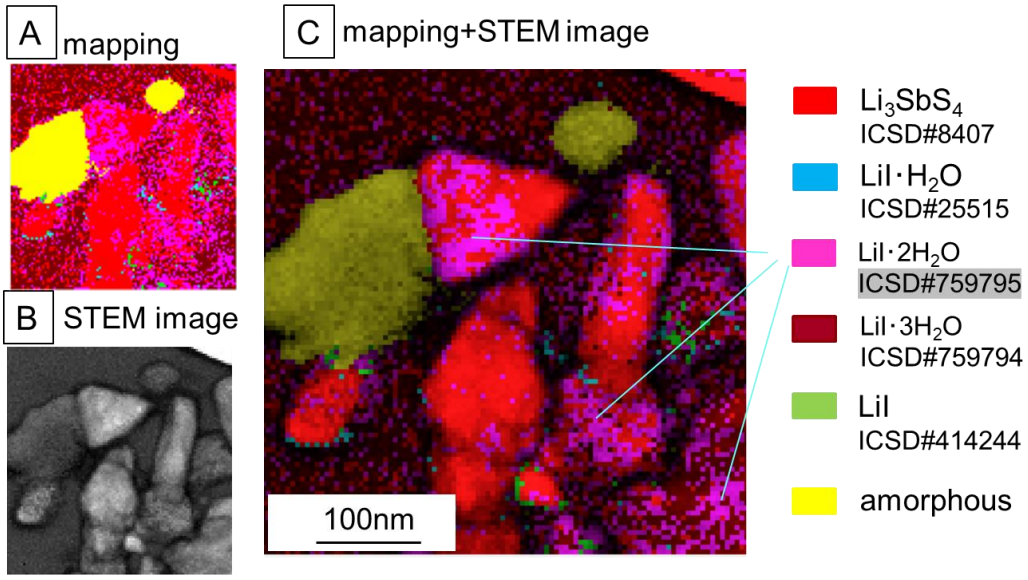

Fig. 4.2.9 Mapping images using Precession electron diffraction method for TEM, (A) is a mapping image using ICSD data, (B) is an STEM image and (C) is a composite image of A and B.

The obtained $60Li_3SbS_4 \cdot 40LiI$ powder has a low ionic conductivity at room temperature due to boundary resistance between the primary particles. However, the ionic conductivity of the obtained sample exhibits significant change at approximately 60 °C due to the changing ionic conductivity of the amorphous or nanocrystalline compound layer containing a large quantity of LiI. The pattern of crystalline LiI was not observed in the XRD pattern of $60Li_3SbS_4 \cdot 40LiI$ in Fig. 4.2.3(A). It suggests that the layers are not crystalline LiI. Liang et al. reported that Al_2O_3–LiI compounds exhibited conductivities on the order of 10^{-5} S cm^{-1} at 25 °C. These conductivities were higher than that of crystalline LiI[20]. The composites of mesoporous Al_2O_3 with LiI were synthesized, and their conductivity were found to be higher than LiI[21]. These results indicate that the LiI nanolayer is related to increasing conductivities, whereas Al_2O_3-LiI compounds and mesoporous composites never show such a sharp increase in conductivity at approximately 60 °C on heating, which was observed for Li_3SbS_4–LiI particles in this study.

To improve the boundary condition of $60Li_3SbS_4 \cdot 40LiI$ particles, mechanical milling for the $60Li_3SbS_4 \cdot 40LiI$ obtained via the IE process was conducted at 360 rpm. Figure 4.2.10(A) shows the XRD patterns of the milled samples. The peaks of $60Li_3SbS_4 \cdot 40LiI$ remained after milling for 20 h and unknown peaks, presumed $LiI \cdot 2H_2O$, reduced. This suggested that LiI and LiI hydrates on the boundary of $60Li_3SbS_4 \cdot 40LiI$ particles became homogeneous though $60Li_3SbS_4 \cdot 40LiI$ particles remained. The unknown peaks disappeared after annealing at 110 °C. LiI hydrates and amorphous LiI were thought to form thin layers on the surface of the $60Li_3SbS_4 \cdot 40LiI$ particles. Figure 4.2.10(B) shows the temperature dependence of conductivities of Li_3SbS_4 and $60Li_3SbS_4 \cdot 40LiI$ after milling and annealing. The milled Li_3SbS_4 (a)' showed higher conductivities than before milling(a). After milling, Li_3SbS_4 existed in amorphous phase due to the observation of halo-pattern in the XRD analysis. Therefore, the milled Li_3SbS_4 possesses more open space for Li ion to pass through among other ions compared to those without milling. The difference on structure and ionic conductivity of glass and glass-ceramic, which is based on the similar phenomenon, are also reported by Kimura et al[17]. In the case of $60Li_3SbS_4 \cdot 40LiI$, the XRD pattern indicated that the crystalline phase remained after milling at 360 rpm for 5-20h. The results suggest that only the surface of $60Li_3SbS_4 \cdot 40LiI$ particles was amorphous. As shown in the Fig. 4.2.9, on the surface of $60Li_3SbS_4 \cdot 40LiI$, a remnant thin layer consisting of amorphous LiI hydrate and crystalline LiI was then further redistributed evenly on the surface with concurrent amorphization during milling process. Therefore, the conductivity at room temperature increased, but that of at 50 ℃ after milling(c) was almost the same the sample before

milling(b). Besides, at near room temperature, the ionic conductivity of milled $60Li_3SbS_4 \cdot 40LiI$(c) was 1.3×10^{-5} S cm^{-1}, which is one order higher than before milling(b). The ionic conductivity further increased after annealing(d) and the temperature dependence of ionic conductivity was following the Arrhenius formula. The XRD pattern of annealed $60Li_3SbS_4 \cdot 40LiI$ in Fig. 4.2.10(A)−(d) was similar to the pattern obtained at 70 °C−90 °C in Fig. 4.2.8(D). Therefore, milling and annealing of $60Li_3SbS_4 \cdot 40LiI$ resulted in formation of a similar sample state of those at 70 °C−90 °C, which remained even after cooling. It was presumed that LiI existed on the surface of $60Li_3SbS_4 \cdot 40LiI$ particles and the boundary of the particles became homogeneous and improved. The Raman spectra results suggested that the crystallinity of milled $60Li_3SbS_4 \cdot 40LiI$ had decreased. This data is illustrated in Fig. 4.2.11.

H_2S gas was not detected from both Li_3SbS_4 and $60Li_3SbS_4 \cdot 40LiI$, although the amount of H_2S gas from Li_3PS_4 reached approximately 5 cm^3g^{-1} for about 4 min. Therefore, $60Li_3SbS_4 \cdot 40LiI$ is a highly air-stable solid electrolyte like Li_3SbS_4 solid electrolyte. The data is shown in Fig. 4.2.12.

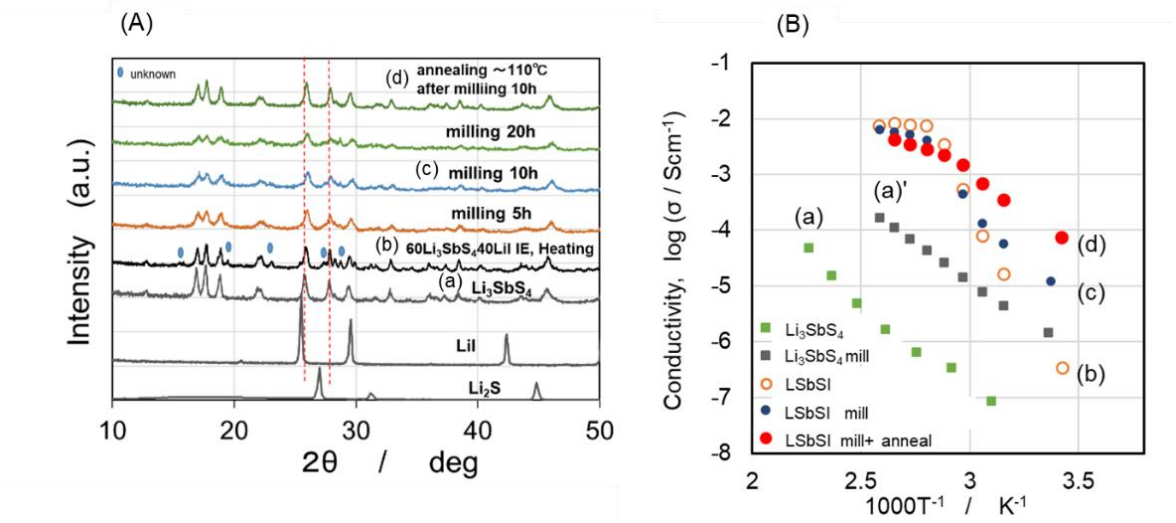

Fig. 4.2.10 (A) XRD patterns and (B) temperature dependence of the ionic conductivity of $60Li_3SbS_4 \cdot 40LiI$ (in mol%) and Li_3SbS_4 milled and annealed after synthesized via the IE process. (a) is Li_3SbS_4 and (a)' is milled Li_3SbS_4. (b) is $60Li_3SbS_4 \cdot 40LiI$ as-ion exchanged, (c) milled 10 h and (d) annealed after milling.

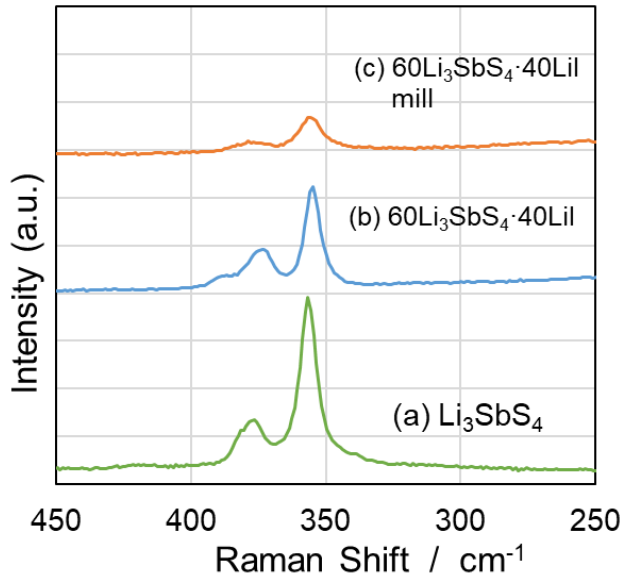

Fig. 4.2.11 Raman spectra of (a) Li_3SbS_4, (b) $60Li_3SbS_4 \cdot 40LiI$ and (c) milled $60Li_3SbS_4 \cdot 40LiI$ synthesized via IE process.

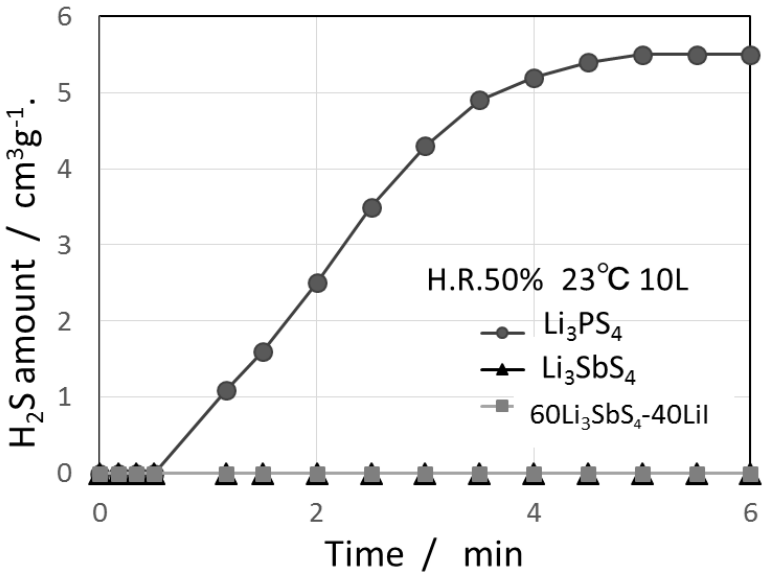

Fig. 4.2.12 Amount of H_2S emission gas of Li_3PS_4, Li_3SbS_4 and $60Li_3SbS_4 \cdot 40LiI$ in the air.

Utilizing the high ionic conductivity of $60Li_3SbS_4 \cdot 40LiI$ at 60 °C, a lithium battery was constructed using this obtained electrolyte with the cathode active material, TiS_2. Figure 4.2.13 shows the SEM image of the composite cathode particle. The TiS_2 particle was covered with $60Li_3SbS_4 \cdot 40LiI$. Figure 4.2.14(A) shows the charge−discharge curves of the cell composed of $50TiS_2 \cdot 50(60Li_3SbS_4 \cdot 40LiI) \cdot 5AB$ | Li_7PS_8I | In-Li at 30 °C. The first discharge capacity was 197 mAh g^{-1} (TiS_2); then, the cell reversibly operated as a lithium secondary battery, although the capacity gradually decreased, as shown in Fig. 4.2.14(B). Figure 4.2.14 also shows the charge−discharge curves (C) and relationships between cycle number and charge-discharge capacities (D) of several current rates of the cell at 60 °C. This shows that the curves of each current rate had almost the same performance and capacities when the charge-discharge cycles were repeated 5 times at the same rate. The capacities quickly recovered when the current rate was returned from 6 to 0.5 C, although the capacities were lower during high rates. After the rate performance measurements, the charge−discharge cycles recovered and continued perfectly at the rate of 1 C.

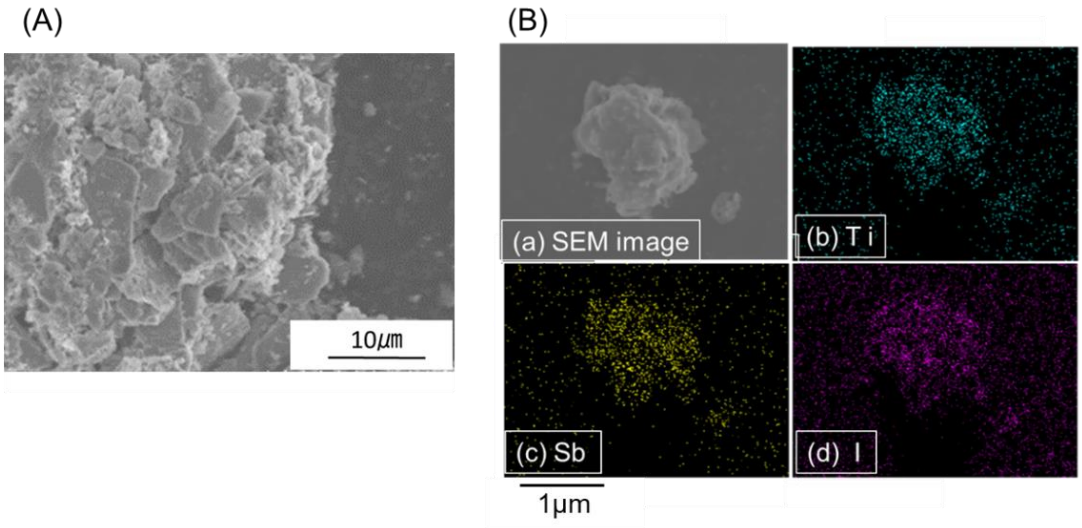

Fig. 4.2.13 (A) SEM image of the TiS_2 composite with $60Li_3SbS_4 \cdot 40LiI$ obtained by the freeze-drying process. EDS mapping observation was conducted in (B), (a) is an SEM image of the sample, and (b), (c) and (d) are mappings of titanium, antimony, and iodide, respectively.

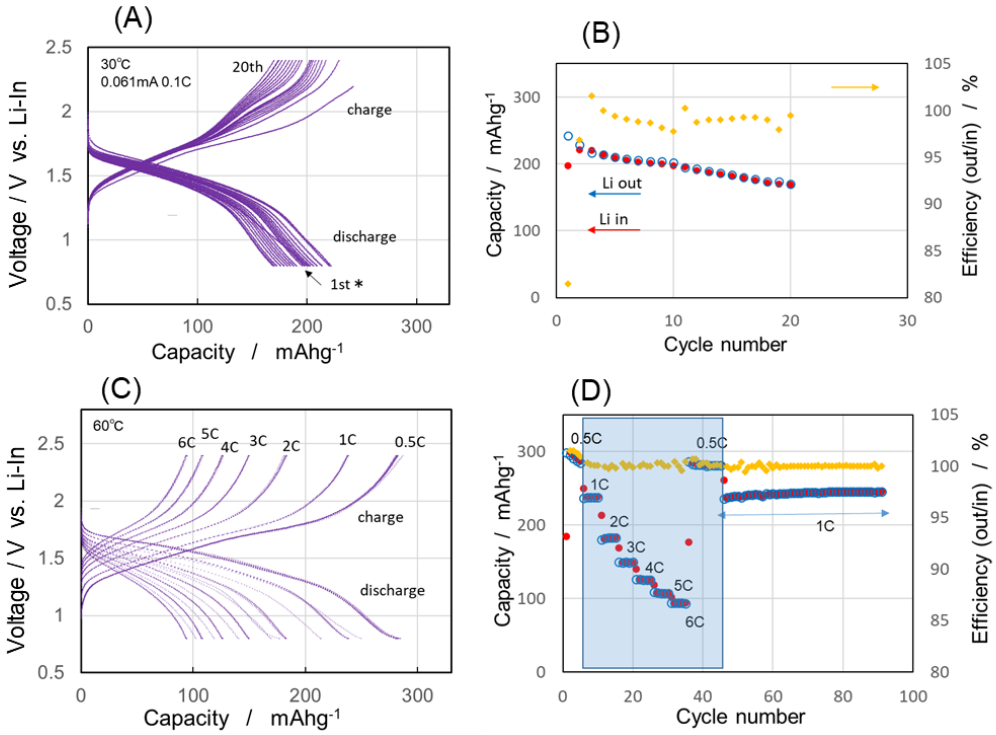

Fig. 4.2.14 (A) is cycling performance of the charge–discharge curves of a cell containing the TiS_2–$60Li_3SbS_4 \cdot 40LiI$ composite as a cathode. (B) is one of discharge capacities and the efficiencies (the discharge/charge-capacity) of the cell at 30 °C. (C) is the rate performance of the cell of charge-discharge curves and (D) is one of discharge capacities at 60 °C. The cell composition of (A)−(D) is $50TiS_2 \cdot 50(60Li_3SbS_4 \cdot 40LiI) \cdot 5AB$ (in wt.%) $|Li_7PS_8I|$In-Li.

4.2.4 Conclusions

Li_3SbS_4 electrolyte was synthesized from an Na_3SbS_4 aqueous solution by ion exchange, freeze-drying, and subsequent heat treatment. The temperature dependence of the ionic conductivities of (100 − *x*) Li_3SbS_4·*x*LiI obtained via the IE process showed a unique behavior, in which the ionic conductivity of $60Li_3SbS_4$ ·40LiI sharply increased from 10^{-7} S cm^{-1} at 25 °C to 8.4×10^{-3} S cm^{-1} at 65 °C. Further, the ion conductivity reached 1.3×10^{-4} S cm^{-1} at 25 °C by homogenizing the surface of the particles using mechanical milling, and annealing. Some XRD measurements and investigation using TEM showed LiI thin layers on the surface of Li_3SbS_4 –LiI primary particles. This is crucial in maintaining the high ion conductivity from around 50 °C to 70 °C to room temperature. The Li_3SbS_4–LiI SEs were stable in ambient air and the cathode composite containing $60Li_3SbS_4$·40LiI showed good charge−discharge performance. Therefore, from the industrial and safety viewpoints, the electrolyte obtained via the IE process is an excellent candidate for all-solid-state lithium batteries.

Supporting information

4.2.S1: Regarding the evaluation method for Li-ion transport number

In this study, the DC ionic conductivity and DC electronic conductivity of $60Li_3SbS_4$·40LiI obtained were 1.2×10^{-4} S cm^{-1} and 1.3×10^{-6} S cm^{-1} at 50 °C, respectively. The total conductivity of the samples was also measured using alternating-current impedance spectroscopy, which was 1.5×10^{-4} S cm^{-1} at 50 °C.

In the DC ionic conductivity measurement of $60Li_3SbS_4$·40LiI, Li foils were used as non-blocking electrodes, which were placed in front of both sides of a steel rod. Therefore, transport ionic species were only Li-ion. The DC ionic conductivity includes Li-ion conductivity and electronic conductivity. The transport number of Li-ion in the DC ionic conductivity refer to the ratio of the Li-ion conductivity and the electronic conductivity. The calculation formula is as follows.

$$T_{\text{Li-ion}} = \sigma_{\text{Li-ion}} / \sigma_{\text{DCion}} = (\sigma_{\text{DCion}} - \sigma_{\text{electronic}}) / \sigma_{\text{DCion}}$$

$T_{\text{Li-ion}}$: the transport number of Li-ion

$\sigma_{\text{Li-ion}}$: the conductivity of Li-ion

σ_{DCion} : the DC ionic conductivity

$\sigma_{\text{electronic}}$: the DC electronic conductivity

$$T = (1.2 \times 10^{-4} - 1.3 \times 10^{-6}) / 1.2 \times 10^{-4} = 0.989$$

References

1) M. Tatsumisago, M. Nagao, A. Hayashi, Recent development of sulfide solid electrolytes and interfacial modification for all-solid-state rechargeable lithium batteries, *J. Asian. Ceram. Soc.* **1**, 17-25 (2013).

2) K. Takada, T. Inada, A. Kajiyama, H. Sasaki, S. Kondo, M. Watanabe, M. Murayama, R. Kanno, Solid-state lithium battery with graphite anode, *Solid State Ionics* **158**, 269-274 (2003).

3) A. Sakuda, A. Hayashi, M. Tatsumisago, Sulfide solid electrolyte with favorable mechanical property for all-solid-state lithium battery, *Sci. Rep.* **3**, 2261-2266 (2013).

4) A. Hayashi, S. Hama, H. Morimoto, M. Tatsumisago, T. Minami, Preparation of Li_2S-P_2S_5 amorphous solid electrolytes by mechanical milling, *J. Am. Ceram. Soc.* **84**, 477-479 (2001).

5) N. Machida, H. Yamamoto, S. Asano, T. Shigematsu, Preparation of amorphous $75Li_2S{\cdot}xP_2S_3{\cdot}(25\text{-}x)P_2S_5$ (mol%) solid electrolytes by a high-energy ball-milling process and their application for an all-solid-state lithium battery, *Solid State Ionics* **176**, 473-479 (2005).

6) M. Calpa, N.C. Rosero-Navarro, A. Miura, R. Jalem, Y. Tateyama, K. Tadanaga, Chemical stability of Li_4PS_4I solid electrolyte against hydrolysis, *Applied Materials Today* **22**, 100918 (2021).

7) Z. Liu, W. Fu, E.A. Payzant, X. Yu, Z. Wu, N.J. Dudney, J. Kiggans, K. Hong, A.J. Rondinone, C. Liang, Amorphous high ionic conductivity of nanoporous β-Li_3PS_4, *J. Am. Chem. Soc.* **135**, 975-978 (2013).

8) N.H.H. Phuc, K. Morikawa, M. Totani, H. Muto, A. Matsuda, Synthesis of plate-like Li_3PS_4 solid electrolyte via liquid-phase shaking for all-solid-state lithium batteries, *Ionics* **23**, 2061-2067 (2017).

9) R. Kanno, T. Hata, Y. Kawamoto, M. Irie, Synthesis of a new lithium ionic conductor, thio-LISICON-lithium germanium sulfide system, *Solid State Ionics* **130**, 97-104 (2000).

10) N. Kamaya, K. Homma, Y. Yamakawa, M. Hirayama, R. Kanno, M. Yonemura, T. Kamiyama, Y. Kato, S. Hama, K. Kawamoto, A. Mitsui, A lithium superionic conductor, *Nat. Mater.* **10**, 682-686 (2011).

11) T. Kaib, S. Haddadpour, M. Kapitein, P. Bron, C. Schröder, H. Eckert, B. Roling, S. Dehnen, New lithium chalcogenidotetrelates, LiChT: Synthesis and characterization of the Li^+-conducting tetralithium ortho-sulfidostannate Li_4SnS_4, *Chem. Mater.* **24**, 2211-2219 (2012).

12) K.H. Park, D.Y. Oh, Y.E. Choi, Y.J. Nam, L.H. Han, J.Y. Kim, H. Xin, F. Lin, S.M. Oh, Y.S.

Jung, Solution-processable glass LiI-Li_4SnS_4 superionic conductors for all-solid-state Li-ion batteries, *Adv. Mater.* **28**, 874-1883 (2016).

13) K. Kanazawa, S. Yubuchi, C. Hotehama, M. Otoyama, S.Shimono, H. Ishibashi, Y. Kubota, A. Sakuda, A. Hayashi, M. Tatsumisago, Mechanochemical synthesis and characterization of metastable hexagonal Li_4SnS_4 solid electrolyte, *Inorg. Chem.* **57**, 9925–9930 (2018).
14) R. Matsuda, T. Kokubo, N.H.H. Phuc, H. Muto, A. Matsuda, Preparation of ambient air-stable electrolyte Li_4SnS_4 by aqueous ion-exchange process, *Solid State Ionics* **345**, 115190 (2020).
15) F. Helfferich, Ion Exchange. *Dover Publications, Inc. New York* (**1995**) 1-25.
16) S. Huber, Lithiumionenleiter, *Dissertation zur Erlangung Doktorgrades der Universitat Regensburg* (2015).
17) T. Kimura, A. Kato, C. Hotehama, A. Sakuda, A. Hayashi, M. Tatsumisago, Preparation and characterization of lithium ion conductive Li_3SbS_4 glass and glass-ceramic electrolytes, *Solid State Ionics* **333**, 45-49 (2019).
18) N.H.H. Phuc, E. Hirahara, K. Morikawa, H. Muto, A. Matsuda, One-pot liquid phase synthesis of (100-*x*) Li_3PS_4-*x*LiI solid electrolytes, *J. Power Sources* **365**, 7-11 (2017).
19) L. Zhang, D. Zhang, K. Yang, X. Yan, L. Wang, J. Mi, B. Xu, Y. Li, Vacancy-contained tetragonal Na_3SbS_4 superionic conductor, *Adv. Sci*. **3**, 1600089 (2016).
20) C.C. Liang, Conduction characteristics of the lithium iodide-aluminum oxide solid electrolytes, *J. Electrochem. Soc.* **10**, 1289-1292 (1973).
21) H. Maekawa, R. Tanaka, T. Sato, Y. Fujimaki, T. Yamamura, Size-dependent ionic conductivity observed for ordered mesoporous alumina-LiI composite, *Solid State Ionics* **175**, 281-285 (2004).

Chapter 5
Fabrication of Self-Standing Electrolyte Sheets Using SiO_2 Fiber for All-Solid-State Batteries

5.1 Fabricating self-standing argyrodite electrolyte sheets containing SiO_2 fiber for all-solid-state batteries

5.1.1 Introduction

Lithium-ion batteries are indispensable for all electronic devices. In a carbon-neutral society, the energy sources of vehicles are changing from gasoline to battery-powered electricity. The safety of batteries used by many people is a particularly important issue. Therefore, all-solid-state lithium-ion batteries (ASSLIBs), in which liquid electrolytes are replaced by solid-state electrolytes (SEs), are of special interest because of their nonflammable and non-leaking properties. In particular, sulfide-based SEs for use in ASSLIBs such as the Li_2S–P_2S_5 system, have been studied actively since the mid-2010s because of their high ionic conductivities and their ability to make good contact with active materials [1–5]. The conductivities of sulfide-based SEs such as $Li_{10}GeP_2S_{12}$ are comparable to those of the organic solvents used in conventional lithium-ion batteries[6,7]. In addition, SEs with the argyrodite structure $Li_{6-x}PS_{5-x}M_x$ such as Li_6PS_5Cl and $Li_{5.5}PS_{4.5}Cl_{1.5}$, exhibited conductivities of 2.4×10^{-3} and 3.9×10^{-3} S cm^{-1} at room temperature, respectively[8–14].

Another important aspect of batteries is their energy density per unit weight and per unit volume. The lighter and smaller the battery pack of a PC, the better it is for practical use. Batteries of electric vehicles also must be lighter and have higher energy densities in order to enable them to travel long distances on a single charge. To increase the energy density of a battery, the active-material ratio of the ASSLIB must be higher. Therefore, the SE separator of an ASSLIB must be thin. Many challenges in fabricating thin SE sheets have been reported recently. Jingyi Wu et al. reviewed these thin SE-separator-related studies[15]. They reported that sulfide SEs such as Li_3PS_4 and Li_6PS_5Cl have been dissolved in organic solvents and subsequently composited with organic polymer sheets[16–19]. Those sheets exhibited good flexibility. In particular, SE sheets using non-woven polyvinylidene difluoride (PVDF) had good flexibility and heat stability, and ASSLIB cells constructed using these sheets showed excellent cycle performance[20,21]. However, Li_3PS_4 and Li_6PS_5Cl dissolved in solvents such as ethanol exhibited low ionic conductivities when they were re-dried and heat-treated[22]. Dissolved

argyrodite-SEs like Li_6PS_5Cl must be heated to a temperature higher than 500 °C to re-crystallize them. For that, SE sheets containing organic polymers are not fully capable of achieving their potential because the SE cannot be heat-treated at sufficiently high temperatures. This indicates that the binder and support in the separator need to be heat resistant. In addition, in many cases the solvent for the polymer precursor affects the crystallization of the SE, and it is difficult to combine both solvent SEs and polymers successfully. When using sheets of organic/inorganic materials as supports, SE solutions cannot be injected into the sheets sufficiently due to the low SE concentration in the solution, and the SE ratio in the resulting sheet is low. Although an SE slurry has a high SE concentration, it cannot penetrate into the sheet, so the obtained SE sheets are uneven. Furthermore, questions about the chemical stability of perfluoroalkyl and polyfluoroalkyl substances (PFAS) have raised concerns about their environmental impact. Improving the materials for ASSLIBs without resorting to PFAS is thus an important challenge.

Also, active material layers containing sulfur are not suitable to be heat-treated at high temperature, which is taken into consideration when fabricating active material composite layers. In case of constructing an SE layer on the active material layer by applying SE slurry, it difficult to select a solvent and heating conditions. This could be solved using self-standing sheets by just sandwiching the SE layer between active layers.

In the present study, I have focused on the high thermal stability[23,24] and high versatility of SiO_2 fibers and have constructed ASSLIBs with all-inorganic materials. I combined argyrodite suspensions in the solvents with SiO_2-fiber suspensions, and I found that the fibers were distributed homogeneously in the SE-composite layer. The structures and ionic conductivities of the resulting SE composites were characterized. In addition, ASSLIBs were fabricated using SE composites containing SiO_2 fibers, and their charge–discharge performances were evaluated.

5.1.2 Experimental

Self-standing sheets of argyrodite SE were synthesized with 20 wt % of SiO_2 fibers suspended in solution. The argyrodite-SE (Li_6PS_5Cl) was prepared via mechanical milling using a planetary ball mill (Fritsch Pulverisette 7 Premium line) and 45 mL zirconia pots containing φ 10 mm zirconia balls at a rotation speed of 510 rpm. The ionic conductivity of the SE was approximately 1.9×10^{-3} S cm^{-1} at 25 °C. Initially, 0.2 g of SiO_2 fibers in 10 mL of ethyl propionate (EP) were shaken with 30 g of φ 4 mm zirconia balls in a centrifuge tube for 15–30 min at room temperature. The obtained SiO_2-fiber

suspension was then added to argyrodite suspension which consisted of 0.32 g of an argyrodite SE powder in 6.4 ml of tetrahydrofuran (THF) and stirred for 30 min at 300 rpm. After that, the 2.0 mL of the mixture containing SiO_2 fibers was poured onto a 30-mm-diameter PTFE plate. The spread suspension on the plate was dried under low pressure at room temperature for 2 h, then left at 80 °C overnight, and finally at 150 °C for 2 h. This procedure resulted in the formation of self-standing sheets of argyrodite SE. The size and thickness of the sheet can be changed by adjusting the amount of plate size and the suspension volume. I punched out some 10-mm-diameter pieces of the obtained sheet and heat treated them stepwise at several temperatures in the range 200 °C –350 °C) for 2 h. I investigated the crystal structures of the samples using X-ray diffraction (XRD) (Rigaku, Smartlab) and Raman spectroscopy (JΛSCO, NRS-4500). I evaluated the temperature dependence of the ionic conductivity using alternating-current impedance spectroscopy from 1 Hz to 1 MHz (Meidenhokuto, HZ-Pro) and from 10 Hz to 3 MHz (Solartron, SI-1260). I observed the cross-sections of the sheets using a scanning electron microscope (SEM) (Hitach, S-4800). I evaluated the characteristics of half cells consisting of Li–In alloy as the reference electrode, an argyrodite composite with SiO_2 fibers (argyro-SE comp–SiO_2 fiber) as the SE separator, and a graphite/ argyro-SE comp–SiO_2 fiber as the negative electrode. I also carried out battery-performance charge-and-discharge tests for full cells consisting of a $Ni_{1/3}Mn_{1/3}Co_{1/3}O_2$ (NMC)– argyro-SE comp as the positive electrode, a argyro-SE comp–SiO_2 fiber as the SE separator, and a graphite– argyro-comp with SiO_2 fibers as the negative electrode.

5.1.3 Results and discussion

To prepare the argyrodite-SE (argyro-SE) suspension for casting onto the PTFE plates, I tested the solvents THF, EP, acetonitrile (ACN), and ethanol, which have been utilized previously to synthesize liquid-phase sulfide electrolytes[4,13]. When argyro-SE was dissolved in solvents containing ethanol, the surfaces of the resulting sheets were inhomogeneous and rough, and they could not be peeled off from the plate after drying. Using ACN as the argyro-SE solvent resulted in a significant decrease in the ionic conductivity. Although the sheets obtained using both THF and EP as the SE solvent could be peeled off successfully, more homogeneous and smoother sheets were obtained when THF was used. The agglomerated SiO_2 fibers were shaken with EP and zirconia balls so that the fibers were finely crushed. I assume that this process activated new surfaces and enabled solvents with higher dielectric constants, such as esters, to coordinate better with the new surfaces. The Si–O–Si bonding reorganized when the solvent evaporated during heat treatment. Also, it is possible that there is a

correlation between SE and Si–O–. Therefore, the SE–SiO_2 composite tissue was reinforced, and it could be peeled off from the plate[25,26].

Figure 5.1.1 shows photographic images of self-standing argyro-SE sheets successfully peeled off from a PTFE plate after drying at 150 °C. This is a scaled-up example with the larger diameter of 80 mm.

Figure 5.1.2 (a) shows the XRD patterns of the argyro-SE sheets with 20 wt% SiO_2 fibers following heat treatment at 150 °C− 350 °C. The XRD pattern at 150 °C shows that the argyrodite structure was maintained in the argyrodite–THF suspension. In the XRD patterns at 150 and 200 °C, broad peaks appeared around $2\theta = 30°$. This indicates that a small amount of the argyro-SE dissolved in THF was amorphous until being heat-treated at 200 °C. When heat treatment was performed at more than 300 °C, the dissolved argyro-SE recrystallized, as can be seen from the higher intensities of the correlated peaks. However, LiCl and unknown peaks increased in the pattern of the sheet heat-treated at 350 °C. Figure 5.1.2 (b) shows the temperature dependence of the conductivities of the sheets after being heat treated at 200 °C, 300 °C, and 350 °C. When heat treated at 300 °C, the conductivities of the sheets were the highest in this heat-treatment range. I therefore selected 300 °C as a suitable heat-treatment temperature.

Fig. 5.1.1 Left image: Photograph of 80-mm-diameter argyrodite SE sheet after drying at 150 ˚C. Right image: Disks punched out from the larger sheet. The weight of each 10-mm-diameter punched-out disk was 5.6 mg, and the thickness was 61 μm after pressurization at 255 MPa. The ionic conductivity was 0.42 mS cm^{-1} at 25 ˚C.

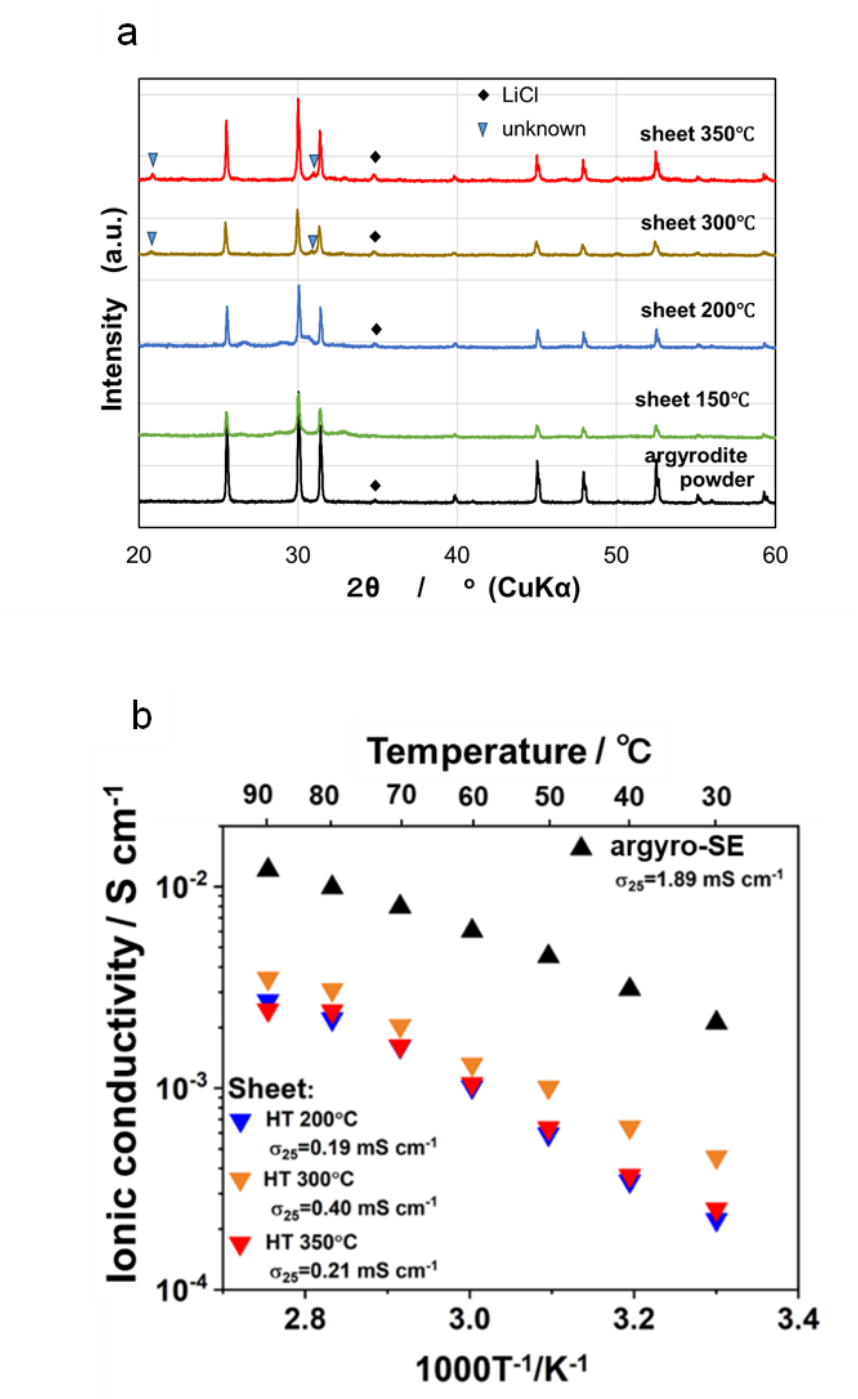

Fig. 5.1.2 (a) XRD patterns of 10-mm-diameter SE sheets heat-treated at 150 ℃, 200 ℃, 300 ℃, and 350 ℃. (b) Temperature dependence of the conductivities of the argyrodite sheets containing SiO_2 fibers after heat trea

I fabricated argyro-SEs containing several different ratios of SiO_2 fibers and evaluated their ionic conductivities. Figure 5.1.3 shows the SiO_2 composition dependence of the ionic conductivities of the obtained argyro-SE containing SiO_2 fibers. I used 80 mg samples of powdered SEs for these measurements. The SE ionic conductivities decreased gradually with higher SiO_2-fibers concentration. Small reduction in conductivity was observed when the SiO_2-fibers concentration used was between 10 % to 20 %. Therefore, the effect on the conductivity reduction due to incorporation of SiO_2-fibers is insignificant. Rather, the main causet is due to the dissolution of the SE in THF [27]. In contrast, low-dielectric-constant solvents such as toluene did not dissolve the argyro-SE; and the SEs were homogeneously dispersed [16]. However, the dispersed SE layer could not be peeled off from the PTFE plate after drying at 150 °C, even though an SE powder dissolved once in toluene and then dried exhibited a higher ionic conductivity than did SE powders obtained from other solvents. I fabricated argyro-SE sheets containing 10, 15, and 20 wt % of SiO_2 fibers. After heat treatment, the SE sheets containing 10 and 15 wt % were too brittle for impedance evaluation and cell fabrication; therefore, I used the 20 wt % sheets for further evaluations.

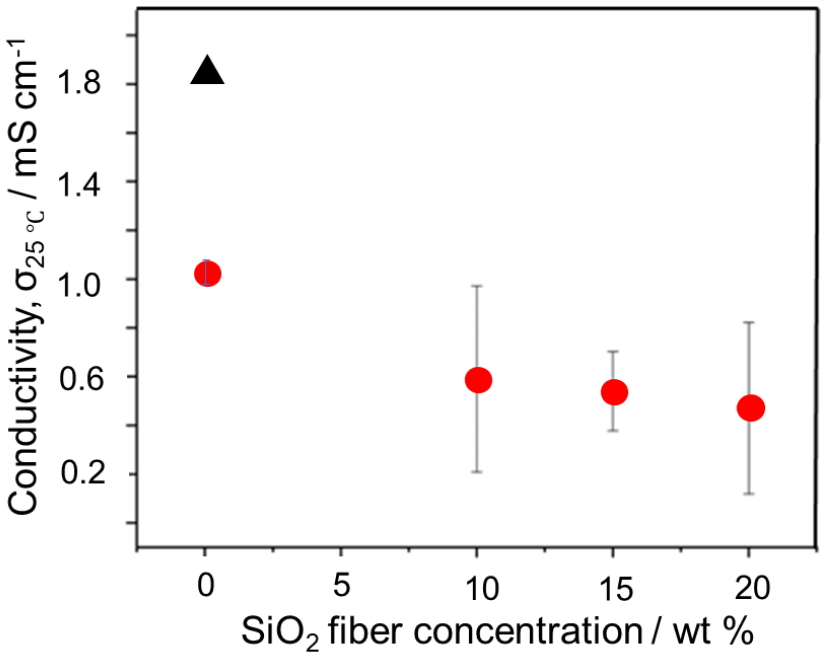

Fig. 5.1.3 SiO_2 composition dependence of the ionic conductivities of the obtained argyrodite-SE–SiO_2 fibers (●). A black triangle (▲) is pristine argyrodite-SE. The measurements used 80 mg samples of powdered SEs.

Figure 5.1.4 shows the Raman spectra of pristine argyro-SE powder and of the obtained argyro-SE powder containing 20 wt % SiO_2 fibers after heat treatment at 300 °C (hereafter, argyro-SE–20% SiO_2 fibers). Both Raman shifts exhibit a large main peak at 426 cm^{-1} and minor ones at approximately 220, 270, 580, and 610 cm^{-1}, which correspond to the PS_4^{3-} units [13, 14]. These peaks of argyro-SE–20% SiO_2 fibers are almost the same as the peaks of the pristine argyro-SE powder, although the intensities of the former peaks are lower. This indicates that the obtained argyro-SE–20% SiO_2 fibers retain its basic structure after being dissolved in the solvent and composited with SiO_2 fibers

The ionic conductivities of the obtained argyro-SE–20% SiO_2 fibers sheets were evaluated using electrochemical impedance measurements after compressing them at 255 MPa in a uniaxial press. Figure 5.1.5 (a) shows Nyquist plots of the electrochemical impedance at room temperature of the pristine argyro-SE powder pellets (black circles), the obtained argyro-SE–20% SiO_2 fibers powder pellets (blown circles), and various layers of sheets (1 sheet, orange; 2 sheets, blue; 3 sheets, red). The sample condition data are in Table 5.1.1. Figure 5.1.5 (b) shows the temperature dependences of the ionic conductivity of these pellets and sheets. Those of argyro-SE-powder containing SiO_2 fibers (blown diamonds) have a larger activation energy than that of pristine argyro-SE; therefore, the ionic conductivity was significantly lower at room temperature than that of pristine argyro-SE. It is assumed that Li-ion conduction is inhibited by the SiO_2 fibers in the SE layers due to their own low Li-ion conductivity. Another reason for the reduced conductivity will be the difficulty in densifying SE pellets containing SiO_2 fibers.

The increasing boundary resistance in the SE layer by adding the SiO_2 fibers caused difficulty in densifying and to be larger activation energy of the SE containing SiO_2 fibers. The corresponding activation energies and ionic conductivities at room temperature are shown in Fig. 5.1.5 (c). As the thickness of the sheet was reduced, the activation energies decreased. Thus, the effect of adding SiO_2 fibers is negligible when the sheets are very thin. However, the ionic conductivities of the sheets were still lower than those of the pristine argyro-SE. Figure 5.1.5 (d) shows the densities of the powder pellets and sheets calculated using the sample values of thickness, diameter, and weight with respect to their ionic conductivities obtained from the electrical-impedance measurements shown in Figs. 5.1.5 (a) and (b). The density of argyro-SE containing SiO_2 fiber powder was lower than that of pristine argyro-SE, and those of the obtained sheets were even lower. This indicates that argyro-SEs with SiO_2 fibers were difficult to densify because argyrodite is hard and highly crystalline. However, it is possible to increase the ionic conductivity of argyro-SE–20% SiO_2 fibers sheets by densifying them using

suitable pressing conditions.

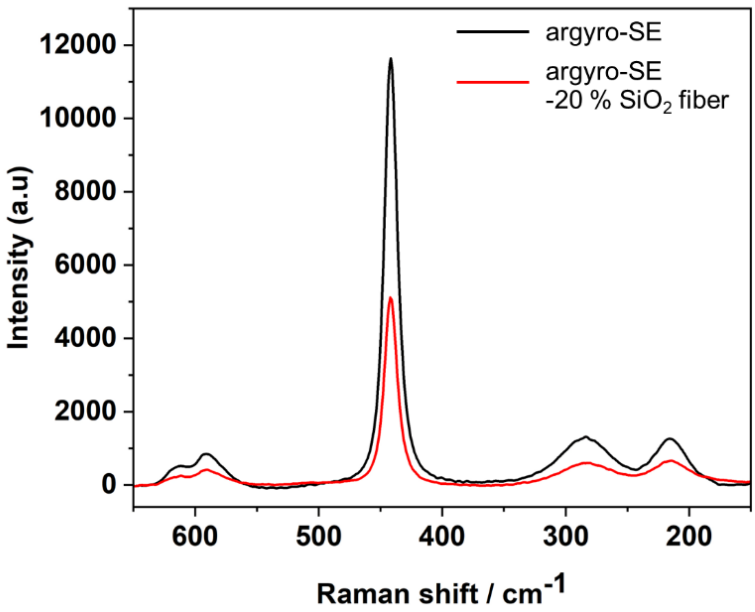

Fig. 5.1.4 Raman spectra of pristine argyrodite-SE powder (black curve) and of the powder obtained from argyrodite-SE with 20 % SiO_2 fibers (red curve).

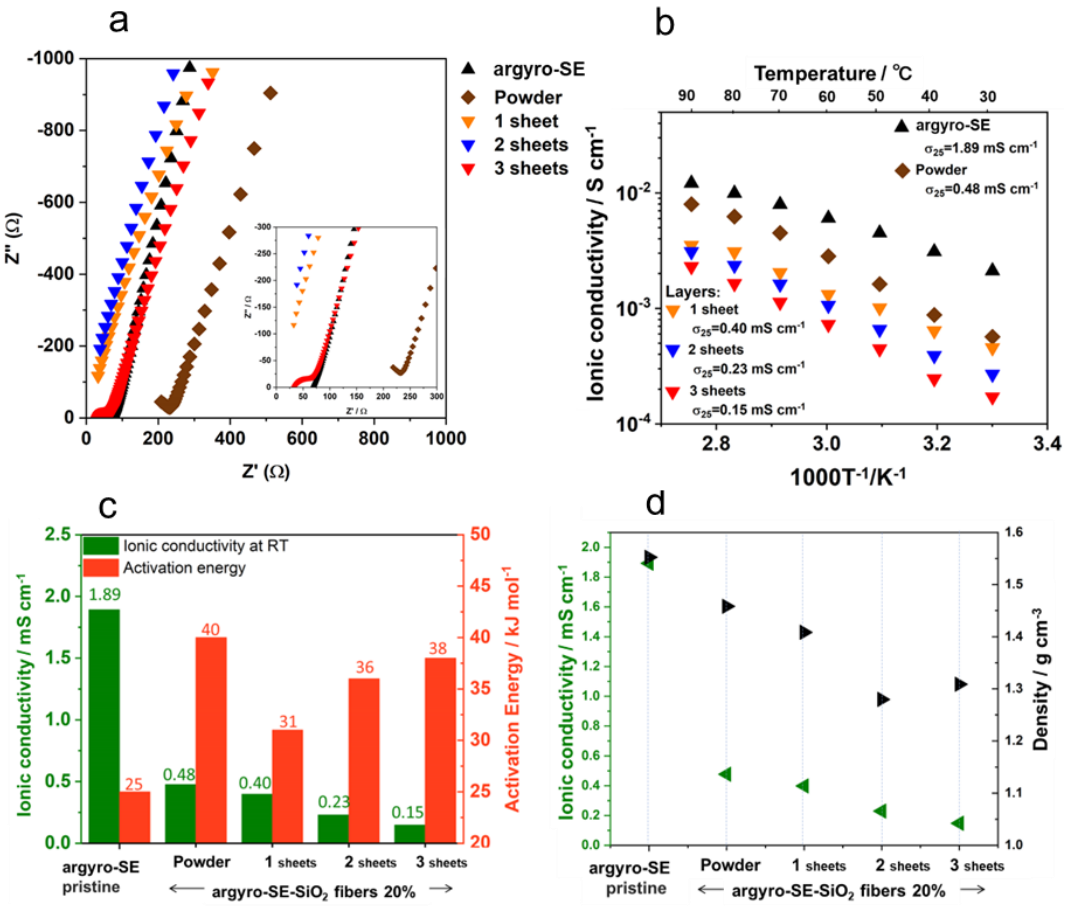

Fig. 5.1.5 (a) Nyquist plots of electrochemical impedance at room temperature from the ionic conductivity of argyro-SE–20% SiO_2 fibers solid electrolytes in various forms. (b) Temperature dependence of the ionic conductivity of argyro-SE–20% SiO_2 fibers measured in various forms. The symbols were shown pristine argyro-SE powder pellets (black), the obtained argyro-SE–20% SiO_2 fibers powder pellets (brown), and various layers of sheets (1 sheet, orange; 2 sheets, blue; 3 sheets, red) in Fig. 5a and 5b. (c) Ionic conductivities and activation energies from argyro-SE–20% SiO_2 fibers in sheet and powder form at room temperature. (d) Relationship between ionic conductivity (green) and density (black).

Figure 5.1.6 (a) shows SEM cross-sectional images of the argyro-SE–20% SiO_2 fibers. The images in panels a1 and a2 (zoom) show the microstructures before the sample was compressed; panels a3 and a4 (zoom) are shown after pressing at 255 MPa; and panels a5 and a6 (zoom) are shown after the sample was compressed at 510 MPa, respectively. The thickness of the sheet compressed at 255 MPa was about half of that before pressing, but spaces were left between the particles, and the argyro-SE particles were separated from each other. In the sheet compressed at 510 MPa, the thickness changed little compared to the 255 MPa case, but the spaces were reduced, and the SE particles adhered to each other. To compare the grain boundary resistances of the sheets compressed at 255 MPa and 510 MPa, I carried out electrochemical impedance measurements at low temperatures. Figure 5.1.6 (b) shows Nyquist plots at −15 °C of the sheets compressed at 255 MPa and 510 MPa and at 20 °C for the sheet compressed at 255 MPa. These resistances, shown in the Nyquist plots, include bulk and the grain boundary resistances. From the results for the sheets compressed at 255 MPa, a linear pattern was detected at 20 °C, but in the Nyquist plot at −15 °C, a semicircle began to appear. Conversely, the sheet compressed at 510 MPa showed an indistinct semi-circular pattern; this indicates that the grain boundary resistance of the sheet after compression at 510 MPa is lower than that of the sheet after compression at 255 MPa, assuming the bulk resistance is not changed by the compaction pressure[28,29].

ASSLIBs using the obtained argyro-SE–20% SiO_2 fibers sheets were tried to fabricate. First, I prepared graphite/ argyro-SE–20% SiO_2 fiber composite sheets. I did this is because the active electrode's surface must be smooth in order to use a thin-layer SE; otherwise, short circuits can occur. Figure 5.1.7 shows the charge–discharge curves of a half-cell using the graphite-composite containing 20% SiO_2 fibers, which I verified to work well as an anode. Second, I fabricated a full-cell using 10 mg of an NMC composite as a cathode, the obtained argyro-SE–20% SiO_2 fibers sheets as separators, and 8 mg of a graphite-composite as an anode. About cathode layers, I thought better that NMC-powder and SE-powder were mixed without SiO_2-fiber and solvents because the sheets in this study were prepared with heat-treatment at 300℃ which is not suitable for cathode material, NMC. As shown in Table 5.1.1, I tested four patterns. Two patterns used one sheet compressed at 255 MPa, and two patterns used two sheets compressed at 510 MPa, both of which performed as rechargeable batteries. Another test involved a short circuit (one sheet compressed at 510 MPa), and an additional test exhibited a very limited capacity (two sheets compressed at 255 MPa). The results indicated that the sheet compressed at 255 MPa retained spaces between the SE particles and that the boundary

resistance increased. The blue line in Fig. 5.1.8 (a) shows the result for the cell using two sheets compressed at 510 MPa as the separator. The discharge capacity was 126 mAh g^{-1}, and it was larger than that of the cell using one sheet compressed at 255 MPa (orange line). The cycle performance of the former cell shown in Fig. 5.1.8 (c) was better than that of the latter. I therefore conclude that, by controlling the appropriate molding pressure, the full cells using the obtained argyro-SE–20% SiO_2 fibers sheets can be operated function effectively as rechargeable ASSLIBs.

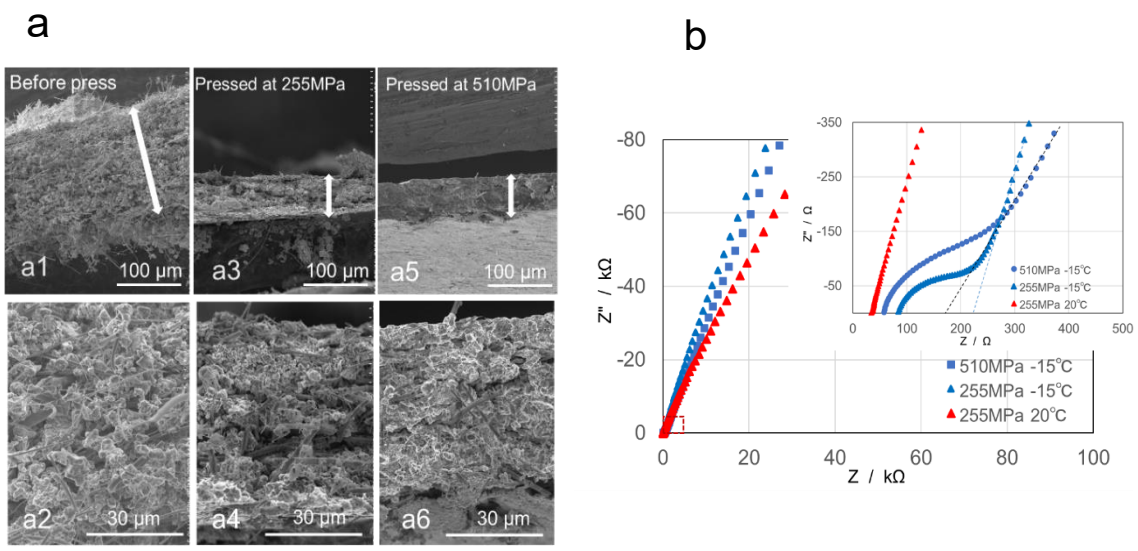

Fig. 5.1.6 (a) SEM cross-sectional images of the obtained argyro-SE–20% SiO_2 fibers sheets, where a1 and a2 are as-prepared after heat treatment and before comression, a3 and a4 are compressed at 255 MPa, and a5 and a6 are comressed at 510 MPa. (b) Nyquist plots of the electrochemical impedance of argyro-SE–20% SiO_2 fibers sheets pressed at 255 MPa and 510 MPa.

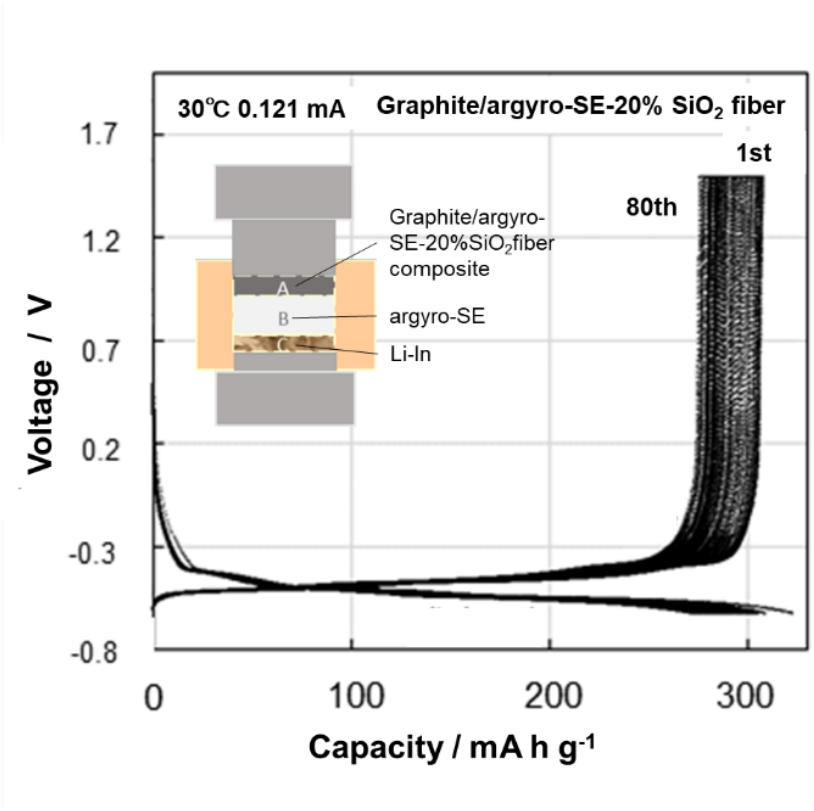

Fig. 5.1.7 Charge–discharge curves of a half-cell using a graphite/argyro-SE–20%SiO_2 fibers composite, argyro-SE, and Li–In alloy as a reference, which was compressed at 255 MPa. The cell configuration is shown in the inset in the figure.

Table 5.1.1 Argyro-SE-20%SiO_2 fiber sheets (ϕ 10 mm) used in full cells in Fig. 5.1.8.

Samples	Weight / g x 10^{-3}		Density / g cm^{-3}	
	255 MPa	510 MPa	255 MPa	510 MPa
1 sheet	7.5		1.41	
2 sheets		16.2		1.45

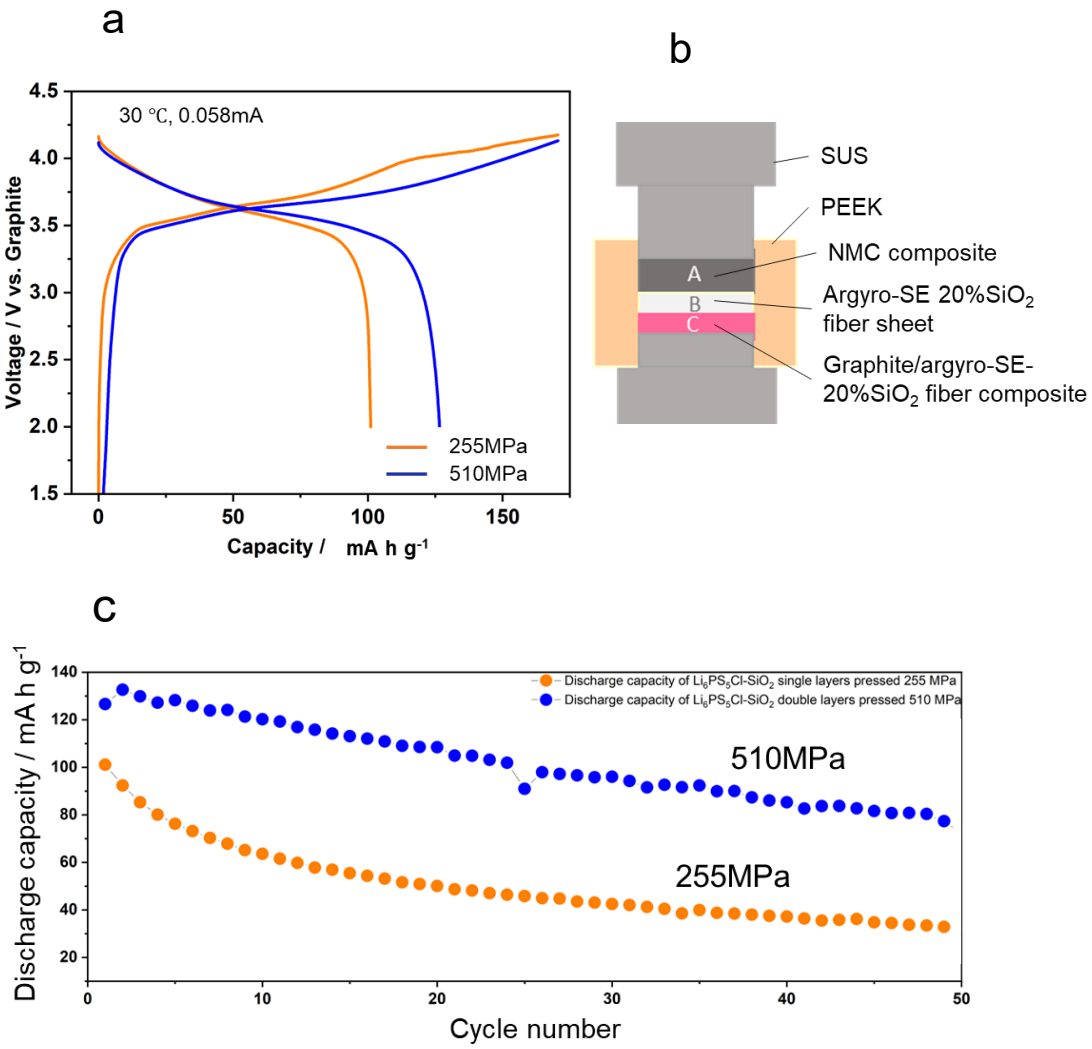

Fig. 5.1.8 Battery performance of NMC composite| argyrol-SE-20% SiO_2 fibers sheet| Graphite/ argyro-SE-20%-SiO_2 fibers composite. (a) 1st charge-discharge curves and (**c**) cycle performance of full cells. The orange line is the cell containing one layer of SE sheet and pressed at 255 MPa. The blue line is the cell containing two layers of SE sheets pressed at 510 MPa. (b) Full-cell configuration.

5.1.4 Conclusions

By combining solvents to disperse SE particles with SiO_2 fibers, I successfully fabricated all-inorganic, self-standing, argyro-SE sheets. They are noncombustible and can be heat-treated at high temperatures. Consequently, SE sheets can be fabricated to function in many situations. The ionic conductivities of the sheets were 4.2×10^{-4} S cm^{-1} at room temperature. I fabricated full cells using these sheets as separators sandwiched between an NMC-composite positive electrode and a graphite-composite negative electrode. After molding a full cell at 510 MPa, it performed well as a rechargeable ASSLIB.

References

1) Y. Seino, T. Ota, K. Takada, A. Hayashi, M. Tatsumisago, A sulfide lithium super ion conductor is superior to liquid ion conductors for use in rechargeable batteries, *Energy Environ. Sci.* **7**, 627–631 (2014**)**.
2) E. Rangasamy, Z. Liu, M. Gobet, K. Pilar, G Sahu, W. Zhou, H. Wu, S. Greenbaum, C. Liang, An iodide-based $Li_7P_2S_8I$ supereionic conductor, *J. Am. Chem. Soc.* **137**, 1384-1387 (2015).
3) N. Kamaya, K. Homma, Y. Yamakawa, M. Hirayama, R. Kanno, M. Yonemura, T. Kamiyama, Y. Kato, S. Hama, K. Kawamoto, A. Mitsui, A lithium superionic conductor, *Nat. Mater.* **10**, 682–686 (2011).
4) N.H.H. Phuc, M. Totani, K. Morikawa, H. Muto, A. Matsuda, Preparation of Li_3PS_4 solid electrolyte using ethyl acetate as synthetic medium, *Solid State Ionics* **288**, 240–243 (2016).
5) A. Sakuda, A. Hayashi, M. Tatsumisago, Sulfide solid electrolyte with favorable mechanical property for all-solid-state lithium battery, *Sci. Rep.* **3**, 2261–2266 (2013).
6) R. Kanno, M. Murayama, Lithium ionic conductor thio-LISICON: The Li_2S-GeS_2-P_2S_5 system, *J. Electrochem. Soc.* **148**, A742–A746 (2001).
7) B. Tao, C. Ren, H. Li, B. Liu, X. Jia, X. Dong, S. Zhang, H. Chang, Thio-/LISICON and LGPS-type solid electrolytes for all-solid-state lithium-ion batteries, *Adv. Funct. Mater.* **32** 2203551 (2022).
8) S. Boulineau, J.M. Tarascon, J.B. Leriche, V. Viallet, Electrochemical properties of all-solid-state lithium secondary batteries using Li-argyrodite Li_6PS_5Cl as solid electrolyte, *Solid State Ionics* **242**, 45–48 (2013).
9) R.P. Rao, S. Adams, Studies of lithium argyrodite solid electrolytes for all-solid-state batteries,

Phys. Status Solid A **208**, 1804–1807 (2011).

10) L. Zhou, K.H. Park, X. Sun, F. Lalere, T. Adermann, P. Hartmann, L.F. Nazar, Solvent-engineered design of argyrodite Li_6PS_5X (x = Cl, Br, I) solid electrolytes with high ionic conductivity, *ACS Energy Lett.* **4**, 265–270 (2019).

11) L. Peng, S. Chen, C. Yu, C. Wei, C. Liao, Z. Wu, H. L. Wang, S. Cheng, J. Xie, Enhancing moisture and electrochemical stability of the $Li_{5.5}PS_{4.5}Cl_{1.5}$ electrolyte by oxygen doping, *ACS Appl. Mater. Interfaces* **14**, 4179–4185 (2022).

12) G.F. Dewald, S. Ohno, M.A. Kraft, R. Koerver, P. Till, N.M. Vargas-Barbosa, J. Janek, W.G. Zeier, Experimental assessment of the practical oxidative stability of lithium thiophosphate solid electrolytes, *Chem. Mater*. **31**, 8328–8337 (2019).

13) R.F. Indrawan, H. Gamo, A. Nagai, A. Matsuda, Chemically understanding the liquid-phase synthesis of argyrodite solid electrolyte Li_6PS_5Cl with the highest ionic conductivity for all-solid-state batteries, *Chem. Mater.* **35**, 2549–2558 (2023).

14) H. Gamo, I. Kusaba, K. Hikima, A. Matsuda, Rapid solution synthesis of argyrodite-type Li_6PS_5X (X = Cl, Br, and I) solid electrolytes using excess sulfur, *Inorg. Chem.* **62**, 6076–6083 (2023).

15) J. Wu, L. Yuan, W. Zhang, Z. Li, X. Xie and Y. Huang, Reducing the thickness of solid-state electrolyte membranes for high-energy lithium batteries, *Energy Environ. Sci.* **14**, 12–36 (2021).

16) R. Xu, J. Yue, S. Liu, J. Tu, F. Han, P. Liu, C. Wang, Cathode-supported all-solid-state lithium−sulfur batteries with high cell-level energy density, *ACS Energy Lett.* **4**, 1073–1079 (2019).

17) Y.J. Nam, S.J. Cho, D.Y. Oh, J.M. Lim, S.Y. Kim, J.H. Song, Y.G. Lee, S.Y. Lee, Y.S. Jung, Bendable and thin sulfide solid electrolyte film: A new electrolyte opportunity for free-standing and stackable high-energy all-solid-state lithium-ion batteries, *Nano Lett.* **15**, 3317–3323 (2015).

18) Y. Li, X. Wang, H. Zhou, X. Xing, A. Banerjee, J. Holoubek, H. Liu, Y. S. Meng, P. Liu, Thin solid electrolyte layers enabled by nanoscopic polymer binding, *ACS Energy Lett.* **5**, 955–961 (2020).

19) D.Y. Oh, K.T. Kim, S.H. Jung, D.H. Kim, S. Jun, S. Jeoung, H.R. Moon, Y.S. Jung, Tactical hybrids of Li^+-conductive dry polymer electrolytes with sulfide solid electrolytes: Toward practical all-solid-state batteries with wider temperature operability, *Materials Today* **53**, 7–15 **(**2022).

20) D.H. Kim, Y.H. Lee, Y.B. Song, H. Kwak, S.Y. Lee, Y. S. Jung, Thin and flexible solid electrolyte membranes with ultrahigh thermal stability derived from solution-processable Li argyrodites for all-solid-state Li-ion batteries, *ACS Energy Lett.* **5**, 718–727 (2020).

21) S. Liu, L. Zhou, J. Han, K. Wen, S. Guan, C. Xue, Z. Zhang, B. Xu, Y. Lin, Y. Shen, L. Li, C.W. Nan, Super long-cycling all-solid-state battery with thin Li_6PS_5Cl-based electrolyte, *Adv. Energy Mater.* **12**, 2200660 (2022).

22) S. Yubuchi, S. Teragawa, K. Aso, K. Tadanaga, A. Hayashi, M. Tatsumisago, Preparation of high lithium-ion conducting Li_6PS_5Cl solid electrolyte from ethanol solution for all-solid-state lithium batteries, *J. Power Sources* **293**, 941−945 (2015).

23) R. Zhang, C. Liu, P. C. Hsu, C. Zhang, N. Liu, J. Zhang, H.R. Lee, Y. Lu, Y. Qiu, S. Chu, Y. Cui, Nanofiber air filters with high-temperature stability for efficient $PM_{2.5}$ removal from the pollution sources, *Nano Lett.* **16**, 3642–3649 (2016).

24) X. Mao, Y. Si, Y. Chen, L. Yang, F. Zhao, B. Ding, J. Yu, Silica nanofibrous membranes with robust flexibility and thermal stability for high-efficiency fine particulate filtration, *RSC Adv.* **2**, 12216–12223 (2012).

25) Z. Li, Y. Zhu, Surface-modification of SiO_2 nanoparticles with oleic acid, *Applied Surface Science* **211**, 315-320 (2003).

26) M. Namvar-Mahboub, M. Pakizeh, Development of a novel thin film composite membrane by interfacial polymerization on polyetherimide/modified SiO_2 support for organic solvent nanofiltration, *Separation and Purification Technology* **119**, 35-45 (2013).

27) J. Ruhl, L. M. Riegger, M. Ghidiu, W. G. Zeier, Impact of solvent treatment of the superionic argyrodite Li_6PS_5Cl on solid-state battery performance, *Adv. Energy Sustainability Res.* **2**, 2000077 (2021).

28) J.S. Park, Y-B. Kim, J. An, F. Prinz, Oxygen diffusion across the grain boundary in bicrystal yttria stabilized zirconia, *Solid State Comm.* **152**, 2169-2171 (2012).

29) P. Braun, C. Uhlmann, A. Weber, H. Stormer, D. Gerthsen, E. Ivers-Tiffee, Separation of bulk and grain boundary contributions to the total conductivity of solid lithium-ion conducting electrolytes, *J. Electroceram.* **38**, 157-167 (2017).

5.2 Fabricating self-standing sulfide electrolyte, $Li_7P_2S_8I$ sheets containing glass fiber for all-solid-state batteries

5.2.1 Introduction

Recently, many studies of SE sheets were shown. About almost all works, the sheets were fabricated using the way that obtained SE was dispersed to the solvent with polymers. In most cases, ionic conductivities of the sheets were one or two orders magnitude lower than pristine SE powders. This content has already been discussed in the previous introduction part of the previous section 5.1, so references have been omitted.

$Li_7P_2S_8I$ (LPSI) is stable against lithium metal and one of the most air-stable SEs in thio-LISICON family like argyrodites though the conductivity of LPSI is slightly lower than argyrodites. The other advantage is that the fabricating temperature of LPSI is lower than that of other SEs. Therefore, in this section 5.2, LPSI sheets containing glass fibers as a support were synthesized directly by applying a liquid phase shaking process.

5.2.2 Experimental

The raw materials with chemical composition(3:1:1), Li_2S (Mitsuwa, 99.9%), P_2S_5 (Aldrich, 99%), LiI (Aldrich, 99%), and 10 wt% of glass fiber were shaken with 30 g of ZrO_2 balls (4 mmφ), and ethyl propionate as a solvent in polypropylene tubes with constant shaking rate at 1500 rpm and 30 ℃ for 3 h. The obtained precursor slurry was poured onto a 30-mm-diameter polytetrafluoro-ethylene (PTFE) plate and dried under low pressure in approximately 5 h while the temperature was gradually increased from 25 to 130 ℃ and heat-treated in argon atmosphere at 150 ℃ for 2 h. This procedure resulted in the formation of self-standing sheets of LPSI. The size and thickness of the sheet can be changed by adjusting the amount of plate size and the suspension volume. Further, LPSI sheets containing spherical graphite as an anode material were fabricated. I punched out some 10-mm-diameter pieces of the obtained sheets and investigated the crystal structures of the samples using X-ray diffraction analysis (XRD) (Smart Lab, Rigaku) and the ionic conductivities at their variations with temperature were measured using alternating-current impedance spectroscopy (SI 1260, Solatron) from 1 MHz to 10 Hz at a temperature of 25 to 150 ℃.

For the fabrication of full cells, obtained sheets of LPSI for the separator and LPSI containing graphite for the anode, and the cathode composite containing $LiNiCoMnO_2$ (Ni:Co:Mn=5:2:3) (NCM),

SE, and acetylene black (70:30:3), were placed each other in a holder made of polyetheretherketone sandwiched between two stainless steel rods of 10 mm diameter and uniaxially pressed into pellets at a pressure of 50 MPa. After that they were placed together and pressed at 250 MPa for 10 min. Subsequently, these pellets were placed in an over cell made of stainless steel and fixed with three bolts and nuts at 10 Nm. Finally, the cells were placed in a glass bottle filled with argon with two lead wires for establishing connections with the electrodes.

5.2.3 Results and discussion

Fig. 5.2.1 shows the schematic image of fabrication of the LPSI sheets and the photo of the obtained LPSI sheet of 30mm diameter. These starting materials and glass fiber were shaken in a centrifuge tube. In Fig. 5.2.2, (a) is a photo image before shaking and (b) is after one. The lump of glass fiber was seen in (a), but the solution in (b) became homogeneous slurry. Even though the sheet contained only 10 wt% of glass fibers, it was possible to peel it off from the PTFE plate. The sheet containing 5 wt% of glass fiber was fragile and it could not be taken out from the plate. (c) is a cross-section SEM image before pressing at 250 MPa and (d) is after one. There is space in the layer of (c). (d) was densified to approximately 60 μm. In Fig. 5.2.3, glass fiber was coated with SE and dispersed in the layer.

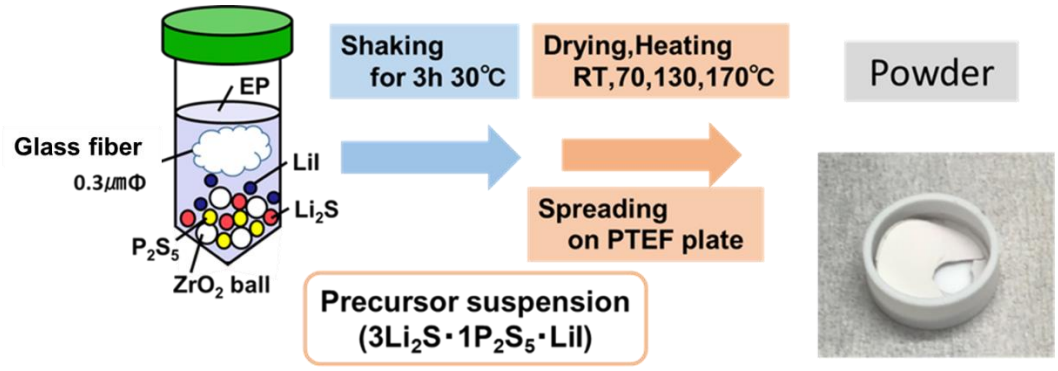

Fig. 5.2.1 Schematic image of fabrication flow of LPSI sheet.

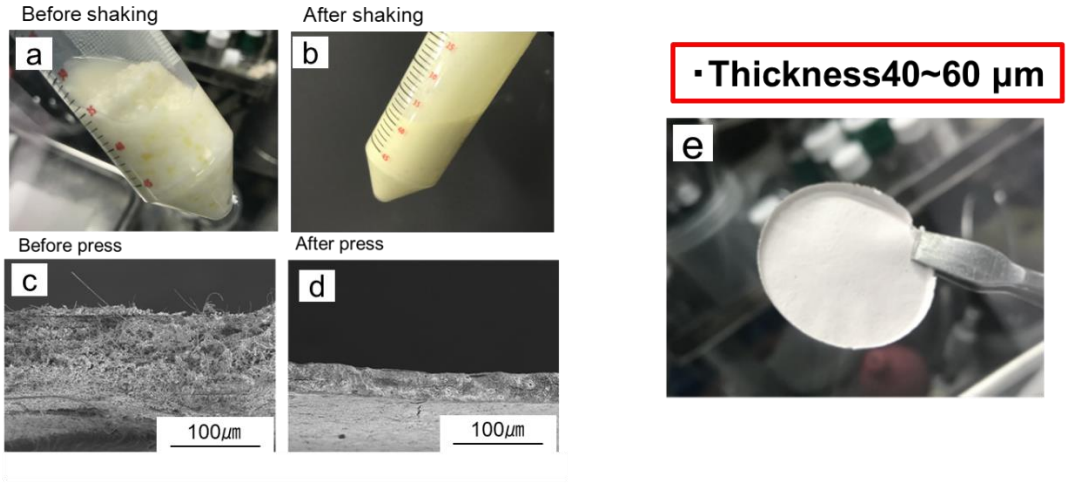

Fig. 5.2.2 Images of starting materials (a) before and (b) after shaking of $Li_7P_2S_8I$. Cross sectional SEM images of the sheet before (c) and after (d) pressed at 250 MPa. (e) is an image of LPSI sheet.

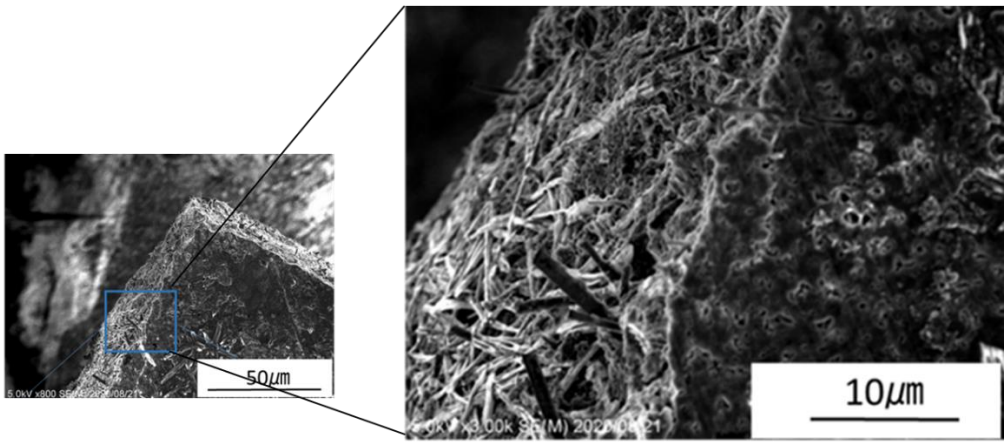

Fig. 5.2.3 SEM images of $Li_7P_2S_8I$ with 10 wt% glass fiber sheets pressed at 250MPa (8.5mg、57～65 μm).

Figure 5.2.4 shows XRD patterns of the obtained $Li_7P_2S_8I$ sheet containing 10 wt% glass fiber, glass fiber, and $Li_7P_2S_8I$ powder synthesized via liquid phase process with heat-treatment at 170°C. LPSI sheet fabricated with glass fiber showed almost same pattern to standard LPSI synthesized via liquid phase processing. Further, it seems to contain high ionic conductivity phase marked blue triangle, which pattern is shown in LGPS. The temperature dependence of ionic conductivity of LPSI sheet was shown in Fig. 5.2.5. It showed comparable with LPSI powder in the region from room temperature to 90 ℃. It is suggested that high conductive phase was synthesized on the glass fiber surface due to silicon or any other chemical containing in the glass fiber. Since the thickness of the LPSI sheet was thin, 61 μm, the measurements above 110 ℃ appear to have been affected the cell resistance.

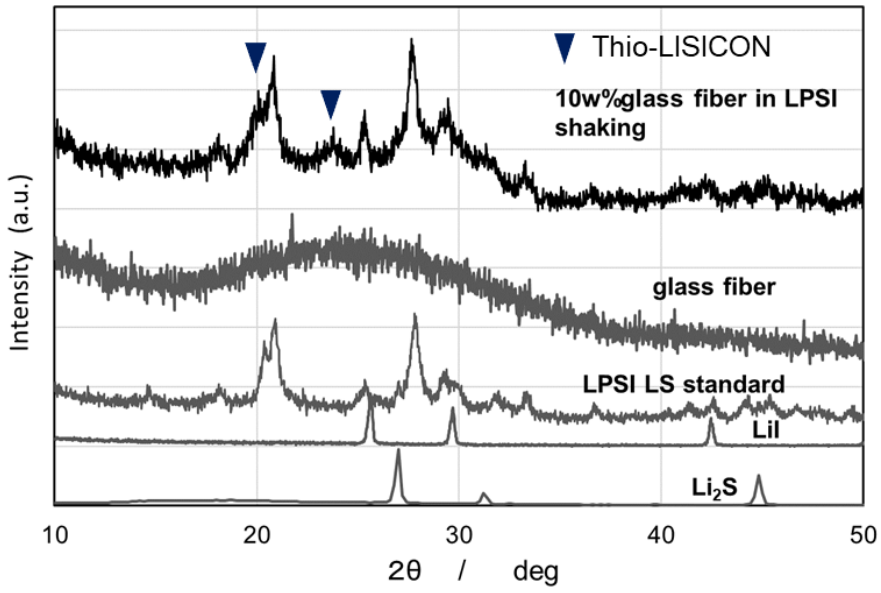

Fig. 5.2.4 XRD patterns of the obtained $Li_7P_2S_8I$ sheet containing 10 wt% glass fiber, glass fiber, and $Li_7P_2S_8I$ powder synthesized via liquid phase process with heat-treatment at 170°C.

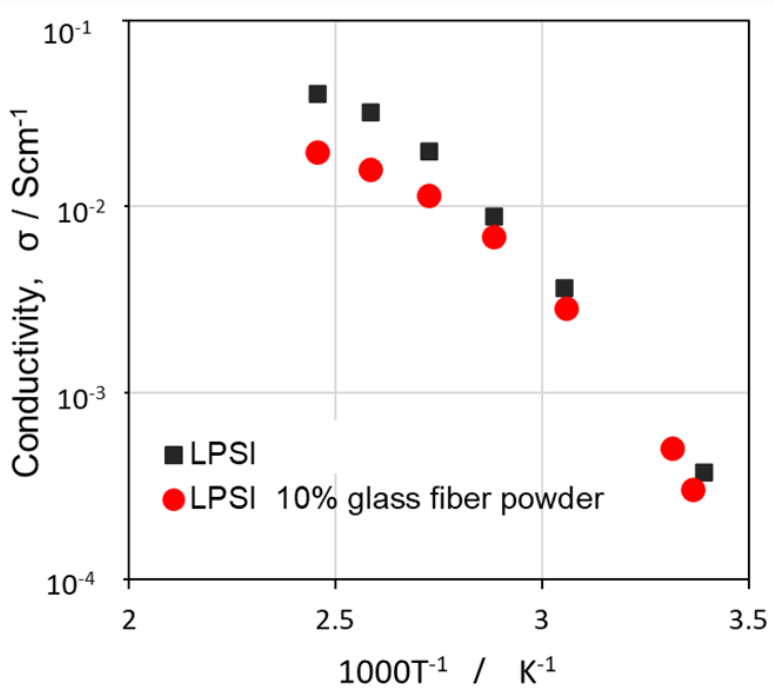

Fig. 5.2.5 Temperature dependence of ionic conductivities of $Li_7P_2S_8I$ and $Li_7P_2S_8I$ containing 10 wt% glass fiber.

Using obtained LPSI-glass fiber sheet for separator, the ASSLIB full cell was built up with NCM cathode composite and graphite containing LPSI sheet as an anode. Because the separator was thin, each layer should be smooth surface. To avoid short circuits, each layer was prepressed and after that they were pressed together at 250MPa. In Fig. 5.2.6, charge-discharge curves of the full cell were shown. This full cell repeatedly charged and discharged well when two LPSI sheets were used for the separator.

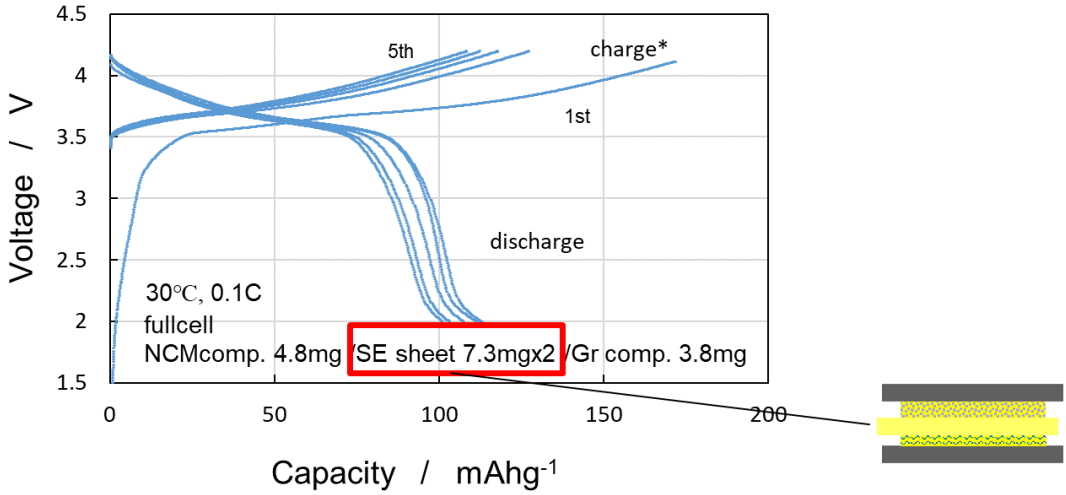

Fig. 5.2.6 Charge-discharge curves of Li-full cell using LPSI SE containing 10 w% glass fiber.

5.2.4 Conclusions

Self-standing LPSI sheets were directly fabricated with glass fiber by only one step without decreasing the ionic conductivity. When 10 wt% glass fiber was added, the sheet was successfully peered it off. The thickness was approximately 60 μm and the ionic conductivity showed 4.2 x 10^{-4} S cm^{-1} at 25 ℃. Using the LPSI sheet for the separator, the ASSLIB full cell was built up and it showed excellent charge-discharge performance.

Chapter 6
Characterization of Silicon as an anode of all-solid-state batteries

6.1 Deterioration analysis of Si composite anodes for all-solid-state batteries during charge–discharge by Auger electron spectroscopy and scanning electron microscopy with energy dispersive spectroscopy

6.1.1 Introduction

All-solid-state lithium batteries (ASSLIBs) using solid electrolytes (SEs) are considered safe because of their nonflammability and non-leakage of the electrolyte solvent. The SEs used in the ASSLIBs must possess high lithium (Li) ion conductivity to supply the ions to electrodes reversibly without the need of liquid-type electrolytes. This is achieved using sulfide SEs, which have higher ionic conductivities compared with organic liquid-type electrolytes at approximately 10^{-2} to 10^{-3} S cm^{-1} [1-3]. Moreover, the sulfide SEs exhibit plasticity with optimum contact between SE particles without sintering at high temperature[4]. The ASSLIB are developed from the composites of a ternary oxide material, $LiNi_xMn_yCo_zO_2$, as the cathode and sulfide SEs and graphite as the anode, and they have been widely studied[5,6].

Recently, the electrification of vehicles and the advancements in robotics has led to an increasing demand for batteries with high capacity and energy density. Si is considered an important material as an anode for ASSLIB while designing a high-energy density battery due to its large theoretical capacity of 4200 mAh g^{-1}. To enhance the capacity of the ASSLIBs, the use of surfer composite cells such as S or Li_2S composites as cathode materials are investigated[7,8]. These materials can achieve a capacity of more than 1000 mAh g^{-1}, which suggests that anodes with larger capacities are required.

In literature, several attempts have been made to utilize Si as an anode in liquid-type lithium batteries; however, it was reported that the anodes were damaged and developed cracks and fractures due to large volume changes of approximately 300% during the charge–discharge cycles[9,10]. Studies on ASSLIB using Si as an anode suggest that one of the problems was the rapid capacity reduction resulting from cracks at the boundary of Si particles[11,12]. The surface roughness findings of Si particles after charge–discharge cycles using cross-section scanning electron microscopy (SEM) have been reported[13]. Meanwhile, the research on ASSLIB using Si anode is limited; hence, it is necessary to

further evaluate the degradation of the Si anode. Herein, two types of sulfide SEs, $Li_{5.5}PS_{4.5}Cl_{1.5}$ (argyrodite)[14,15] and $Li_2S-P_2S_5-LiI$ system[16,17], were synthesized, and full cells were fabricated using the SE and Si composite anodes. These cells were investigated for charge–discharge cycling and the cross-section of the cells were observed before and after cycling, particularly for Si composite anodes.

6.1.2 Experimental

Preparation of electrolytes. $Li_{5.5}PS_{4.5}Cl_{1.5}$ electrolyte powder (argyro-SE) was synthesized via mechanochemical ball milling. The raw materials, Li_2S (Mitsuwa, 99.9%), P_2S_5 (Aldrich, 99%), and LiCl (Aldrich, 99.998%) were milled with fifteen balls of ZrO_2 (10 mmφ) at 600 rpm for 20 h in zirconia pots and heat-treated at 440 ℃ for 2 h. $Li_7P_2S_8I$ (LPSI-SE) was synthesized via a liquid phase shaking process. [16] The raw materials, Li_2S, P_2S_5, and LiI (Aldrich, 99%) were shaken with 30 g of ZrO_2 balls (4 mmφ), and ethyl propionate as a solvent in polypropylene tubes with constant shaking rate at 1500 rpm and 30 ℃ for 3 h. The obtained precursor slurry was dried in approximately 5 hPa while the temperature was gradually increased from 25 to 130 ℃ and heat-treated in argon atmosphere at 170 ℃ for 2 h.

Material characterization. The electrolyte powders thus obtained were evaluated using X-ray diffraction analysis (XRD) (Smart Lab, Rigaku). The ionic conductivities and their variations with temperature were measured using alternating-current impedance spectroscopy (SI 1260, Solatron) from 1 MHz to 10 Hz at a temperature of 25 to 150 ℃.

Fabrication of cells. Argyro-SE was used as a separator and an additive for active materials to increase their Li-ion conductivities, and the full cell fabricated using argyro-SE was named ASSLIB-argyro. Similarly, the full cell fabricated using LPSI-SE was named ASSLIB-LPSI. Cathode composites were prepared by mixing $LiNi_{1/3}Co_{1/3}Mn_{1/3}O_2$:SE:acetylene black (AB) in a 70:30:3 by weight ratio using an agate mortar. Anode composites were prepared by mixing silicon (Si) powder (Kojundo Chemical Laboratory; 5 μm):SE:AB in a 80:20:20 by weight ratio using the agate mortar. For the fabrication of full cells, 50 mg of SE was placed in a holder made of polyetheretherketone sandwiched between two stainless steel rods of 10 mm diameter and uniaxially pressed into pellets at a pressure of 50 MPa. Then, one side of the rods was removed, and 20 mg of cathode composite was placed and pressed at ~150 MPa for 5 min. Next, another side of the rods was removed, and 3 mg of anode composite was placed and pressed at ~250 MPa for 15 min. The obtained pellets with layers cathode

composite/SE/anode composite were ~500 μm thick and 10 mm in diameter. Subsequently, these pellets were placed in an over cell made of stainless steel and fixed with three bolts and nuts at 10 Nm. Finally, the cells were placed in a glass bottle filled with argon with two lead wires for establishing connections with the electrodes.

Analysis of cross-section of cells. The full cell pellets were removed from the cell folder before and after charge–discharge tests and cut using a punching device (Nogamigiken). The surface of the cell's cross-section was cleaned using a cross-section polisher (IB-19520CCP, JEOL) and was observed using a scanning electron microscope (SEM) (JSM-IT800, JEOL) with energy dispersive spectroscopy (EDS) (Gather-X, JEOL). Further, the Auger electron spectroscopy (AES) (JAMP-9510F, JEOL) was used to analyze the polished surfaces. All the analyses were performed under inert conditions.

6.1.3 Results and Discussion

Figures 6.1.1a and 6.1.1b show the XRD patterns of argyro-SEs, LPSI-SE, and the raw materials (Li_2S and LiI). The XRD pattern of the obtained Cl-rich argyro-SE was identical to that of the Li_6PS_5Cl (ICSD#131109). XRD peaks for the raw materials were not detected in the pattern of the argyro-SE. As revealed by Fig. 6.1.1b, LPSI-SE exhibited lower crystallinity than argyro-SE. The SEM images of argyro-SE (Fig. 6.1.1c) and LPSI-SE (Fig. 6.1.1d) are shown. Particle sizes of the obtained SEs ranged 1–5 μm and were aggregated to >10 μm. Temperature dependence of ionic conductivities of the SEs is also shown in Fig. 6.1.1e. Argyro-SE exhibited high ionic conductivity ($\sigma_{25\,°C}$ = 4.4 mS cm^{-1}) suggesting its high crystallinity. The ionic conductivity of LPSI-SE ($\sigma_{25\,°C}$ = 1.5 mS cm^{-1}) was slightly lower than that of argyro-SE, but it is expected to exhibit plasticity due to its low crystallinity.

Figures 6.1.2a and 2b show charge–discharge curves of ASSLIB-argyro and ASSLIB-LPSI from 1st to 5th discharge at 30 °C; the current rates were 0.1 C. Figure 6.1.2c shows the cycle performances of the full cells from 1st to 50th cycle. The capacities shown in Fig. 6.1.2 were calculated based on the weight of NMC in the cathode. Given that the effective capacities of NMC and Si were 170 and 3800 mAh g^{-1}, respectively, 30% of the total Si capacity in the anode was required for charge–discharge cycling. The discharge capacity of ASSLIB-argyro (red diamond in Fig. 6.1.2c) was higher than that of ASSLIB-LPSI (the black circle in Fig. 6.1.2c). However, it gradually decreased and became lower than that of the ASSLIB-LPSI after the 15th cycle. The ASSLIB-LPSI maintained the capacity although its primary capacity was lower than that of ASSLIB-argyro. The Nyquist plots of

impedance measurement of ASSLIB-LPSI after 1st and 11th charge were shown in Fig. 6.1.3.

To investigate the cause of the deterioration of full cells, their cross-section surfaces were observed using SEM-EDS. Figure 6.1.4 shows a backscattered electron image and six EDS mapping images (C, O, Si, P, S, and Cl) of the cross-section of the full cell pellets using argyro-SE after the 50th charge–discharge cycle. At the anode, Si particles were bright white due to their higher atomic weight as compared with SE. Dark regions were observed at the anode near the boundary of the separator, which suggests a low concentration of Si, and the presence of oxygen corresponded to the EDS mapping image of oxygen. Figure 6.1.5 shows that the line analysis of the cross sections of ASSLIB-argyro (Fig. 6.1.5a) after the 50th charge–discharge taken from EDS mapping data in Fig. 6.1.4 and (Fig. 6.1.5b) before cycles. In Fig. 6.1.5, the horizontal axis represents the distance from an electron collector at the anode. Further, the green line, which represents oxygen in Fig. 6.1.5a, has peaks near the edge of the anode and that of the cathode. The green line in Fig. 6.1.5b does not exhibit any peaks at the anode area.

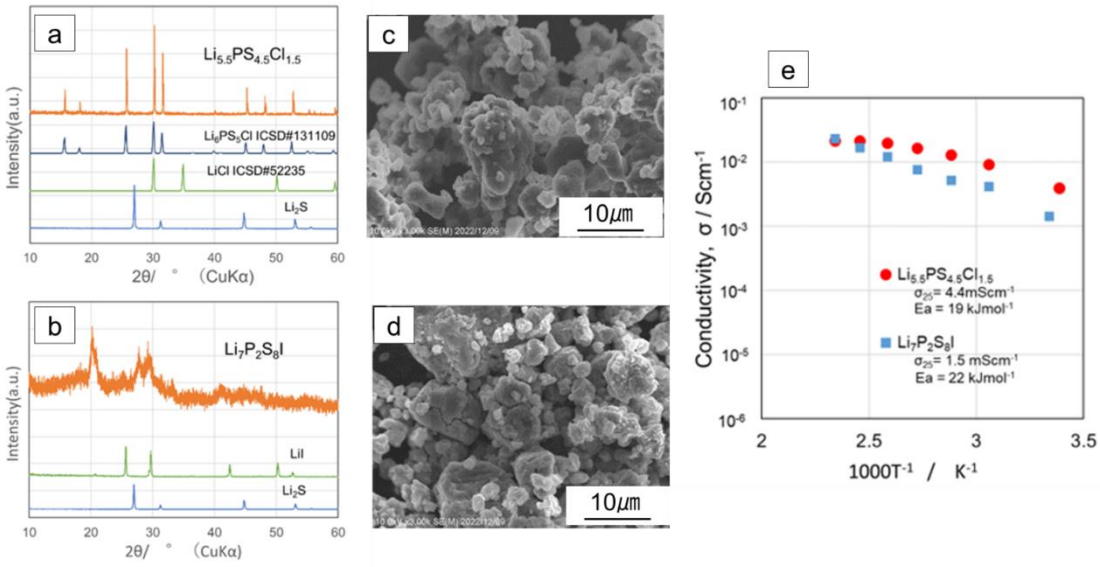

Fig. 6.1.1 Electrolytes characters used in all-solid-state lithium batteries (ASSLIBs). X-ray diffraction (XRD) patterns and scanning electron microscope (SEM) images of $Li_{5.5}PS_{4.5}Cl_{1.5}$ (a, c), LPSI milled after liquid phase synthesis (b, d), and the temperature dependence of conductivities (e).

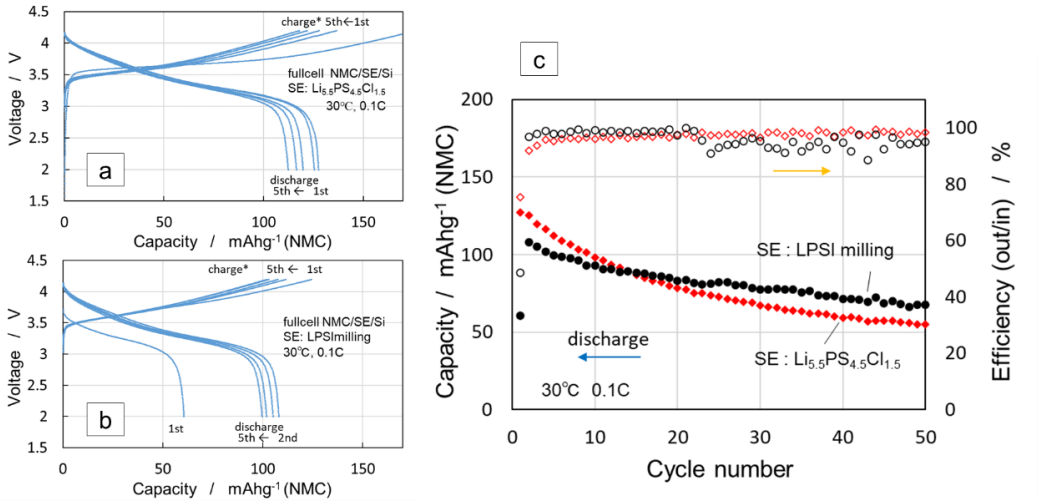

Fig. 6.1.2 Charge and discharge curves of ASSLIBs (a, b) configured as follows: $LiNi_{0.33}Co_{0.33}Mn_{0.33}O_2$ (NMC) composite 20 mg | SE 50 mg | Si composite 3 mg. (c) is the cycle performance of discharge capacities and efficiency (discharge; Li-ion out from anode/charge; Li-ion into anode).

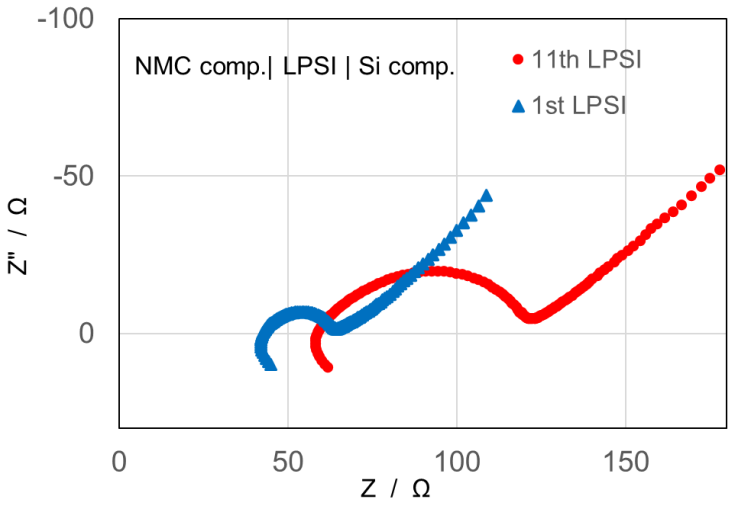

Fig. 6.1.3 Nyquist plots of electronic impedance measurements of ASSLIB-LPSI after the 1st and 11th charge. The blue triangles (▲) and the red dots (●) represent the plot obtained after the 1st and 11th charge, respectively.

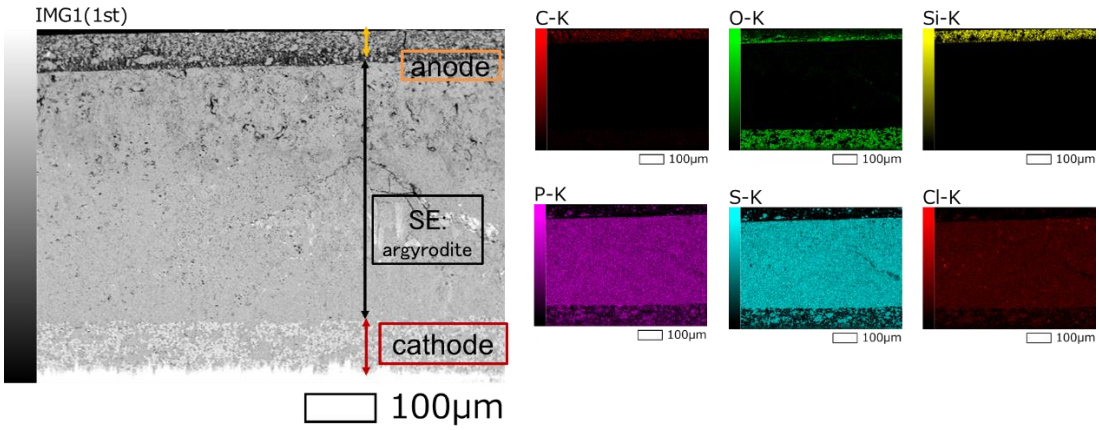

Fig. 6.1.4 Cross-section SEM image and the element mappings of ASSLIB-argyro after 50th cycle using scanning electron microscopy with energy dispersive spectroscopy (SEM–EDS).

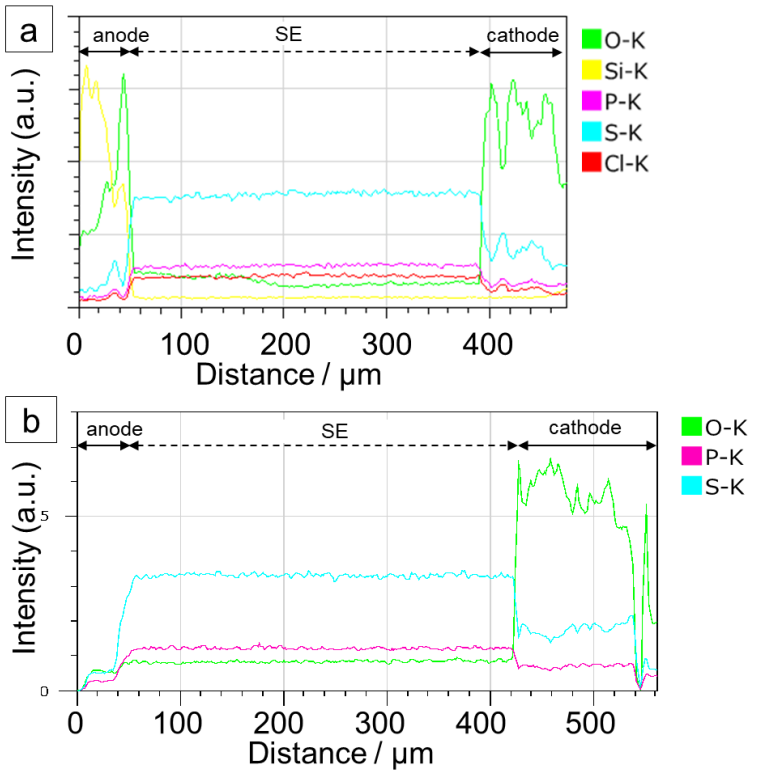

Fig. 6.1.5 Line element analysis of the cross sections of ASSLIB from the anode to cathode using SEM-EDS. (a) after the 50th cycle and (b) before the cycle for ASSLIB-argyro.

The Si used for the electrode in our study is a commercial reagent and contains more oxygen than Si materials commonly used in electronic devices. The purity of the Si reagent is 99.9%. The thickness of native oxide layers on the Si particles (5 μm in diameter) was calculated and estimated to be 1.5 nm assuming that the remaining 0.1% consisted entirely of oxygen. However, oxygen could not be observed in the Si anode probably due to the sensitivity limit before charge–discharge (Fig. 6.1.5b) using SEM–EDS mapping. Therefore, the oxygen-rich belt was formed in the boundary area during charge–discharge cycling.

Figure 6.1.6 shows the cross-section SEM-EDS images of anode layers of the ASSLIB-argyro pellet zoomed up Fig. 6.1.4 and that of the ASSLIB-LPSI pellet. EDS mappings were used to study the elemental distribution and were composed of colored elements. The green parts corresponding to oxygen are shown in both (a) and (b); they are located on the surface and/or boundary of Si particles at the edge of the anode near the electrolyte separator. The concentration of elements observed in the EDS mappings of Fig. 6.1.6 (C, Si, P, and S) and others was considerably lower than that of the oxygen. It is plausible that the oxygen observed in the dark anode areas was from the oxides containing lithium, which is hardly detected by EDS due to being light element. Some cracks were observed in both pellets, which might have been produced during the sample processing for SEM observation. In regions containing oxygen, small cracks were observed for the ASSLIB-LPSI pellet, which may be due to the low hardness of LPSI.

AES of the cross-section of the anode layers was carried out to analyze the oxides generated during charge–discharge cycling at the anode layers. In this analysis, the Auger electrons produced by electron beam irradiation are detected and compared with known standards to determine the chemical composition of the sample surface. Figure 6.1.7a shows Auger spectra of the two dark parts at the cross-section of the anode area of ASSLIB-argyro pellet, in which the central part is shown in a green square and the other boundary part near SE is shown in a red square. The spectrum of the boundary parts showed larger peaks corresponding to lithium than those of the central parts. This indicates that Li^+ ions remain in the anode despite discharging; moreover, they were present in large amounts near the boundary of the SE. Thus, the charge–discharge reactions do not proceed homogeneously, but rather from the separator toward the electron collector. Two small Si peaks were observed on the red spectrum indicated by the dark parts near the boundary. One of the peaks near 80 eV corresponds to silicon oxides[18,19]. It is suggested that the oxidation of Si, the anode active material, occurred during the charge–discharge cycle, resulting in the formation of silicon oxide in small amounts. Figure 6.1.7b

shows the AES spectra of ASSLIB-LPSI after 50 charge–discharge cycles, which indicates the same tendency as that of the ASSLIB-argyro. From the spectrum, the oxygen peak on the central part of the spectrum of ASSLIB-LPSI was smaller than that of the boundary and the ASSLIB-argyro. This suggests that the Si area utilizing the charge–discharge reaction of ASSLIB-LPSI is narrower than that of the ASSLIB-argyro as the ionic conductivity of LPSI is lower than that of the argyrodite. Figure 6.1.7c shows the enlarged spectra of the low energy region near 50 eV in Fig. 6.1.7a and 6.1.7b, along with the spectra of standard material, metal Li, Li_2O, LiCl, and Li_2CO_3. Auger spectra obtained from the cross-section of the ASSLIB anode area, especially the boundary parts of both ASSLIBs, show three peaks at approximately 40, 34, and 24 eV, which corresponded to Li_2O compared with the spectra of standard materials. Furthermore, according to the shape of the spectrum at approximately 24 eV, LiCl is present in the anode of ASSLIB-argyro due to containing Cl in the electrolyte. However, EDS mappings and Auger spectra show the presence of the oxygen layers near the separator. Therefore, the oxygen layers near the separator are mainly Li_2O. Consumption of a limited number of Li^+ ions in a full cell system to produce Li_2O leads to reduced cell capacity due to Li^+ ion depletion and increased irreversible capacity. Moreover, covering Si particles in the anode with Li_2O increases the resistance as the ionic conductivity of Li_2O is lower than that of the SE.

Finally, it is necessary to discuss the sources of oxygen. Figures 6.1.8a and 6.1.8b show the oxygen concentration mapping and the line element analysis, respectively. As seen in the SE area of Fig. 6.1.8a, an oxygen layer was not observed on the side of the cathode active material containing oxygen, but an oxygen layer of ~145 μm was observed on the anode side. According to the line element analysis, the intensity of oxygen on the anode side of SE was higher than that on the cathode side, suggesting that cathode active materials are not the sources of oxygen generated in the anode after charge–discharge cycles. Furthermore, the oxygen layers were not observed in the cross-section of the anode area of the cells using graphite as anode active materials with the same configuration. In contrast, the presence of an oxygen layer was confirmed in a cell comprising lithium–sulfur batteries configured as Si composite | argyro-SE | Li_2S composite. The SEM–EDS images of the cross-section of these cells are shown in Fig. 6.1.9 (using graphite as anode active materials) and Fig. 6.1.10 (using lithium sulfide as cathode active materials). These findings indicate that the phenomenon of oxide formation is not caused by the contamination from SE or ambient air but by the Si itself, which has a certain amount of hydroxide ions on the particle surface. Presumably, the SE near the anode was damaged by the diffused hydroxides that permeated from the Si surface to the SE, which led to a decreased capacity

of full cells that use Si as an anode active material. In terms this damage, ASSLIB-LPSI maintained slightly better discharge capacity than ASSLIB-argyro, although its initial capacity was lower than that of argyro, which must be related to the higher stability of LPSI toward humidity than argyrodite[20-24].

.

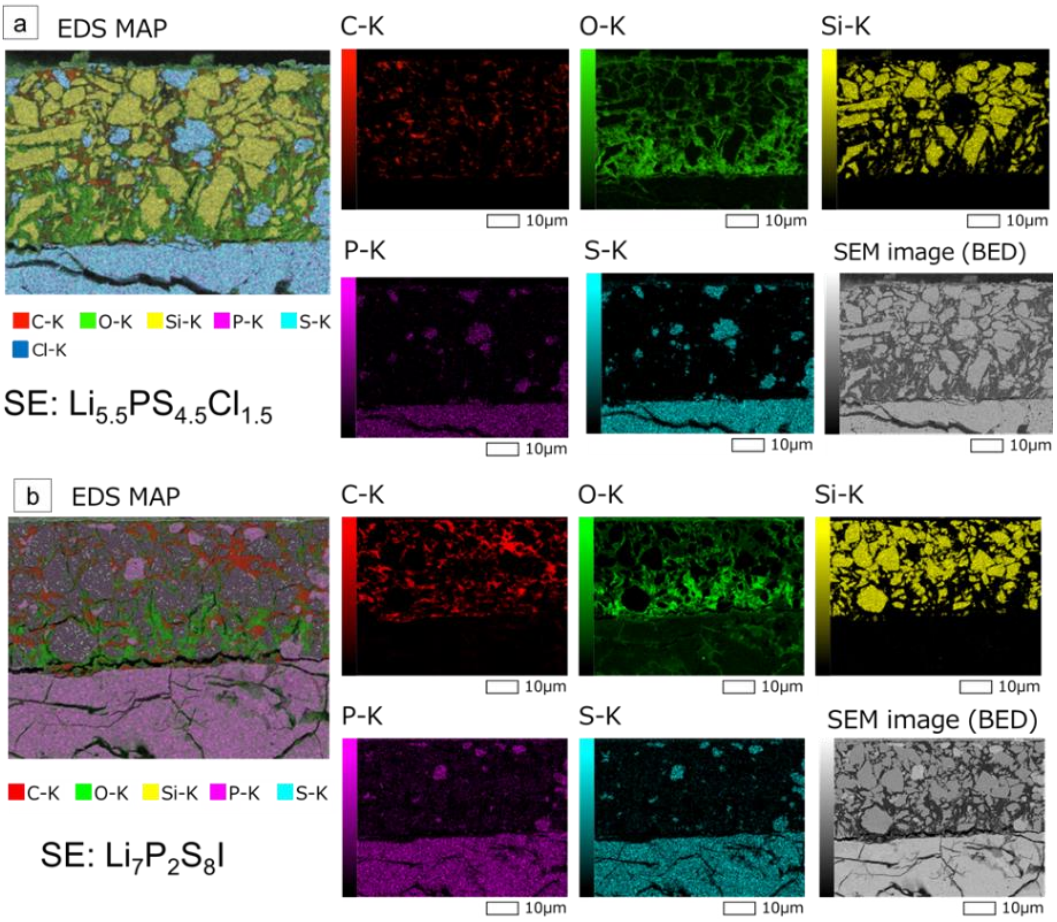

Fig. 6.1.6 Cross-section SEM images and the element mappings of ASSLIB anode using SEM–EDS. (a) ASSLIB-argyro and (b) ASSLIB-LPSI.

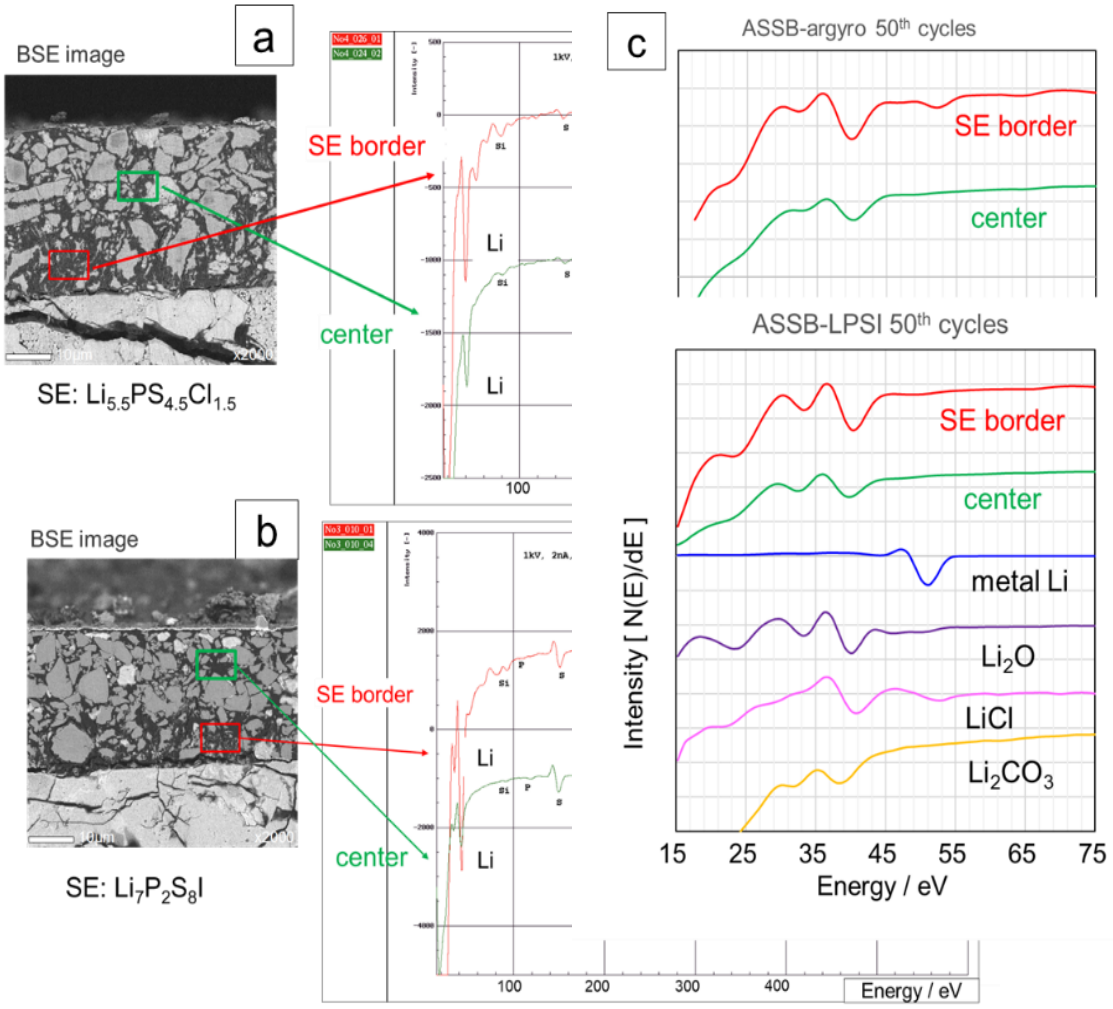

Fig. 6.1.7 Auger electron spectroscopy (AES) spectra of the cross-section surface of anode layers (Si composite). (a) ASSLIB)-argyro and (b) ASSLIB-LPSI after the 50th charge–discharge cycle with the SEM images using backscattering electrons. (c) enlarged spectra of (a) and (b) with spectra of metal Li, Li_2O, LiCl, and Li_2CO_3.

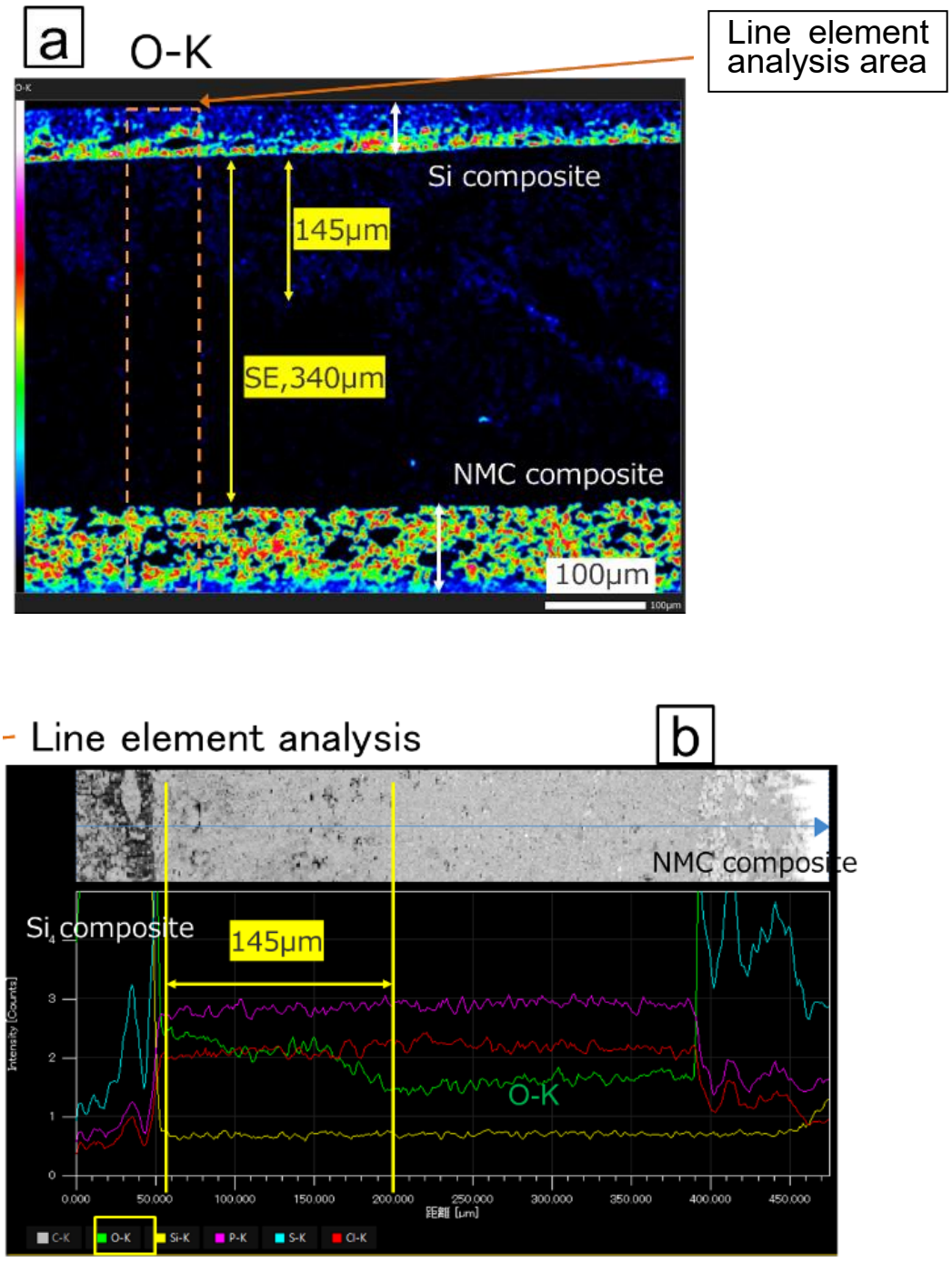

Fig. 6.1.8 Elemental mapping of the cross-section of ASSLIB-argyro using SEM-EDS (a) and the line element analysis results (b).

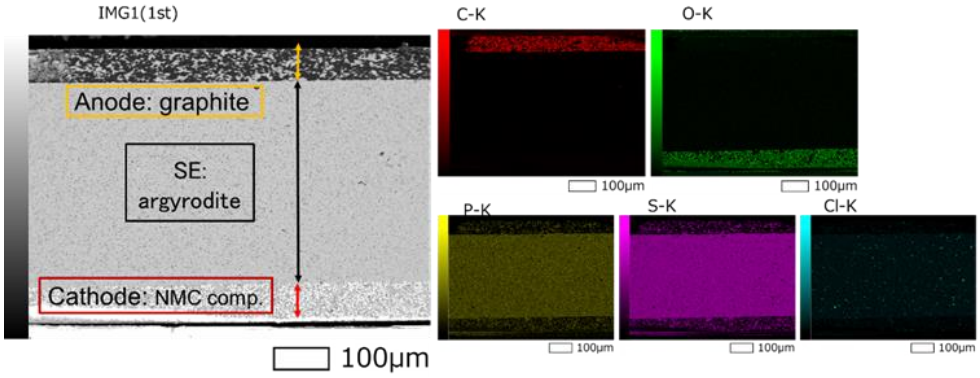

Fig. 6.1.9 Cross-section SEM image and the element mappings of ASSLIB-argyro after 50th cycle using graphite as anode active materials by scanning electron microscopy with energy spectroscopy (SEM–EDS).

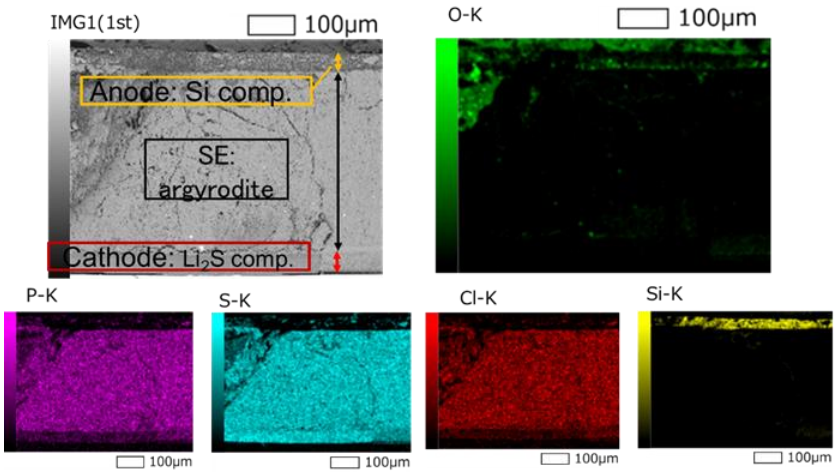

Fig. 6.1.10 Cross-section SEM image and the element mappings of Lithium-sulfur ASSLIB-argyro after 53th cycle using Li_2S composites as cathode and Si composites as anode by SEM-EDS.

6.1.4 Conclusions

The full cells of ASSLIB with Si composites as anodes were fabricated using two types of SE, namely argyrodite and LPSI. The presence of Li_2O in both the anode layers of the cells that used argyrodite and LPSI after the 50th charge–discharge cycle was confirmed. The reaction of oxygen with lithium ions progressed from the SE side to the electron collector side. The formation of Li_2O was one of the causes for the decreased capacity of the cells; these phenomena occurred when Si composites were used as anode active materials. Therefore, while designing full cells using Si as an anode, it is crucial to suppress Li_2O generation during charge–discharge cycles.

References

1) R. Kanno, M. Murayama, Lithium ionic conductor thio-LOSICON: The Li_2S-GeS_2-P_2S_5 System, *J. Electrochem. Soc.* **148**, A742− A746 (2001).

2) E. Rangasamy, Z. Liu, M. Gobet, K. Pilar, G. Sahu, W. Zhou, H. Wu, S. Greenbaum, C. Liang, An iodide-based $Li_7P_2S_8I$ supereionic conductor, *J. Am. Chem. Soc.* **137**, 1384-1387 (2015).

3) A. Hayashi, K. Minami, S. Ujiie, M. Tatsumisago, Crystal structure of a superionic conductor, $Li_7P_3S_{11-z}$ glass-ceramic electrolytes, *J. Non-Cryst. Solids* **356**, 2670− 2673 (2010).

4) A. Sakuda, A. Hayashi, M. Tatsumisago, Sulfide solid electrolyte with favorable mechanical property for all-solid-state lithium battery, *Sci. Rep.* **3**, 2261-2266 (2013).

5) S. Yang, K. Yamamoto, X. Mei, A. Sakuda, T. Uchiyama, T. Watanabe, T. Takami, A. Hayashi, M. Tatsumisago, High rate capability from a graphite anode through surface modification with lithium iodide for all-solid-state batteries, *ACS Appl. Energy Mater.* **5**, 1, 667-673 (2022).

6) N. Zhang, A. Beutl, K. Rajinovic, J. Kahr, M. Jahn, M. Nestoridi, Scalable preparation of practical 1Ah all-solid-state lithium-ion batteries cells and their abuse tests. *J. Energy Storage* **59,** 106547 (2023).

7) M. Nagao, A. Hayashi, M Tatsumisago, High-capacity Li_2S-nanocarbon composite electrode for all-solid-state rechargeable lithium batteries, *J. Mater. Chem.* **22**, 10015-10020 (2012).

8) H. Gamo, N.H.H. Phuc, M. Ikari, K. Hikima, H. Muto, A. Matsuda, Electrochemical redox of Li_2S− CaS and− CaX_2 (X=Cl, Br, and I) cathode materials for all-solid-state lithium-sulfur batteries, *Electrochim. Acta* **431**, 141149 (2022).

9) D.H. Kim, H.A. Lee, Y.B. Song, J.W. Park, S.M. Lee, Y.S. Jung, Sheet-type Li_6PS_5Cl-infiltrated Si anodes fabricated by solution process for all-solid-state lithium-ion batteries. *J. Power Sources* **426**, 143-150 (2019).

10) R. Miyazaki, N. Ohta, T. Ohnishi, I. Sakaguchi, K. Takada, An amorphous Si film anode for all-solid-state lithium batteries, *J. Power Sources* **272**, 541-545 (2014).

11) J.R. Szczech, S. Jin, Nanostructured silicon for high capacity lithium battery anodes. *Energy Environ. Sci.* **4**, 56-72 (2011).

12) H. Wu, Y. Cui, Designing nanostructured Si anodes for high energy lithium ion batteries, *Nano Today* **7**, 414-429 (2012).

13) M. Yamamoto, Y. Terauchi, A. Sakuda, A. Kato, M. Takahashi, Effects of volume variations under different compressive pressures on the performance and microstructure of all-solid-state batteries,

J. Power Sources **473**, 228595 (2020).

14) L. Zhou, K.H. Park, X. Sun, F. Lalere, T. Adermann, P. Hartmann, L.F. Nazar, Solvent-engineered design of argyrodite Li_6PS_5X (x = Cl, Br, I) solid electrolytes with high ionic conductivity. *ACS Energy Lett.* **4**, 265-270 (2019).

15) L. Peng, S. Chen, C. Yu, C. Wei, C. Liao, Z. Wu, H. L. Wang, S. Cheng, J. Xie, Enhancing moisture and electrochemical stability of the $Li_{5.5}PS_{4.5}Cl_{1.5}$ electrolyte by oxygen doping, *ACS Appl. Mater. Interef.* **14**, 4179-4185 (2022).

16) N.H.H. Phuc, E. Hirahara, K. Morikawa, H. Muto, A. Matsuda, One-pot liquid phase synthesis of (100− x) Li_3PS_4− xLiI solid electrolytes. *J. Power Sources* **365**, 7-11 (2017).

17) S. Spannenbergen, V. Miß, E. Klotz, J. Kettner, M. Cronau, A. Ramanayagaehbergm, F. Capua, M. Elsayed, R. Krause-Rehberg, M. Vogel, B. Roling, Annealing-induced vacancy formation enables extraordinarily high Li^+ ion conductivity in the amorphous electrolyte 0.33 LiI + 0.67 Li_3PS_4. *Solid State Ionics* **341**, 115040 (2019).

18) K. Nishiguchi, Y. Takahashi, K. Takahashi, Application of Auger analysis to titanium/silica interface, *Yousetsugakkai ronbunsyu* **9**, 537-544 (1991).

19) L. Buzi, Y. Yang, F.J. Dominguez-Gutierrez, A.O. Nelson, M. Hofman, P.S. Krstic, R. Kaita, B.E. Koel, Hydrogen retention in lithium and lithium oxide films, *J. Nucl. Mater.* **502**, 161-168 (2018).

20) H. Muramatsu, A. Hayashi, T. Ohtomo, S. Hama, M. Tatsumisago, Structural change of Li_2S− P_2S_5 sulfide solid electrolytes in the atmosphere, *Soild State Ionics* **182**, 116-119 (2011).

21) M. Calpa, N.C. Rosero-Navarro, A. Miura, R. Jalem, Y. Tateyama, K. Tadanaga, Chemical stability of Li_4PS_4I solid electrolyte against hydrolysis, *Appl. Mater. Today* **22**, 100918 (2021).

22) R.F. Indrawan, T. Yamamoto, N.H.H. Phuc, H. Muto, A. Matsuda, Liquid-phase synthesis of 100Li_3PS_4-50LiI-$x$$Li_3PO_4$ solid electrolytes, *Solid State Ionics* **345**, 115184 (2020).

23) H. Tsukasaki, H. Sano, K. Igarashi, A. Wakui, T. Yaguchi, S. Mori, Deterioration process of argyrodite solid electrolytes during exposure to humidity-controlled air, *J. Power Sources* **524**, 231085 (2022).

24) G.F. Dewald, S. Ohno, M.A. Kraft, R. Koerver, P. Till, N.M. Vargas-Barbosa, J. Janek, W.G. Zeier, Experimental assessment of the practical oxidative stability of lithium thiophosphate solid electrolytes, *Chem. Mater*. **31**, 8328-8337 (2019).

Chapter 7
General Conclusions

This thesis reported the preparation of sulfide solid electrolytes via LS process and active material composites with them via SEED process. These materials were built up to ASSLBs. In the fabrication of ASSLBs, I identified key challenges that must be overcome, proposed improvement methods for each, and evaluated the results.

Chapter 1 described the general introduction of this thesis, and I have provided an overview of each chapter.

Chapter 2 described the review of the liquid phase shaking process based on our laboratory's works. LPS was synthesized via LS process and the obtained LPS was evaluated as an electrolyte using XRD analysis, Raman, EIS, cyclic voltammogram. LPS via LS process was meta-stable ß-phase structure and the ionic conductivity was 1.5 x 10^{-4} S cm^{-1}. Further, the LPS was mixed with NMC and evaluated as a cathode for ASSLB. LPSI was synthesized via LS process. It was indicated that the structure of LPSI was similar to the structure of Li_4PS_4I and the ionic conductivity was 3.8 x 10^{-4} S cm^{-1}. By adjusting the reaction conditions, a phase similar to the thio-LISICON region II observed in LGPS appeared in LPSI. The ionic conductivity reached 1.0 x 10^{-3} S cm^{-1}at 25 ℃.

Chapter 3 described the synthesis of the cathode composite using the SEED method. LPS was directly produced on the active material NMC on the basis of the liquid-phase shaking process. The impedance profiles showed that the composite interface between LPS and the active material by the SEED method maintained good contacts after the 10th charge-discharge cycles. Also, crystalline LPSI electrolyte was directly produced on the active material NMC by the SEED method. The charge-discharge profiles of the all-solid-state cells show that the composite interface between LPSI and the active material formed by SEED method has good contacts.

SG particles used as anodes for ASSLBs were coated with the sulfide solid electrolyte LPSI using the SEED process, and ASSLIBs were assembled using the obtained SG composites, sulfide solid electrolyte, argyrodite, and LPSI. Cross-sectional observation using SEM confirmed that the LPSI coating was not only on the surface of the SG particles but also inside them. When the weight ratio SG to LPSI was 87:13, the interfacial contact area increased, resulting in good output performance for the ASSLIB. To further enhance the charge–discharge performance, a hetero-SE coating was applied. In this approach, SG particles were first coated with an ultra-thin LPSI layer and then hand-mixed in a mortar with an argyrodite SE. When the thin-coated SG (SG: LPSI = 97:3) was

mixed with the argyrodite SE (SG:total SE =70:30), the ASSB exhibited an excellent capacity retention rate owing to the improved interface contact between the SG particles and SEs. Boundary control between active materials and SEs is one of the most critical issues for fabricating ASSLBs. This LPSI coating via SEED process is a promising method to improve the problem.

Chapter 4 described the Li_4SnS_4 electrolyte was prepared from Na_4SnS_4 aqueous solution by ion exchange, freeze drying and subsequent heat-treatment. Na ions in the Na_4SnS_4 were almost exchanged to Li ions using cation exchange resins. The ionic conductivity of Li_4SnS_4 obtained by a twice-repeated ion exchange and heat-treated at 240 ℃ showed 1.0×10^{-4} S cm^{-1} at 25 ℃. The XRD pattern of the Li_4SnS_4 after exposure to ambient air and re-heat-treatment at 240 ℃ was essentially the same as before. Because of its stability in both the atmosphere and water, it was suggested that the Li_4SnS_4 obtained via this IE process could be recycled as electrolyte for ASSLBs. Li_3SbS_4 electrolyte was synthesized from an Na_3SbS_4 aqueous solution by ion exchange, freeze-drying, and subsequent heat treatment. The temperature dependence of the ionic conductivities of $(100 - x)$ $Li_3SbS_4{\cdot}xLiI$ obtained via the IE process showed a unique behavior, in which the ionic conductivity of $60Li_3SbS_4{\cdot}40LiI$ sharply increased from 10^{-7} S cm^{-1} at 25 °C to 8.4×10^{-3} S cm^{-1} at 65 °C. Further, the ion conductivity reached 1.3×10^{-4} S cm^{-1} at 25 °C by homogenizing the surface of the particles using mechanical milling and annealing. Some XRD measurements and investigation using TEM showed LiI thin layers on the surface of Li_3SbS_4–LiI primary particles. This is crucial in maintaining the high ion conductivity from around 70 °C to room temperature. The Li_3SbS_4–LiI SEs were stable in ambient air and the cathode composite containing $60Li_3SbS_4{\cdot}40LiI$ showed good charge−discharge performance. Therefore, from the industrial and safety viewpoints, the electrolyte obtained via the IE process is an excellent candidate for ASSLBs.

Chapter 5 described fabrication of all-inorganic, self-standing, argyro-SE sheets by combining solvents to disperse SE particles with SiO_2 fibers. The ionic conductivities of the sheets of 61 μm in thickness were 4.2×10^{-4} S cm^{-1} at 25 ℃. I fabricated full cells using these sheets as separators sandwiched between an NCM-composite positive electrode and a graphite-composite negative electrode. After molding a full cell at 510 MPa, it performed well as a rechargeable ASSLB. Further, I have devised a simpler method for manufacturing LPSI electrolyte sheets. Self-standing LPSI sheets were directly fabricated with 10 wt% glass fiber by only one step without decreasing the ionic conductivity. Using the LPSI sheet for the separator, the ASSLB full cell was built up, and it showed excellent charge-discharge performance. This process saves on the solvents used for resolving and the

heat resources consumed during heat treatment. For mass production, saving energy reduces costs and is important for building a sustainable society.

Chapter 6 described that the full cells of ASSLB with Si composites as anodes were fabricated using two types of SE, namely argyrodite and LPSI. The presence of Li_2O in both the anode layers of the cells that used argyrodite and LPSI after the 50^{th} charge–discharge cycle was confirmed. The reaction of oxygen with lithium ions progressed from the SE side to the electron collector side. The formation of Li_2O was one of the causes for the decreased capacity of the cells; these phenomena occurred when Si composites were used as anode active materials. Therefore, while designing full cells using Si as an anode, it is crucial to suppress Li_2O generation during charge–discharge cycles.

Chapter 7 described the general conclusions and future works of this thesis.

Future work

Through this work, I have handled several sulfide solid electrolytes such as Li_3PS_4-LiI, Li_4SnS_4 and Li_3SbS_4-LiI. Especially, LPSI is a promising material for ASSLB. First, about starting materials, rare-earth elements were not contained, they are not expensive, Second, they did not contain dangerous elements and flammable solvents. Third, the temperature of heat treatment is low, which is gentle for the earth. Fourth, LPSI is stable against metallic lithium due to its resistance to reduction. Finally, it is stable against humidity compared to other phosphorus-containing sulfide solid electrolytes. In Chapter 5, I introduced self-standing LPSI sheet. This sheet has excellent ability to the separator for ASSLBs. I would like to improve the conductivity and the mechanical strengthen of the sheets by (1) adding more flexible support materials like silicone, and (2) recombining support materials using sol-gel process.

On the other hand, Li_4SnS_4 prepared by IE process is very stable in aqueous solution, so it does not decompose when dissolved in water and does not generate H_2S gas. It can also be recycled. I want to consider the effective use of Li_4SnS_4. However, Li_4SnS_4 has low reduction resistance, making it difficult to use lithium and silicon as anode active materials. I would like to research available negative electrode materials, of which keypoints are (1) electcochemical stability for reduction voltage, (2) large capacity, and (3) low volume change during charge-discharge cycles.

Recently, lithium-ion batteries are widely used in everyday items, including those used in vehicles and portable devices. I believe that further improving the safety of lithium batteries is a crucial misson for the battery material reseachers and battery developers.

List of Publications

Journal papers

1. **R. Matsuda,** E. Hirahara, N.H.H. Phuc, H. Tsukasaki, S. Mori, A. Matsuda, "Preparation of $LiNi_{1/3}Mn_{1/3}Co_{1/3}O_2/Li_3PS_4$ cathode composite particles using a new liquid-phase process and application to all-solid-state lithium batteries," Journal of the Ceramic Society of Japan, Vol. 126, No. 10, pp.826–831, 2018.
2. **R. Matsuda,** T. Kokubo, N.H.H. Phuc, H. Muto, A. Matsuda, "Preparation of ambient air-stable electrolyte Li_4SnS_4 by aqueous ion-exchange process," Solid State Ionics, Vol. 345, 115190 (4 pages), 2020.
3. **R. Matsuda,** H. Muto, A. Matsuda, "Air-stable Li_3SbS_4–LiI electrolytes synthesized via an aqueous ion-exchange process and the unique temperature dependence of conductivity," ACS Applied Materials Interfaces, Vol. 14, No. 46, pp. 52440-52447, 2022.
4. **R. Matsuda,** A. Tanaka, K. Yanagihara, Y. Sasaki, K. Hikima, H. Muto, A. Matsuda, "Deterioration analysis of Si composite anodes for all-solid-state batteries during charge-discharge by Auger electron spectroscopy and scanning electron microscopy with energy dispersive spectroscopy," Journal of Physical Chemistry C, Vol. 127, No. 33, pp. 6508–16514, 2023.
5. **R. Matsuda,** I. Y. Malya, T. Matsushita, K. Hikima, A. Matsuda, "Fabricating self-standing argyrodite electrolyte sheets containing SiO_2 fibers for all-solid-state batteries," Solid State Ionics, Vol. 417, 116684 (7 pages), 2024.
6. **R. Matsuda,** M. Takahashi, K. Hikima, H. Muto, A. Matsuda, "Hetero-coating of spherical graphite with sulfide solid electrolytes via the SEED process for all-solid-state lithium batteries," Journal of the Ceramic Society of Japan, Vol. 133, No. 9, pp. 569-576, 2025.

Proceedings

1. **Reiko Matsuda,** Eito Hirabara, Nguyen Huu Huy Phuc, Hiroyuki Muto, Atsunori Matsuda, "Composite cathode of NCM Particles and Li_3PS_4-LiI electrolytes prepared using the SEED method for all-solid-state lithium batteries," IOP Conference Series Materials Science and Engineering, Vol. 429, No. 1, 012033 (5 pages) 2018.

Acknowledgements

The studies in this doctoral thesis have been conducted in the department of electrical and electronic information of engineering, Toyohashi University of Thchnology.

I would like to sincerely express my gratitude to Professor Dr. Ryoji Inada, Department of Electrical and Electronic Information Engineering, and professor Dr. Takanori Mizushima of Department of Applied chemistry and Life Science, Toyohashi University of Technology, for their critical reading of the thesis and many useful suggestions for its improvement. I would express my deepest gratitude to Professor Dr. Hiroyuki Muto, Institute of Liberal Arts and Science, Toyohashi University of Technology, for his useful suggestion and kind encouragement through this work.

I would also express my deepest gratitude to Professor Dr. Atsunori Matsuda for his continuous guidance and encouragement. I would like to express my gratitude to Associatate Professor Go Kawamura, Associate Professor Tan Wai Kian, and Assistant Professor Kazuhiro Hikima of Toyohashi University of Technology, for their great supports.

Dr. Nguyen Huu Huy Phuc of Hochiminh City University of Technology provided great insight and vision into my research.

I would like to thank of my dissertation research group members of Toyohashi University of Technology. I would particularly thank Dr. Hideto Yamada, Dr. Shota Azuma, Ms. Ikuyo Kusaba, Mr. Eito Hirahara, Mr. Takumi Kokubo, Mr. Matsushita Takuya, and the secretarial staff for their collaborations. Especialy, I would like to express my deepest gratitude to my colleagues Ms. Masayo Takahashi, Dr. Radian Febi Indrawan, and Dr. Irine Yunhafita Malya for their invaluable support in my research and laboratory life.

I would like to express my sincere thanks to Emeritus Professor Dr. Tsutomu Minami for his encouraged words, which suprred me on, and I felt motivated, Emiritus Professor Dr. Masahiro Tatsumisago, Professor Dr. Akitoshi Hayashi, Professor Dr. Shigeo Mori, and Associate Professor Dr. Atsushi Sakuda of Osaka Metropolitan University as well as Professor Dr. Nobuya Machida of Konan University for their assistance and useful discussion. I also thank Mr. Itayama of LIBTEC and Mr. Sasaki et al. of JEOL Ltd. for their assistance and useful discussions regarding the SEM and TEM analysis.

This study was partially supported by the SOLiD-EV and SOLiD-Next projects of the New

Energy and Industrial Technology Development Organization (NEDO), Japan, and the Advanced Low Carbon Technology Special Research for Innovative Next Generation Batteries (JST-ALCA-SPRING) program of the Japan Science and Technology Agency. This research was financially supported by Grant-in-Aid for Scientific Research from the Ministry of Education, Culture, Sports, Science and Technology of Japan.

Finally, I would like to express my deepest gratitude and respect from bottom of my heart to my husband, Dr. Atsumori Matsuda, and to thank my family, my daughters, my son, my sisters, and their families. I would like to deliver my thanks to my parents and grandparents.